

**The effect of lithology, sub-bed scale heterogeneities, and
mechanical stratigraphy on fault and fracture properties in
coal bearing sequences**

Billy J. Andrews BSc. (Hons)

Thesis submitted for Degree of Doctor of Philosophy

Department of Civil and Environmental Engineering

Faculty of Engineering

University of Strathclyde

July 2020

Declaration

'This thesis is the result of the author's original research. It has been composed by the author and has not been previously submitted for examination which has led to the award of a degree.' 'The copyright of this thesis belongs to the author under the terms of the United Kingdom Copyright Acts as qualified by University of Strathclyde Regulation 3.50. Due acknowledgement must always be made of the use of any material contained in, or derived from, this thesis.'

Signed: Billy Andrews

Date: 11/11/2019

Abstract

While sub-surface extraction of coal in the UK has ceased, renewed interest into the internal structure and growth of faults cutting coal measures exists due to applications for mine geothermal projects and analogues for natural gas plays in the Southern North Sea. In this study three field sites are used with detailed field observations, geological mapping, and sedimentological classification undertaken to understand the role lithology and sub-bed scale heterogeneity plays in the deformation of UK Carboniferous Coal Measure.

This study demonstrates, and suggests methods to limit, geologists' own biases during fracture data collection that can influence the data collected, and hence the derived statistics used for fracture modelling. Biases are also introduced when the temporal evolution and connectivity of individual sets of fault-fracture networks are not considered when assessing connectivity.

Unlike binary mechanically layers sequences (e.g. limestone/marl), we find the presence of shale inter-beds and the abundance of sub-bed scale sedimentary heterogeneities (e.g. channel coals) to strongly affect the development fault and fractures. Where jointing exists at the time of faulting, fault-growth was found to be restricted by favourably orientated structures. The thickness and composition of fault-rock is controlled by lithological juxtaposition, with organic fragments found along principle displacement zones of faults of all sizes, even where organic rich layers have apparently not been cut.

This study also shows faults that form following the collapse of Pillar and Stall mine workings are strongly affected by mechanical stratigraphy, with the height disruption controlled by a combination of the width of the stall, and the distribution and thickness of competent sandstone layers. Collapse leaves a clay-rich anthropogenic sedimentary layer which will retard the flow of groundwater in abandoned pillar and stall workings. These findings will improve our ability to assess geo-technical risk in ex-coal mining areas and de-risk shallow mine geothermal projects.

Acknowledgements

Firstly, I would like to extend a huge thank you to my supervisors Zoe Shipton and Richard Lord for their time, energy, and insightful discussions. I would like to particularly thank Zoe, who despite being head of department managed to fit in reading this rather large text! You have enabled me to grow and pursue different ideas leading to the rich data set that underpins this thesis, even if the 'Billy effect' was sometimes on show. I would also like to extend my thanks to the research group FAFF (Faults and Fluids Flow), for the engaging research environment and helping me to extend my research network beyond the confines of the University. Jen Roberts and Lucy McKay, you are truly inspirational geologists that have been integral to the completion of the thesis. Jen, I thank you for all your help and support, particularly in the preparation and publication of my 1st paper. You helped me, along with Zoe, develop from an academic writing toddler, to a published academic. Lucy, thank you for the science discussions and helping me remain (somewhat) sane as a geologist in an engineering department. From the early inception of ideas for both our projects, through days in the field including an enforced lock-in due to civil unrest, to discussing parenthood. Thank you for being an amazing colleague and friend.

Outside the research group are a number of people whom I would like to extend my thanks to, both at the University of Strathclyde and beyond. To all of 'Bobs crew' who supported me through the trying start of my PhD, and throughout the process through countless trips to the pub. In Particular JT, for always asking how I was and supporting me through the difficult times with your legendary stories (charging elephants). I would like to extend my greatest appreciation to those who believed in me despite having dropped out of university multiple times due to mental health. Without Phil Murphy and Zoe Shipton showing faith in my ability to overcome past struggles, none of this would have been written and I would not be a geologist! Thank you to the TSG community for showing me my true passion in 2015 in Edinburgh, and for the many enjoyable AGMs since.

Geoff Lloyd, thank you for your support during my time at Leeds, and for giving me my first taste of research. Zoe Cumberpatch, I need to thank you for pushing me in my work while at the University of Leeds and proving that you are indeed the Superior Geologist and I 'just map'. From all the structural geology coping pints, to working together following our undergraduate degrees (when the Billy-Zoe effect is not interfering) you have always been

a great friend and inspiration. Your finest achievement has to have been managing to not only show me why sedimentary logging had a point, but that I should in fact use it to help underpin my PhD! Thanks for being awesome!

Most importantly, I would like to thank my family, friends, and fiancé for their unending patience and support throughout my PhD. Dave you helped me on this path by showing me the complexity of rocks on all those family walking holidays. I still remember discussing dykes on the Isle of Skye and realising that understanding such processes was the route I wanted to pursue. Thank you 'Thing 1' and 'Thing 2' (Parents) for being so crazy not even the Cat in the Hat has any chance of controlling you. It's a long way from those dark days in William Street, and I would never be the person I am now without your endless kindness and support. The bi-weekly weekend craziness and hilarity was a very welcome distraction from research! Thank you John for the important pub sessions while back in Newcastle throughout the long process, and being a great mate! Thank you Rob and Luke for your assistance in the field. I think Luke wins the ability to hold a tape measure, however, your photography skills were impressive Rob! Thank you Jake for letting me stay when I had the conference in Liverpool and chatting over the years as I got myself back on track.

Finally, and certainly not least I need to thank my two amazing Molly's! Molly Black, how could I have done this without you! I am so lucky to have met you and your unwavering support is truly inspirational and keeps me going. From enforcing that I have down-time through walks in Kelvingrove Park, trips away to Mull and Ireland to supporting me from a distance in our year apart you have helped me get through this process as a stronger, happier, and more confident person. I will always remember and appreciate the great where were hunt of 2019, the confused species was rampant through there pages and with your help the invasive species was 'hopefully' kept in check! Thank you for being you and helping me be me.

Moo, thank you so much for being so incredible, insane, loving, and understanding!! We have so much fun together, and one day I will explain how important those walks in the woods were to getting my PhD. Even know you are only six, the understanding and support you showed to me in the final couple of months when I occasionally had to work late, or at weekends I was down was amazing. From the moment you were born, you changed my life, helped me tackle mental health struggles and gave me a purpose. Thank you and I can't wait for many more pixy chats and Sloe walks.

Table of contents

Chapter 1: Introduction	25
1.1 Geological faults & architecture	25
1.2 Rationale for studying faults in coal bearing successions.....	29
1.3 Project aims and methods	31
1.4 Thesis structure.....	33
Chapter 2: The role of coal in the faulting of mechanically layered sequences: Implications for mine safety and geothermal resources.....	35
2.1 Rationale	35
2.2 Introduction	36
2.3 Undeformed coal	38
2.4 Deformed coal.....	42
2.4.1 Naturally deformed coal	42
2.4.2 Mechanical properties of deforming coal.....	47
2.4.3 Deformation of coal towards a fault zone & studies of faulting style	51
2.5 Discussion.....	60
2.5.1 Comparison of coal bearing successions with mechanically stratified lithologies:	60
2.5.2 Implications for coal mining.....	62
2.5.3 Implications for shallow mine geothermal	64
2.6 Concluding remarks	65
Chapter 3: How do we see fractures? Subjective Bias in fracture data collection.	67
3.1 Declaration of work:	67
3.2 Abstract.....	67
3.3 Introduction	68
3.3 Fracture data collection and analysis.....	70
3.4. Study methods	74

3.4.1 Study area	74
3.4.2 Fracture data collection procedure	75
3.4.3 Post-workshop analysis.....	78
3.4.4 Analytical framework.....	79
3.5. Results.....	81
3.5.1 Linear Scanlines.....	81
3.5.2 Circular Scanlines: Topological sampling and fracture mapping	84
3.5.3 Window sampling	89
3.5.4 Areas of increased uncertainty: A case study using Circle 8.....	91
3.5.5 The effect of working in groups	92
3.5.6 Time taken to collect data	95
3.5.7 Experience.....	96
3.6 Effect of subjective bias on the derived fracture statistics.....	97
3.7 Discussion.....	102
3.7.1 Scanline validity and appropriate data collection method.....	102
3.7.2 Causes of subjective bias: operator bias and fracture network characteristics .	106
3.7.3 Recommendations for reducing subjective bias.....	112
3.7.4 Wider geoscientific implications.....	116
3.8 Conclusions	118
Chapter 4: The role of lithology and bed scale heterogeneity on fracture trace length and topology. A case study of the UK Carboniferous Coal Measures.	120
4.1 Rationale	120
4.1 Introduction	121
4.2 Geological setting.....	122
4.3 Methods.....	126
4.3.1 Network Topology.....	126
4.3.2 Field procedure	128

4.4 Results.....	131
4.4.1 Mechanical stratigraphy	131
4.4.2 Fracture data.....	133
4.4.3 Network topology	141
4.4.4 Sub-bed scale observations	143
4.5 Discussion.....	149
4.5.1 Effect of the plane of observation: Section view changes in mechanical strength	149
4.5.2 The effect of mechanical stratigraphy and sub-bed scale sandstone bodies on fluid flow.	153
4.5.3 Use of field data for assessing sub-surface fracture patterns	155
4.6 Conclusions	157
Appendix: Sub-bed scale sedimentary logs	160
Chapter 5: The role of pre-existing jointing on damage zone evolution and faulting style of thin competent layers in mechanically stratified sequences, a case study from the limestone coal formation at Spireslack SCM.	
5.1 Abstract.....	162
5.2 Introduction	163
5.3 Geological setting.....	165
5.3.1 Spireslack SCM	166
5.4 Methods.....	167
5.4.1 Field mapping.....	167
5.4.2 Analysis of fault and fracture networks.....	167
5.5 Results.....	170
5.5.1. General fracture observations	170
5.5.2 Fault observations.....	175
5.6 Discussion.....	187

5.6.1 The role of lithology in faulting style: self-juxtaposed vs non-self juxtaposed faulting	187
5.6.2 Jointing and the effect of pre-existing weaknesses on deformation style and fault growth.....	189
5.6.3 Effect on flow pathways:.....	191
5.7 Conclusions	194
Chapter 6: The internal structure of faults cutting coal bearing successions: A case study using the Northumberland Basin.	196
6.1 Rationale	196
6.2 Introduction	196
6.3 Methods of data collection	199
6.3.1 Faults used in this study.....	199
6.3.2 Field mapping & structural logs:	201
6.3.3 Post-fieldwork data analysis	202
6.4 Results.....	202
6.4.1 Fault kinematics	202
6.4.2 Fault zone structure	205
6.4.3 Fault rock lithologies.....	209
6.4.4 Fault-strand maps	218
6.5 Discussion.....	227
6.5.1: Fault and fault-rock orientation: implications for the Northumberland Basin .	227
6.5.2 Fault architecture and localisation of strain.	233
6.6 Concluding remarks	239
Chapter 7: The lithology, internal structure and deformation style of collapsed pillar and stall coal mines: Implications for shallow mine geothermal.	240
7.1 Rationale	240
7.2 Introduction	241

7.3 Geological history	246
7.4 Methods.....	249
7.4.1. Fracture mapping (Spireslack SCM)	249
7.4.2. Field investigation (Whitley Bay)	250
7.5 Results.....	251
7.5.1. Spireslack SCM High wall	251
7.5.2. Whitley Bay exposure	257
7.6 Discussion.....	264
7.6.1. Processes involved in the formation of collapsed pillar and stall workings	264
7.6.2. Implications for shallow mine geothermal	272
7.7 Conclusions	276
Chapter 8: Conclusions and further work.....	278
List of references.....	287

List of figures

Figure 1.1: Internal structure of a fault zone: a) Typical fault internal structure of a fault core, adapted from Caine et al. (1996), with inserts of typical lithologies and structural features (Micarelli et al., 2003; Peacock et al., 2017; McKay et al., 2019); b) line drawing of a pull-apart filled with folding and localised brecciation, Flamborough Head, UK (Peacock and Zhang, 1994); c) graphical representation of the influence of mechanical stratigraphy on fault propagation and displacement (Ferrill and Morris, 2008).	27
Figure 2.1: Coal classification schemes (redrawn from Thomas (2013)). Colours represent the overarching terminology used in this thesis of ‘lignite’, ‘sub-bituminous’, ‘bituminous’, ‘anthracite’ and ‘meta-anthracite’	38
Figure 2.2: Characteristics of undeformed coal. (a) variations in coal seam thickness and splits (Thomas, 2013), (b) coal cleats (adapted from Laubach et al., 1998), (c) representative sedimentary logs of coal bearing successions (Thomas, 2013), and (d) stratigraphy and mechanical stratigraphy from Whitley Bay, Northumberland (UK), see Chapter 4 for details.	41
Figure 2.3: Bed shear zones & effect of partings/bumps (redrafted from Li, 2001); b) example of a rock-burst caused by a failed pillar (Kaiser and Cai, 2012); c) the effect of a strong and weak parting on the deformation of coal-rock-coal partings (Liu, C.-P. Lu, et al., 2019) (c) highlights the modelled evolution of micro-fractures when a parting is both weaker (e.g. sandstone) and weaker (e.g. shale) than the coal seam. The evolution of vertical stress, cumulative acoustic emission counts, strain and kinetic energies from both cases are also presented.....	47
Figure 2.4: Mechanical properties of coal. a) Peak strength under triaxial compression for regular and calcite-rich coal (Solid line represents the regression line, with dashed representing the 95% confidence level) (Gao et al., 2016). b) Simulated fracture development in normal and calcite coal (Gao et al., 2016). c) Failure strength against angle of cleats relative to loading direction for Brazilian tests and calculated curve (Y.W. Li et al., 2016). d) Fracture patterns under different loading angles after Brazilian splitting tests (50 mm diameter samples) (Y.W. Li et al., 2016). Indirect tensile strength of dry (f) and saturated (g) coal under different loading direction and impact conditions (Zhao et al., 2016a).....	50

Figure 2.5: Fault scaling and restriction. a) Example of fault-strands recorded on mine abandonment plans in an area of Markham Colliery, Derbyshire Coalfield, UK, centred on a NE striking fault zone; the area was initially described by Rippon, (1985), redrawn from (Walsh et al., 2003); b) Conceptual model of the interaction of sub-parallel faults (Gupta and Scholz, 2000); c) Trace geometries and throw profiles for a segmented fault, Barnsley seam, Silverwood Colliery, South Yorkshire (Huggins et al., 1995); d) maximum displacement-length scaling plot, Hail Creek, NE Australia (Carvell et al., 2014); e) Dip dimension vs strike dimension for laterally (open circles) and vertically (crosses) restricted faults (Nicol et al., 1996). 52

Figure 2.6: Field photographs of faults cutting coal measures: a) & b) normal faults cutting interbedded limestones and marls (Delogkos, Manzocchi, et al., 2017; Delogkos et al., 2018); c) photomontage of a fault of a fault strand at Greenburn SCM, Ayrshire, Scotland (Leslie, Browne, et al., 2016); d) tree trunk and associated faulting in Konin Lignite Mine, Poland (Widera, 2013); e) LiDAR data from Delhi open cast coal mine, Northumberland, UK (Jones et al., 2010) 56

Figure 2.7: Hydrogeological properties of inflow events: a) schematic showing the factors which effect groundwater flow events in the vicinity of a geological fault (Bu, 2013); b) photograph of an inflow event (Gao et al., 2018); c) groundwater flow-rate evolution during an inflow event which occurred in Ganhe Coal Mine, Shanxi, China (Qi et al., 2014). 57

Figure 3.1: Location map highlighting (a) the local geology and (b) the location of the study area, located near Whitley Bay, Northumberland (UK). Grid lines are annotated with UK national grid numbers. Field photographs of both linear (c) and circular (d) scanline methods are also shown (L3 [NZ34717545] and C8 [NZ34377609] respectively). The geological map is modified from Geological Map Data BGS © UKRI (2018), where stratigraphy is as follows: PLCM-SDST = Pennine Lower Coal Measures – Sandstone; PLCM-MDSS = Pennine Lower Coal Measures – Mudstone, siltstone and Sandstone; Pennine Middle Coal Measures – Sandstone; PLCM-MDSS = Pennine Middle Coal Measures – Mudstone, siltstone and Sandstone. 75

Figure 3.2: The interpreted fracture traces for Line 6 (length 1.45 m). (a) The digitised fracture networks for all workshop participants. (b) Field photograph of Line 6. (c) Fracture trace length histograms (bin = 0.1 m) for participants who recorded a low to high number of fractures. The corresponding digitised fracture trace is also highlighted in the appropriate colour. Key differences in the interpreted fracture networks are highlighted using

participants who selected a low (Participant 28, 9 fractures), medium (Participant 10, 17 fractures) and high (Participant 14, 25 fractures) number of fractures. 83

Figure 3.3: Results of the fracture data from circular scanlines (C1-7) collected in the field by 7 participants (labelled A-G, though A, E and F did not complete all of the scanlines). (a) the number of fractures that intersected the circular scanlines (n). (b) fractures that terminated in rock (i-nodes). (c) fractures that terminated against another fracture (y-nodes). (d) fractures that intersect another fracture (x-nodes). Participants C and D repeated some of their measurements for selected circles and this is indicated by two bars in their column for that circle. 86

Figure 3.4: Recorded fracture data (n, and node counts) and the time taken to undertake n and node counts for workshop (WS) participants (P) and groups (G). The data for each attribute has been colour-coded according to where the reported value for the parameter ranked for that circle. Data are presented in the order that they were completed in the workshop. 87

Figure 3.5: Node triangles for workshop participants and groups. For individual circles (a), Participants 5, 21, and 11 were highlighted to show the consistency the way participants classified nodes. Participants were selected according the whether they reported a low (P5), medium (P21) or high (P11) node count. Similarly, for group circles (b) Groups 7 and 12 were highlighted as groups who recorded a high and low node count. 88

Figure 3.6: Fracture trace length distributions for (a) individual and (b) group window sampling data. The results are presented as both histograms and normalised cumulative frequency curves of fracture trace length with bin widths of 0.05 m for individual and 0.1 m for group window sampling data. The range in the relative percentage of small fractures observed in the data is highlighted using Participants and groups who consistently observed a high and low percentage of small fractures (Participant’s 3 and 24 and Groups 12 and 11 respectively). 88

Figure 3.7: A detailed study of the areas which cause increased uncertainty in Circle 8. The figure comprises of clean field photographs of Circle 8 with the (a) heat map of y-node point density, (b) heat map of fracture trace density and (c) areas identified as problem areas. In panel (d) the close up of areas 1, 2 and 3 along with the features recorded by Participants 11, 18 and 21 are shown. See text for full description. 94

Figure 3.8: The impact of participant experience on the collection of fracture data. (a) The time taken in seconds to record fracture data (n and node counts) from circular scanlines

both in the field and workshops. (b) The impact of experience on the recorded y-count and number of fractures in individual scanlines and the time taken to complete the workshop tasks. 95

Figure 3.9: Topological sampling results for individuals and groups for circular scanlines 1, 3, 4, 5 and 8. Each histogram reports the results for all workshop participants. The statistics have been derived from the data for each participant. Data is presented as both bar charts and shaded histograms with the bin width, b , indicated on the chart (please note the bin width varies between circles as a function of the range in reported or calculated values). In all cases the y-axis represents frequency and is scaled so the shape of the distributions can be assessed. 98

Figure 3.10: The effect of subject bias on the validity of circular scanlines. The number of terminations recorded by individuals or groups is displayed for each circle and colour coded depending on where a valid (>30 , green), possibly valid (20-30, yellow) or invalid (<20 , red) number of terminations were recorded. 104

Figure 3.11: The impact of interpreter style on fracture statistics of a synthetic fracture network. (a) statistically valid topological sampling within a circular scanline for a fracture network which only considers the large scale fracture network. (b) statistically valid topological sampling within a circular scanline for the same large scale fracture network as (a), however, also capturing small scale fractures at fracture intersections. (c) The topology attributes (n , i -, y - and x -nodes), derived fracture statistics and node triangle of the different interpretations of the fracture network. 105

Figure 4.1: Location map, adapted from Andrews et al. (2019) highlighting (a) the local geology and (b) the location of the study area, located near Whitley Bay, Northumberland (UK). Grid lines are annotated with UK national grid numbers. Field photographs of (c) section view (bed-scale) fracture map (S1) and (d) bed-parallel view experiment (Cx) are also shown. The geological map is modified from Geological Map Data BGS © UKRI (2018), where stratigraphy is as follows: PLCM-SDST = Pennine Lower Coal Measures – Sandstone; PLCM-MDSS = Pennine Lower Coal Measures – mudstone, siltstone and sandstone; Pennine Middle Coal Measures – sandstone; PLCM-MDSS = Pennine Middle Coal Measures – mudstone, siltstone and sandstone. For detailed stratigraphy see Figure 4.2. 124

Figure 4.2: Litho-stratigraphic and rebound profiles as measured for the bed-scale observations. Colour for mean mechanical rebound values match Sx. Examples of sub-bed

scale sedimentary logs and rebound profiles 21/1 and 21/4 are provided in the appendix to this chapter.	126
Figure 4.3: Topological sampling notation: (a) Standard topological notation after Sanderson and Nixon (2015); (b) topological sampling within a circular scanline, following the methodology of Procter and Sanderson (2017); (c) amended node notation used in this study; (d) node-triangle, showing end-member fracture networks and the position (a), (b), and (c) would plot; (e) i-node and (f) y-node triangles, showing typical 'end-member' cases and the position fracture map (c) would plot.....	127
Figure 4.4: A comparison of bed- and sub-bed scale sedimentary logs and mechanical stratigraphy: a) A section of the stratigraphy covered by the bed-scale logging (see Figure 4.2) and included parts of Beds 13 and 14; b) The same section of stratigraphy logged at a cm-scale resolution with mechanical stratigraphy undertaken for each sub-bed scale sedimentary unit.....	132
Figure 4.5: Graphs of rebound value against grain size (presented as Phi) for a) bed-scale presented by the lithofacies introduced in Table 4.1 and b) sub-bed scale experiments. Linear coefficient of determination (R^2) are presented for each graph.	133
Figure 4.6: Example fracture maps for both map- and section- view. Data is presented by lithofacies and displays the standard topological sampling introduced in Figure 4.2.....	136
Figure 4.7: Joint dip, strike and trace length for bed parallel and bed-perpendicular experiments. Data is presented by lithofacies (Sx). Dip and strike data are presented using equal area stereographic projections created using Stereonet 10.1.1 (Allmendinger et al. 2013; Cardozo and Allmendinger, 2013). Data is contoured by 1% area with the value of each contour provided next to each stereonet. Strike data is presented using normalised histograms with a bin-width of 10°. Dip data is presented using box and whisker diagrams.	137
Figure 4.8: Trace length data. a) normalised trace length and branch length histograms for map-view experiments, and branch length histograms for section view. Blue lines represent the average value of all experiments for that bin. Box and whisker plots for the ratio of branch length and bed-thickness presented b) by litho-facies and c) for each experiment. Experiments where the bed-thickness is low (c. 5 cm) did not typically show bed-bound branches, and are not included in this figure.	138

Figure 4.9: Topological data presented by litho-facies. Results are presented for (a) map-view and (b) section view experiments. An explanation of each triangle is provided in Figure 4.3.	141
Figure 4.10: Example fracture maps linked to mechanical stratigraphy. Rebound values represent the mean for the specific sub-bed unit, with error bars representing plus and minus one standard deviation. Detailed sedimentary information for both logs are provided in the appendix to this chapter.	145
Figure 4.11: Field photographs of key sedimentary features: a) bed- and sub-bed bound joints cutting S3 (base) and S4 (top) near C3. b) Conjugate joints cutting the tip of a channelised sandstone body south of S6. c) Interacting joints on the bedding plane of S4 (CC4). d) Alteration halos surrounding channel coals, organic draped ripples and joints south of C6. e) Mineralised joints and cleats within the High Main Seam near C10. f) Joints increasing near the edge of a coarse channelised sandstone bode north of C28. g) Interaction of ripples, soft-sediment deformation, jointing and lithology with alteration halos. H) Interaction of channel coal ‘partings’ with alteration halos.	148
Figure 5.1: Location map: a) Map of UK coalfields (adapted from Donnelly (2006)) showing the location of Spireslack SCM and Structural features of the Midland Valley of Scotland; b) Regional geology of Spireslack open cast coal mine (after Ellen et al. (2019)); c) Regional stratigraphy of Spireslack SCM (after Ellen et al. (2019)).	165
Figure 5.2: Typical fracture properties for McDonald Limestone & McDonald Coal: a) barren joints observed away from faults across the southerly dipping (c. 40°) McDonald Limestone bedding plane; b) Mineralised N-S trending calcite veins, offsetting abutting E-W ladder joints on the bedding plane of the McDonald Limestone; c) annotated field photograph and interpretation of a multi-phase composite calcite vein exposed in the vicinity to a small offset fault along the McDonald Limestone Pavement; d) bedding plane exposure of mineralised fractures present within the Muirkirk 6’ coal; e) annotated hand specimen displaying the vein relationships present during the faulting of the Muirkirk 6’ coal; and f) the larger-scale mineralisation pattern as you move towards small offset faults in the Muirkirk 6’ coal.	174
Figure 5.3: Geological map of Spireslack SCM: a) Geological map undertaken as part of this study, displaying the locations of the detailed map-view fracture maps shown in Figure 5.5; b) Annotated photogrammetry of the high wall displaying the key stratigraphic horizons and faults (Ellen et al., 2019); c) Fault kinematics by lithology, stereographic projections are	

created using Stereonet 10.1 and contours represent 1% area; and d) box and whisker plots for fault dip by lithology..... 175

Figure 5.4: Characteristic observations of Self Juxtaposed Faults (SJFs): a) Small-offset (c. 15 cm) fault strands and relay structures, and b) tension gashes and small offset normal faults exposed within the McDonald Seat Earth in seat-earth exposed to the far west of Spireslack SCM; c) symmetric damage zone and thick zone of ankerite mineralisation along a c. 40 cm offset dextral offset fault cutting the Muirkirk 6' Coal; d) bed-parallel thrusts and folding developed within the shale which underlies the McDonald Limestone to the NE of the site; e) the development of small pods of fractured McDonald Coal along a small offset sinistral fault exposed to the SW of the site; f) the interaction between faults and joints along the southerly dipping bedding plane of the McDonald Limestone. 177

Figure 5.5: Fracture maps with increasing intensity of faulting: For each digitised map the exported fault (red lines) and fracture (dark grey lines) maps, along with the interpretation areas used for the analysis (light grey) are provided. The orientation data, colour coded by sets, is then provided using length weighted rose diagrams with 5° bin widths. Trace length is presented as trace-length histograms as well as normalised trace-length histograms with bin widths of 0.25 m. Histograms are colour coded to match the sets outlined in the orientation data. 181

Figure 5.6: Large offset fault characteristics: a) complex fault mesh consisting of multiple strands of sinistral and dextral strike slip fault planes (offset marked with arrows) picked out by shallow striations and the offset of the McDonald Limestone bedding plane; b) field photograph of a ~3 m offset fault strand within the complex mesh which displays multiple generations of fault striations, with local dextral reactivation separating striations belonging to set 2; c) fault architecture and d) view along strike of a 3 to 5 m offset fault strand exposed along the southerly dipping bedding dip-slope; fault architecture of the same 5 m offset fault cutting e) lithologies surrounding the McDonald Seat Earth, and g) interbedded sandstones, siltstones and shales of the Lower Limestone Coal Formation; f) primary slip plane of the ~80 m offset fault which cuts the west of the site; and h) shallowly dipping, sinistral dip-slip fault plane within a ~2 m thick sandstone bed of the Limestone Coal Formation..... 182

Figure 5.7: Digitised fault strands of sinistral faults cutting the Limestone Coal Formation exposed along the high wall: a) sinistral fault which displays between 2 and 5 m of throw

and has been cut by a later Paleogene dyke which is not observed with the main PDZ; b) sinistral fault with displays between 2 and 8 m throw along two PDZs.	186
Figure 5.8: Network topology data. Node and branch triangle (after Sanderson & Nixon (2015)) are presented for the full-network, mineralised fault strands, and open joints, for each of the three sample areas shown in Figure 5.5. Branch data is then presented by sets, as outlined in figure 5.5, to investigate the directionality of network connectivity.	193
Figure 6.1: Regional and local geology: a) Key structure and distribution of Carboniferous lithologies within the Northumberland Trough (after (Chadwick et al., 1995); re-mapping undertaken as part of this study for b) Howick and c) Whitley Bay highlighting key structures and areas of detailed study.	199
Figure 6.2: Stereographic projections of fault, fracture, and bedding data presented by fault zone. Stereographic projections were created using Stereonet 10.1 (Allmendinger et al., 2013; Cardozo and Allmendinger, 2013).	205
Figure 6.3: Annotated features of faults (horizon numbers for faults at Whitley Bay correlate to bed numbers used in Chapter 4): a) dextral offset fault cutting sandstone-rich lithologies at Whitley Bay displaying an asymmetric damage zone; b) and c) dextral offset fault strands cutting interbedded lithologies exposed at Whitley Bay; d) interaction between dip-slip and dextral fault strands within the Hartley Steps Fault Zone, Whitley Bay; e) HW fault strands at Howick cutting interbedded silicilastics, carbonates and coal; f) small offset splay of the CPFZ.	205
Figure 6.4: Structural logs of the fault core. Areas outlined in blue were logged in detail and detailed orientation data collected. Fault unit boundaries were correlated between these logs, using printed field photos to ensure that the geometries are honoured. a) SMBZ which cuts interbedded heterolithic sandstones, siltstones, shale and coal; b) Howick Strand 1 which separates limestones of the Acre Limestone in the FW from silicilasts in the HW; and c) Howick Strand 2 which cuts across many of the FW fault strands observed at Howick.	209
Figure 6.5: Fault rock lithologies: a) Fault-core lens and radial shear development along HPFZ; b) alteration of the High Main Seam and local development of tectonically deformed coal along HPFZ; c) lineations developed between channel coals and organic rich shale in the vicinity of SMBFZ.	210

Figure 6.6: Fault gouge: a) FG1 developed along NSMBFZ; b) FG3 developed within heterolithics close to SMBFZ; c) fragments of FG1 and FG2 found within rock-pools along the CPFZ; d) FG2 and interpretation of key structures developed within HSFZ. 213

Figure 6.7: FB1: a) FB1 developed along the main strand of CPFZ; b) highly altered layered fault-rocks (FG3, Cataclasite, FB1 and fault-core lenses) associated with a minor splay cutting heterolithics near SMBFZ; c) altered pod of FB1 along HSFZ with dip-slip lineations developed along the HW; d) xCT imagegry showing the density contrasts and highlighting the distribution of organic contents (green). 215

Figure 6.8: FB2 and FB3: a) pod of FB3 which forms along a y-shear to the HSFZ which displays no apparent offset; b) FB3 along a y-shear associated with the HMFZ where the organic rich shale matrix has been coalified; c) FB2 associated with SMBFZ which displays shallow angle lineations along slip surfaces which bound the breccia; d) Pod of FB2 found along a T-shear associated with the NSMBFZ. 216

Figure 6.9: Fault map for NSMBFZ (plan view) undertaken using 0.5 m grid mapping. The map was created using a 50 cm² grid laid out over the outcrop, with key features mapped onto graph paper. The mapped area displays little topography and the bedding planes for beds 16 and 17 are at the same level. 219

Figure 6.10: Section view of fault strands: a) fault-map of the CPFZ main strand outlining the distribution of fault-rock and fault-related fractures. The map was undertaken by laying a vertical tape measure over the outcrop (similar to observed in panel b) with features drawn onto graph paper. Clasts represent true clast geometry and highlight the high degree of rounding within this breccia zone; b) field photograph of a splay associated with SMBFZ. Numbers relate to the features discussed in the main text. 220

Figure 6.11: Fault gouge maps undertaken using 5cm² scale grid mapping: a) small section of the main fault strand of North St Mary's Bay Fault Zone (location shown on Figure 6.1); b) Section of the dip-slip strand of the HSFZ; and c) a section of the main strand of major fault at Howick. 224

Figure 6.12 (previous page): Riedel shear geometries observed over four orders of magnitude at Whitley Bay. a) Typical riedal shear geometries, with the colour of each component carried on to the simplified maps. Simplified fault maps for: b) field-scale geological mapping undertaken for this study and expanded to include key faults cutting St. Mary's Island; c) SMBFZ structural log; and NSMBFZ d) grid map and e) fault core. For full maps please refer to Figures 6.1c, 6.4a, 6.6 and 6.8. 230

Figure 6.13: Clast and lens orientation and relationships between aspect ratio and clast area: a) normalised orientation histograms for lenses, clasts, and linear features; b) comparison between 2D area exported from ArcGIS and the Equivalent Circular Area (ECA); c) relationship between aspect ratio and ECA for lenses and clasts; d) Normalised trace length by orientation; e) Aspect ratio by ECA for fault-rock lithologies.....	230
Figure 6.14: Clast aspect ratio compared to the distance from the main PDZ for that scale of observation.	238
Figure 7.1: Typical UK mining methods. (b, c and d redrawn from Bruyn and Bell (1999) a) bell pit, b) Bord-and-pillar workings, Newcastle upon Tyne (17th Century), c) Stoop and room workings, Scotland (17th Century), d) Pillar and stall workings, South Wales (17th Century), e) Photograph of pillar and stall workings, Beamish open air museum.	243
Figure 7.2: Geological setting. a) location of field sites and UK coal fields (after (Donnelly et al., 2008), b) geology surrounding the workings at Whitley Bay (The map is modified from Geological Map Data BGS@UKRI (2018)), c) geology of Spireslack SCM and surrounding area (after (Ellen et al., 2019), d) Chrono-stratigraphy, formations and lithofacies of both field sites (Chadwick et al., 1995; Browne et al., 1999).....	247
Figure 7.3: High wall deformation: a) Digitised fault and fracture network, with mapped horizons matching the schematic log; b) subsidence of beds with key deformation patterns marked, c) fractures colour coded by apparent dip.	253
Figure 7.4: Fault (a) and fracture (b) data from the digitised high wall and scanlines undertaken along the high wall at Spireslack SCM. Fault and fracture data exported from the digitised maps include: i) trace length data presented in a trace length histogram with bin-widths of 0.5 m and 0.1 m respectively; and ii) apparent dip which is presented on length weighted rose-diagrams with bin width of 10°. Fault-data from scanlines is presented through: a) the change in apparent dip along the scanline; b) number of faults per meter observed along the scanline; and c) fault-length presented as box and whisker plots.	255
Figure 7.5: Workings of the High Main Seam (HMS) at Whitley Bay: a) photomontage of the workings with the location of logs marked; b) interpretation of collapse lithologies; and c) sedimentary logs through the undeformed HMS at the base of Hartley Steps and through the workings at the locations marked in (a).	257
Figure 7.6: Facies photographs and associated clast and kinematic data. a) Undeformed High Main Seam, with yellow discolouration along the cleat network. B) Unaltered and altered shale underlying the unworked pillar. Stereonet displays the planes, poles to planes,	

and principle stress axis inferred for the yellow alteration planes. C) Coal breccia which onlaps onto the north of the pillar. Orientation data for clast bedding and foliation are presented, along with clast area distributions calculated using the equivalent circular area (ECA) method. D) CoB (altered and unaltered) which onlaps onto the coal breccia. The clast-area (ECA) distribution and orientation of clast bedding is presented. E) The overlying altered shale, with orange alteration along bedding planes. The dip of shale beds is presented, along with the inferred principle stress axis. F) Foliated red-orange foliated muds, which display onlapping relationships onto underlying clast 258

Figure 7.7: FC stacking patterns. View is towards the west onto the sub-vertical outcrop. 260

Figure 7.8: Northern Pillar: a) annotated field photograph displaying key structural elements of the pillar edge; b) scanline through the edge of the pillar, as marked in a..... 263

Figure 7.9: Evolution of mine collapse, see text for description of each stage. 269

List of tables

Table 1.1: Fault rock classification scheme used in this study, from Woodcock and Mort (2008).....	29
Table 2.1: Classification of Tectonically Deformed Coals (TDCs).....	44
Table 2.2: Lithologies and coal thickness at several coal fields. References: 1) Personal data, see Chapter 4; 2) (Li, 2001); 3) (Greb et al., 1992); 4) (Ellen et al., 2016); 5) (Ellen et al., 2019)	54
Table 3.1: Summary and definition of fracture statistics that can be derived from methods used in this work. Table adapted from Zeeb et al. (2013). Ni = number of i-nodes, Ny = number of y-nodes, Nx = number of x-nodes, r = radius of circular scanline, N = number of fractures, A = Area, n = number of fracture intersections with the scanline (either linear or circular), L = length of scanline, s = spacing between adjacent fracture traces on the scanline, tl = individual fracture trace length, F = fracture abuts against another fracture, R = fracture terminates into rock (n.b. some authors also distinguish stratabound fracture terminations), 'Yes' for trace length distribution & network topology indicates you can use that method to carry out the technique.....	72
Table 3.2: Summary of circular (C) and linear (L) scanlines completed in the field and workshops (WS1 & WS2). Whether these were completed individually (i) or in groups (g) is noted. 'Order' refers to the order the scanlines were completed in the workshops. Four of the circular scanlines (C2,3,4,5) were completed both in the field and in the workshop, but none of the linear scanlines were completed in both, due to workshop time constraints. Window sampling, whereby participants drew out the interpreted fractures as well as completing topological sampling, was only completed by Participants 1, 3, 11 and all of Workshop 2 (WS2). The workbooks used in this study are supplied in the supplementary information (S3 & S4).....	76
Table 3.3: Summary of the level of geological training, and experience in geological fieldwork and fracture data collection, reported by field and workshop (WS) participants. Individual participant responses are provided in the Supplementary Information (S2).	78
Table 3.4: Summary table of raw linear scanline results where i = individual, G = groups, # = number of participants/groups. *only two participants recorded time for this scanline **P10 did not record time taken to count nodes ***P23 did not trace fractures so only have spacing and time information.....	81

Table 3.5: Summary of fracture data and time taken for circular scanlines 1, 5 and 8, in the field and workshop, either working individually (i) or in groups (g). The data are presented in the order scanlines were completed in the workshops.....	84
Table 3.6: Summary of fracture parameters reported for window sampling. Data is presented in the order the scanlines were undertaken within the workshops. (i) and (g) denote whether the scanline was undertaken individually or as a group.....	91
Table 3.7: Summary of the broad trends in fracture statistics derived from the three methods we explored, presented in Figure 3.9.....	101
Table 4.1. Litho-mechanical facies scheme used as a framework for bed-scale and bed-parallel fracture maps.....	129
Table 4.2: Rebound properties of identified litho-facies.....	131
Table 4.3: Branch aspect ratio	153
Table 4.4: Summary of typical joint properties. Note: there are not enough data points to fully classify S5a.	159
Table 5.1: Self Juxtaposed Fault (SJF) characteristics.	178
Table 5.2: Network characteristics for the sample areas outlined in Figure 5.5	181
Table 5.3: Overview of network properties for: a) the combined fault and fracture network; b) the mineralised fault network; and c) the joint network which does not display mineralisation or reactivation during faulting.	192
Table 6.1: Summary of fault-zones characterised in this chapter. *The throw for CPFZ refers to the strands investigated in this study and not the overall throw on the fault zone (estimated at c 200 m (Jones and Dearman, 1967)).....	200
Table 6.2: Summary of fault, fracture, and bedding data presented for each fault zone. ..	203
Table 6.3: Characteristic properties of fault-core maps. *Sub rounded clasts are only observed within the high strain zone close to the footwall fault strand. **The hanging wall fault strand of HSFZ is straight, however, the footwall displays several undulations. ***Footwall strand not mapped, however, displays a planar appearance at a field-map scale.	227
Table 7.1: Key points in the mining history of the UK, Great Northern Coalfield and Glenbuck, Ayrshire. References; 1) Bell (1986), 2) Bruyn & Bell (1999), 3) Smails (1935), 4) Healy & Head (1984), 5) Campbell (1955), 6) Powley & Gillian (2015), 7) Leslie et al. (2016a), 8) Fielding (1982), 9) Dearman et al. (2000), 10) Page (1907), 11) Smailes (1938), 12) Nef (1965), 13) Galloway (1898).....	242

Table 7.2: Characteristics properties of the zones of damage above NFC workings.....	254
Table 7.3: Fault offset and bed-section statistics by mapped horizons.....	256
Table 7.4: Facies description and interpretation of depositional environment. References: 1) Fielding (1984b); 2) Fielding (1982); 3) Younger et al. (2002); 4) Godyń (2016); 5) c.f. Woodcock & Mort (2008); 6) Martin & Maybee (2000); 7) Koken & Constantinescu (2008); 8) Lokhande et al. (2005).	261
Table 7.5: Comparison of mine and cave collapse facies.	271

Chapter 1: Introduction

1.1 Geological faults & architecture

Faults accommodate the majority of geological strain in the upper crust and are often associated with earthquakes (e.g. Scholz (1998)), effect sub-surface fluid flow (e.g. Agosta *et al.* (2010); Bense *et al.* (2013); Scibek *et al.* (2016)) and decrease the strength of a rock mass (Islam and Shinjo, 2009; Childs *et al.*, 2009). Fault planes rarely occur as discrete planar features, instead occurring as a fault zone consisting of a fault core, which accounts for the majority of strain at a given location along the fault, surrounded by a damage zone (Figure 1.1a) (Caine *et al.*, 1996; Wibberley *et al.*, 2008; Faulkner *et al.*, 2010). A fault core can either be a single strand (e.g. parts of the San Andreas Fault (Chester *et al.*, 1993) and the Highland Boundary Fault, Scotland (McKay *et al.*, 2019) , or multiple anastomosing high strain zones which act to entrain lenses of undeformed, or fractured, host rock into the fault core (e.g. the Carboneras fault, SE Spain (Faulkner *et al.*, 2003)). The damage zone of a fault consists of subsidiary faulting, fractures, veins and folding (Kim *et al.*, 2004; Faulkner *et al.*, 2010).

As displacement along a fault increases, the length of a fault also increases (e.g. (Watterson, 1986; Cowie and Scholz, 1992; Childs *et al.*, 2009). However, faults rarely evolve in isolation, and multiple faults will grow at any one time, eventually interacting causing strain and displacement to be transferred between strands (Fossen and Rotevatn, 2016). Where a succession consists of layers with different mechanical strengths, faults are often vertically segmented (e.g. Childs *et al.* (1996); Schöpfer *et al.* (2006), (2016); Ferrill & Morris (2008)). For example, Peacock & Zhang (1994) showed that in the chalk and marl sequences exposed at Flamborough, vertical segmentation of faults is observed, which effect the properties and internal structure of the fault zone (Figure 1.1b). At relatively low displacement the growth of these faults is partially controlled by the ratio of competent to incompetent layers (Ferrill and Morris, 2008; Ferrill *et al.*, 2017). In sequences with more competent lithologies faults propagate for a large distance at low displacements, whereas in more incompetent lithologies faults propagate over much lower distances, with multiple strands taking up the strain even at high displacements (Figure 1.1c) (Ferrill and Morris, 2008). Faults typically nucleate as steeply dipping strands in competent layers, which

become connected in incompetent layers (Schöpfer et al., 2006; Schöpfer et al., 2007; Ferrill and Morris, 2008; Ferrill et al., 2017).

As displacement increases, the fault zone widens through the incorporation of wall rock material (Schöpfer et al., 2016), and the removal of asperities (Sagy et al., 2007). The fault plane straightens through the break-down of wall rock and forms fault rocks, which in the brittle regime can include gouge, breccia, cataclasite and pseudotachylyte (Sibson, 1977). Throughout this thesis fault-rocks are described using the classification scheme of Woodcock and Mort (2008) (Table 1.1). Fault rock lithologies and fault core thickness is affected by the lithologies cut by the fault, fault type, and displacement along the fault (Sibson, 1977; Shipton et al., 2006; Van der Zee et al., 2008; Torabi and Berg, 2011; Torabi, Alaei, et al., 2019). The thickness, type, and distribution and fault-rock lithologies in the fault core is strongly affected by lithological juxtapositions along the fault (Sibson, 1977; Chester and Chester, 1998; Agosta and Aydin, 2006; De Paola et al., 2008; Walker et al., 2013; Bullock et al., 2014).

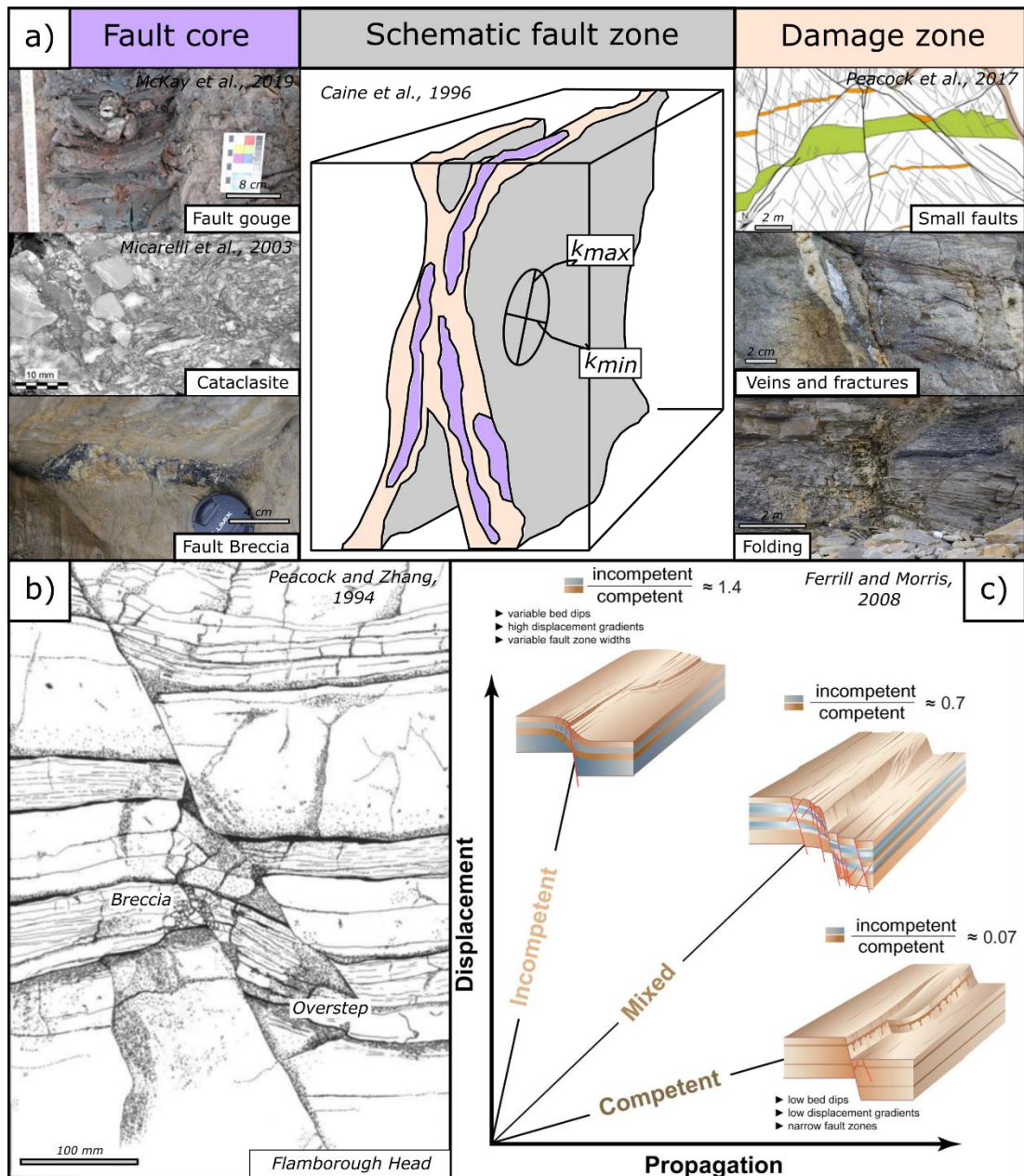


Figure 1.1: Internal structure of a fault zone: a) Typical fault internal structure of a fault core, adapted from Caine et al. (1996), with inserts of typical lithologies and structural features (Micarelli et al., 2003; Peacock et al., 2017; McKay et al., 2019); b) line drawing of a pull-apart filled with folding and localised brecciation, Flamborough Head, UK (Peacock and Zhang, 1994); c) graphical representation of the influence of mechanical stratigraphy on fault propagation and displacement (Ferrill and Morris, 2008).

Faults can act as a barrier, baffle, or conduit to fluid flow (Caine et al., 1996), which can lead to localised zones of mineralisation (e.g. gold) (Sillitoe, 2000; Tripp and Vearncombe, 2004; Jolley et al., 2004), compartmentalisation of hydrocarbon reservoirs (Aydin, 2000; Jolley et al., 2010), or leakage of CO₂ from storage sites (Shipton et al., 2004; Zhang et al., 2008; Roberts et al., 2017). It is however notoriously difficult to predict the effect faults will have on subsurface fluid flow (Bense *et al.* 2016 *and references therein*). Damage zones may be complicated through the interaction of fault strands, with zones of damage overlapping leading to a heterogeneous deformation pattern to develop (Kim et al., 2004; Gudmundsson et al., 2010). The orientation and connectivity of high permeability pathways (including fractures and interconnected high permeable lithologies (Bense et al., 2013; Choi et al., 2016; McCay et al., 2019), combined with the local hydraulic gradient can lead to across-, up-, or along-fault flow to occur (Bense et al., 2013). Although most fluid flow occurs through fault damage zones, flow through the fault core can occur. For example, the presence of fault-core lenses (Gabrielsen *et al.* 2016, *and references therein*), 'holes' in a clay-rich fault cores (De Rosa et al., 2018) in clastic lithologies, or dissolution features and uncemented breccias in carbonates (Torabi, Johannessen, et al., 2019) could act to provide flow pathways through the fault core.

Outcrop studies of fault zones have highlighted the spatial and temporal variability in fault properties both along strike and down dip (e.g. De Rosa *et al.* (2018); McKay *et al.* (2019)). Fluid flow can vary through time, with pathways becoming open and closed with changes in stress state (Sibson, 1990; Wang and Park, 2003; Cherubini et al., 2014; Comerford et al., 2018), or through previous pathways becoming mineralised (Sheldon and Ord, 2005). One key way of furthering our understanding of fault-related fluid flow is through the field characterisation of fault zone properties and mapping out likely conduits for flow. To improve our ability to predict fluid flow it is important to understand the spatial arrangement and heterogeneity of low permeability fault rocks, veins, and fractures in the fault zone.

		Non-foliated	Foliated	
>30% large clasts (>2 mm)	75 to 100% large clasts (>2 mm)	Crackle breccia		
	60 to 75% large clasts (>2 mm)	Mosaic breccia		
	30 to 60% large clasts (>2 mm)	Chaotic breccia		
<30% large clasts (>2 mm)	Incohesive		Fault Gouge	
	Cohesive	Glass or devitrified glass	Pseudotachylyte	
		0 to 50% matrix (<0.1 mm)	Protocataclasite	protomylonite
		50 to 90% matrix (<0.1 mm)	(meso)cataclasite	(meso)mylonite
		90 to 100% matrix (<0.1 mm)	Ultrocataclasite	Ultramylonite
		Pronounced graub growth		blastomylonite

Table 1.1: Fault rock classification scheme used in this study, from Woodcock and Mort (2008).

1.2 Rationale for studying faults in coal bearing successions

Coal is found in many sedimentary basins and has been deposited during several geological time periods (e.g. Carboniferous, Cretaceous and Tertiary) (Thomas, 2013). Coal is a sedimentary rock comprised nearly completely of plant debris which was deposited in peat swamps (O’Keefe et al., 2013) and later converted to coal through the process of coalification during burial and/or tectonic events (Dawson et al., 2012; O’Keefe et al., 2013; Thomas, 2013). The process of coalification causes a series of bio-chemical, geochemical, and metamorphic reactions which convert the organic material to convert first to peat, then onto the various ranks of coal (peat, lignite, sub-bituminous, bituminous, semi-anthracite, anthracite) (O’Keefe et al., 2013). Due to coalification processes, coal also contains several sets of naturally occurring fractures called cleats (Laubach et al., 1998). The properties of the cleat network are a function of coal composition, seam thickness, rank, and sub-bed scale heterogeneities (e.g. partings) (Close and Mavor, 1991; Laubach et al., 1998; Dawson and Esterle, 2010; Dawson et al., 2012). The strength of coal varies depending on the rank, type, and orientation of the cleat network relative to an applied stress field (Laubach et al.,

1998; Liu et al., 2016), but generally coal can be considered as a weak, pre-fractured lithology.

Despite the widespread occurrence of coal, relatively few studies have investigated the effect of the presence of coal on the faulting behaviour of coal-bearing successions. The large scale geometry of faults, investigated using mine abandonment plans, suggest the growth of faults in these lithologies are typically vertically restricted, and small faults can form at a high angle to the main fault trend (Huggins et al., 1995; Cartwright et al., 1995). The most common form of faulting in coalfields, particularly the UK, are tectonic normal faults (Rippon, 1985; Walsh and Watterson, 1988). The dips of tectonic faults in coal measures usually exceed 55°, and display median dips between 65° and 68° (Walsh and Watterson, 1988 *and references therein*). Many studies investigate the mechanical behaviour of coal in isolation, in particular how tectonically altered coals form (e.g. (Cao et al., 2003; Ming et al., 2011; Ju et al., 2012; Godyń, 2016), and change towards a fault zone (Li et al., 2018). It is also common to model the reactivation and fluid flow along faults into coal mines (Islam and Shinjo, 2009; Lianchong et al., 2011). However, in attempts to constrain mining hazards many such modelling studies apply single values to key fault properties (e.g. thickness and strength) and do not capture any heterogeneity or the effect of mechanical stratigraphy. Studies to date do not typically investigate the whole sedimentary succession and hence, our understanding of how coal effects the growth of faults within the full sequence remains largely unknown.

Improving our knowledge of the brittle deformation of coal-bearing sequences has many industrial applications. Although the extraction of coal has diminished in recent years, it remains an integral part of several countries' economies (e.g. Poland (Kuchler and Bridge, 2018) and China (Qi et al., 2016)). One of the key risks, particularly as mining progresses deeper, is the reactivation of faults causing dangerous 'outbursts' or 'inflow events' to occur (e.g. (Frodsham and Gayer, 1999; Cao et al., 2001; Guo et al., 2009; Islam and Shinjo, 2009; Bu, 2013; Wang et al., 2013). In many models used for the prediction and mitigation of these phenomena faults are considered as a single planar feature, with properties remaining constant both along strike and down dip. Field classification of fault zone heterogeneity, and spatial arrangement of fault rocks will inform these models, in particular the location and persistence of high risk tectonically deformed coal (Ju and Li, 2009; Ju et al., 2012).

Where the sub-surface extraction of coal has ceased abandoned coal mines may be exploited for mine-water geothermal projects (e.g. Sanner 2001; Malolepszy *et al.* 2005; Watzlaf & Ackman 2006; Monaghan *et al.* 2017). Faults and bed-bound joint networks can combine to act as conduits for mine-water flow (Li *et al.*, 2012; Bu, 2013; Huang, 2014). This can lead to the loss of heat in a mine-water geothermal target or the unpredictable contamination of ground-and surface-water resources through acid mine drainage (e.g. Younger, 2002). To predict flow in target workings it is important to understand the geological complexity and water capacity of a site (Malolepszy, 2003). This includes how geological structures (e.g. faults) act to form unpredicted flow pathways, how the overlying stratigraphy deforms above workings during collapse, and how the water capacity changes as collapse progresses.

1.3 Project aims and methods

The overall aim of this thesis is to improve understanding of the internal structure and evolution of faults and fractures in coal bearing sequences in the UK. This is achieved through detailed fieldwork, accompanied by fault and fracture mapping at two locations in the Northumberland Basin (Whitley Bay and Howick), and one in the Midland Valley of Scotland (Spireslack SCM (Surface Coal Mine), Ayrshire). The thesis looks to address the following research questions:

RQ1: Does subjective bias in the characterisation of fault and fracture networks effect the resulting statistical data collection, and how can this effect be minimised?

RQ2: What role does lithology, sub-bed scale heterogeneity and pre-existing weaknesses play on joint network characteristics and the development of fault damage zones?

RQ3: What are the types and spatial heterogeneity of fault rock developed in coal bearing succession, and how does this vary with displacement and different lithological juxtapositions?

RQ4: How do coal measures behave when abandoned pillar and stall mine workings collapse, and how will this affect the geothermal potential of a site? How mine workings collapse will in part be controlled by the mechanical properties of the overlying lithologies.

Quantifying fracture patterns is a key element of answering RQ2-4 to understand the fundamental processes involved in the faulting of coal measures. RQ1 therefore investigates the individual bias in fracture data collection and ways to limit the effect of

subjective bias in the output statistics in order. In sedimentary successions which contain competent and incompetent lithologies, such as fluvial-deltaic coal-bearing sequences, the nature of mechanical contrasts has been shown one of the primary effects on the style and evolution of faults and joints (e.g. Ferrill & Morris (2008); Laubach *et al.* (2009)). Therefore RQ2 and RQ3 investigate how the presence of coal and organics effects the properties of joint networks, how faults grow through those joint networks, how faults and joints interact as displacement increases, and the type and spatial distribution of fault rock in coal bearing lithologies. RQ4 builds on RQ2 and RQ3 in the context of anthropogenic deformation and investigates whether we can use the knowledge gained from how faults and joints form to inform the processes at work during the collapse of pillar and stall mine workings.

Overall these problems will combine to improve our understanding of how the presence of a weak, fractured, stratigraphic unit (coal) effects the brittle deformation of the whole sequence. This combined with understanding how pillar and stall workings collapse will improve our ability to de-risk shallow, low enthalpy geothermal projects which look to utilise abandoned mine workings.

Whitley Bay, located 4.5 km north of the basin-bounding Ninety Fathoms Fault in the Northumberland Trough, UK, was chosen for its 1.2 km long exceptional exposures of interbedded sandstones, siltstones, shales, seat-earth and coals of the Westphalian B Middle Pennine Coal Measures. Coal represents around 5-8% of the studied succession, which includes the historically important 2 m thick High Main Seam. Exposures of primarily strike-slip faults, with subsidiary dip-slip fault strands are visible both in the cliff and along the wave-cut platform enabling plan view and cross sections to be investigated. Fault offset ranges from the 25 m main strand of the Crag Point Fault Zone, to cm-scale offsets. The exact offset of faults is difficult to quantify due to the amount of out-of-plane motion. Some faults mapped as normal faults in previous studies (Jones and Dearman, 1967; De Paola *et al.*, 2005) exhibit only strike-slip kinematic indicators. The bedding at the location is shallowly dipping ($\sim 5-8^\circ$), which enables the stratigraphy to be traced across many different faults in the area.

Spireslack SCM (Surface Coal Mine) is an abandoned open cast coal mine in the South Ayrshire coal field of the Midland Valley of Scotland. Exceptional exposures of lower Carboniferous rocks which includes a complete section of the Limestone Coal Formation, are found along the 1 km long, 100 m deep 'canyon' exposed during mining operations

(Leslie, Browne, et al., 2016; Ellen et al., 2019). Lithologies include limestones, sandstones, seat-earths, shales and coal (5.4%) which includes the historically important Muirkirk 9' and 6' Coals. Several strike-slip fault zones, along with at least five Paleogene basaltic dykes, cut the site and are exceptionally exposed both in high wall and dip-slope.

In contrast, the limestones, sandstones, siltstones and coals exposed at Howick, contain less than 2% coal, with only the 6" thick Parrot Seam present in the succession. In addition, the close proximity of the site to the Whin Sill has caused the increase of coal rank, and later coalification of organic rich shales. This enables a comparison between coal-measures which contain different amounts of coal in the succession and for the role of organics to be further investigated.

Detailed (1:2,000) geological mapping onto air-photographs was undertaken at all three sites to capture the broad structure and identify fault strands for further analysis. Lineament mapping of faults, fractures, and mine workings was completed on a high resolution (pixel size <5 cm) photomontage of the high wall at Spireslack SCM. This was complemented with the fault and fracture mapping of a high-resolution photomontage of the McDonald Limestone exposed on the dip-slope. The stratigraphy at Whitley Bay was logged, and along with the mechanical stratigraphy (c.f. Ferrill & Morris 2008), were used as a framework to understand the role of lithology and sub-bed scale heterogeneity on fault and fracture properties. Fracture data was collected using fracture mapping onto field-photographs, along with the completion of circular sample windows to classify joint properties at Whitley Bay. Detailed fault mapping and structural logs (c.f. (McKay et al., 2019) were undertaken along several fault strands, both at Whitley Bay and Howick, which ranged in displacement from <5 cm to c. 25 m. An exposure of collapsed pillar and stall workings of the High Main Seam at Whitley Bay was also classified using a sedimentological approach.

1.4 Thesis structure

The thesis is structured as a series of chapters in journal article format, of which one has been published (Chapter 3), and the rest representing early drafts. The chapters aim to address the research questions raised in the objectives for this project. A statement of authorship will be provided at the start of each chapter which outlines area of the thesis where other researches contributed to the work.

Chapter 2 provides a detailed review into the current knowledge in the field of faults which cut coal bearing stratigraphy. This chapter provides much of the rationale for this thesis.

Chapter 3 investigates the effect of subjective bias on the collection of fracture data, both in the field and workshop environment. This work underpins many of the ways in which fracture data are collected throughout the thesis and has been published in the special issue of Solid Earth “Understanding the Unknowns: uncertainty in geoscience” (Andrews et al., 2019).

Chapter 4 uses detailed sedimentary logging and mechanical stratigraphy to investigate the role of lithology and sub-bed scale heterogeneity on joint networks. The work highlights the importance of the plane of investigation, comparing results in bed-parallel and bed-perpendicular view, and linking this to the stratigraphic succession.

Chapter 5 provides an overview of the faulting style at Spireslack SCM (Surface Coal Mine), Ayrshire. A combination of geological mapping, detailed observations of fault zones, and fracture mapping of a limestone bedding plane and the high wall are used to investigate the effect of different lithologies and pre-existing structures on faulting style.

Chapter 6 investigates the fault-core lithologies developed in coal bearing sequences and looks to understand the effect of coal and organics in fault rock development. This chapter also looks at the relationship between fault-core thickness and displacement and compares findings to other lithologies.

Chapter 7 investigates the internal structure and damage caused by collapsed pillar and stall coal mine workings. The deformation of the overlying stratigraphy is investigated through detailed fracture mapping of the high-wall at Spireslack SCM. This was complimented by a detailed description, using a sedimentological approach, of the lithologies and structure of a 12.5 m long outcrop of workings at Whitley Bay. Both sites enabled the processes which occur during the collapse of pillar and stall workings to be investigated.

Chapter 8 summarises the findings of the previous chapters and provides recommendations for areas of further work.

Chapter 2: The role of coal in the faulting of mechanically layered sequences: Implications for mine safety and geothermal resources.

2.1 Rationale

Coal bearing successions are commonly found both globally and through geological time, often preserved within basins that display a long history of faulting. Faults cutting coal measures may significantly complicate coal extraction, decrease the stability of abandoned mine workings, and influence groundwater flow patterns within the basin. Despite the clear need to understand the behaviour of these faults, surprisingly few studies investigate how the presence of coal, combined with typical lithologies found within the fluvial-deltaic sequences that it is deposited within, affect the internal structure and growth of faults. Many researchers instead have considered how coal deforms in isolation. Coal is an unusual lithology in that it contains two roughly orthogonal sets of opening mode fractures, termed cleats, which research shows, strongly affect the mechanical properties of coal. However, coal typically constitutes less than 10% of the stratigraphic succession and seams rarely have thicknesses above a few meters. This means that all but the smallest faults will interact with the more than a single lithology, which typically include sandstones, siltstones, shales, seathearts and coals.

This chapter reviews the primary sedimentary processes that lead to the development of coal and provides an overview of how the mechanical properties of coal evolve. I then review the literature on fault attributes (e.g. dip and flow properties) and fault growth processes which have been derived from both mine abandonment plans and field evidence, along with discussing groundwater flow during inflow events. Finally, the current understanding and suggestions for future research are provided through: a) comparing sand/shale sequences which do not contain coal; b) considering the implications for subsurface coal extraction; and c) considering implications for low-enthalpy mine geothermal.

2.2 Introduction

Geological faults are known to strongly affect the mechanical strength and fluid flow properties of a rock mass. Many of the world's coal bearing basins contain numerous faults that: a) considerably increase the complexity and risk of coal extraction (Beamish and Crosdale, 1998; Cao et al., 2001; Coolen, 2003; Xu, 2011; Qi et al., 2014); b) decrease the long term stability of abandoned coal workings, and increase the risk of ground deformation of the overlying lithologies (e.g. Donnelly, (2006); Donnelly et al. (2009); Swift, (2014)); and c) complicate the hydro-geological properties of the basin (Jolley et al., 2010; Bense et al., 2013). Faults form sets in response to regional stress fields at the time of formation and are often observed as a zone of brittle deformation comprising of a fault core, where the majority of slip occurs, surrounded by a damage zone of subsidiary slip planes and fractures (Caine et al., 1996).

Due to the long history of coal mining, there is a significant volume of research into faults cutting coal. However, these this has focused on the: a) large-scale properties and evolution of the fault network (Watterson, 1986; Huggins et al., 1995; Nicol et al., 1996); b) properties of deformed coal in isolation (Ju et al., 2012; Godyń, 2016); and c) the groundwater flow and mechanical properties of fault zones in the vicinity to underground mining operations (Islam and Shinjo, 2009; Bu, 2013; T. Li et al., 2016). While field studies do exist (e.g. Jones and Dearman (1967); Carvell et al. (2014); Leslie et al. (2016); Delogkos et al. (2017)) they do not focus on the effect lithology has on the internal structure and growth of faults. For example, Færseth et al., (2007) and Gabrielsen et al., (2016) study the fault strand exposed at Whitley Bay, and used in this study (Hartley Steps Fault Zone), to investigate how shale-smears and fault-core lenses develop in the fault core.

Improving our understanding of faults cutting coal measures not only has implications for mining, but is also relevant to several industrial processes including: coal bed methane production (Guo et al., 2014); shallow mine geothermal (Malolepszy, 2003; van der Zee and Urai, 2005; Watzlaf and Ackman, 2006); underground coal gasification (Bhutto et al., 2013); carbon capture and storage (CCS) (Gale, 2004); and the mitigation of underground coal fires (Wolf and Bruining, 2007). To understand the properties of sub-surface faults industries need to be able to predict fault zone properties such as: a) thickness (of damage zone and fault core); b) trace length of individual fault strands; and c) the connectivity of the fault-fracture network. It is important to consider the level of spatially and temporal variability

these properties (McKay et al., 2019.; De Rosa et al., 2018) and how they evolve as displacement increases (Walsh et al., 2002; R.J. Lunn et al., 2008; Torabi, Johannessen, et al., 2019) and. Due to modelling constraints and the limited data on faults cutting coal bearing lithologies, many studies assign a single set of properties to a planar fault zone. This leads to the oversimplification of fault properties which in the case of sub-surface coal mining can lead to the loss of life through unexpected blow-out or inflow events (Islam and Shinjo, 2009; Guo et al., 2009; Bu, 2013).

Successions which consist of lithologies with contrasting rheological properties (e.g. tensile strength, elastic stiffness, brittleness and fracture mechanics) commonly develop mechanical stratigraphy (D.A. Ferrill and Morris, 2003; Morris et al., 2009; Ferrill et al., 2017). Fluvial-deltaic sequences are one such example and typically consist of interbedded limestones, sandstones, siltstones, seat-earth, and coals. (Thomas, 2013) (Figure 2.2). Research into mechanically layered sequences has focused on: a) fault growth, in particular of normal faults (Ferrill et al., 2017); b) the controls behind the vertical restriction of faults (Wilkins and Gross, 2002; Soliva and Benedicto, 2005; Ferrill et al., 2014); c) the effect of layering on folding and fault-bend folds (Fischer and Jackson, 1999; Chester, 2003; Lăpădat et al., 2017); and d) the development of fault rock (Wibberley et al., 2008; Woodcock and Mort, 2008; Torabi, Johannessen, et al., 2019). Much of this work concentrates on 'binary' systems which consist of competent limestones and/or sandstones interbedded with incompetent shales and/or marls. However, the sedimentary architecture of fluvial-deltaic successions exhibit many small scale, laterally discontinuous sedimentary structures (e.g. channelised sand layers, mud-draped ripples, soft-sediment deformation, and channel coals (Fielding, 1985; Fielding, 1986a; Besly and Fielding, 1989; Thomas, 2013) and coal, in addition to sandstone and shale.

To understand the internal structure, fluid flow properties, and temporal evolution of faults cutting coal measures it is important to classify the properties and distribution of all mechanical units which make up the stratigraphic succession (Ferrill et al., 2017).

Therefore, this chapter begins by reviewing the properties and depositional processes of coal, and the sedimentary successions in which it is found (section 2.4.1). This is followed by a review of naturally deformed coal (Section 2.4.1) and how rock-deformation experiments have been used to understand the mechanical properties of coal, and how these evolve during deformation (Section 2.4.3). Faults which cut the full sequence are then considered

(Section 2.4.4), for research which uses field examples, mine abandonment plans, and hydrogeological data from inflow events. Finally future areas of research are suggested by highlighting: a) how faults cutting fluvial-deltaic sequences compare to those cutting binary mechanically layered sequences (Section 2.5.1); b) implications for sub-surface coal mining (Section 2.5.2); and c) implications for low-enthalpy mine geothermal projects (Section 2.5.3).

2.3 Undeformed coal

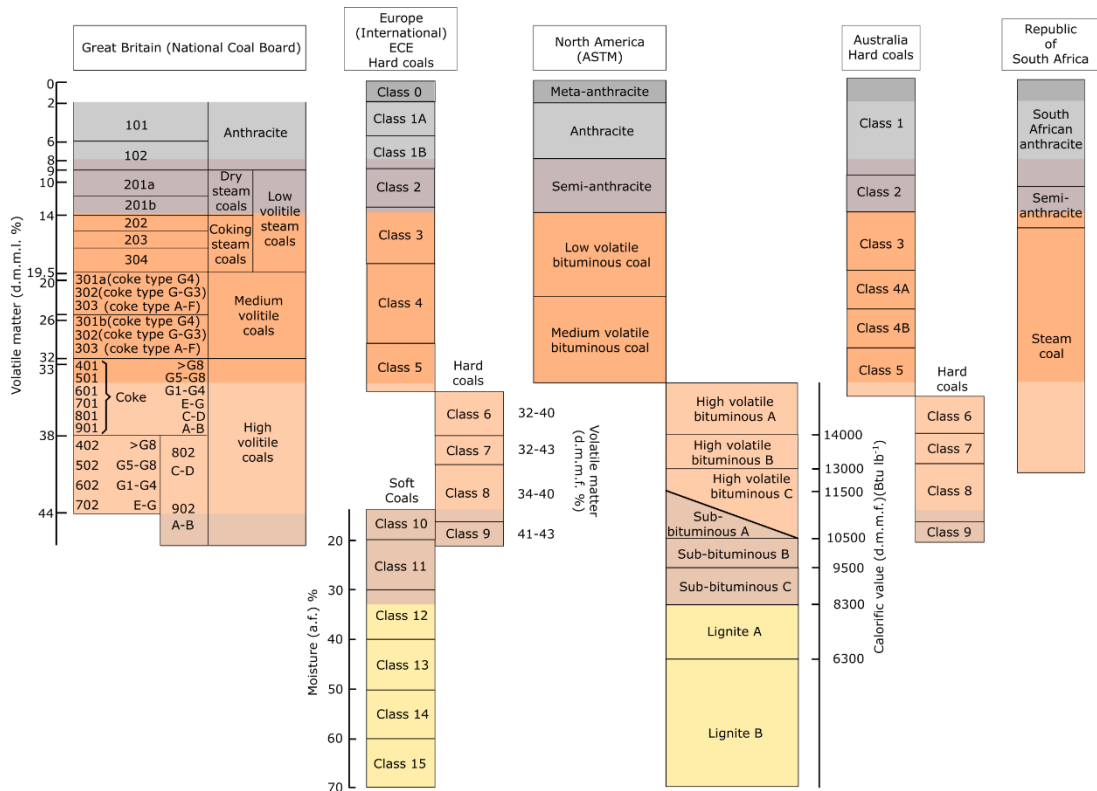


Figure 2.1: Coal classification schemes (redrawn from Thomas (2013)). Colours represent the overarching terminology used in this thesis of 'lignite', 'sub-bituminous', 'bituminous', 'anthracite' and 'meta-anthracite'.

Coal is an unusual lithology in that it is a complex sedimentary rock composed largely, but not entirely, of plant debris and derivatives deposited in peat bogs (O'Keefe et al., 2013). The properties of a particular coal seam are determined by a combination of depositional environments, the composition of the deposited material, and the degree of coalification that has occurred during and following burial (Dawson et al., 2012; Thomas, 2013; O'Keefe et al., 2013). Coalification is the series of bio-chemical, geochemical, and metamorphic reactions which convert the deposited organic matter into peat, then onto the various ranks of coal (Taylor et al., 1998; O'Keefe et al., 2013). As coalification increases, the rank

progresses from Lignite through to Meta-anthracite (ASTM classification, see Figure 2.1 for global classification schemes). Coalification is primarily driven by an elevated temperature over a sufficient period of time, with pressure also having a minor effect at low ranks (Hilt, 1873; O'Keefe et al., 2013; Thomas, 2013). Elevated temperatures typically occur during burial, however, can also be achieved where coal is in proximity to, or in contact with, igneous bodies (Hilt, 1873; Ward, 1984; Thomas, 2013). Ranks up to bituminous coal can be attained through burial alone, however, higher ranks require additional heat input (Stach et al., 1982).

Although coal seams are often regionally extensive, variations in the thickness and structure of a seam can occur (Figure 2.2). Seams often split along strike into one or more 'leaves' separated by layers of non-coal material termed 'partings' or 'bands' (Christopher R. Fielding, 1984; Moore, 1991; Thomas, 2013). Splits may be simple and represent a period of clastic deposition which replaced organic accumulation (e.g. from a crevasse splay), or complex and often associated with growth faulting (Christopher R. Fielding, 1984; Fielding, 1986b; Thomas, 2013). The thickness and quality of coal seams can change spatially due to: (a) variable clastic input caused by marine intrusion, overbank flooding, or nearby volcanic activity; (b) the presence of washouts, whereby a section of the seam is partly, or fully, removed during deposition due to wave or river action; or (c) the presence of ridges in the seam floor, termed floor rolls, caused by the differential compaction of peat around pre-existing clastics (Forgeron et al., 1986; Cairncross et al., 1988; Greb et al., 2001). Many coal bearing sediments were deposited in, or on the margins of an active tectonic basin. Basin evolution is often associated with active faulting (e.g. South Wales) and/or high subsidence rates that lead to slope instabilities and the presence of slumping, load and flame structures, and sand-injectites within the sedimentary succession (Elliott, 1989; Greb et al., 2001; Thomas, 2013).

Coal is characterised by a blocky appearance caused by two perpendicular sets of densely spaced (cm-scale) opening mode fractures called cleats (Laubach et al., 1998) (Figure 2.2b). Sets are easily distinguishable and consist of an earlier through going set, termed face cleats, and a subordinate set which abuts against the pre-existing face cleats which are termed butt cleats (Laubach and Tremain, 1991; Tremain and Laubach, 1991; Kulander and Dean, 1993). Laubach and Tremain (1991) highlighted the hierarchical nature of cleats with three sub-divisions:

- **Master cleats** [*<10 cm height*] extend throughout the whole coal seam including any partings that may be present.
- **Primary cleats** [*1-10 cm height*] extend the thickness of a coal bed.
- **Tertiary cleats** [*<1 cm height*] terminate within the coal bed.

Typically, cleats are planar, although occasionally curve in plan view, and form at right angles to bedding (Laubach et al., 1998; Dawson and Esterle, 2010; Liu et al., 2016). Coal cleats form in a response to shrinkage due to the loss of volatiles (Ting, 1977; Ryan, 2003) and a combination of stress release and extensional strain during burial (Olson, 1993; Bai and Pollard, 2000; Golab et al., 2013; Rodrigues et al., 2014). The orientation of cleats may be influenced by tectonic stress (Rippon et al., 2006; Paul and Chatterjee, 2011) with face cleats forming perpendicular to the least compressive principal stress (σ_3) (Kulander and Dean, 1993; Paul and Chatterjee, 2011).

To understand the mechanical and fluid flow properties of coal the spacing, orientation, aperture, trace length, connectivity, and mineralisation of cleats in the network needs to be classified (Close and Mavor, 1991; Laubach et al., 1998; Ortega et al., 2006). Similarly to other jointed lithologies (e.g. sandstone), cleat length, aperture (typically <0.2 mm (Close and Mavor, 1991)), and length distributions scale with the thickness of the coal seam (Mcquillan, 1973; Close and Mavor, 1991; Tremain and Laubach, 1991; Laubach et al., 1998). Dull coals have wide cleat spacing of the order 5 to 10's cm, whereas bright coals have a tighter, cm-scale, cleat network (Ryan, 2003; Dawson and Esterle, 2010). As rank increases cleat spacing initially decreases from peat to sub-bituminous coal (Law, 1993; Laubach et al., 1998). At higher ranks a large degree of scatter is observed (Law, 1993; Laubach et al., 1998) as cleats become annealed (Su et al., 2001). For the analysis of trace length and spacing, cleats need to be considered based on their set (face/butt), hierarchy (master/primary/tertiary), and litho-facies (e.g. bright or dull) (Dawson and Esterle, 2010).

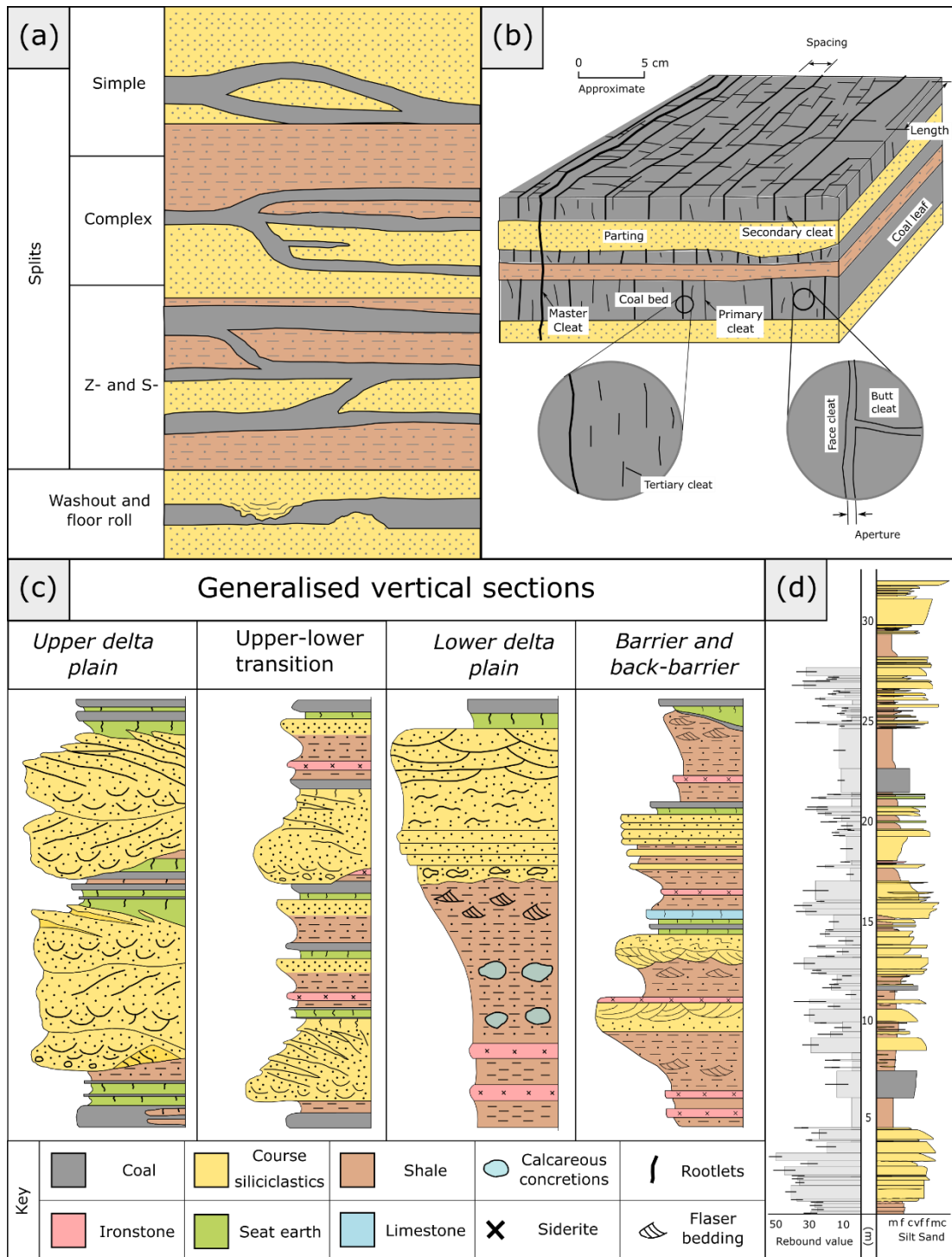


Figure 2.2: Characteristics of undeformed coal. (a) variations in coal seam thickness and splits (Thomas, 2013), (b) coal cleats (adapted from Laubach et al., 1998), (c) representative sedimentary logs of coal bearing successions (Thomas, 2013), and (d) stratigraphy and mechanical stratigraphy from Whitley Bay, Northumberland (UK), see Chapter 4 for details.

Although heterogeneities exist, both at the seam and sub-seam level, coal seams can be considered a laterally extensive stratigraphic layer. Lithologies which accompany coal in the stratigraphic succession include sandstones, siltstones, shales, paleo-soils, and occasionally limestones. These lithologies are deposited as repeated cycles termed 'cyclothem' which are typically 10s of meters thick (Horne et al., 1978; Coleman and Prior, 1982; Holz et al., 2002). Coal deposition models consist of three subtly different facies (Horne et al., 1978); a) coastal barrier and back barrier, b) lower delta plain, and c) upper delta and alluvial plain as outlined in Figure 2.2c.

2.4 Deformed coal

Since the early days of coal mining it has been recognised that faulting may: a) effect the properties and quality of coal (e.g. Hull, (1873); Smalls, (1935); Shepherd et al., (1981); Beamish and Crosdale, (1998)); b) localise deformation along bed-parallel shear zones (Bustin, 1982; 1986; Frodsham and Gayer, 1999; Li, 2001; Li et al., 2003); or c) cause widespread folding and disruption within a coal-field (Coolen, 2003; Robeck, 2005; Leslie, Browne, et al., 2016). Tectonic deformation leads to Tectonically Deformed Coals (TDCs) through the development of a dense fracture network prior to crushing and grinding processes which eventually destroy the original structure (Shepherd et al., 1981; Cao et al., 2000; Ju et al., 2012; Godyń, 2016). Deformation of coal leads to increased fracture intensity coupled with the crushing and grinding of the coal matrix (Shepherd et al., 1981; Cao et al., 2000). The location and intensity of this deformation may be limited to a single seam (e.g. Pingdingshan, China) (Li, 2001; Cao et al., 2001) or distributed throughout all seams in the stratigraphic succession (e.g. South Wales) (Frodsham and Gayer, 1999; Fowler and Gayer, 1999)).

2.4.1 *Naturally deformed coal*

The structural texture of a given coal varies depending on: a) the tectonic environment; b) the intensity of deformation; and/or c) the initial composition and coalification of the seam. Due to the global exposures of coal and different approaches used by authors to describe deformed coal, a wide array of classification schemes for TDCs have been developed (Table 2.3). I describe the textural evolution of deformed coal using the broad classifications of cataclastic and granular coal for coal that has deformed in a brittle manner, and mylonitic coal where ductile deformation features are observed.

As strain increases, micro fractures begin to develop, which initially do not disaggregate the cleat network (Jiang et al., 2004; Godyń, 2016). The location of microfractures is initially widely spaced before localising along a discrete shear plane where grain crushing may be observed (Ju and Li, 2009; Godyń, 2016). These shear planes act to disrupt the primary structure and rotate blocks of coal bounded by cleats which leads to a lenticular structure being developed (Ming et al., 2011). As fracturing increases a greater proportion of coal becomes crushed within a network of interlinking shear-fractures, leaving large clasts (2 to 5 mm) suspended in a fine matrix (Jiang et al., 2004; Ming et al., 2011; Godyń, 2016). At this stage the primary structures of the coal seam begin to be significantly disrupted such that in some areas original features are lost altogether (Frodsham and Gayer, 1999; Ming et al., 2011; Godyń, 2016). Once the fine matrix becomes dominant it is termed granulitic or cataclastic coal (Cao et al., 2000; Cao et al., 2001; Cao et al., 2003; Jiang et al., 2004; Godyń, 2016), where the matrix typically has a particle size below 10 microns (Godyń, 2016). Initially isolated undeformed grains will survive, however, as deformation increases the texture becomes banded until no grains that display primary structure remain and the primary layering and cleats are blurred by deformation features (Ju and Li, 2009; Godyń, 2016).

At high levels of strain and/or temperature, coal may deform in a ductile manner leading to the development of mylonitic coal (Table 2.1). Initially orientated sub millimetre clasts are found within a granular texture along with local folding developed (Cao et al., 2000; Li et al., 2003; Jiang et al., 2004; Godyń, 2016). Clasts then decrease in size leading to the loss of recognisable coal clasts, and plastic flow becomes common leading to the local development of an folds and S-C fabrics (Jiang et al., 2004; Godyń, 2016). As deformation increases, a mylonite type structure develops with clear directionality, ductile flow of vitrinite, and the development of undulous extinction (Ju and Li, 2009; Ming et al., 2011).

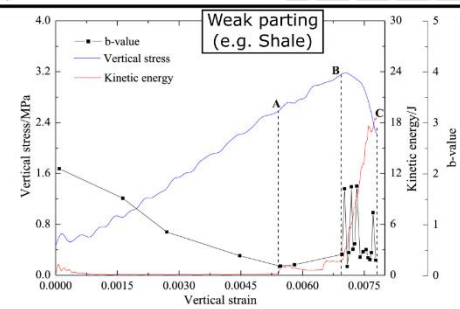
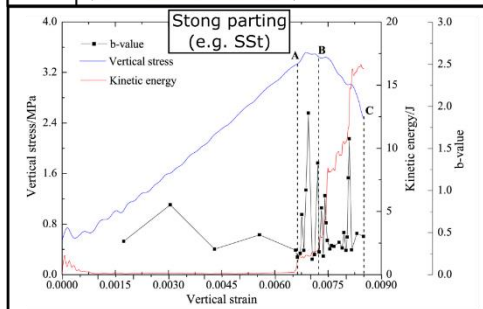
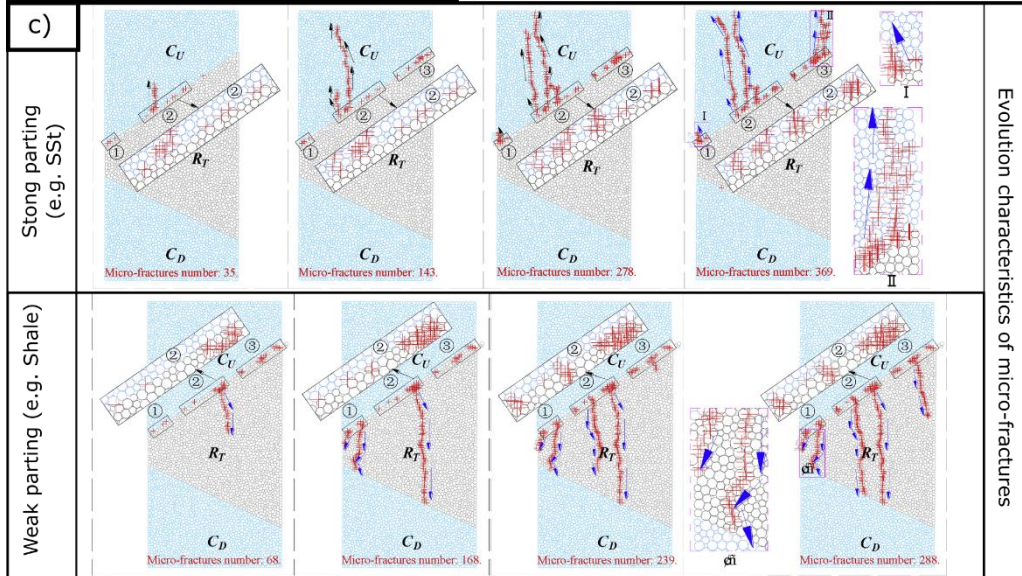
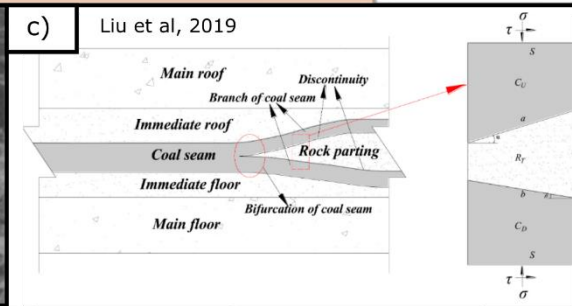
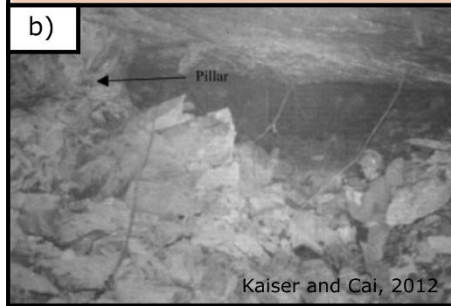
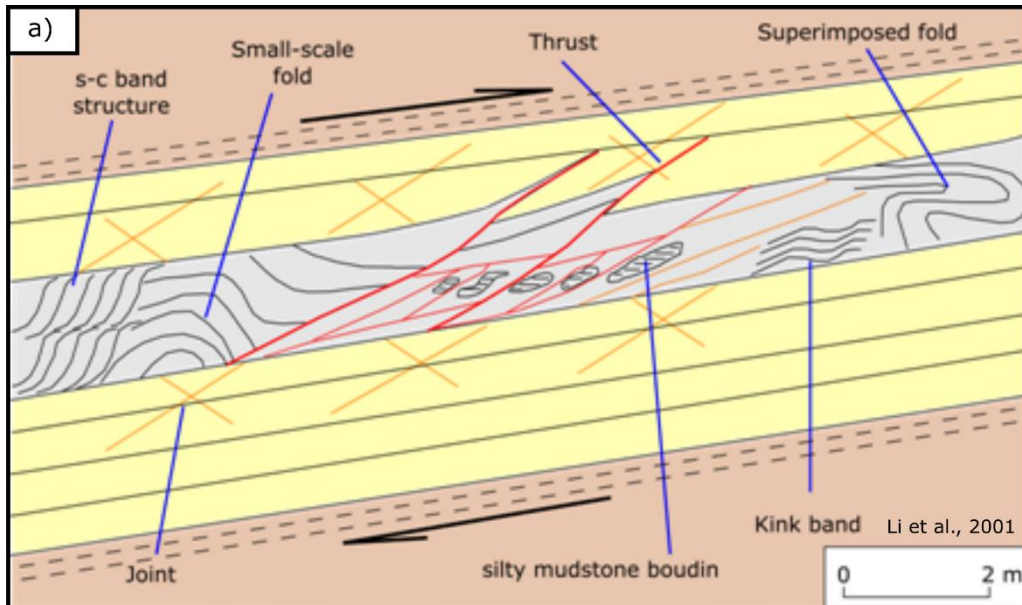
Deformation style	Unaltered	Characteristic features																																		
Plastic deformation	The coal displays a very dense fracture network that gives a cataclastic granular texture with clasts <1 mm. Some directionality and ductile deformation may be present.	The primary structure is difficult to observe and a layered structure is not clearly seen.	The texture becomes banded with only small particles displaying the original structure remain.	The coal displays a 'granulitic' texture whereby the coal has been ground and dislocated and the original structure disaggregated. Isolated grains may survive, however, Particles are less rough and > 10 microns.	A high degree of fracturing is visible and a 'porphyroclastic texture' is developed with large (2 – 5 mm) clasts suspended in a fine matrix. The original structure of the coal is difficult to distinguish and only visible in large clasts.	A very dense network of irregular fractures with some isolated grain crushing. Displacement and a degree of blurring of the primary structure is visible into a lenticular structure.	A dense network of irregular fractures where the primary structure remains clearly visible.	The coal displays an irregular pattern of exo-microfractures which show no clear displacement and original layering remains intact.	Initial structure	(Jiang et al., 2004)																										
											Mylonitic system	Mylonite coal	Wrinkle coal	Squamaceous coal																						
												Mylonite proper	Mylonite structures	Pre-Mylonite	Cataclastic coal																					
														5. Briquetted coals	4. Mylonitized coals	3. highly Fractured coal																				
	Mylonite coal	Mylonite coal	Mylonite coal	Cataclastic coal	Cataclastic coal																															
	Brittle deformation	Series of ductile deformation	Ductile structural	Mylonite coal	C2	C1	Wrinkle coal	Scale coal	Thin-Layer coal	Schistose coal	Mortar coal	Cataclastic coal	Primary cataclastic	Normal coal	(Cao et al., 2000; Cao et al., 2001; Cao et al., 2003)																					
																Series of brittle deformation	Mortar Structure coal	Cataclastic structure coal	B	A	Ju and Li 2009	Ming et al., 2011														
																							Schistose structure coal	Mortar Structure coal	Cataclastic structure coal	Cataclastic coals	Rakowski et al. 1977 (cited in									
																												Schistose structure coal	Mortar Structure coal	Cataclastic structure coal	Granular coal	Li et al., 2003)				
																																	Schistose structure coal	Mortar Structure coal	Cataclastic structure coal	Cataclastic coals
		Series of brittle deformation	Mortar Structure coal	Cataclastic structure coal	Cataclastic coal	Cataclastic coal	Cataclastic coal	Cataclastic coal																												
Cataclastic coal									Cataclastic coal	Cataclastic coal	Cataclastic coal	Cataclastic coal																								
Series of brittle deformation		Mortar Structure coal	Cataclastic structure coal	Cataclastic coal	Cataclastic coal	Cataclastic coal	Cataclastic coal																													
								Cataclastic coal	Cataclastic coal	Cataclastic coal	Cataclastic coal	Cataclastic coal																								
Series of brittle deformation		Mortar Structure coal	Cataclastic structure coal	Cataclastic coal	Cataclastic coal	Cataclastic coal	Cataclastic coal																													
								Cataclastic coal	Cataclastic coal	Cataclastic coal	Cataclastic coal	Cataclastic coal																								
Series of brittle deformation	Mortar Structure coal	Cataclastic structure coal	Cataclastic coal	Cataclastic coal	Cataclastic coal	Cataclastic coal																														
							Cataclastic coal	Cataclastic coal	Cataclastic coal	Cataclastic coal	Cataclastic coal																									
Series of brittle deformation	Mortar Structure coal	Cataclastic structure coal	Cataclastic coal	Cataclastic coal	Cataclastic coal	Cataclastic coal																														
							Cataclastic coal	Cataclastic coal	Cataclastic coal	Cataclastic coal	Cataclastic coal																									
Series of brittle deformation	Mortar Structure coal	Cataclastic structure coal	Cataclastic coal	Cataclastic coal	Cataclastic coal	Cataclastic coal																														
							Cataclastic coal	Cataclastic coal	Cataclastic coal	Cataclastic coal	Cataclastic coal																									
Series of brittle deformation	Mortar Structure coal	Cataclastic structure coal	Cataclastic coal	Cataclastic coal	Cataclastic coal	Cataclastic coal																														
							Cataclastic coal	Cataclastic coal	Cataclastic coal	Cataclastic coal	Cataclastic coal																									

Table 2.1: Classification of Tectonically Deformed Coals (TDCs).

2.4.1.1 Soft coal bands and the effect of in-seam heterogeneities.

Soft coal bands (SCBs), where a coal seam has been deformed through bed-parallel shear (Bustin, 1982; Bustin, 1986; Frodsham and Gayer, 1999; Li, 2001), are important as they increase the risk of outburst events (Li, 2001). SCBs act to significantly weaken the coal seam (Li, 2001), and are most commonly observed in areas of compressive deformation within thick coal seams and/or where shale partings are present (Frodsham and Gayer, 1999; Li, 2001). SCBs may locally cause the seam to display an increased rank (Fowler and Gayer, 1999; Li, 2001) which has been attributed to either frictional heating (Bustin, 1983; Guo and Han, 1999) or pulses of hot fluid (Fowler and Gayer, 1999).

The internal structure of SCBs can be complex and spatially heterogeneous with both brittle and ductile features present (Figure 2.3a). SCBs often have an absence of bedding structure and an increased occurrence of TDCs, in particular cataclastic coal (also termed friable coal) (Li, 2001; Le et al., 2010). Minor structures include small thrusts, strongly vergent folds, and cleavage (Li, 2001 *and references therein*). SCBs generally display relatively uniform thickness, however, thrusts may locally thicken the seam through imbrication (Frodsham and Gayer, 1999; Li, 2001). Cleavage, and associated structures (e.g. S-C bands, cleavage duplexes) can be observed at both a macro- and microscopic scale (Bustin, 1982; Bustin, 1983; Li, 2001) and eventually destroy the primary cleat network (Hathaway and Gayer, 1996). Ductile deformation is not uniformly found throughout a seam, and instead is only locally developed in association to thrusting (Hathaway and Gayer, 1996; Li, 2001; Le et al., 2010).



Variation curves of vertical stress, cumulative AE event count, and strain and kinetic energies

Figure 2.3: (previous page) Bed shear zones & effect of partings/bumps (redrafted from Li, 2001); b) example of a rock-burst caused by a failed pillar (Kaiser and Cai, 2012); c) the effect of a strong and weak parting on the deformation of coal-rock-coal partings (Liu, C.-P. Lu, et al., 2019) (c) highlights the modelled evolution of micro-fractures when a parting is both weaker (e.g. sandstone) and weaker (e.g. shale) than the coal seam. The evolution of vertical stress, cumulative acoustic emission counts, strain and kinetic energies from both cases are also presented.

Partings, which may be shale or sandstone, impart a mechanical heterogeneity into the coal seam which acts to localise deformation and increase the risk of rockbursts (Petukhov and Linkov, 1979; Tan et al., 2016; Liu et al., 2019a ; b; Lu et al., 2019; Yang et al., 2019) and pillar collapse (Kaiser and Cai, 2012) during sub-surface mining (Figure 2.3). The mechanical boundary between the coal and parting, which is often inclined relative to bedding, may promote failure as stress states change during mining operations (Liu et al., 2019a; b).

Whether a parting will affect the stability of a coal seam depends on: a) the applied normal and shear stresses, often related to mining operations; b) the strength contrast between the parting and coal; c) the strength and frictional properties of the mechanical boundary; and d) the angle of the parting relative to the applied stress (Liu, 2019a; b *and references therein*). The failure along the coal-parting interface causes increased fracturing of either the coal or parting, depending on the relative strength and the contact angle between the lithologies (Figure 2.3c) (Kaiser and Cai, 2012; Liu, 2019a; b). Where the parting is thin, both edges of the parting may act as a plane of weakness. When this occurs it is the plane at the greatest angle to the applied stress which fails first, accompanied by the generation of fractures in the surrounding lithologies (Liu, et al., 2019a). Within SCBs partings partings may become disaggregated and tectonically emplaced along SCBs which leads to unpredictable geomechanical properties (Li, 2001).

2.4.2 Mechanical properties of deforming coal

The mechanical properties of a coal are controlled by the compressive and tensile strengths, elastic moduli, Poisson's ratio, and fracture stiffness (Zhao et al., 2016a). These properties control the style in which coal deforms, whether dynamic failure will occur and cause rock bursts, and potentially effect the deformation style of the coal-bearing sequence. The mechanical properties of coal are primarily studied through rock deformation experiments (e.g. Cao et al., (2003); Wang et al., (2013); Zhao et al., (2016); Tan et al., (2016); Gao et al., (2016)) and will be summarised in this section.

During progressive deformation rocks develop both tensile and shear fractures, with tensile fractures forming perpendicular to the loading direction and shear fractures forming at a high angle (Shiotani et al., 2001; Paterson and Wong, 2005). The sample will eventually fail when peak strength is reached and a through-going shear band will form cutting the whole sample. Unlike homogenous rocks (e.g. granite), coal contains natural fractures due to the presence of closely spaced bed-partings and cleats (e.g. Laubach *et al.* (1998)). Many authors have found that lithologies which contain pre-existing weaknesses display inhomogeneous strength characteristics (e.g. Zhang, 2011; Cho 2012 Chen 1988 akalloeian 2000 Zhang 2016 Dehler 2007 (Chen et al., 1998; Dehler and Labuz, 2007; Zhang et al., 2011; Cho et al., 2012; Y.W. Li et al., 2016). The tensile failure of favourably orientated cleats dominates the early deformation of coal due to its low tensile strength (typically < 5 MPa) (Zhao et al., 2016a). Depending on the orientation of the cleat network relative to the loading direction it is common for cleats to become reactivated, leading to highly asymmetric deformation patterns (Zhao et al., 2016a; Y.W. Li et al., 2016). This is particularly the case when face-cleats are orientated at 45° to the applied stress (Zhao et al., 2016a; Y.W. Li et al., 2016) where Li et al (2016) found the strength of coal samples to decrease by a factor of nearly two (Figure 2.4c) (Y.W. Li et al., 2016). The style of fracturing can be classified as 4 major patterns depending on the relative orientation to the applied stress to the internal structure of the sample, α (Figure 2.4) (Y.W. Li et al., 2016).

1. Thoroughgoing vertical fractures which form roughly parallel to the loading direction when $\alpha = 0^\circ, 15^\circ, \text{ or } 90^\circ$.
2. Cleats become reactivated by shear when α is between 30° and 75° .
3. Complex fracture networks develop that deviate from loading direction and initiate at the loading point.
4. Shear reactivation of cleats away from the centre of the sample.

Due to the unique properties of coal, the mechanical properties are affected not only by strain rate and loading direction, but also the following factors:

- **Coal mineralogy:** The presence of non-organic mineral particles can affect the strength of coal (Cai et al., 2015; Gao et al., 2016). For example, Gao et al (2016) found that the presence of calcite in a coal sample acted to increase the Young's modulus (from 2.5 to 3.3) and decrease the peak strength and brittleness of the coal (Figure 2.4a). This led to different fracture patterns

being observed in samples which contained calcite and those which did not (Figure 2.4b).

- **Wetness of coal:** The tensile and uniaxial compressive strength (UCS) of coal has been found to depend on moisture content (Zhao et al., 2016a). Similarly to sandstone UCS is greater for dry samples when compared to saturated coal (Colback and Wiid, 1965; Hawkins and McConnell, 1992), while tensile strength was found to be higher for saturated samples, however, tensile strength was strongly dependent on loading rate (Figure 2.4f,g) (Zhao et al., 2016a).
- **Mineral fill:** The mineralisation of cleats, particularly with ankerite, is commonly observed in coal seams (e.g. the McDonald Coal, Ayrshire (UK) (Ellen et al., 2016)). Espinoza et al. (2016) found that mineralised cleats could act as stress concentrations leading to the development of fractures and an increase in the brittleness of the coal.
- **Loading/unloading:** Mechanical properties of coal vary under loading and unloading conditions. G. Yin et al. (2015) found that increased unloading rate corresponds to a lower compressive strength and ductile strain in coal samples.
- **Sorption strain:** Micro-fractures can lead to the migration of coal-bed methane from the matrix into the cleat network (Wang et al., 2013). This alters the structure of the coal due to sorption strains (Karacan et al., 2008; Majewska et al., 2009) and reduces the peak-strength of the coal (Wang et al., 2013; Vishal et al., 2015).

Overall, coal may be considered a weak, pre-fractured lithology whose deformation characteristics depend on strain-rate, loading direction, and several additional factors as outlined above.

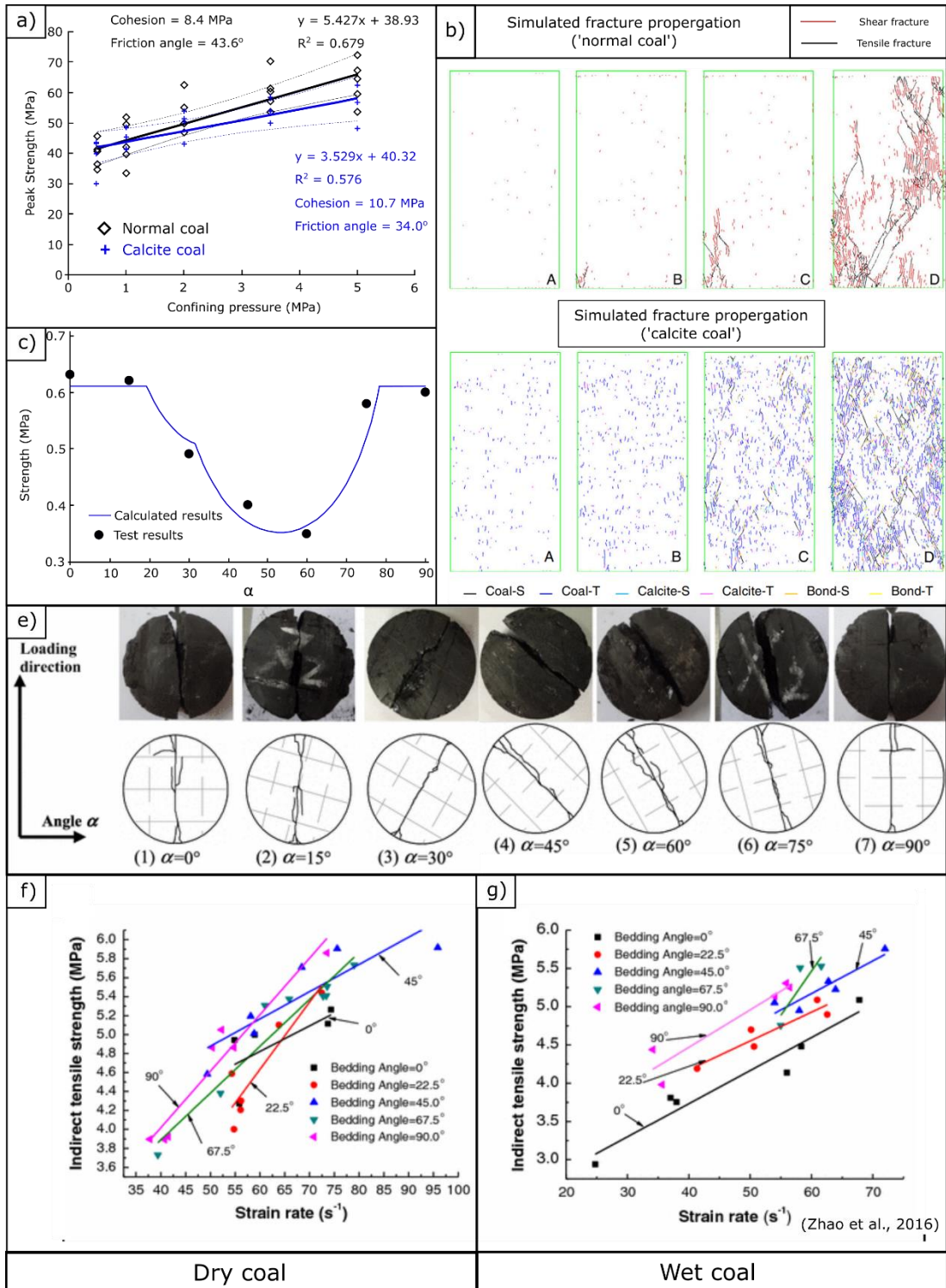


Figure 2.4: Mechanical properties of coal. a) Peak strength under triaxial compression for regular and calcite-rich coal (Solid line represents the regression line, with dashed representing the 95% confidence level) (Gao et al., 2016). b) Simulated fracture development in normal and calcite coal (Gao et al., 2016). c) Failure strength against angle of cleats relative to loading direction for Brazilian tests and calculated curve (Y.W. Li et al., 2016). d) Fracture patterns under different loading angles after Brazilian splitting tests (50 (Figure 2.4 caption

continued) mm diameter samples) (Y.W. Li et al., 2016). Indirect tensile strength of dry (f) and saturated (g) coal under different loading direction and impact conditions (Zhao et al., 2016a).

2.4.3 Deformation of coal towards a fault zone & studies of faulting style

2.4.3.1 Large scale properties of faults in coal measures

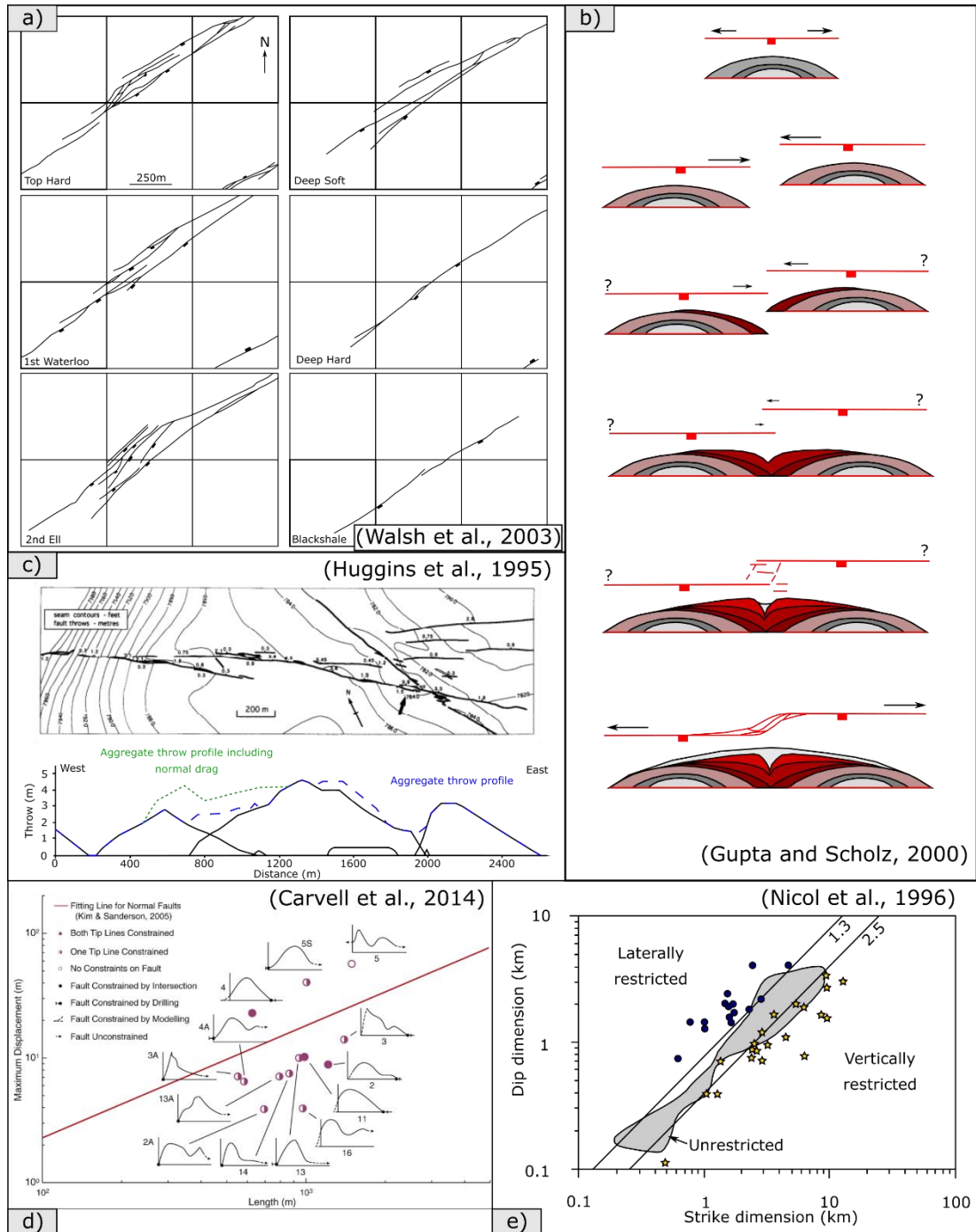


Figure 2.5(Previous page): Fault scaling and restriction. a) Example of fault-strands recorded on mine abandonment plans in an area of Markham Colliery, Derbyshire Coalfield, UK, centred on a NE striking fault zone; the area was initially described by Rippon, (1985), redrawn from (Walsh et al., 2003); b) Conceptual model of the interaction of sub-parallel faults (Gupta and Scholz, 2000); c) Trace geometries and throw profiles for a segmented fault, Barnsley seam, Silverwood Colliery, South Yorkshire (Huggins et al., 1995); d) maximum displacement-length scaling plot, Hail Creek, NE Australia (Carvell et al., 2014); e) Dip dimension vs strike dimension for laterally (open circles) and vertically (crosses) restricted faults (Nicol et al., 1996).

Since 1872 the UK government has required coal mines to undertake detailed surveys, such as those shown in Figure 2.5a, to recorded the extent and geological structure of worked coal seams. Mine abandonment plans have been used to understand: a) the strain partitioning within the basin (Waldron, 2004; Waldron, 2005; Bailey et al., 2005); b) fault transfer and displacement patterns (Huggins et al., 1995; Nicol et al., 1996); c) fault scaling relationships (Walsh et al., 2002; Carvell et al., 2014); and d) complex 3D fault and fold relationships (e.g. Ellen et al., (2016); Leslie et al., (2016)). Faults in coal measures are typically either syn-sedimentary growth faults that formed early during basin evolution or tectonic faults that formed once peat has been coalified (Walsh and Watterson, 1988). Growth faults display shallow dips ($<55^\circ$, median = 47°), rarely effect more than a single cyclothem (Walsh and Watterson, 1988), and often cause coal seams to split (Fielding, (1984); Fielding, (1986); Broadhurst and France, (1986).

The most common form of faulting in coalfields, particularly the UK, are tectonic normal faults (Rippon, 1985; Walsh and Watterson, 1988). The dips of tectonic faults in coal measures usually exceed 55° , and display median dips between 65° and 68° (Walsh and Watterson, 1988 *and references therein*). This is in contrast to Hail Creek Coal Mine, NE Australia where Carvell et al (2014) found the dip of normal faults within coal to be lower (Mean = $43^\circ \pm 7^\circ$) than other lithologies in the sequence (e.g. sandstone; mean = $65^\circ \pm 8^\circ$). Strike slip faults cutting coal at Spireslack SCM show similar dips in coal with average values of 49° observed in coal seams (see Chapter 5). Fault-dip values from mine plans are likely higher because they represent the average dip of the fault plane between two or more seams worked from the same colliery (Walsh and Watterson, 1988), and hence will be effected by the steep dips of fault strands within competent layers.

Mine abandonment plans provided the cornerstone for understanding of how segmented fault-strands interact and evolve from isolated faults to kinematically linked strands (e.g. Cowie and Scholz, (1992); Huggins et al., (1995); Nicol et al., (1996); Walsh et al., (2003);

Kim and Sanderson, (2005)). Much of this work used throw profiles, where fault throw is recorded along the strike of a fault in outcrop or recorded on a mine plan (Figure 2.5b). Initially fault strands grow in isolation (Figure 2.5c; Stage 1 to 2), with displacement increasing towards the centre of the strand (Dawers et al., 1993; Scholz et al., 1993; Huggins et al., 1995; Dawers and Anders, 1995; Kim and Sanderson, 2005). As faults grow towards each other (Stage 3 to 4), throw begins to transfer between strands until subsidiary faults and fractures occur within a 'relay zone' that separates the two fault strands (Stage 4 to 5) (Huggins et al., 1995; Kim and Sanderson, 2005; Fossen and Rotevatn, 2016). Finally, the fault strands breach this zone leaving a throw profile which mimics that of an isolated fault (Figure 2.5b; Stage 6)(Gupta and Scholz, 2000). In coal mines relay zones are characterised by faults with <2 m throw and are nearly always only recorded within a single coal seam, with displacement dying out between seams (Figure 2.5a) (Huggins et al., 1995; Nicol et al., 1996; Soliva and Benedicto, 2005).

The vertical restriction of faults is common when a strong mechanical stratigraphy is developed (Wilkins and Gross, 2002; Long and Imber, 2011). This causes the majority of faults in coal measures to display high aspect ratios between length and displacement (mean = 2.6 compared to 2.15, (Nicol et al., 1996)) elongated along strike compared to what is expected for a given displacement (Figure 2.5d) (Nicol et al., 1996; Childs et al., 1996; Soliva and Benedicto, 2005). Small offset faults often occur at an oblique angle to the main fault trend and abut against pre-existing larger structures (Huggins et al., 1995; Waldron, 2004; Waldron, 2005). These faults are laterally restricted, and display low trace lengths, large throw gradients, and therefore high displacement: length (D:L) ratios (Figure 2.5e) (Nicol et al., 1996; Peacock, 2001; Crider and Peacock, 2004; Soliva and Benedicto, 2005).

Mine plans provide information for faults with throws greater than c. 15 cm (Huggins et al., 1995; Waldron, 2005), and represent an extensive dataset for faults over a wider area than field-observation, and at a far greater resolution than 3D seismic (c. 30 m) (Yielding et al., 1996). However only the faults which occur within the worked area and that effected the extraction of coal are recorded (Waldron, 2005). Additionally, in areas of geological complexity, the spacing of pillars (coal left behind to support the roof), was reduced (Bruyn and Bell, 1999) and areas in proximity to large faults were not worked (due to the degradation of coal quality and increased risk). Due to this it is often impossible to deduce

from mine plans alone whether throw occurs along multiple small offset fault strands, or a single large fault. This highlights the importance of using field evidence to understand both how coal changes towards a fault zone, and how the internal structure of a fault zone develops.

2.4.3.2 The internal structure of fault-zones from field evidence

While several studies either investigate the large scale structure of coalfields (Section 2.4.3.1) or the way that coal deforms in isolation (Section 2.4.1), relatively few look at the field-scale internal structure of faults cutting coal bearing successions. Coal seams are thin, typically ranging from < 1 m up to 5 m (See Table 2.2), and hence all but the smallest faults will cut multiple lithologies. In this section, I discuss faults that cut the full stratigraphic sequence that have been investigated in the field. Industry commonly models the behaviour of faults as a planar feature with a set of unique properties; however, faults in coal measures often display complex 3D structures (Figure 2.6).

Location	Coal field	Coal Thickness (m)			Lithologies (%)					
		Min	Max	Average	Coal	Sst	Siltstone	mudstone	Limestone	Seat earth
Whitley Bay, Northumberland ¹	Great Northern Coalfield (UK)	0.23	1.38	0.94	8.9	32.1	28.3	29.6	-	1.1
Henan Province ²	Pingdingshan Coalfield (China)	1.2	5.8	2.17	4.5	39.3	31.6	21.1	3.5	-
Paradise coal, Kentucky [No. WKUG11] ³	Western Kentucky Coalfield (USA)	0.81	1.80	1.30	8.4	9.5	38.5	35.2	8.3	-
Paradise coal, Kentucky (USA) [No. WKUG10] ³	Western Kentucky Coalfield (USA)	0.89	2.03	1.35	7.7	25.0	32.3	29	6.0	-
Mainshill Wood Succession ⁴	Muirkirk & Douglas Coalfield (UK)	0.29	4.65	1.23	4.9	43.7	-	41.7	3.3	6.4
Spireslack SCM ⁵	Muirkirk & Douglas Coalfield (UK)	0.47	1.74	0.93	5.4	43.6	-	38.7	-	12.4

Table 2.2: Lithologies and coal thickness at several coal fields. References: 1) Personal data, see Chapter 4; 2) (Li, 2001); 3) (Greb et al., 1992); 4) (Ellen et al., 2016); 5) (Ellen et al., 2019).

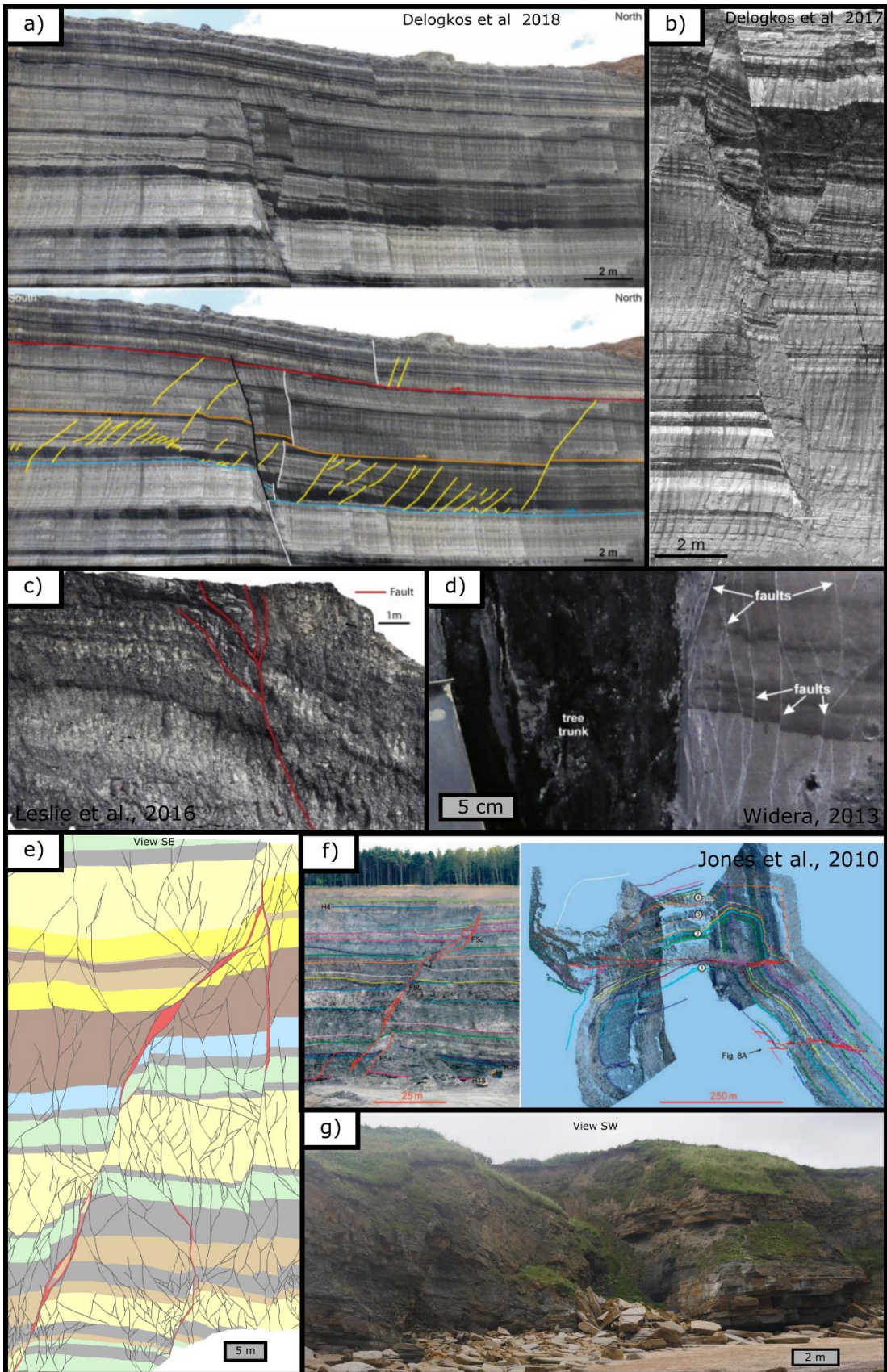


Figure 2.6: (Previous page) Field photographs of faults cutting coal measures: a) & b) normal faults cutting interbedded limestones and marls (Delogkos, Manzocchi, et al., 2017; Delogkos et al., 2018); c) photomontage of a fault of a fault strand at Greenburn SCM, Ayrshire, Scotland (Leslie, Browne, et al., 2016); d) tree trunk and associated faulting in Konin Lignite Mine, Poland (Widera, 2013); e) LiDAR data from Delhi open cast coal mine, Northumberland, UK (Jones et al., 2010).

At an outcrop scale, faults cutting coal measures rarely occur as a single fault strand, but instead as multiple anastomosing strands (Figure 2.6) (Donnelly, 2006; Færseth et al., 2007; Ellen et al., 2016; Leslie, Browne, et al., 2016; Gabrielsen et al., 2016)). For example, Færseth et al. (2007) recorded 15 slip planes on the 17 m cumulative throw Hartley Steps Fault Zone, Northumberland (UK), with each fault strand ranging from below a cm up to 6 m throw. In many faults cutting coal measures throw is primarily accommodated on a major fault strand, with subsidiary deformation occurring along several subsidiary strands and through the rotation of bedding between faults (Jones and Dearman, 1967; Færseth et al., 2007; Delogkos, Manzocchi, et al., 2017). The formation of multiple stands is promoted where faults branch at mechanical boundaries (Soliva et al., 2006; Leslie, Browne, et al., 2016) which are common within the cyclical stratigraphy (Figure 2.6c). Individual fault strands may either display a planar appearance (Ulusay and Yoleri, 1993; Delogkos et al., 2017), such as those observed in Figure 2.6a), or curve (e.g. Figure 2.6c, e, f) due to variations in fault dip or listric nature of the fault (Walsh and Watterson, 1988; Walsh and Watterson, 1989). In addition to the vertical restriction observed on mine plans (Nicol et al., 1996), decimetre scale mechanical boundaries imparted by the cyclical stratigraphy lead to a hierarchical pattern of vertical restriction observed at an outcrop scale (Figure 2.6a, b).

Grouping individual fault strands into a single fault zone is often challenging (Delogkos, Manzocchi, et al., 2017), and it is only when faults interact via soft and/or hard linkage where this is possible (Walsh & Watterson, 1991; Walsh, 2003). Fault zone are characterised by asymmetric damage zones with increased damage often observed in the hanging wall (Weber et al., 1978; Kim et al., 2004). Damage zones commonly contain: subsidiary fault strands; folding; mineralisation; and the development of bed-parallel slip (Faulkner et al., 2010). The width, behaviour, and distribution of these features is dependent on the lithologies cut by the fault, and in particular whether the material behaves brittlely or ductilely (Weber et al., 1978; Donnelly, 2006). In the vast majority of basins it was observed that faulting occurred following the coalification of peat (Shepherd et al., 1981; Walsh and Watterson, 1988), with coal behaving in a brittle manner (Walsh and

Watterson, 1988). This leads to sedimentary units which contain a high proportion of coal and sandstone behaving in a brittle manner and deforming along discrete slip planes (Weber et al., 1978), and those which contain a high proportion of shale behaving ductily with folding commonly observed (Weber et al., 1978; Walsh and Watterson, 1988; Huggins et al., 1995; Delogkos, Manzocchi, et al., 2017). Small-scale heterogeneities may also effect deformation style, for example, Widera (2013) noted that the presence of a fossilised tree trunk acted to localise sub-cm scale faulting (Figure 2.6d).

Research into the normal faults which cut interbedded Lignites and marls exposed at the Kardias Mine in the Ptolemais Basin (Greece) show that weak lithologies, particularly shales, can act as décollements and promote bed-parallel slip (Delogkos, Manzocchi, et al., 2017; Delogkos, Childs, et al., 2017; Delogkos et al., 2018). Repeated episodes of normal faulting and bed-parallel slip can lead to sections of stratigraphy either being removed or repeated within the fault zone (Delogkos, Childs, et al., 2017; Delogkos et al., 2018). Where two large offset bed-parallel slip horizons are present, subsidiary deformation may occur (e.g. Bookshelf fault patterns; Figure 2.6a) which resembles fault patterns observed in vertically segmented faults (e.g. Peacock and Zhang (1994); Childs et al. (1996)). Bed parallel slip is also commonly observed throughout many UK coal fields, with flexural slip nucleating along shales in the sequence (Donnelly, 2006), and leading to the development of 'clay mylonites' (Stimpson and Walton, 1970).

The fault core in coal measures typically contains a mix of fault rocks controlled by the lithology cut by the fault and include: fault-core lenses; fault breccia; shale smear; and fault gouge. Fault-core lenses often develop, which comprise of relatively undeformed sandstone, siltstone, and/or coal surrounded by high strain zones (Færseth et al., 2007; Gabrielsen et al., 2016) due to the variable dip of fault strands in different lithologies (Carvell et al., 2014). While brittle lithologies typically form fault breccias (Davatzes and Aydin, 2005; Woodcock and Mort, 2008), this is only observed for thick (>10 cm) sandstone beds (Walsh and Watterson, 1988; Carvell et al., 2014), and the brecciation of coal is rarely observed (Carvell et al., 2014).

Due to the abundance of shale in coal-bearing succession (40 to 60%), shale smears are common (Lindsay et al., 1993; Lehner and Pilaar, 1997; Bense and Van Balen, 2003; Pei et al., 2015). In addition to shale smear, poorly consolidated sand and gravel may become injected along a fault plane (Houtgast et al., 2002; Bense and Van Balen, 2003). The high

clay content in fluivial-deltaic successions also enables fault gouge to develop, usually along major fault zones (Zwingmann et al., 2004; Donnelly, 2006). The width of fault gouge varies along fault planes, however, is rarely thicker than 50 cm (Weber et al., 1978; Ulusay and Yoleri, 1993; Færseth et al., 2007). Little, if any relationship is observed between fault core thickness and the throw on a given fault (Knott, 1994). For example, next to no fault rock is developed in the lignites and marls studied by (Delogkos et al., 2017). It has been both reported that clasts within fault gouge are rare (Weber et al., 1978), or that clasts derived from the wall rock are incorporated (Ulusay and Yoleri, 1993), which can often include coal (Zwingmann et al., 2004; Færseth et al., 2007).

2.4.3.4 Hydrogeological properties of coal bearing faults

Whether a fault will behave as a barrier, baffle, or conduit for fluid flow will depend on the internal structure of the fault-zone and local hydraulic head (Bense et al., 2013). Due to the geological risk posed by ground water inflow events during coal extraction there is a large body of research into flow rates along coal bearing faults (Wang and Park, 2003; Wu et al., 2004; Wu and Wang, 2006; Huang et al., 2012; Bu, 2013; Huang et al., 2014; Zhang et al., 2014; Hua, 2016). Inflow events are characterised by an influx of groundwater from the seam floor, roof, or working face either immediately as the face is being worked (Shi and Singh, 2001; Wang et al., 2013), or after a period of time following mining operations (Wu et al., 2004; Huang, 2014; Zhang et al., 2014). Inflow events have been linked to coal extraction above an over-pressured limestone aquifer, pillar collapse, mining induced fractures intersecting the aquifer, inflow along faults, or a combination of the above (Bu, 2013).

Inflow along a fault will occur once a hydraulic pathway between an over-pressured aquifer and the workings is formed. Such pathways will utilise natural fractures within the fault damage zone as well as induced fractures caused by mining operations (Xu, 2011; Bu, 2013; Huang et al., 2014; Huang, 2014; Zhang et al., 2014; S. Yin et al., 2015) (Figure 2.7a). Once an event is initiated, a complex, non-linear, evolution of groundwater flow occurs from initial seepage through a number of phases illustrated by flow-rate variation with time (Qiao et al., 2013; Huang, 2014; Qi et al., 2014) (Figure 2.7c). This illustrates that the hydrogeological properties of the fault does not remain static, and instead evolves through time as hydraulic head decreases and flow pathways open and close through the migration of fines (Qi et al., 2014).

Inflow events illustrate that in order to understand the sub-surface flow through coal bearing faults it is important to consider: a) the hydrogeological properties dip and depth of the fault zone (Zhang et al., 2014; Chen et al., 2016); b) the thickness and lithologies of the stratigraphic succession between the aquifer and working face (Zhao, 2012; Huang et al., 2014; Zhao et al., 2016a; Chen et al., 2016); c) the hydraulic pressure of the source aquifer (Sun and Xu, 2016); and d) the temporal evolution of flow pathways connecting the aquifer and working face (Bu, 2013). Pathways may vary with changes in stress caused by continued mining operations or the reactivation of faults (Shi and Singh, 2001; Islam and Shinjo, 2009; Bu, 2013). Similar factors will apply to natural environments (e.g. the migration of hydrocarbons from source to reservoir) and highlights that flow pathways can vary through time.

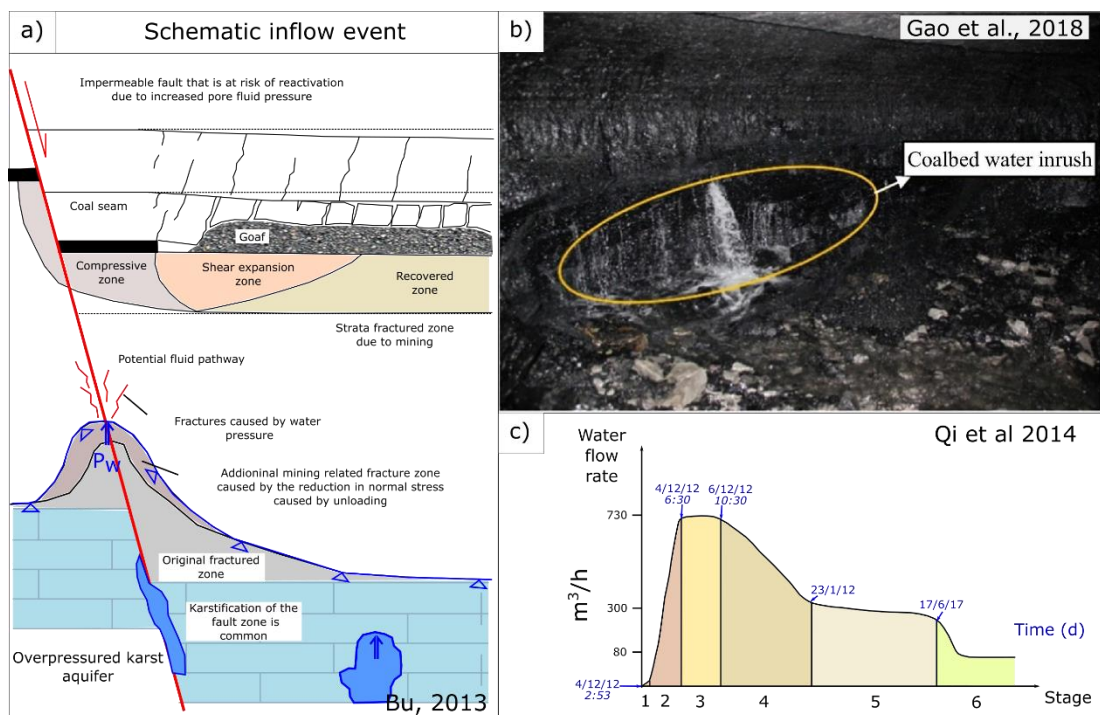


Figure 2.7: Hydrogeological properties of inflow events: a) schematic showing the factors which effect groundwater flow events in the vicinity of a geological fault (Bu, 2013); b) photograph of an inflow event (Gao et al., 2018); c) groundwater flow-rate evolution during an inflow event which occurred in Ganhe Coal Mine, Shanxi, China (Qi et al., 2014).

2.5 Discussion

2.5.1 Comparison of coal bearing successions with mechanically stratified lithologies:

The percentage and thickness of coal seams in the sequence varies between coalfields (Table 2.2). For example, in the Pingdingsham Coalfield (China), coal represents less than 5% of the succession, however, occurs in seams as thick as 5.8 m (Li, 2001). In contrast, coal represents 9% of the logged succession of Westphalian B Pennine Middle Coal Measures exposed near Whitley Bay, Northumberland (UK) and discussed in Chapter 4. In the logged section, coal occurs as thin seams, which range in thickness from 0.23 to 1.38 m. The percentage of coal for all examples in Table 2.2 is below 10%, with the rest of the succession consisting of sandstones, siltstones, mudstones, limestones, and seat earths. This demonstrates that considering the brittle deformation of coal in isolation would ignore over 90% of the stratigraphy. Seams are also thin, so the majority of faults will cut multiple lithologies.

The concept of mechanical stratigraphy (see Ferrill *et al.* (2017) for a review for normal faulting) has been primarily developed through the study of interbedded carbonate (Ferrill and Morris, 2008; Laubach *et al.*, 2009; Ferrill *et al.*, 2012; Ferrill *et al.*, 2014; Agosta *et al.*, 2015) and siliciclastic sequences (Wilkins and Gross, 2002), however it has also been shown to be important for other lithologies (e.g. ignimbrites (Soden and Shipton, 2013; Soden *et al.*, 2014)). Mechanical stratigraphy is the subdivision of a rock mass into discrete intervals defined by the mechanical properties of that interval (Corbett *et al.*, 1987; Cooke, 1997). These properties strongly affect fault zone architecture and growth (e.g. Childs *et al.* (1996); Ferrill and Morris (2008)).

Fault evolution in mechanically layered sequences is primarily controlled by:

- a) The ratio between relative thicknesses of strong and weak units, which can effect the ratio of displacement to propagation (Ferrill and Morris, 2008; Ferrill *et al.*, 2017).
- b) The strength contrast between mechanically layered units and the strength of the boundary between them (Schöpfer *et al.*, 2007; Ferrill and Morris, 2008).
- c) The confining pressure at the time of faulting with faults developed at low confining pressure (shallow burial) found to display high fault zone complexity (Schöpfer *et al.*, 2007; van Gent *et al.*, 2010).

To understand the evolution of faults within coal-measures it is key to understand the behaviour of not only coal (as discussed in sections 2.4.1 and 2.4.2) but how coal affects the deformation of the full succession. Coal is typically considered a weak lithology, so could be expected to play a similar role to shale in multi-layered sequences, however, unlike clay-rich units coal behaves in a brittle manner (Section 2.4). Similar to sand-shale sequences (e.g. Wilkins and Gross (2002)) faults in coal display complex along-strike and down-dip segmentation (sections 2.4.3.1 and 2.4.3.2). It is however, unclear what the underlying control is on this segmentation and whether coal, which typically accounts for around 5% of the succession (Table 2, Figure 2.2), has any effect.

The lithology surrounding coal in the succession can vary (Thomas, 2013), with shale and sandstone 'roofs' commonly observed (Christopher R. Fielding, 1984; Thomas, 2013). Coal may form immediately above shale (e.g. the High Main Seam, Northumberland (UK)), or a paleosol (seat earth) (e.g. the Muirkirk Coal, Ayrshire (UK)). Coal may also cut down through the succession where partings develop (Christopher R. Fielding, 1984; Fielding, 1986a), which combined with variable lithological associations will complicate the mechanical stratigraphy. Much of the work to date focuses on 'binary' successions of sandstone/shale or limestone/marl, however, fluvial-deltaic sequences can not be considered as these due to the complex sedimentary architecture (Section 2.3). The cyclical successions are known to strongly vertically restrict the growth of faults in these successions, with small offset faults only recorded in single cyclothems (Walsh and Watterson, 1988; Huggins et al., 1995). Sub-bed scale variations in lithology and sedimentary structure are common, with heterolithic units containing non-laterally extensive sandstone bodies present. This will act to further complicate fault growth, at a scale far below that observed in binary mechanically layered sequences.

As burial increases, confining pressure also increases causing faulting style and typically become simpler with depth (Scholz, 2019). Burial also leads to the dynamic change in the mechanical properties of coal as rank increases (Section 2.4). As rank increases during burial cleat intensity increases and spacing between cleats decreases causing a reduction in coal strength (See section 2.4.2). However, in basins where igneous activity occurs, rank can be further increased towards anthracite. This causes the reduction in cleat spacing and an increase in coal strength. Over half of the succession may be comprised of shale, whose deformation style is controlled by consolidation state (Nygård et al., 2006; Yuan et al., 2017).

As a general rule, shale will deform in a ductile manner during burial, and brittely during uplift (Yuan et al., 2017). Because the mechanical properties of coal and shale change during burial it is particularly important to understand the basin evolution when studying fluvial-deltaic sequences.

Fault-rock development is in part controlled by the lithologies cut by the fault (e.g. Sibson (1977); De Paola et al. (2008); Bullock et al. (2014)). Current work has suggested faults in coal measures may either contain very little fault rock (Delogkos, Manzocchi, et al., 2017; Delogkos, Childs, et al., 2017; Delogkos et al., 2018), or develop a wide range of fault-gouge, fault-breccia and fault-core lenses (Færseth et al., 2007; Gabrielsen et al., 2016). In sand-shale sequences clay-smearing is common and acts to strongly reduce the hydraulic conductivity of a fault zone (Bense and Van Balen, 2003; Takahashi, 2003; Bense and Balen, 2004). However, in coal measures although shale represents a high proportion of the succession (c. 50%, Figure 2.2 & Table 2.2), it is not evenly distributed throughout the succession (Figure 2.2). The cyclicity of the succession, which typically repeats over a 10s of meter scale, likely promotes the development of a heterogeneous fault core which changes considerably along-strike and down-dip. This cyclicity will also lead to a wide range in damage zone properties, which are likely to become well developed in sand rich packages, and less well developed where shale dominates.

Key remaining questions

- 1) *Does coal behave as a weak or strong lithology when considering the mechanical stratigraphy of coal measures?*
- 2) *What is the type and spatial distribution of fault rocks developed along faults cutting coal bearing sequences?*
- 3) *How does the complex sedimentary architecture present in fluvial-deltaic environments effect the evolution of faults in coal measures and does this differ from 'binary' mechanically layered sequences?*
- 4) *How does burial history and igneous activity effect fault growth in coal measures?*

2.5.2 Implications for coal mining

The two major hazards associated with faults in underground coal extraction are groundwater inflow events and blow-outs. Groundwater inflow occurs when a hydraulic pathway is created that links a high-pressure aquifer and the working face (Bu, 2013). This

enables groundwater to flow into a working, with rates evolving through time (Section 2.4.3.4). Inflow events often coincide with fault reactivation (Shi and Singh, 2001; Islam and Shinjo, 2009; Bu, 2013). However, faults in UK coal measures have been shown to be vertically restricted and initially grow as isolated strands (Section 2.4.3.1). It is therefore unclear what controls the location of high-risk transmissive faults within a basin.

To understand whether a fault will be transmissive to flow, it is important to understand what controls the internal structure, which is difficult to do by remote sources (e.g. seismic). Field studies (Section 2.4.3.2) suggest faults rarely occur as a single strand and instead develop multiple anastomosing strands. The high shale content suggests the development of shale smears and fault gouge should dominate incompetent lithologies (Bense and Van Balen, 2003; Takahashi, 2003). This combined with widespread fault breccia developed where sandstones are juxtaposed suggests faults in coal-measures should develop a semi-continuous low permeable fault-core. However, Delogkos et al., (2017; 2018) found little to no fault rock along faults cutting lignites and marls in the Ptolemais Basin (Greece). This highlights the need for further work to identify typical fault-rock lithologies and quantify the up-dip and along-strike heterogeneity in fault properties. This will help explain the flow pathways groundwater utilises during inflow events and whether faults could act as leakage pathways within mine geothermal target.

Blow-outs are caused where extensive tectonically deformed coal (TDC) occurs (Li, 2001; Chen, 2011). However, surprisingly little work has been done to investigate the distribution of TDCs along faults and how this varies along strike and down dip. To date research has focused on the deformation within single coal seams for compressional environments (e.g. Frodsham and Gayer (1999); Li (2001)). Delogkos et al., (2017) demonstrate bed-parallel slip is also commonly observed in extensional settings, however, the lithological control on these structures remains unclear. The classification of TDCs is partly based on normal faults in China (Cao et al., 2003; Ju and Li, 2009), and Poland (Godyń, 2016), and shows TDCs can be widespread in these environments. Although studies such as these highlight the deformation towards a fault, it does not investigate the fundamental controls which cause TDCs to be entrained into a fault zone, and how TDCs become transported within the fault core.

Key remaining questions

- 1) *What is the spatial distribution of low permeability fault rock and how can this effect connection pathways between over-pressured groundwater aquifers and the working face?*
- 2) *What is, and what controls, the spatial distribution of tectonically deformed coals in extensional and strike slip environments?*

2.5.3 Implications for shallow mine geothermal

Subsurface extraction of coal in the UK has drastically declined in recent years, with the last subsurface mine in Scotland closing in 2002 (Leslie, Browne, et al., 2016). This has left an extensive number of abandoned pillar and stall workings (up to 70,000; Deb and Choi, 2006), which flood as groundwater returns to pre-mining levels (Younger, 1995; Loredó et al., 2016). These flooded mine workings may provide an aquifer for low-temperature mine geothermal projects (Malolepszy et al., 2005; Watzlaf and Ackman, 2006; Monaghan et al., 2017). To de-risk these projects it is important to characterise the fluid-flow properties of the target mine, which may include the combined network of mine workings, geological structure (fault and fractures), and the permeable lithologies in the succession.

For a target mine to be successful, groundwater flow along stalls is required, often conceptualised as within open voids between the pillars of coal that were left to support the roof (Bruyn and Bell, 1999). However, following mining operations workings may collapse leading to wide-spread subsidence, fault reactivation and ground deformation (Donnelly, 2006; Bell and Donnelly, 2006; Donnelly et al., 2008; B. A. Poulsen and Shen, 2013). The collapse of the roof causes stalls to become clogged and deformation to propagate upwards accommodated along several fault strands (Carter et al., 1981; Garrard and Taylor, 1988). The study of natural faults in coal measures and how the stratigraphic succession effects fault development will help further our understanding of how coal mine collapse. For geothermal targets it is also important to understand whether the overlying fault and fracture network could cause unpredictable fluid flow pathways and loss of heat.

During shallow mine geothermal operations, groundwater will flow in stalls which have not collapsed, and around pillars. Mining operations will have unloaded these pillars, which decreases their mechanical strength and increase the permeability of the coal (S. Yin et al., 2015; Zhao et al., 2016b). Following groundwater recharge pillars will become re-saturated,

further reducing uniaxial compressive strength (Colback and Wiid, 1965; Zhao et al., 2016b). The presence of faulting may lead to the rotation of cleats (Rippon et al., 2006; Paul and Chatterjee, 2011) promoting shear failure (Y.W. Li et al., 2016), and cause pillars to fail. While pillar width in the proximity to geological structures (i.e. faults) was often increased to accommodate the decreased mechanical strength (Bruyn and Bell, 1999), the likelihood of pillar failure and roof collapse remains increased. Where pillar failure occurs in the proximity to a fault, reactivation of the fault can occur (Donnelly, 2006; Donnelly et al., 2008). The reactivation of the fault will also promote further collapse and lead to the reduction of open space where groundwater can flow.

Where faults have little to no across fault permeability, fault reactivation may be stimulated by a change in fluid pressure on the fault (Handin et al., 1963; Byerlee, 1978). Fault reactivation can lead to considerable surface deformation and damage to infrastructure (Bell and Donnelly, 2006; Donnelly, 2006; Donnelly et al., 2009). An example of this occurred in the Houghton-le-Spring area (near Sunderland, UK) where changes in groundwater level due to pumping led to the reactivation of the Houghton Cut Fault (Young and Lawrence, 2001). This led to widespread surface deformation and the partial closure of a major road (A690) which connects Sunderland and Durham. Whether a fault will act as a potential leakage pathway and whether the stimulation of groundwater during production could cause fault reactivation are key risks associated with shallow mine geothermal.

Key remaining questions:

- 1) *How will the faults in target workings react to the perturbation of groundwater caused by geothermal operations?*
- 2) *Can geological fault and fracture networks combine to cause unexpected flow pathways for groundwater and heat?*
- 3) *How do shallow 'anthropogenic' faults that form in the response to the collapse of mine workings differ from geological faults that formed at deeper levels?*

2.6 Concluding remarks

This review has highlighted clear gaps in our understanding of how the presence of a naturally fractured lithology (coal) and the complex stratigraphic relationships observed within fluvial-deltaic sequences affect the faulting behaviour of the whole succession. The field classification of faults cutting coal measures, in particular the internal structure and how it evolves with increasing displacement, remains a key research gap. Because fluvial-deltaic sequences contain a several, decimetre thick, beds with variable mechanical

properties (including heterolithic beds), it is unlikely that these successions can be considered as in the same way as 'binary' mechanically layered sequences. These findings have important implications for the sub-surface extraction of coal and shallow mine geothermal projects. A number of research suggestions are provided, and in the rest of the thesis I will utilise the field classification of faults to understand the role of mechanical stratigraphy in the growth of faults in fluvial-deltaic sequences.

Chapter 3: How do we see fractures? Subjective Bias in fracture data collection.

Billy J. Andrews¹, Jennifer J. Robers¹, Zoe K. Shipton¹, Sabina Bigi², M. Chiara Tartarello², and Gareth Johnson^{1,3}

1) Department of Civil and Environmental Engineering, University of Strathclyde, Glasgow, G11XJ, Scotland

2) Department of Earth Science, Sapienza University of Rome, P.le Aldo Moro, 5, 00185 Rome, Italy

3) School of GeoSciences, University of Edinburgh, Edinburgh, EH93FE, Scotland

3.1 Declaration of work:

Chapter 3 has been published in the Special Issue “Understanding the Unknowns: the impact of uncertainty in the geo-sciences” of *Solid Earth* with the supplementary information available at <https://doi.org/10.5194/se-10-487-2019-supplement>. Initial discussions and planning of the paper were undertaken by all authors, with BJA and JRR designing the workshops. The paper was prepared by BJA and JRR, with contributions from all authors.

Full citation: Andrews, B.J., Roberts, J.J., Shipton, Z.K., Bigi, S., Tartarello, M.C. and Johnson, G., 2019. How do we see fractures? Quantifying subjective bias in fracture data collection. Solid Earth, 10(2), pp.487-516.

3.2 Abstract.

The characterisation of natural fracture networks using outcrop analogues is important in understanding subsurface fluid flow and rock mass characteristics in fractured lithologies. It is well known from decision sciences that subjective bias can significantly impact the way data are gathered and interpreted, introducing scientific uncertainty. This study investigates the scale and nature of subjective bias on fracture data collected using four commonly applied approaches (linear scanlines, circular scanlines, topology sampling, and window sampling) both in the field and in workshops using field photographs. We demonstrate that geologists’ own subjective biases influence the data they collect, and, as a result, different participants collect different fracture data from the same scanline or

sample area. As a result, the fracture statistics that are derived from field data can vary considerably for the same scanline, depending on which geologist collected the data. Additionally, the personal bias of geologists collecting the data affects the scanline size (minimum length of linear scanlines, radius of circular scanlines, or area of a window sample) needed to collect a statistically representative amount of data. Fracture statistics derived from field data are often input into geological models that are used for a range of applications, from understanding fluid flow to characterising rock strength. We suggest protocols to recognise, understand, and limit the effect of subjective bias on fracture data biases during data collection. Our work shows the capacity for cognitive biases to introduce uncertainty into observation-based data and has implications well beyond the geosciences.

3.3 Introduction

Natural fracture networks exert a strong control on the hydrogeological and mechanical properties of a rock mass, and are useful indicators of palaeo-stress directions. Geological models that depict the spatial distribution and nature of a fracture network rely on input data (either distributions or mean values) of fracture statistics to provide a geologically reasonable model of the subsurface. Models such as discrete fracture networks (DFNs) may be used for estimating up-scaled permeability (e.g. (Min et al., 2004; Bigi et al., 2013)) or for rock mechanics analysis (Jing and Hudson, 2002; Harthong et al., 2012), with applications, including understanding fluid flow in tight oil and gas reservoirs (Aydin, 2000) and hydrogeology (Comerford et al., 2018), and assessing rock strength for mine engineering (Mas Ivars et al., 2011). Four methods for characterizing natural fractures in outcrops: linear scanlines (Priest and Hudson, 1981; Priest, 1993); circular scanlines (Mauldon et al., 2001; Rohrbaugh et al., 2002)(Mauldon et al., 2001; Rohrbaugh et al., 2002)(Mauldon et al., 2001; Rohrbaugh et al., 2002); topology sampling (characterising node types; Manzocchi, 2002; Sanderson and Nixon, 2015, 2018); and tracing out the fracture network (window sampling;(Wu and D. Pollard, 1995)). These methods handle orientation, censoring or truncation biases (Mauldon et al., 2001; Zeeb et al., 2013), and heterogeneity in the fracture network (Watkins et al., 2015) with different degrees of success. Here, we explore how each of these methods are susceptible to subjective uncertainties related to observer biases. Furthermore, we characterise how much the degree of variability introduced by subjective uncertainties is dependent on the method of data collection.

Uncertainties in geological data can be broadly split into objective and subjective uncertainty (Tannert et al., 2007). Objective uncertainty (also called external, aleatory inherent, structural, random, or stochastic uncertainty) refers to more traditional concepts of uncertainty, such as precision or processing error in a technique or a dataset, and can be represented through error bounds. Subjective uncertainty (also called epistemic, knowledge, functional, or internal uncertainty) arises from the mind, that is, stems from biases that affect how individuals perceive, gather and interpret geological data (Bond et al., 2015). Subjective uncertainty is common in geosciences where developing geological models typically relies on extrapolation of sparse data (Wood and Curtis, 2004), but its magnitude and impact is difficult to quantify (Bond et al., 2015).

The collection of fracture attributes will be affected by subjective biases. Depending on the aims of a study (e.g., determining the connectivity and permeability of the fracture network; determining strength of a fractured rock mass; understanding paleo-stress conditions), these attributes could include the number of fracture sets; orientations, trace lengths, degree of clustering, and aperture of the fracture population in a set; and the topology and intensity of the network (Jolly and Cosgrove, 2003; Watkins et al., 2015; Lei et al., 2017). The presence and amplitude of these biases may also be affected by the study medium. For example, previous work has investigated the operator, used here to describe the person undertaking the interpretation, variability extracting lineament or landform data from remote sensing (e.g. LANDSAT imagery or aerial photographs) (Burns et al., 1976; Burns and Brown, 1978; Huntington and Raiche, 1978); DEMs (Hillier et al., 2015) and LiDAR datasets (Scheiber et al., 2015). Differences in operator interpretations can occur due to: (a) technical factors in data acquisition, for example, band width for Landsat data, image quality for aerial photographs or illumination direction for LiDAR; (b) the scale of observation, for example, 1: 20,000 compared to 1: 5,000; and (c) inter-operator differences (i.e. human factors). Scheiber et al. (2015) found inter-operator replicability to be poor for bedrock lineaments interpreted from airborne LiDAR by six operators'. Significant variability was observed in the number, trace-length and orientation of the reported lineaments. Burns et al. (1976) attributes a difference of 8% in interpretations to 'human factors' for lineaments identified using aerial photography. While differences in inter-operator interpretation has been previously identified, the underlying human factors causing these differences remain unclear. It is also unclear how such factors affect the collection of fracture data either in the field or from field photographs.

In this study, we investigate the magnitude and source of subjective uncertainty in fracture data collected by linear scanlines, circular scanlines, fracture topology and window sampling. Fracture data were collected from Carboniferous rocks cropping out near Whitley Bay, Northumberland (UK) in two phases: (1) in the field where 7 participants collected fracture data directly from outcrop; and (2) two classroom workshops during which 29 participants with different levels of geological training and expertise collected fracture data from field photographs. In both the field and classroom, the participants collected fracture data individually and in small groups. We compare the values collected by individual participants for the same sample (scanline, circle, window sample etc). It is the values as reported by the participants rather than the underlying statistics of the measured fracture networks that is the focus of this work. We quantify and compare the scale of subjective uncertainty for each method, and identify “problem areas” or factors that amplify the subjective uncertainty. We consider the effect of the variations due to subjective uncertainty on fracture statistics derived from the data, and propose a number of protocols to limit operator bias in collaborative work.

3.3 Fracture data collection and analysis

Linear scanlines are a quick and relatively simple way of systematically collecting fracture data (Ortega et al., 2006; Chesnaux et al., 2009; Agosta et al., 2010; Tóth, 2010; Guerriero et al., 2011; Bigi et al., 2015). This method was developed in rock engineering for a quantitative description of discontinuities in rock masses (Priest, 1993), and then adopted to describe natural fracture networks (Becker and Gross, 1996; Van Dijk et al., 2000; Newman, 2005; Peacock and Sanderson, 2018). The method involves laying out a tape measure on the outcrop and measuring both the number (N) and the attributes of fractures which intersect the scanline (e.g. orientation, spacing, length above and below the scanline, aperture, type of terminations, filling or mineralization) (Priest and Hudson, 1981; Priest, 1993). To fully sample a fracture network, multiple linear scanlines should be completed with different orientations, and the Terzaghi correction should be applied to reduce orientation bias (Terzaghi, 1965; Mauldon and Mauldon, 1997). The goal is to collect enough data to obtain a statistical distribution for each of the main fracture parameters rather than a mean value. It has been recommended that over 225 fractures should be sampled by the population of linear scanlines for the method to estimate accurately the characteristic of a fracture network (Zeeb et al., 2013).

Circular scanlines provide estimates of fracture attributes based on the number of fractures intersecting a circular scanline, n , and the number of fracture trace endpoints, m , within a circular window (Mauldon et al., 2001; Rohrbaugh et al., 2002). The fracture density, intensity, and an estimate of mean trace length for the scanline can be calculated from the n and m values (Mauldon et al., 2001). To be statistically valid, the number of fracture end points (m) should exceed 30 (Rohrbaugh et al., 2002), however, values between 20 and 30 can also be considered reliable (Procter and Sanderson, 2017). This rule defines the radius of the scanline as a function of fracture density and limits the use of the technique in areas of poor exposure and low-density fracture networks. A circular scanline is a maximum likelihood estimator (Lyman, 2003) and does not suffer from the same orientation biases observed in linear scanlines (Mauldon et al., 2001). Circular scanlines are ideal for rock masses with evenly distributed fracture attributes, but may need to be combined with other methods to give a true representation of the heterogeneity of the fracture network (Watkins et al., 2015).

Fracture topology describes a fault or fracture network as a series of branches and nodes (Manzocchi, 2002; Sanderson et al., 2018; Procter and Sanderson, 2017; Sanderson and Nixon, 2015; Laubach et al., 2018). A branch is a fracture trace with a node at each end that can be classified as terminating into rock at i -nodes (unconnected terminations), abutting against another fracture at a y -node, or crossing another branch at an x -node. Topology may be combined with circular scanlines by assessing the nodes present within the circular window and using the sum of i - and y - nodes as the number of trace end points (m -value) in the circle (Procter and Sanderson, 2017). The relative frequencies of different node types (i , y and x) can be plotted on a triangular diagram for the purposes of characterizing and quantifying the connectivity of a fracture network (Manzocchi, 2002; Sanderson and Nixon, 2015).

Finally, window sampling is a technique where all fractures within a given sample area (window) are traced out either by hand, or on a computer, and the resulting traces used to calculate the fracture statistics (Pahl, 1981; Priest, 1993; Wu and D. Pollard, 1995). This technique is often utilised to analyse remote-sampling data such as aerial photographs (Healy et al., 2017), Unmanned Aerial Vehicle (UAV) images (Salvini et al., 2017), bathymetry (Nixon et al., 2012), or satellite imagery (Koike et al., 1998), as well as in outcrop studies (Belayneh et al., 2009). It has been suggested that a minimum of 110 fractures need to be

sampled to statistically describe the fracture network using window sampling (Zeeb et al., 2013).

Using these four methods, fracture parameters can be collected to calculate key fracture statistics, for example, trace *length* (mean and distributions), fracture abundance (*Intensity* and *Density*), and connectivity (Summarised in Table 3.1).

Fracture statistic	Notation	Definition (unit)	Input parameters and calculation		
			Linear	Circular scanline	Window sampling
Density (D)	Areal (P20)	Number of fractures per unit area (m^{-2})	-	$D = \frac{(N_i + N_y)}{2\pi r^2}$	$D = \frac{N}{A}$
Intensity (I)	Linear (P10)	Number of fractures per unit length (m^{-1})	$I = \frac{n}{L} = \frac{1}{S}$	$I = \frac{n}{4r}$	-
	Areal (P21)	Fracture length per unit area ($m \times m^{-2}$)	-	-	$I = \frac{\sum tl}{A}$
Spacing (S)	Linear	Spacing between fractures (m)	$S = \frac{\sum s}{(N - 1)} = \frac{1}{I}$	-	-
Mean trace length (TI)	TI	Mean fracture length (m)	$TI = \frac{\sum l}{N}$	$TI = \frac{n}{(N_i + N_y)} \times \frac{\pi r}{2}$	$TI = \frac{\sum l}{N}$
Network topology	Topological sampling	Defining fracture nodes as I, y and x.	-	Yes	Yes
Connectivity	Using node topology (Pc)	Percentage of connected branches	-	$Pc = \frac{3N_y + 4N_x}{N_i + N_y + N_x}$	$Pc = \frac{3N_y + 4N_x}{N_i + N_y + N_x}$
	Using trace end classification (Pf)	Percentage of connected fractures	$Pf = \frac{F}{R + F} \times 100$	-	-
Trace length distribution	TI distribution (tl)	Distribution of individual fracture trace lengths	Yes	-	Yes

Table 3.1: Summary and definition of fracture statistics that can be derived from methods used in this work. Table adapted from Zeeb et al. (2013). N_i = number of i-nodes, N_y = number of y-nodes, N_x = number of x-nodes, r = radius of circular scanline, N = number of fractures, A = Area, n = number of fracture intersections with the scanline (either linear or circular), L = length of scanline, s = spacing between adjacent fracture traces on the scanline, tl = individual fracture trace length, F = fracture abuts against another fracture, R = fracture terminates into rock (n.b. some authors also distinguish stratabound fracture terminations), ‘Yes’ for trace length distribution & network topology indicates you can use that method to carry out the technique.

Trace length, and trace length distribution are key fracture parameters for DFN simulations (e.g., in simulating fracture-hosted fluid flow. Trace lengths may be measured directly with the linear scanlines and window sampling, or estimated using the circular scanline method). Challenges to determining the trace lengths of individual fractures include: the scale of observation used to collect the data (Zeeb et al., 2013); classification of fracture intersections (Ortega and Marrett, 2000); and the fracture fill properties (Olson et al., 2009). Mean trace length is a commonly used fracture statistic and is useful where the fractures in a network are evenly distributed (Mauldon et al., 2001). However fracture modelling typically uses a statistical distribution representative of the fracture length population rather than the mean (Neuman, 1993). Trace length distribution, obtained from measuring individual fractures, should be used when investigating sub-surface fluid flow or characterising spatial variations in fracture trace length (Watkins et al., 2015). We investigate the impact of subjective bias on mean trace length for all four methods, including the range of reported trace lengths for linear scanlines and window sampling and trace length distribution for window sampling.

The characterisation of fracture networks and comparison of techniques is greatly confounded by inconsistencies in terminology. Because fractures may be sampled using techniques which are either 1-dimensional (scanlines, boreholes), 2-dimensional (maps, surface exposure), or 3-dimensional (rock volumes), numerous different methodologies and terminology have arisen to characterise the abundance of fractures in a network. One of the most widely used methods to characterise a network is to define the number of fractures (N) normalised to line length (L), sample area (A) or sample volume (V) depending on the dimension of sampling. In the literature, this statistic is either termed *fracture intensity* (I) or *fracture frequency* (f) (Sanderson and Nixon, 2015). For linear scanlines, *fracture spacing* can be regarded as the inverse of *fracture intensity* for a single set of sub-parallel fractures (Sanderson and Nixon, 2015). Fracture abundance within a network may also be expressed as the total trace length per unit area (Dershowitz and Einstein, 1988; Rohrbaugh et al., 2002). This statistic is either termed *fracture intensity* (Sanderson and Nixon, 2015) or *fracture density* (Nixon et al., 2012; Zeeb et al., 2013). One attempt to simplify the use of terms is to use the P_{xy} terminology as defined by (Dershowitz and Einstein, 1988) where x denotes the dimension of the sampling region (1 = line, 2 = area, 3 = volume) and y denotes the dimension of the feature (0 = number, 1 = length, 2 = area, 3 = volume). For the purposes of our study, we use the term *fracture intensity* (I) to refer to

number of fractures per line length (P10, for linear scanlines) or fracture length per unit area (P21, for circular scanlines), and we use *fracture density* for number of fractures per unit area (P20) (Table 3.1).

It is also important to understand how individual fractures relate to each other; particularly how the individual fractures connect, and hence contribute to the strength or fluid flow through the rock mass. The number of connections on a fracture trace (C_L) is a commonly used measure of connectivity (e.g. Manzocchi, 2002). However, a fracture network consisting of only y and x nodes could have different C_L values depending on the fracture intensity (Sanderson and Nixon, 2015). It has been suggested that it is better to either consider the average number of connections per branch (C_B) (Ortega and Marrett, 2000) or the proportion of connected nodes (P_c) (Sanderson and Nixon, 2015). In our study, we use the proportion of connected nodes for circular scanline and window sampling. To measure connectivity in linear scanlines, the percentage of connected fracture trace ends is reported (Table 3.1).

3.4. Study methods

3.4.1 Study area

The field site is located in the Northumberland Basin, just north of Whitley Bay, NE England (Figure 3.1). The Northumberland Basin is a 50 km wide, ENE-WSW trending half-graben formed during mid-late Carboniferous extensional reactivation of the underlying Iapetus Suture (Johnson, 1984; Chadwick et al., 1995). The stratigraphy consists of thinly (cm - dm) bedded sandstones, siltstones, shales, seat earth, and coals of the Middle Coal Measures (Westphalian B). At the field site the easily accessible and well exposed wave-cut platform clearly exhibits two sets of faults and sub-vertical joints ($>75^\circ$) which trend E-W to NE-SW and N-S respectively.

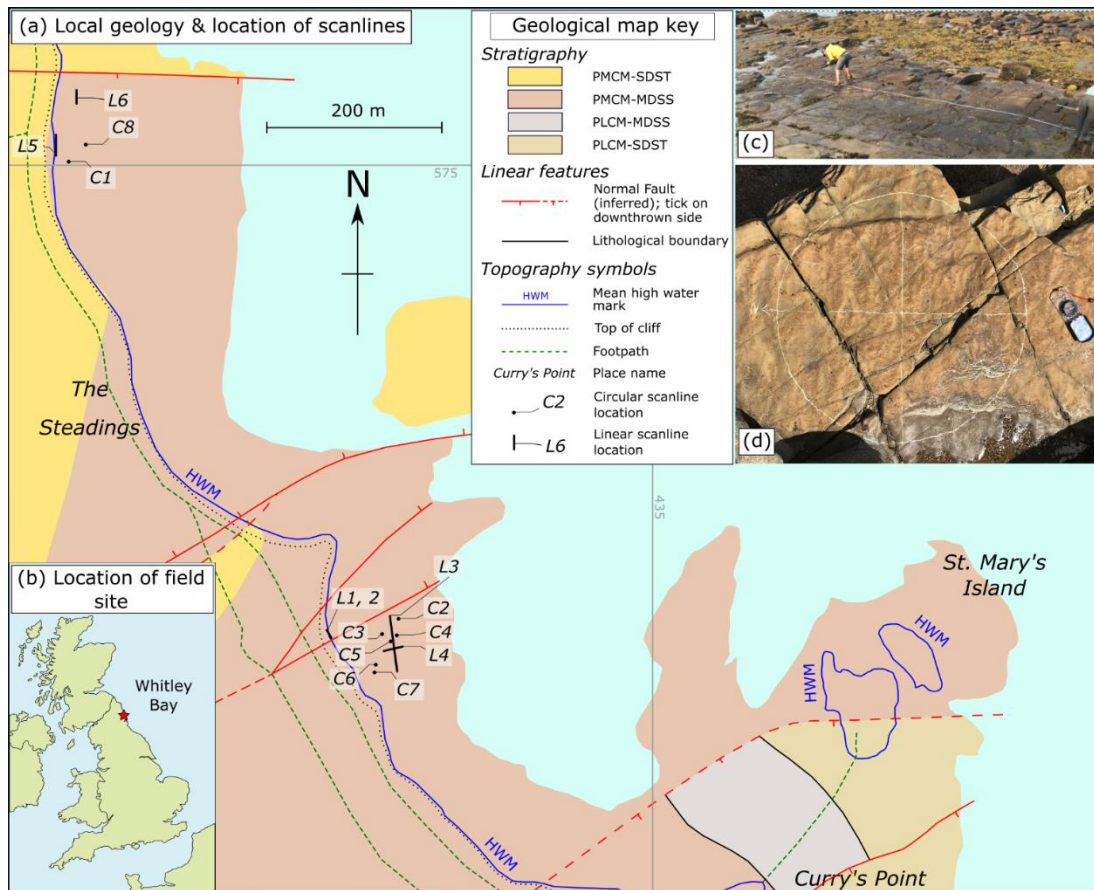


Figure 3.1: Location map highlighting (a) the local geology and (b) the location of the study area, located near Whitley Bay, Northumberland (UK). Grid lines are annotated with UK national grid numbers. Field photographs of both linear (c) and circular (d) scanline methods are also shown (L3 [NZ34717545] and C8 [NZ34377609] respectively). The geological map is modified from Geological Map Data BGS © UKRI (2018), where stratigraphy is as follows: PLCM-SDST = Pennine Lower Coal Measures – Sandstone; PLCM-MDSS = Pennine Lower Coal Measures – Mudstone, siltstone and Sandstone; Pennine Middle Coal Measures – Sandstone; PLCM-MDSS = Pennine Middle Coal Measures – Mudstone, siltstone and Sandstone.

3.4.2 Fracture data collection procedure

Six linear scanlines were set up by laying out a tape measure on sandstone beds, both in map and cliff section (Figure 3.1c). Participants were asked to identify for each fracture: a) the intersection distance along the tape and b) the length and termination (into rock, abutting against another fracture or not seen/obscured) of the fracture either side of the tape. Eight circular scanlines were drawn with chalk directly onto the sub-horizontal bedding planes of three separate, decimetre thick, medium grained sandstone beds (Figure 3.1d). The location and radius for all circular scanlines, apart from C6, were selected by the lead author (Participant G/11) in order to represent what they believed to include a

statistically significant number of fracture terminations (i.e. $m < 30$; Table 3.2). C6 was selected by Participant F.

Method	Field		Workshop			Length or radius/m	
	Completed?	i g	Completed?	i g	Order		
Circular	C1	✓	✓	✓ (WS1&2)	✓	3	1.0
	C2	✓	✓	✗			1.0
	C3	✓	✓	✓ (WS1&2)	✓	5	1.0
	C4	✓	✓	✓ (WS1&2)	✓	4	1.0
	C5	✓	✓	✓ (WS1&2)	✓	2	1.0
	C6	✓	✓	✗			0.73
	C7	✓	✓	✗			1.21
	C8	✗		✓ (WS1&2)	✓	1	0.5
Linear	L1	✓	✓	✗			1.0
	L2	✓	✓	✗			1.0
	L3	✓	✓	✗			15.0
	L4	✓	✓	✗			7.5
	L5	✗		✓ (WS1&2)	✓		6.55
	L6	✗		✓ (WS1&2)	✓		1.45
Window sampling	C1			✓ P1,3,11 & WS2	✓	3	0.5
	C3			WS2	✓	5	1.0
	C4			WS2	✓	4	1.0
	C5			✓ P1,3,11 & WS2	✓	2	0.5
	C8			✓ P1,3,11 & WS2	✓	1	0.5

Table 3.2: Summary of circular (C) and linear (L) scanlines completed in the field and workshops (WS1 & WS2). Whether these were completed individually (i) or in groups (g) is noted. 'Order' refers to the order the scanlines were completed in the workshops. Four of the circular scanlines (C2,3,4,5) were completed both in the field and in the workshop, but none of the linear scanlines were completed in both, due to workshop time constraints. Window sampling, whereby participants drew out the interpreted fractures as well as completing topological sampling, was only completed by Participants 1, 3, 11 and all of Workshop 2 (WS2). The workbooks used in this study are supplied in the supplementary information (S3 & S4).

A N-arrow and NS/EW lines were drawn onto the circle to aid observation. Participants counted the number of intersections with the circumference (n). Following the methodology of Procter and Sanderson (2017), participants were asked to identify the number of i-, y- and x- nodes within the circles. Finally, window sampling was conducted by tracing out the fracture networks on photographs of the circular scanlines in the

workshops. Our study did not aim to collect sufficient fractures to represent the fracture network at the field site, and the tested scanlines were not designed to be statistically representative.

Fieldwork was undertaken by 7 participants (labelled A-G) in July 2018 with fracture data collected using field notebooks from 7 circular and 4 linear scanlines (Table 3.2). There was no particular guidance as to how the participants collected the scanline data, but no more than one person or one group collected fracture data from a scanline at any one time, so as to avoid influencing the data collected by other participants. For the same reason, participants did not annotate or disturb the rock or scanline. Orientation and aperture data were also measured in the field, but they are not included in this study because they generally are not included in circular scanline methods and cannot be measured from field photographs in the workshops. Three of the fieldwork participants also completed the workshop tasks (Participant C = Participant 8; Participant D = Participant 10; Participant G = Participant 11).

Workshop 1 (WS1) was held in September 2018 in Glasgow, with 11 participants (labelled P1-11). Workshop 2 (WS2) was held in October 2018 in Rome with 18 participants (P12-29). Participants were recruited from the authors' research groups (the Faults and Fluid Flow research group within the Centre for Ground Engineering & Energy Geosciences at the University of Strathclyde and the Tectonics and Fluid Chemistry Lab of Earth Science Dept. at Sapienza) as well as colleagues from their departments: participation was voluntary and all data were anonymised for analysis. Each 2-part workshop lasted 3 hours. In the first part, participants worked individually to complete 3 circular and 1 linear scanline, and in the second part, worked in small groups to complete 2 circular and 1 linear scanline (Table 3.2). Participants were provided with A3 (29.7 x 42.0cm) colour photographs of the scanlines. WS1 participants were encouraged to annotate these with the observed fracture intersections and interpreted termination type, whereas WS2 participants were specifically asked to trace out the interpreted fracture network (i.e. to undertake window sampling). Both workshops enabled us to investigate the impact of subjective bias, however, the fracture maps from WS2 enabled us to examine the impact on window sampling along with investigating the root cause of differences for participant classification of nodes.

Group	#	Geological training					Familiarity with geological fieldwork					Familiarity with collecting fracture data				
		None	Low	Mediu	High	(Other)	None	Low	Medium	High	(Other)	None	Low	Medium	High	(Other)
Field	7	1	0	3	3	0	1	0	3	3	0	1	0	3	3	0
WS1	11	2	2	3	2	2	2	1	5	1	2	3	2	5	1	0
WS2	18	3	0	6	9	0	3	6	3	6	0	6	5	5	2	0

Table 3.3: Summary of the level of geological training, and experience in geological fieldwork and fracture data collection, reported by field and workshop (WS) participants. Individual participant responses are provided in the Supplementary Information (S2).

To examine the effect of geological experience on subjective uncertainty, participants were asked to indicate their level of geological training, familiarity with geological fieldwork, and their level of experience collecting fracture data (summarised in Table 3.3, questionnaire provided in Supplementary Information, S1). In the workshops, a small number of participants (Participants 2, 5, 24 and 28) consistently reported anomalously high n-values compared to the node counts. Three of these participants (Participants 2, 5 and 28) had no formal geological training or experience in geological fieldwork and fracture data collection. It is possible that these participants only considered fractures that intersected the edge of the circle in their interpretation, neglecting fractures within the circle that do not intersect the circumference, and introducing a different source of subjective error.

3.4.3 Post-workshop analysis

For the workshop data, we digitised the interpreted fracture traces and node classification for all participants who traced the networks (see Table 3.2) using ArcGIS. Individual fracture trace lengths for all scanlines, and the distance along the scanline that each fracture intersected linear scanlines were exported as 'Arcmap unit' lengths. These lengths were then scaled to the field to enable comparison of the fracture statistics. In some cases, the counts of n or node types reported by participants differed from the count indicated on the worksheet (see S7). In these cases, to be consistent with field-data collection, we take the value reported by the participant. Digitised networks from Circle 8 were used as a case example to (a) construct heat maps of point density for n, i, y-, x- nodes, and line density for

fracture traces, and (b) identify areas within the circular scanline with the greatest variability in the identification and quantification of fracture characteristics such as trace, node type, termination etc.

Fracture statistics were calculated for the data populations from the different fracture characteristics that were measured or counted, and then were then investigated as a function of the field and workshop participants. We report on the impact of subjective bias for the following fracture statistics: *fracture intensity (I)*, *fracture density (d)*, the *connectivity of the network (Pc & Pf)*, *mean trace length (TI)*, and *trace length distributions (tl)*. Statistics are calculated using the equations outlined in Table 3.1.

In theory, each of the scanlines have a 'true' value for each of the fracture parameters (number and type of fracture intersections and terminations, i.e. n , N_i , N_y and N_x). In this paper, we are not interested in defining that 'true' value, rather we wish to explore the ranges in reported values from different participants, showing the scale of subjective bias for the collected data, and the factors that affect this range. Therefore, we define the uncertainty, or level of variability, present in fracture data collection and the related statistics as a function of the observers/operators.

3.4.4 Analytical framework

We describe the quantitative fracture data that the participants collected using the following approaches:

Spatial distribution and node triangle space: Several fracture attributes are determined by the spatial distribution of features, e.g. fracture traces, within a sample area. For linear scanlines, we visually determine the relative location of interpreted fracture traces from the digitised data. For circular scanlines, the spatial distribution of nodes is represented via point density heat maps, generated from digitised data in ArcGIS, and used to identify areas of uncertainty. We also visually compare the participants' interpretation using node triangle plots. For example, for all circular scanlines, we compare the relative position of node data interpreted for each participant.

Range/variability: The spread of data is described using the range between the minimum and maximum value for a given parameter or statistic (e.g. fracture count), and the quartile-based coefficient of variance (QCV, Equation 1).

$$QCV = \frac{Q3-Q1}{Q2} \quad \text{(Equation 1)}$$

QCV is interpreted in a similar manner to the standard coefficient of variation (CV) and provides a dimensionless measure of variability which can be used to compare between scanlines and attributes. QCV is more appropriate than the standard CV for this study because much of the data do not display a normal distribution. Further, the median and IQR are less susceptible to being skewed by outliers. We describe variability using the following descriptors: *very low* (QCV = 0.00 to 0.10), *low* (QCV 0.11 to 0.25), *moderate* (0.26 to 0.50), *large/high* (QCV = 0.51 to 0.70), *very large/high* (QVC = 0.71 to 1.00) and *extreme* (QCV >1.01).

Co-variance: We describe the strength of the relationship between quantitative data (e.g. fracture count and time taken) using the linear coefficient of correlation (R^2). Trends are described using the following descriptors: *no* ($R^2 < 0.35$), *very weak* (R^2 0.35 to 0.50), *weak* (R^2 0.51 to 0.70), *moderate* (R^2 0.70 to 0.9) and *strong* ($R^2 > 0.90$).

Consistency: Consistency can be used to describe two different aspects of the data. First, it can describe the rank position of participants for a specific reported (e.g. n-point count) or calculated (e.g. fracture intensity) value across all scanlines. In this case, high consistency would describe a participant that remains within 3 rank positions for a reported or calculated value for all circles. In contrast, low consistency would describe a participant who ranks highly in once scanline and low on another. Consistency uses descriptors depending on the range in rank position across scanlines as follows: *no* (> 16 rank positions for individual and > 6 for group exercises), *low* (15 to 11 rank positions for individual and 4 to 6 for group exercises), *moderate* (7 to 10 rank positions for individual and 2 to 4 for group exercises) and *high* (< 7 rank positions for individual and < 2 for group exercises). Consistency is also used to describe the range/variability, quantitative data or visual assessments across all scanlines within a method.

For **qualitative data**, such as the degree of experience of collecting fracture data, statistical interrogation is not appropriate, given the potential for ambiguity in the response categories; the categories are not necessarily linear, and participants may judge “high”, “moderate” and “low” differently. Instead, we visually interpret trends in qualitative data,

and use numerical indicators, such as the range or median, to interpret trends across participant responses and their interpretation.

3.5. Results

3.5.1 Linear Scanlines

Scanline	Individual/ #	Fracture count				Trace length (m)						Time (minutes)				
		Min	Ma	Me	QCV	Min	Ma	Me	QCV	Min	Ma	Me	QCV			
L1	Field i 6	3	10	7.0	0.71	0.03	2.22	0.58	0.36	0.40	0.15	5:32*	9:00*	7:16*	0.24	
L2	Field G 3	7	14	12.0	0.29	0.01	1.78	0.43	0.17	0.26	0.21	-	-	-	-	
L3	Field G 3	21	38	26.0	0.33	0.04	23.08	1.21	0.69	0.54	0.18	10:00	13:00	10:00	0.15	
L4	Field G 2	18	19	18.5	0.03	0.05	14.4	2.29	0.61	1.17	0.69	-	-	-	-	
L6	WS1 i 11	10	23	14	0.39	0.02	0.61	0.21	0.39	0.19	0.43	2:17	8:40	4:58*	0.33	
	WS2 i 18	9	25	21	0.38	0.03	0.72	0.24	0.28	0.23	0.27	1:51	24:00	6:12*	0.66	
L5	WS1 G 5	22	31	22	0.23	0.12	2.72	0.86	0.73	0.70	0.82	5:57	9:35	7:33	0.24	
	WS2 G 7	15	28	20	0.40	0.14	2.43	0.96	0.21	0.86	0.47	5:00	13:00	8:17	0.57	

Table 3.4: Summary table of raw linear scanline results where i = individual, G = groups, # = number of participants/groups. *only two participants recorded time for this scanline **P10 did not record time taken to count nodes ***P23 did not trace fractures so only have spacing and time information.

The results of statistical analysis of fracture data collected from linear scanlines are shown in Table 3.4. The range in the number of fractures interpreted to intersect the scanline varied between participants and between scanlines both in the workshop and the field. For example, in the field, QCV ranges from 0.03 for Line 4 to 0.71 for Line 1 (Table 3.4). The variability in the trace length data depended on the scanline being sampled, more so than which participant was sampling, and could be as low as 0.15 (L1) or as high as 0.82 (L5, WS1). We find that there is greater variability in the minimum recorded trace length (high to extreme), than the maximum recorded trace length (moderate to high). For example, for Line 6, participants reported minimum trace length ranging from 0.02 to 0.23, and maximum trace lengths ranging from 0.25 to 0.72 m (See S5). It is clear that the interpretations by participants differed about individual fracture terminations. For example, for one fracture intersecting Line 3, Participants G + F interpreted that after 8.0 meters the

fracture terminated against another fracture, whereas Participants C + D felt that it terminated in an area of no exposure after 22.0 m (S5). The correlation between the number of fractures intersecting a linear scanline and the range of reported fracture trace lengths by participants for that scanline shows weak to no trend in the field (e.g. $R^2 = 0.59$ for Line 1) and no trend in the workshop (e.g. $R^2 = 0.24$ for Line 1). That is, our results indicate that trace length is not correlated to the number of interpreted fractures.

The fracture traces drawn onto photographs in the workshops helped us to understand the underlying controls on differences in interpretation. We examined the fracture traces of Line 6 in detail and the interpreted fracture networks can be considerably different (Fig. 2). All participants identified two large fractures located roughly 1/3 and 2/3 of the way along Line 6, however participants differed greatly in their interpretations of the first third of the scanline: Participant 28 does not identify any fractures, whereas Participants 10 and 14 identified 3 and 10, fractures respectively. Such differences between participants' observations could be a function of the site; the fractures are partly obscured by water and have thin fracture traces. These 'hairline' fractures are also present in other parts of the scanline and in all cases increase the observation variation between participants. Also in Line 6, a feature trending at a low angle to the scanline half way along was only identified by 14 of 29 (48%) participants. Where this feature is identified, it is also the longest visible fracture trace that transects the scanline, and so identifying this fracture affects the trace length statistics. Our analysis suggests that the main source of uncertainty for characterizing fractures along photographs of linear scanline is the decision of how a fracture terminates, and hence how long the fracture is interpreted to be.

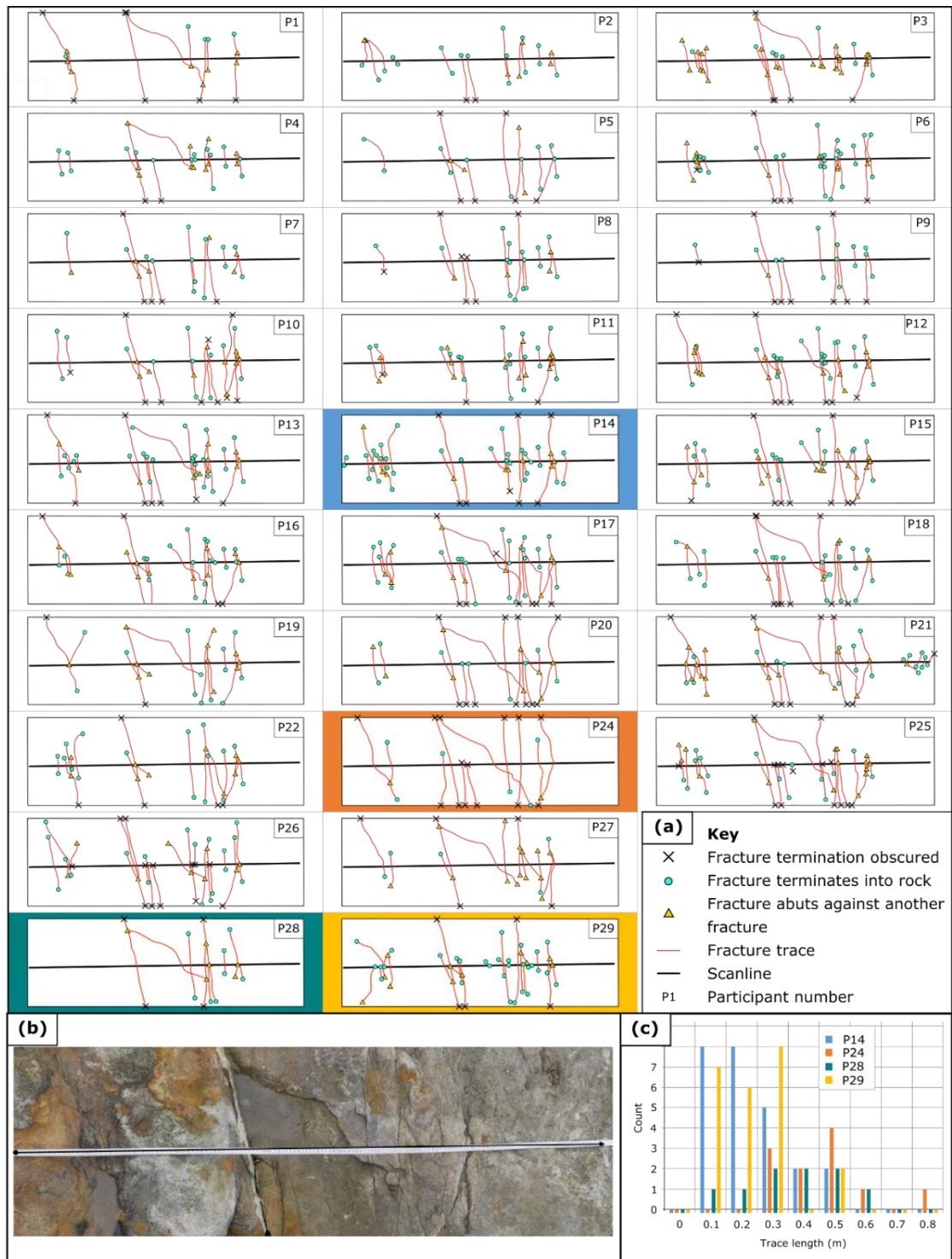


Figure 3.2: The interpreted fracture traces for Line 6 (length 1.45 m). (a) The digitised fracture networks for all workshop participants. (b) Field photograph of Line 6. (c) Fracture trace length histograms (bin = 0.1 m) for participants who recorded a low to high number of fractures. The corresponding digitised fracture trace is also highlighted in the appropriate colour. Key differences in the interpreted fracture networks are highlighted using participants who selected a low (Participant 28, 9 fractures), medium (Participant 10, 17 fractures) and high (Participant 14, 25 fractures) number of fractures.

3.5.2 Circular Scanlines: Topological sampling and fracture mapping

		n-point						Node Count												
		i/g	n			t (sec)			i-node			y-node			x-node			t (sec)		
			Range	media	QCV	Range	Media	QCV	Range	Media	QCV	Range	Media	QCV	Range	Media	QCV	Range	Media	QCV
C1	Fiel	i	15-21	17	0.16	19-42	29.5	0.39	0-3	0.5	3.5	12-21	19	0.22	6-14	7	0.32	137-230	172	0.33
	WS 1	i	14-23	18	0.22	36-99	68	0.87	0-12	1	2.0	1-38	19	0.74	4-11	7	0.43	119-447	240	0.77
	WS 2	i	11-25	18.5	0.30	15-295	82	1.41	0-6	1	2	4-34	18	0.81	4-14	7.5	0.50	82-114	289.5	1.11
C5	Fiel	i	14-19	15.5	0.16	14-43	21	0.64	4-8	5	0.45	28-47	34.5	0.38	2-8	3.5	1.07	127-245	165.5	0.32
	WS 1	i	7-18	12	0.25	20-120	47	0.78	3-14	5	0.9	4-34	20	0.33	1-6	2	0.75	150-117	317	0.46
	WS 2	i	9-18	12	0.08	20-298	67.5	0.95	0-32	4.5	1.39	7-41	14	0.50	0-11	1.5	1.17	60-105	281	1.09
C8	WS 1	i	10-25	23	0.17	29-180	78	0.77	2-11	5	0.5	1-60	26	0.5	2-22	10	0.3	150-780	378	0.8
	WS 2	i	16-32	24	0.22	45-240	107	0.48	1-16	4	0.5	5-45	19.5	0.92	5-18	10.5	0.48	30-144	599	0.64
C4	Fiel	i	12-20	15	0.13	24-50	41	0.41	5-19	13	0.31	20-34	29	0.17	0-4	0	-	147-215	167	0.35
	WS 1	g	11-18	14	0.36	60-330	97	0.49	7-19	9	0.22	6-27	11	0.73	1-4	3	0.67	324-521	405	0.16
	WS 2	g	10-18	14	0.39	64-323	129	0.96	5-23	5	0.9	5-27	11	0.50	0-3	1	1.5	115-720	290	1.35
C3	Fiel	i	19-30	22	0.05	24-58	38.5	0.68	3-15	7	1.0	21-33	29	0.24	6-16	8	0.5	162-282	261	0.15
	WS 1	g	18-22	19.5	0.17	55-90	77.5	0.25	4-20	5.5	0.86	19-24	23	0.05	5-11	5.5	0.41	208-521	322	0.29
	WS 2	g	14-23	16	0.13	52-713	129	1.77	2-54	7	1.43	11-22	18	0.39	3-10	4	0.38	143-600	360	0.63

Table 3.5: Summary of fracture data and time taken for circular scanlines 1, 5 and 8, in the field and workshop, either working individually (i) or in groups (g). The data are presented in the order scanlines were completed in the workshops.

We present the results of circular scanlines and topological scanlines together because participants defined nodes within sample circles for both sets of measurements. For the circular scanlines, the number of fracture terminations (m), although not explicitly discussed in this section, is equivalent to the total number of i - and y -nodes.

The reported values for n -points and topological characterisation for circles undertaken in the field are presented in Figure 3.3. The number of fracture intersections with the edge of a circle (n) displayed very low to low variability as recorded by the field participants (QCV ranged from 0.05 to 0.19; S7). However, there is greater spread in the number of reported nodes identified within a circle. The scale of variance depends on the properties of the circle that is being sampled; variance ranged from very low for Circle 1 (QCV = 0.03) to high for Circle 6 (QCV = 0.62). All node types (i -, y - and x -nodes) displayed a wide spread in variability, ranging from low to extreme across different circles.

Similar reporting behaviour is observed for data collected in workshops, however, the workshop data is even more variable than field data (Figure 3.4; Table 3.5). However, when particularly large variability was observed for a topological parameter (e.g. y -nodes), it was not necessarily replicated for the counts of other parameters (e.g. n -points) for the same circle. For example, the number of y -nodes interpreted in the field varied greatly for Circle 6 (7 to 27; QCV = 0.66), even though this circle had the smallest range in values for n -points (6 to 9; QCV = 0.19). In this case, clearly the participants saw almost the same fracture *intersections with* Circle 6 (i.e. subjective bias for n -points is small). At the same time, the participants differed in their observations and classifications of fracture characteristics *within* the circle, leading to a greater range in the number of fracture intersections there. The consistent observation is that subjective bias affects node counts more than n -point counts, but that the degree of variability is dependent on the sample site – i.e. the characteristics of the circle being sampled.

No single circular scanline was particularly prone to subjective bias for all of the studied fracture parameters. For example, compared to other circular scanlines, the variability in data collected from Circle 3 is small for n -points and y -nodes, but is one of the most variable for i -nodes and shows moderate variability for x -nodes. In contrast, the variability in data collected from Circle 7 is small for n -points, but displays high variability in y -nodes, very high in i -nodes and extreme in x -nodes (Table 3.5). The trends are seen in both field and workshop data.

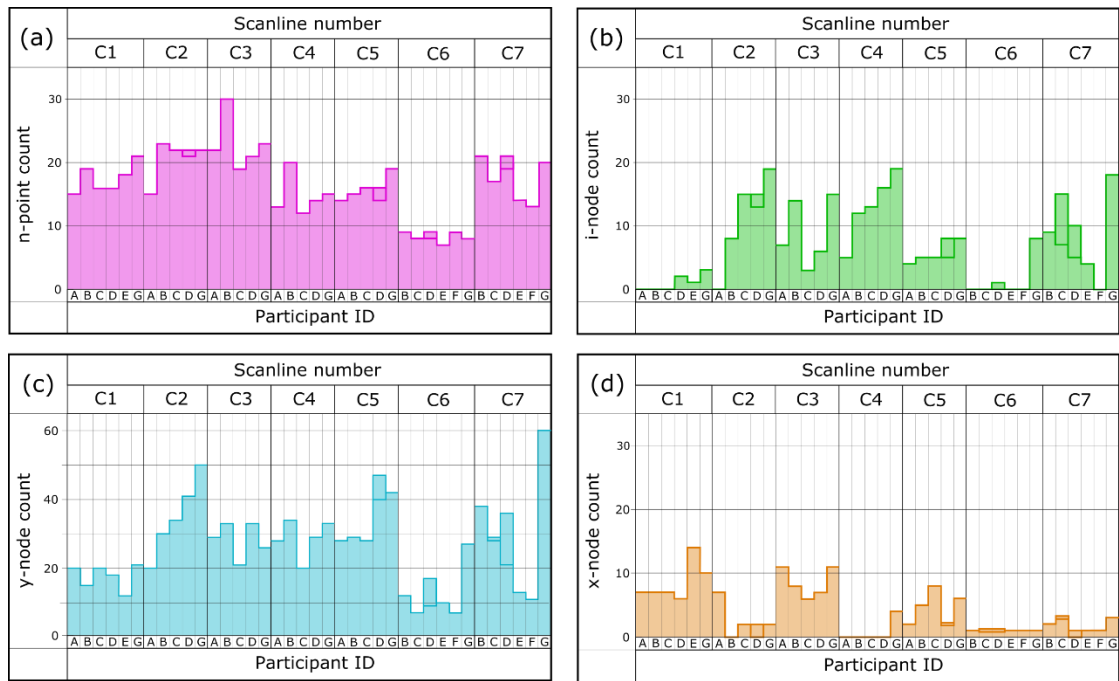


Figure 3.3: Results of the fracture data from circular scanlines (C1-7) collected in the field by 7 participants (labelled A-G, though A, E and F did not complete all of the scanlines). (a) the number of fractures that intersected the circular scanlines (n). (b) fractures that terminated in rock (i-nodes). (c) fractures that terminated against another fracture (y-nodes). (d) fractures that intersect another fracture (x-nodes). Participants C and D repeated some of their measurements for selected circles and this is indicated by two bars in their column for that circle.

Although individual circles displayed considerable variability between participants, many participants remained consistent in their observations between different circles (Figure 3.3 and 3.4). For example, Participants A and C, or Participant 2, tended to report lesser counts for all circles than Participant G, or Participant 13. That said, when Participants C and D repeated the data collection exercise for the same scanline in the field, there were differences within the repeat data (Figure 3.3), although it was far less than the discrepancy between participants. The level of consistency depends both on the participant and attribute being measured. For example, for circles undertaken in the workshops by individual participants, node count displays a high degree of consistency (6.6), whereas n-point count displays moderate consistency (9.7). When individual participants are inspected, the level of consistency between scanlines ranged from 1 (Participant's 2, 3 and 13) to 19 (Participant 9). It is clear that some participants displayed a greater level of consistency (e.g. Participant 28), while other participants' interpretations varied from one circle to another (e.g. Participant 9). The relative proportion of specific node classification (e.g. y-nodes) remained consistent between circles (Figure 3.5). For example, Participant 11

consistently recorded more y-nodes when compared to other participants, while Participants 5 and 21 tended to record more i- and x- nodes. The same trends are seen both in field data and workshop data collected as groups.

(a)		Count												Time (s)					
		n-point			i-node			y-node			x-node			n-point			Node		
	P	C8	C5	C1	C8	C5	C1	C8	C5	C1	C8	C5	C1	C8	C5	C1	C8	C5	C1
Workshop 1	1	23	11	21	4	9	2	22	24	32	12	2	7	78	70	68	540	324	337
	2	11	8	16	2	4	2	1	4	1	3	3	8	107	59	99	378	317	259
	3	24	14	20	5	12	1	60	34	38	10	2	7	46	-	72	460	1177	447
	4	22	12	16	6	3	0	28	17	18	9	1	7	106	53	50	602	333	119
	5	10	7	14	5	3	1	1	7	5	2	1	5	83	70	70	172	150	120
	6	25	14	23	4	5	12	27	26	29	12	1	11	52	32	51	312	330	416
	7	20	11	17	2	3	0	13	20	16	9	2	10	120	30	60	480	300	300
	8	25	16	19	6	7	3	26	12	20	15	6	8	36	28	38	150	150	211
	9	25	14	16	5	5	0	33	24	12	12	4	5	180	120	60	780	480	240
	10	21	12	18	2	5	0	23	19	19	22	1	4	29	20	49	171	186	141
	11	24	18	19	11	14	2	47	31	27	10	2	5	47	41	36	242	184	125
Workshop 2	12	24	13	18	4	4	2	42	26	25	8	1	6	102	298	295	1200	235	290
	13	26	18	25	15	32	6	45	41	34	18	6	10	180	60	60	1380	900	540
	14	28	12	21	4	7	1	23	16	18	9	1	9	109	80	107	705	451	538
	15	25	16	22	2	5	1	31	32	34	16	5	8	129	64	80	864	737	528
	16	24	13	19	5	13	1	14	14	20	12	0	4	105	89	230	660	600	259
	17	19	11	20	3	6	2	20	15	13	13	7	14	94	58	48	622	310	509
	18	26	12	19	3	2	0	19	13	10	15	2	7	134	71	84	504	235	186
	19	22	9	20	4	4	3	26	14	32	8	1	4	210	112	176	598	350	430
	20	16	12	18	1	2	1	5	23	18	5	2	6	45	240	254	125	325	217
	21	25	14	22	4	7	4	6	10	12	18	11	8	55	33	45	295	237	289
	22	18	11	13	5	3	0	7	11	4	7	1	10	98	131	74	730	517	550
	23	25	11	15	16	11	6	8	9	10	6	2	7	120	60	120	300	120	540
	24	22	12	11	4	3	0	7	7	9	12	2	6	120	120	120	600	180	240
	25	23	12	16	2	2	0	18	11	21	6	0	6	70	20	40	240	60	180
	26	32	12	17	8	11	2	29	14	25	12	3	8	121	34	46	458	165	138
	27	20	12	15	4	2	0	21	18	12	9	0	7	52	25	32	527	252	213
	28	16	12	13	1	0	0	7	9	5	9	1	10	46	21	15	30	60	82
29	27	14	21	8	9	1	22	18	25	13	1	10	240	90	180	1440	1050	1140	
(b)		Count								Time (s)				Key					
		n-point		i-node		y-node		x-node		n-point		Node		Rank for n-point and node counts	Rank for n-point and node time				
	G	C4	C3	C4	C3	C4	C3	C4	C3	C4	C3	C4	C3						
Workshop 1	1	14	22	7	20	17	24	3	11	330	90	521	521						
	2	13	18	11	4	11	19	1	6	62	82	324	208						
	3	18	-	19	-	27	-	4	-	97	-	405	-						
	4	11	18	9	5	9	23	2	5	60	73	357	332						
	5	18	21	9	6	6	23	4	5	110	55	420	312						
Workshop 2	6	18	23	14	11	13	17	1	6	120	60	600	360						
	7	18	18	5	3	27	22	3	3	129	129	720	600						
	8	14	14	5	7	14	18	1	4	323	713	115	143						
	9	12	16	5	16	11	22	1	3	184	389	445	168						
	10	10	16	5	4	5	13	2	4	116	113	290	465						
	11	12	18	5	2	8	11	0	10	300	240	120	360						
	12	17	16	23	54	8	22	3	4	64	52	140	205						

Figure 3.4 (Previous page): Recorded fracture data (n, and node counts) and the time taken to undertake n and node counts for workshop (WS) participants (P) and groups (G). The data for each attribute has been colour-coded according to where the reported value for the parameter ranked for that circle. Data are presented in the order that they were completed in the workshop.

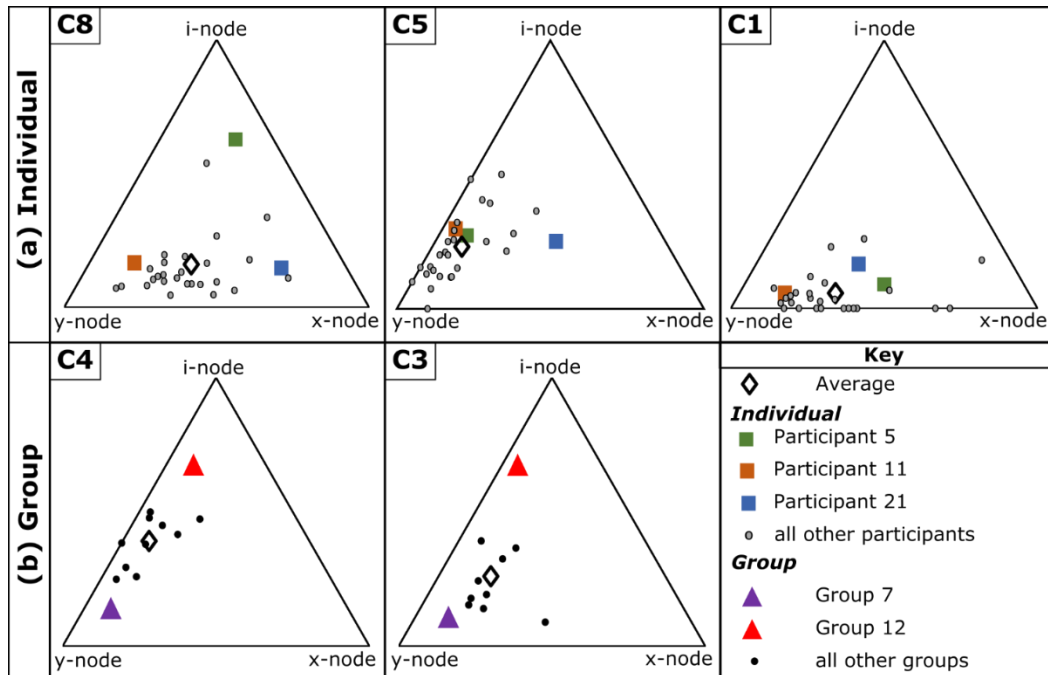


Figure 3.5: Node triangles for workshop participants and groups. For individual circles (a), Participants 5, 21, and 11 were highlighted to show the consistency the way participants classified nodes. Participants were selected according to whether they reported a low (P5), medium (P21) or high (P11) node count. Similarly, for group circles (b) Groups 7 and 12 were highlighted as groups who recorded a high and low node count.

In general, the scale of uncertainty (the range in reported values) in the workshop data is greater than field data as indicated by a wider range in reported values and higher QCV. Overall, the number of fractures reported was larger in the field data than the workshop data. For example, the reported number of fracture intersections in Circle 3 in the field (Fig. 3) ranged from 19 (Participant C) to 30 (Participant B), whereas from the workshops ranged from 14 (Group 8) to 23 (Group 6) (Figure 3.4). Similarly, the number of y-nodes is generally greater in the field and the range in values for each circle is less extreme – e.g. in the number of y-nodes for Circle 5 ranged from 28 (Participant C) to 47 (Participant D) in the field (QCV = 0.38; Fig. 3C), and from 4 (Participant, P2) to 41 (P13) in the workshops (QCV = 0.81; Figure 3.4). It is possible that in the field participants could observe fractures in more detail (e.g. the hairline fractures in Fig. 2) resulting in more consistency in their reported values.

In our data there was a clear discrepancy between the number of nodes or n-points *reported* by participants during the workshops and the number *recorded* in the paper copies of interpreted circular or linear scanlines. Participants tended to report a smaller number of nodes or n-points than they had drawn on their worksheets. While the magnitude of this error varied both between participants and between scanlines, the differences were consistently higher for data collected within an area (i.e. node counting) compared to that collected along a sample line (i.e. n-points). This counting error was much more pronounced within the circle than around the edge, suggesting that as data gatherers we are relatively good at counting when we follow a sample line (e.g. edge of a circle or linear scanline). However, when counting within a sample area the accuracy of results is reduced.

3.5.3 Window sampling

For window sampling, the number of recorded fractures displayed moderate to high variability (Table 3.6), with the largest variation occurring for Circle 4 (11 to 29; QCV = 0.76). The maximum trace length reported by all participants remained fairly consistent (QCV ranging from 0.01 for Circle 8 to 0.29 for Circle 1). However, considerable variability in trace length distributions was observed between participants (Figure 3.6), with the number of small fractures recorded across all scanlines displaying the most variability. For example, the number of fractures below 0.2 m recorded for Circle 8 ranged from 7 to 41, which represents 36.8% and 75.9% of the reported fractures for both participants. This is also seen in the minimum reported trace length data, which displayed very high to extreme variability (e.g. 0.02 to 0.11 m for Circle 4; QCV = 0.94). While the number of small fractures recorded by participants varies between circles, whether a participant records a high or low relative percentage of small fractures remains consistent. For Circles 8, 5 and 1, Participant 3 consistently recorded a high percentage of small fractures, whereas Participant 24 consistently recorded a low percentage of small fractures (Figure 3.6a). In short, participants either consistently record the presence of small fractures in a network, or consistently do not record the existence of small fractures in a network. For trace lengths longer than about 15-20% of the diameter of the circle, the shape of the distributions remains consistent across all participants, indicating that the larger traces in the fracture network are consistently identified independent of participant (Figure 3.6).

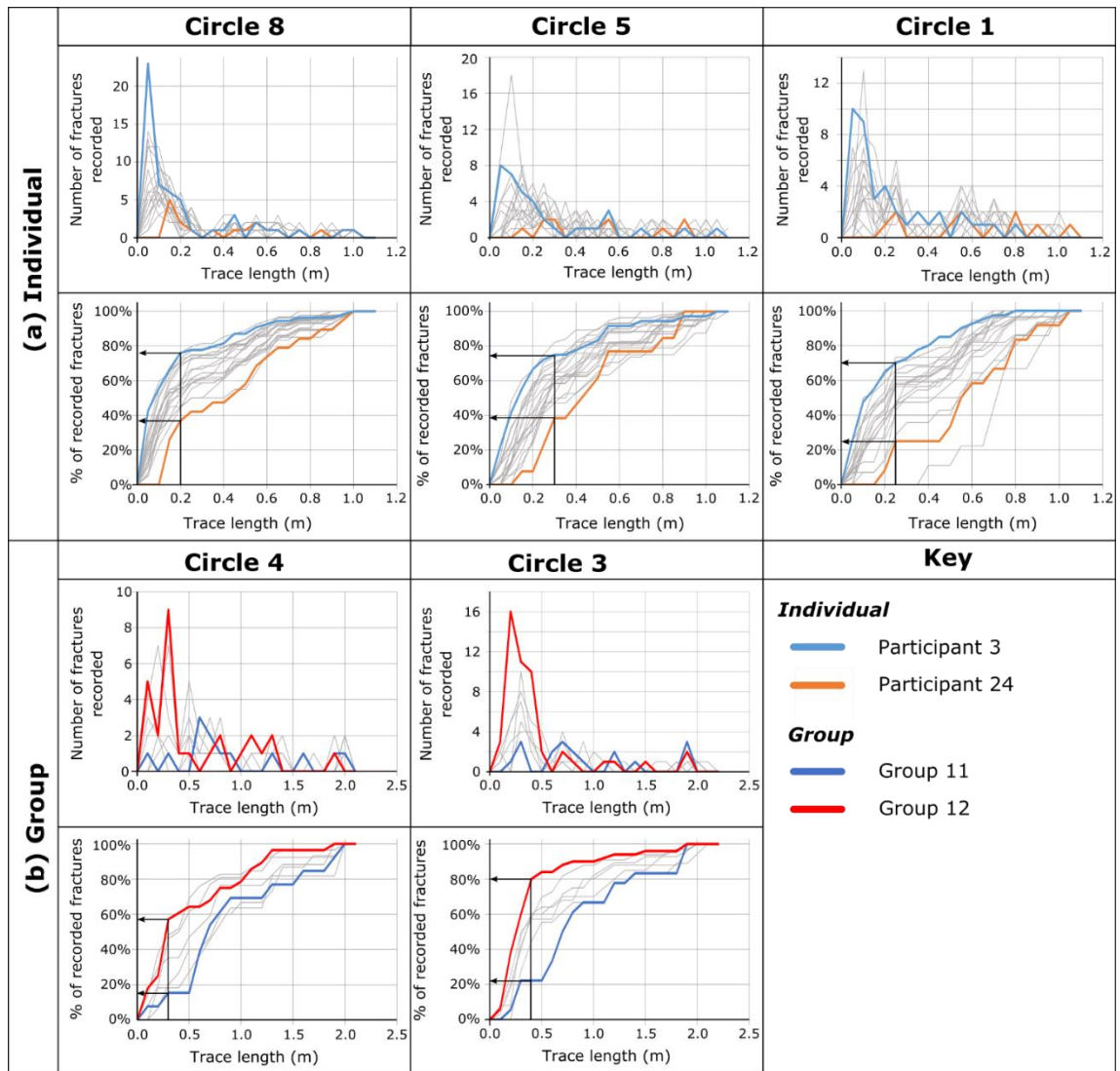


Figure 3.6: Fracture trace length distributions for (a) individual and (b) group window sampling data. The results are presented as both histograms and normalised cumulative frequency curves of fracture trace length with bin widths of 0.05 m for individual and 0.1 m for group window sampling data. The range in the relative percentage of small fractures observed in the data is highlighted using Participants and groups who consistently observed a high and low percentage of small fractures (Participant's 3 and 24 and Groups 12 and 11 respectively).

Circle	Number of participants	Number of fractures		Trace length (m)						
		Range	Median	QCV	Min	Max	Mean	QCV	Median	QCV
8 (i)	20	18-54	30.5	0.49	0.01-0.10	0.70-0.98	0.27	0.31	0.17	0.43
5 (i)	20	13-56	22.5	0.48	0.02-0.12	0.68-1.05	0.33	0.40	0.24	0.39
1 (i)	20	9-40	23.5	0.44	0.01-0.40	0.67-1.03	0.37	0.37	0.30	0.95
4 (g)	7	11-29	17	0.76	0.02-0.11	1.89-1.95	0.69	0.47	0.52	0.60
3 (g)	7	18-50	25	0.46	0.04-0.22	1.82-2.01	0.61	0.26	0.38	0.26

Table 3.6: Summary of fracture parameters reported for window sampling. Data is presented in the order the scanlines were undertaken within the workshops. (i) and (g) denote whether the scanline was undertaken individually or as a group.

3.5.4 Areas of increased uncertainty: A case study using Circle 8

To highlight potential causes of differences in interpretation, Figure 3.7d compares the interpretations of fracture traces and nodes in three particular ‘problem areas’ (so called owing to how differently these parts were interpreted), from end-member Participants 11, 18 and 21, who reported high, medium, and low node counts respectively. Area 1 is well exposed and contains several intersecting fractures. The nature of the connections was interpreted differently by each participant. Participant 21 interpreted only the major fractures coming into the junction, and depicted the fractures interesting in a star-like formation. Participant 18 interpreted a standard x-node, with a second larger fracture terminating against the NE-SW trending fracture (y-node), and also notes an E-W trending fracture linking the two major fractures and cutting the third (three x-nodes). Participant 11 differed from Participant 18 by interpreting the NE-SW fracture trace as being offset by the NW-SE fracture, such that the x-node interpreted by Participants 21 and 18, was instead interpreted as two y-nodes. Area 2 is a complex intersection of a number of NW-SE fractures with part of the photographed exposure obscured by shadow (a clear limitation of interpreting the scanline from photographs rather than in the field). Participant 21 did not interpret the fractures obscured by shadow, whereas Participant 18 did. Participant 11

depicted a number of smaller fractures which Participants 18 and 21 did not identify. Area 3 is an intersection of two large fractures which is obscured by a coarse sand infill. Both Participant 18 and 11 interpreted the obscured connection as a simple x-node, whereas Participant 21 felt that the fracture bifurcated to frame the area of no exposure. Participant 18 and 21 interpreted the other fully exposed connections similarly (although Participant 21 does not depict a fracture to the south of the sand fill), whereas once again Participant 11 identifies several additional smaller and complicated fractures and fracture connections, particularly y-nodes. In each case, it appears that participants effectively 'self-censored' their data according to their 'preferred' minimum trace length, and had different approaches to areas of shadow or obscured outcrop. The different geometry of the interpreted fracture intersections would result in significant differences in interpreted fracture development history.

When analysing the node classifications and interpreted trace lengths for all circles it was found that in many cases the fracture networks depicted or interpreted were not viable: in other words, there were undefined nodes or intersections that had a non-compatible number of branches entering the node (e.g. 4 nodes for a y-node or 5 for an x-node). Occurrences of these undefined or floating nodes were more common in WS1 than WS2, perhaps because WS2 participants were specifically asked to draw out the fracture network on their photographs.

3.5.5 The effect of working in groups

Large variability in the number of reported fractures in the field was also seen when linear scanlines were undertaken as pairs, for example for linear scanline 3 counts ranged from 21 (Participant C + D) up to 30 (Participant A + B). The groups are obviously made up of participants who have different 'eye for detail'. When working individually, Participants C and D both recorded small fracture counts, while Participant B recorded the highest. There is a suggestion in the data that when working as pairs, groups tended towards the more detailed member, for example Participant F recorded the lowest fracture count when working individually, however, in a group with Participant G recorded a higher than average fracture count. This was also discussed in the discussion following workshop 1.

No clear differences can be seen between data collected individually or as groups for either circular scanlines (Table 3.5; Figure 3.4) or window sampling (Table 3.6; Figure 3.6b). Although the group circles have smaller y-counts and greater mean trace length values, the

differences are not enough to be confident that the effects are due to working in groups rather than differences in the fracture network. This is due to the limited number of circles completed, the fact no circles which were completed individually were completed as a group and that there is a large spread in variability between participants observed between different circles. That said, groups generally reported more complex fracture networks with a higher reported number of small fractures. When working as groups that included a naturally detailed and naturally less detailed participant, the results tended to be more detailed: compare participants 2 and 11's recorded values when working individually or together as Group 3 (S7).

There is also no difference in the level of variability for any particular parameter reported for either topological sampling within a circular scanline or window sampling (e.g. γ -node count, number of fractures etc.). For example, node counts display QCV values of 0.48 to 1.00 for individual circles and 0.40 to 1.00 for group circles. This suggests that working as a group does not affect the level of subjective bias in the dataset. Similarly, to when working individually, the majority of groups show high levels of internal consistency in the number of reported fractures (7 out of 12 groups). Groups also displayed internal consistency in the relative percentage of small fractures (Figure 3.5b) and node types (Figure 3.4b) reported across different sample circles.

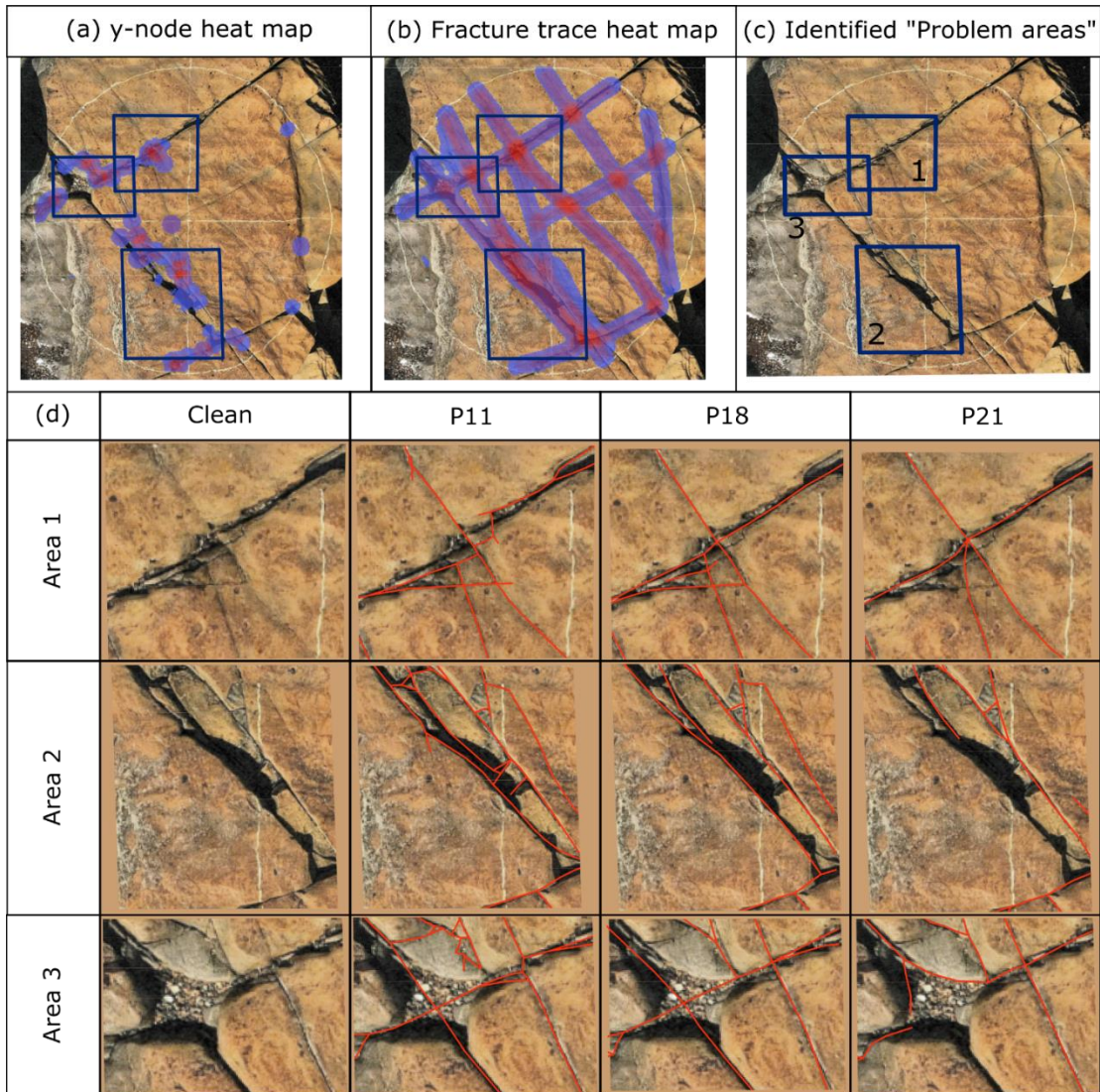


Figure 3.7: A detailed study of the areas which cause increased uncertainty in Circle 8. The figure comprises of clean field photographs of Circle 8 with the (a) heat map of y-node point density, (b) heat map of fracture trace density and (c) areas identified as problem areas. In panel (d) the close up of areas 1, 2 and 3 along with the features recorded by Participants 11, 18 and 21 are shown. See text for full description.

3.5.6 Time taken to collect data

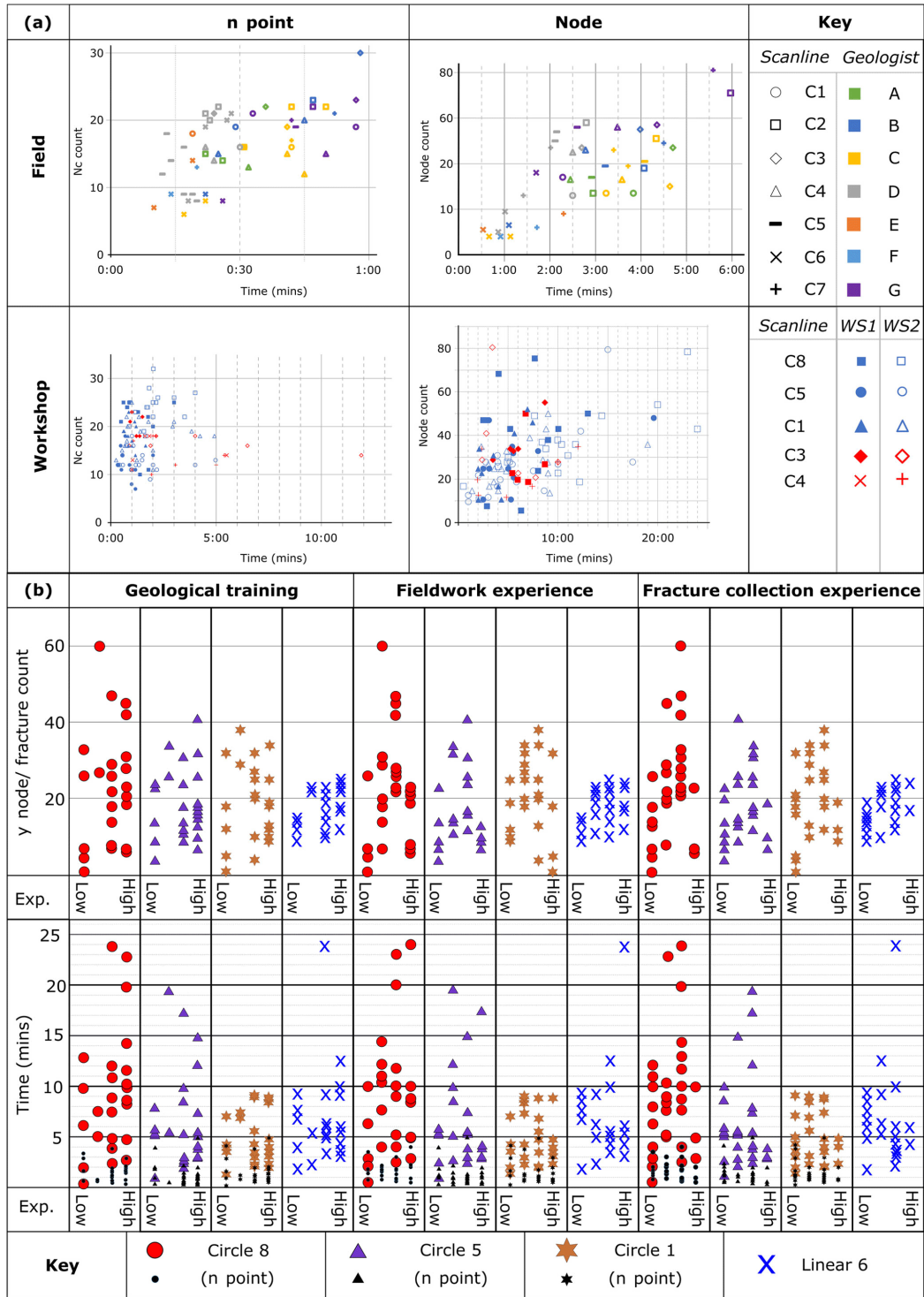


Figure 3.8: The impact of participant experience on the collection of fracture data. (a) The time taken in seconds to record fracture data (n and node counts) from circular scanlines both in the field and workshops. (b) The impact of experience on the recorded y-count and number of fractures in individual scanlines and the time taken to complete the workshop tasks.

In the field, the time taken to undertake counts of n-points and nodes varied not only as a function of participant, but also the circle being sampled. It was not clear if it took longer for participants to count more n-points or nodes, with the trend being non-existent to very weak for n-points (R^2 ranging from 0.003 to 0.37) and non-existent to weak for nodes (R^2 ranging from 0.04 to 0.70). For workshop data no trend was observed between the time taken to record, or the variability in, the number of reported fractures observed (Fig. 8a). Both the time taken and magnitude of the variability was considerably greater in the workshops compared to the field. For example, Circle 5 took participants between 1 and 17 minutes in the workshop (QCV = 0.94), and 2 minutes 21 seconds to 4 minutes 26 (QCV = 0.64) seconds in the field.

Window sampling, which was undertaken in WS2, took longer than circular scanlines for the same circle in WS1, however, this difference is small. While it took 1.3 to 3.2 times as long to record n values, the relative time taken to undertake topological sampling within the circle is comparable for circles completed both as individuals (0.85 to 1.6) and in groups (0.95 to 1.05). Thus, although circular scanlines are often suggested as a quick way of gathering fracture data, it does not take significantly longer to trace out the fracture network. This observation suggests a similar amount of data could be collected using both methods.

While some participants took much longer than others, the participants were often (18 out of 29 Participants) internally consistent in the time taken to complete their tasks (Figure 3.3 & 3.8). For example, C and G tended to take longer than A or D in the field, and in Workshop 2, Participant 29 consistently took longer than Participant 25. Although this was often observed, some participants displayed low to no consistency in time taken between scanlines. For example, Participant 25 ranked 3rd quickest for Circle 8 and 28th quickest for Circle 1 in the time taken to count n-points. No correlation was found between average rank position and range in rank position for the time taken to either recorded n-point data ($R^2 = 0.025$) or node data ($R^2 = 0.001$).

3.5.7 Experience

The relationship between experience and the number of node counts has a large amount of scatter (Figure 3.8b). Generally, participants with less experience undertaking geological field work or collecting fracture data counted fewer nodes than more experienced participants, however the trend is very weak. Perhaps counter-intuitively, experience does

not reduce the time taken to collect fracture data (Figure 3.8b). However, for node counts, the fastest experts are still notably slower than the fastest inexperienced Participant. Also, more experienced participants do not appear to characterise with more detail than those with less geological training or experience. It is possible that participants with experience in fracture analysis will consider the connections they observe, whereas beginners will draw the traces that they see without considering the implications of those connections (i.e. implied cross-cutting relationships).

3.6 Effect of subjective bias on the derived fracture statistics

The variability in the collected fracture parameters will affect the derived fracture statistics in different ways. No particular equation for the calculated statistics (Table 3.1) has statistically sensitive relationship to subjective bias for a particular fracture attribute. To identify which fracture statistics are most susceptible to subjective bias, we discuss and compare the results from all methods in terms of the relative ranges of values.

The effect of subjective bias on *mean trace length* depends on the method that the statistic is being derived from. For linear scanlines the variability depends on the scanline being sampled. For example, small variability is seen for Line 2 where values range from 0.33 to 0.49 m (QCV = 0.17), compared to 0.89 to 3.70 m (QCV = 0.61) in Line 4. For topological sampling within a circular scanline low to very high variability is observed between participants in the field, with QCV ranging from 0.13 for Circle 3 to 0.82 in Circle 7. Variability is higher in workshop data, where moderate to high QCV values are observed (0.34 to 0.72), with both group circles displaying moderate variability (0.34 and 0.38). Mean trace length derived from window sampling displays moderate variability across all Circles sampled (QCV 0.26 to 0.47) and displayed lower variability compared to trace length derived for the same circle using topological sampling. Mean trace length derived from window sampling was consistently less than that derived from circular scanlines of the same circle. For example, mean trace length for Circle 5 derived from window sampling ranged from 0.19 to 0.46 m (S8).

For linear scanlines, no correlation was observed between the number of observed fractures and fracture trace length. For example, Participants B and G both recorded 10 fractures intersecting Line 1, however, the derived mean trace lengths were 0.62 m and 0.25 m respectively (see, S5). This outcome contrasts with window sampling, where mean trace length decreases as fracture count increases ($R^2 = 0.79$ for Circle 8, see S8), and

circular scanlines where mean trace length is a function of the number of fractures intersecting and terminating within a circle.

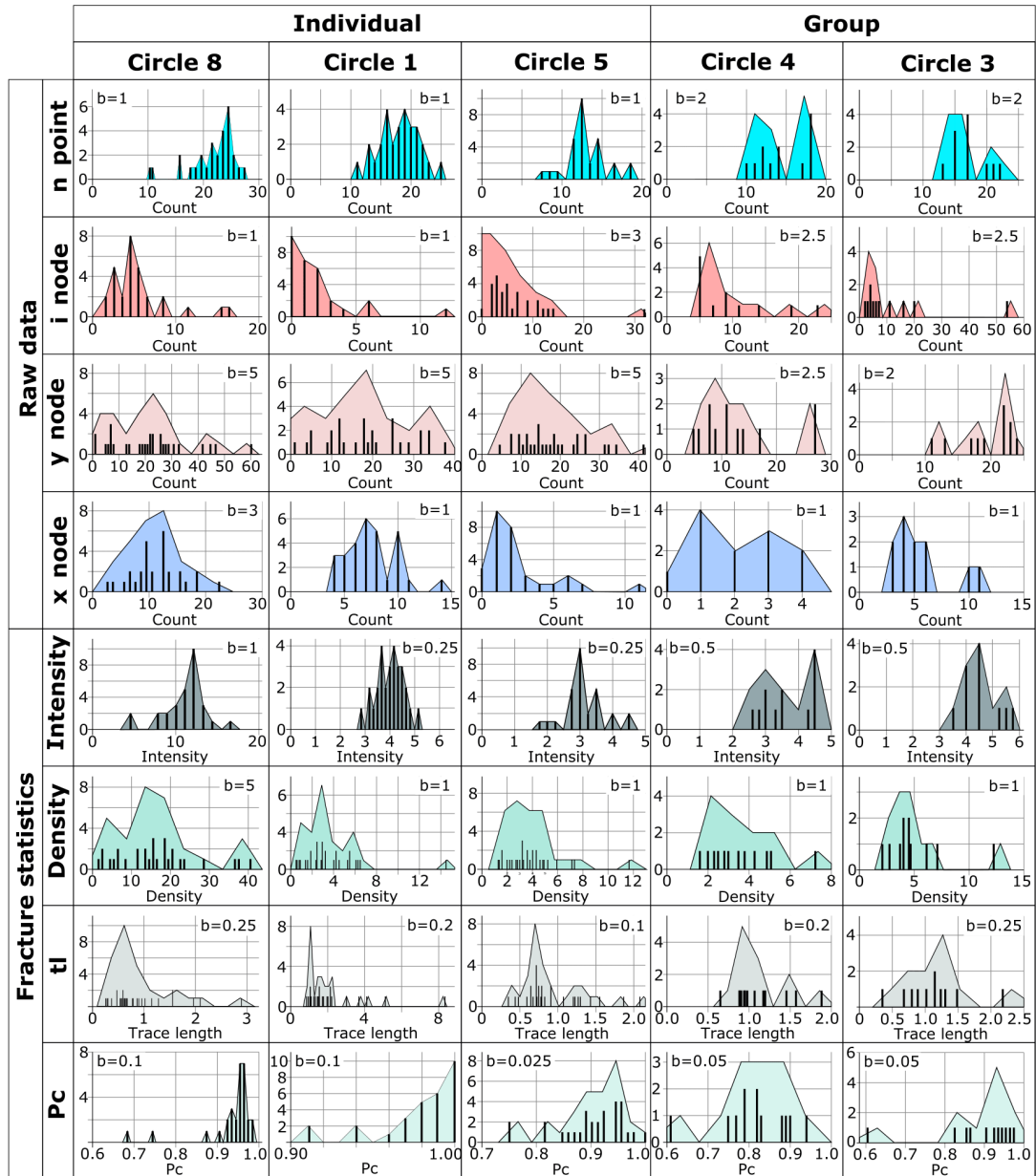


Figure 3.9: Topological sampling results for individuals and groups for circular scanlines 1, 3, 4, 5 and 8. Each histogram reports the results for all workshop participants. The statistics have been derived from the data for each participant. Data is presented as both bar charts and shaded histograms with the bin width, b , indicated on the chart (please note the bin width varies between circles as a function of the range in reported or calculated values). In all cases the y-axis represents frequency and is scaled so the shape of the distributions can be assessed.

Fracture density, which is calculated for circular scanlines and window sampling has moderate to high variability between participants. For both methods the level of variability depended on the circle being sampled, along with whether the analysis was undertaken in the field or in the workshops. For example, fracture density derived from circular scanlines ranged from 3.82 to 7.48 F/A for Circle 3 (QCV = 0.13) up to 2.12 to 10.6 F/A for Circle 6 (QCV = 0.68) in the field and from 2.07 to 12.1 F/A for Circle 3 (QCV = 0.34) up to 0.48 to 6.53 F/A for Circle 1 (QCV = 0.79). For window sampling participant's statistics displayed moderate to very high variability within circles (QCV 0.44-0.76). A larger value for fracture density is obtained using window sampling is used for the same circle, as shown in Circle 8, where window sampling derived fracture density ranged from 22.9 to 68.8 F/A compared to 1.9 to 41.4 for circular scanlines. Variability between participants is lower for window sampling compared to circular scanlines when samples are undertaken individually, however, show more variability when undertaken as a group.

Across all methods, *fracture intensity* has the smallest amount of variability between participants, however, differences are still observed between methods. When linear scanlines are used the amount of variability depends on the scanline being sampled. For example, Line 4 ranges from 0.93 to 0.98 f/m (QCV = 0.03) whereas Line 1 ranges from 2.31 to 7.69 f/m (QCV = 0.71), with the majority of scanlines displaying low to moderate variability. When fracture spacing, instead of number of fracture reported, is used to calculate fracture intensity more variability in values is observed, primarily due to the large difference in the minimum reported fracture spacing of participants across all circles. Unlike for linear scanlines, fracture intensity represents a robust statistic for both circular scanlines and window sampling. This is emphasised by the QCV values for circular scanlines, both in the field (QCV 0.03 to 0.21) and workshop (0.19 to 0.43), along with those for window sampling (0.11 to 0.21). Fracture intensity estimates using circular scanlines derived from field data generally provide a higher value than when the same circle is analysed in the workshop. For example, Circle 3 ranges from 4.75 to 7.5 f/m from field data and 3.5 to 5.75 from workshop data. Fracture intensity derived from window sampling is consistently lower than that derived from circular scanlines for the same circle.

The *connectivity* of the network (*percentage of connected fractures, Pf*) is highly variable for values gathered by participants using linear scanlines, with the magnitude of the variability dependent on the scanline being sampled. For circular scanlines and window

sampling, where the percentage of connected branches (P_c) is used, connectivity represents a robust statistic with very low QCV values (e.g. 0.00 to 0.06 for field data). The maximum reported values for P_c remain the same when field and workshop data are compared, however, the lowest reported values are consistently lower in the workshops for any given circle.

Subjective bias impacts all data collection methods (Table 3.7). Window sampling appears to be the method which is least effected by subjective bias. Out of the methods tested in the workshops, window sampling displays the lowest variability between participants for all of the parameters: intensity (low), density (moderate to high), mean trace length (moderate) and connectivity (very low). Additionally, because this method requires the network to be drawn out, it is possible to check for the existence of 'floating nodes' and other irregularities in the recorded fracture network. Linear scanlines had the greatest variability between parameters.

The different fracture statistics also display different degrees of subjective bias. *Fracture intensity* represents the most robust statistic as it shows the least variability in data collected by different participants for a given scanline. In contrast, *mean trace length* and *fracture density* both display considerable variability in the reported data, particularly when derived from workshop data. The *connectivity* of the network was found to be robust for topological sampling, however, considerable variability existed in the values reported from linear scanlines. When participants traced out fractures while completing linear scanlines or window samples, it was possible for us to identify the causes of differences in participant observations; differences that affect the derived fracture statistics.

Statistic	Circular Scanline – topology	Circular Scanline - Window	Linear Scanline
Intensity	Very low to low variability when derived from field data and low to moderate when workshop data is used. For Circle 1, 4 and 5 the calculated intensity from workshop and field data were very similar, however, the calculated intensity for Circle 3 was much lower in the workshop. In all cases ranges are greater when workshop data is used, particularly for Circles 1 and 5.	Low spread between participants within circles. In all cases, apart from Circle 4, intensity calculated using window sampling is lower than that derived for node counting for a given circle.	Variability, which ranged from very low to high, depends on the scanline being sampled. For example, Lines (Line 1, Line 6) than others (Lines 3 - 5, all low intensity, have small range).
Density / Spacing	Low to high spread when derived from field data and moderate to very high when workshop data is used. Density calculated from workshop in all cases apart from Circle 1 is lower than when calculated from field data.	Moderate to high spread. Values consistently higher in workshop data when window sampling data is used compared to node counting, particularly Circle 8. Can be both comparable to field density (Circle 4) or considerably higher (Circle 1).	Variability in mean spacing values depends on the scanline being sampled, ranging from very low to very high. Maximum reported spacing had low spread, whereas, minimum spacing ranged from low to extreme variability depending on the scanline being sampled. Equally large range in workshops and field.
Mean trace length	Low to moderate spread when derived from field data and moderate to high when workshop data is used. How similar the range in reported values are between workshop and field data varies for different circles.	Moderate spread across all circles. The extremes in the ranges observed in mean trace length estimates are considerable lower than for node counting. Of all methods window sampling provides the smallest estimate for mean trace length.	Moderate to Highly variable for most scanlines. Equally large range in workshops and field. Maximum reported trace lengths generally much larger than for other methods, due to the different scale of observation.
Connectivity	Very low spread, both between circles, between methods, and settings (field vs workshop).	Not assessed separately from node classifications.	Spread depends on the scanline being sampled and ranges from very low to extremely variable. Equally large range in workshops and field.

Table 3.7 (Previous page): Summary of the broad trends in fracture statistics derived from the three methods we explored, presented in Figure 3.9.

3.7 Discussion

Subjective bias in fracture data collection has implications for the validity or reliability of the models that the data informs, such as the derived fluid flow parameters, rock strength characteristics or paleostress conditions. Here, we explore these implications. Further, we draw on participants' discussions during the workshop and field activities to propose potential reasons for the differences in observations between participants.

3.7.1 Scanline validity and appropriate data collection method

As for all forms of sampling for data collection, scanlines must contain enough data points to be statistically valid, where the required number of data points depends on investigated characteristic of the fracture network. However, our data demonstrate that in addition to the fracture network characteristics, the required scanline size (length of a linear scanline, circumference of a circular scanline or area of a window sample) is also dependent on who is collecting the data.

Different participants clearly observed different numbers of fractures in the same scanline (Table 3.6, Figure 3.2). Zeeb et al. (2013) suggest that a minimum of 225 fractures are sampled for linear scanlines and 110 fractures for window sampling. For Line 3 participants reported between 1.4 and 2.5 fractures per metre. If we apply Zeeb's recommendations, the cumulative length of scanline for the person who reported a lower number of fractures per metre would need to be nearly twice the length (160m) of the representative scanline for the person reporting higher fracture numbers (90m). The number of fractures in Circle 5 reported for window sampling ranged from 13 to 56, which means between 2 and 9 circles of this size would need to be analysed to statistically represent the network. The variation between how participants view the fractures therefore results in significantly different lengths of scanline or numbers of circles to capture a representative sample of that network. Our data show that there is not a great degree of difference in the time taken by participants to characterise the same fractures network, albeit with different detail. However, the simple fact that one geoscientist needs to find over 4 times more locations to draw out circles of the same radius on a particular outcrop will likely mean that collecting equivalent datasets may take longer for a less detail-oriented participant. Where a detailed-orientated operator may fall down, however, is when a fracture network displays a degree

of heterogeneity or clustering. In this case, although a detailed-orientated operator would report the required number of fractures according to Zeeb et al. (2013), they may fail to cover enough ground to understand the spatial distribution of fractures the way a less detail-orientated operator would.

The appropriate *radius* of the sample window is also dependent on the sampling behaviour of the operator. For circular scanlines it is widely agreed that a minimum of 20-30 fracture terminations within a circle is appropriate to derive fracture statistics or undertake topological sampling, and the circle radius must be adjusted to capture enough fractures or fracture terminations (Rohrbaugh et al., 2002; Procter and Sanderson, 2017). Figure 3.10 shows the proportions of valid (capturing >30 terminations) and invalid (capturing <20 terminations) results for the circular scanlines in this study. Out of the 29 participants that collected data from Circle 8 in the workshops, 12 identified over 30 fractures and so report valid results, another 8 collected over 20 fractures and their results are potentially valid, whereas 9 valid reported fewer than 20 fractures and so the statistics derived from their sample may be unrepresentative. Since the number of fractures identified in the field is generally higher than in workshops, a greater proportion of field participants reported sufficient terminations within the circle to be statistically valid. For example, all field participants report valid data for Circle 4, whereas only 3 of the 9 groups in the workshops do.

In this work, the location and radius of all scanlines except C6 were selected by Participant G/11, who tended to be more detailed than other participants. This participant recorded enough terminations to class their data as valid for all sampled circles. Therefore, this participant chose a circle radius appropriate to the level of detail to which *they* identify and characterise fractures, but which is not appropriate for other less detailed observers. This effect is demonstrated in Figure 3.11, which shows a synthetic fracture set interpreted by an operator who gathered less detail-focused observations (Figure 3.11a) and an operator who gathered more detailed information (Figure 3.11b). A statistically valid circular scanline (>30 fracture terminations) is drawn onto the interpreted network and the resulting differences in the fracture topology and the fracture statistics shown (Table C inset). For this example, for the scanline to be statistically valid, its radius must be 3 times larger for operator (a) than operator (b).

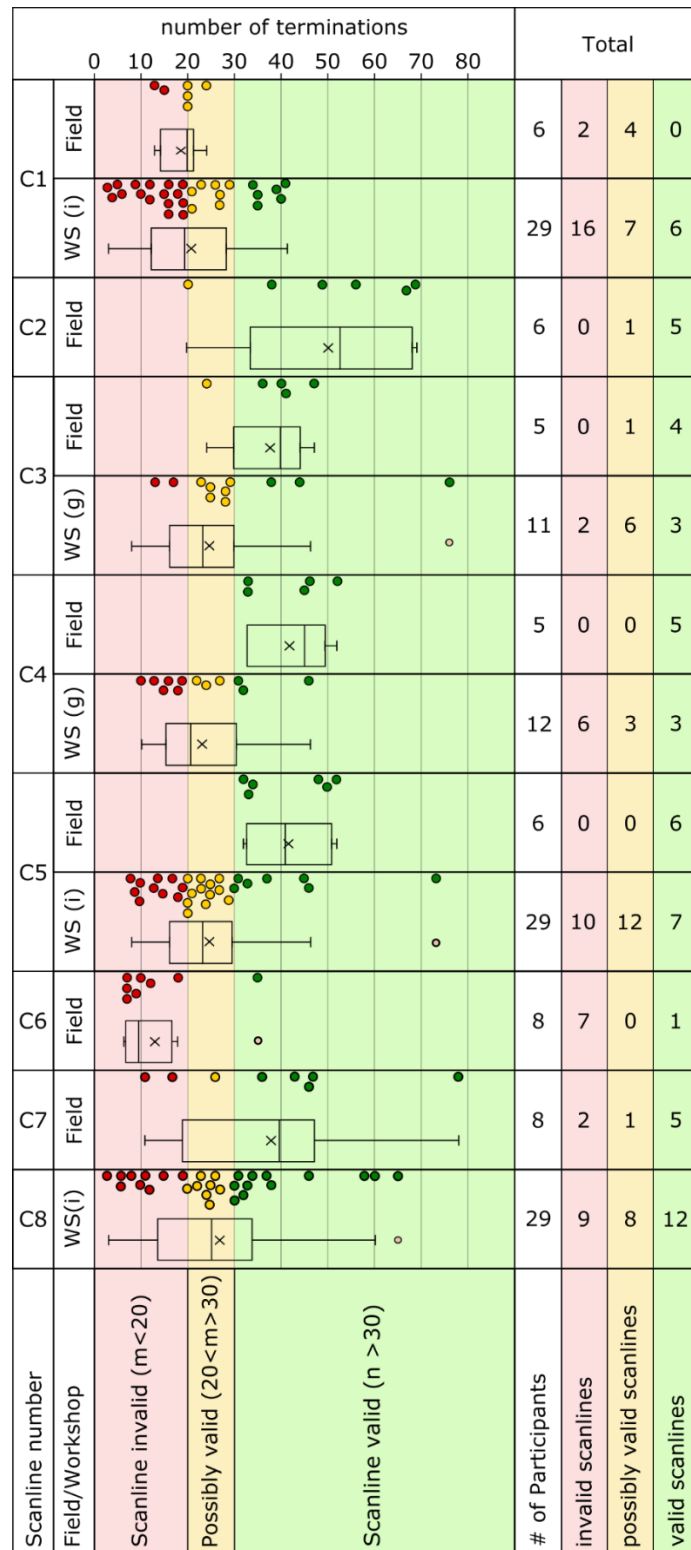


Figure 3.10: The effect of subject bias on the validity of circular scanlines. The number of terminations recorded by individuals or groups is displayed for each circle and colour coded depending on where a valid (>30, green), possibly valid (20-30, yellow) or invalid (<20, red) number of terminations were recorded.

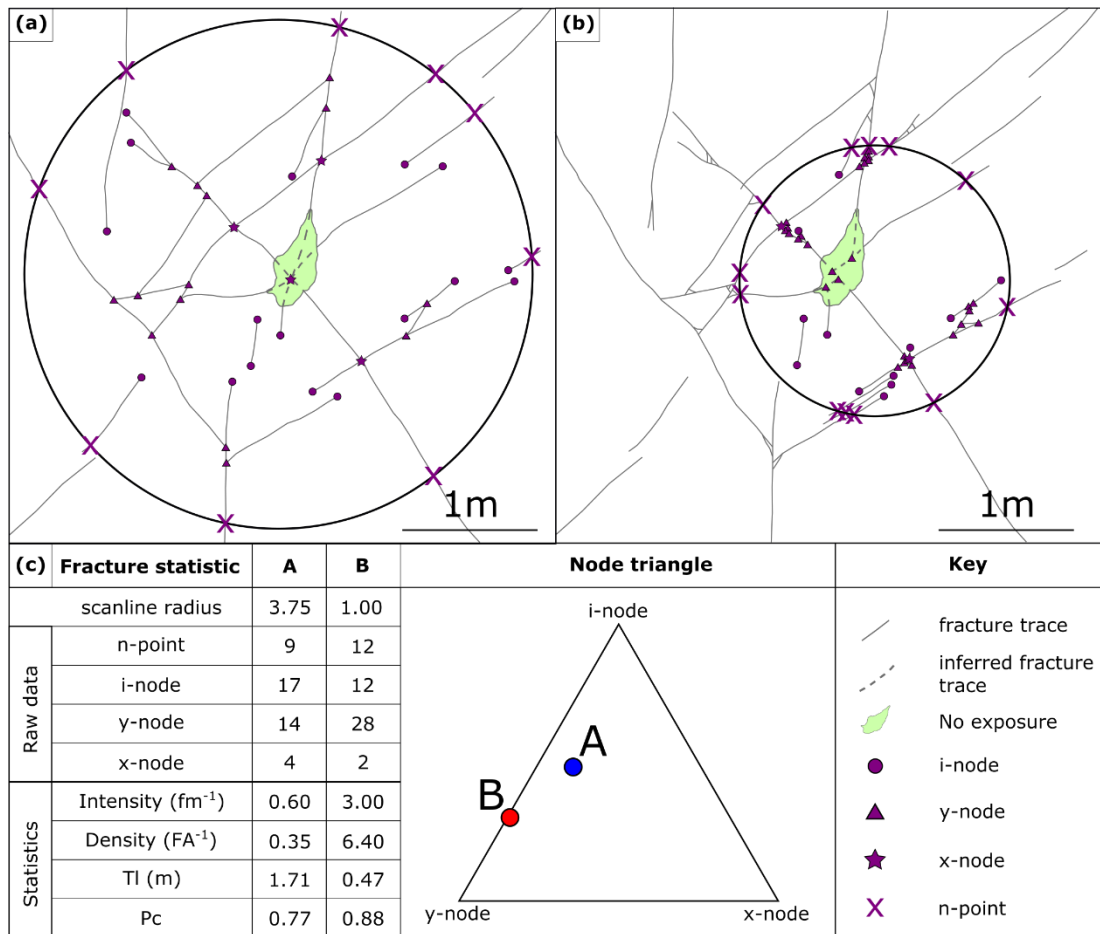


Figure 3.11: The impact of interpreter style on fracture statistics of a synthetic fracture network. (a) statistically valid topological sampling within a circular scanline for a fracture network which only considers the large scale fracture network. (b) statistically valid topological sampling within a circular scanline for the same large scale fracture network as (a), however, also capturing small scale fractures at fracture intersections. (c) The topology attributes (n, i-, y- and x-nodes), derived fracture statistics and node triangle of the different interpretations of the fracture network.

How detailed a fracture network is interpreted to be by an operator therefore affects the derived fracture statistics (Figure 3.11c). The more detail focused interpretation (Figure 3.11b) has more y-nodes, but similar counts of n, i-nodes and x-nodes. As a result, the connectivity of the interpreted network in part (b) is greater than that in part (a). The other fracture statistics (intensity, density and trace length) are very different between different levels of interpretation detail. For example, the density of fractures in part (b) is over 18 times larger than that of part (a) and mean trace length reduces from 1.71 m for part (a) to 0.47 m for part (b). This variability is primarily due to the required circle radius, which is used to calculate fracture statistics using circular scanlines (Table 3.1), changed in order to capture the minimum number of fracture terminations. For our data, if participants who

recorded insufficient fracture terminations in their samples (i.e. less than 20) to be considered statistically valid are disqualified (i.e. removed from the dataset), the maximum trace length and density are more affected by subjective bias than the fracture intensity and connectivity. For example, the calculated maximum trace length for Circle 8 decreases from 2.88 to 0.92 m, and the maximum density for Circle 5 decreases from 46.5 to 12 f/A.

Different fracture data collection methods are chosen depending on the aims of the study, the way the fracture network is presented within the outcrop (or core) and the homogeneity of the fracture network. Our data suggest that window sampling is the least effected by subjective bias. In the process of drawing out the fracture network, the operator is required to consider the fracture geometries, evidence for fracture timing (e.g. cross-cutting mineral fill types), and the implications of this for the fracture statistics. There may be similarities with the findings of Macrae et al. (2016), who showed in a randomised controlled trial of industry experts that the quality of a seismic interpretation could be increased by explicitly requesting interpreters of seismic data to describe the temporal geologic evolution of their interpretation.

3.7.2 Causes of subjective bias: operator bias and fracture network characteristics

Human factors: We observe considerable variability between participant's interpretations, something which has also been observed by Peacock et al. (*in press*) in the reported values of joint intersections on a bedding plane, additionally our data shows individuals display a degree of internal consistency (Figure 3.3 and 3.4). That is, individuals exhibited personal characteristics or traits through the data that they gathered: they were either more detail-orientated, or they were less detail-orientated.– allowing them to focus on gathering a larger volume of data. We suggest that this reflects an operator's personal approach to data collection: variability in data that is collected by a single person is likely to be internally consistent from one data-gathering exercise to the next. Care therefore needs to be taken when comparing results from different operators. Our data shows it is important to consider whether you are working with a 'detailed' person who will likely wish to include data on smaller/more detailed structures, or if you are working with a person who is more likely to focus on 'the big picture' and to gather a higher volume of data from a greater number of sample locations in the same amount of time.

It is interesting to consider why people tend to be internally consistent in their data gathering approach, yet different from each other. It is likely that they consciously or

subconsciously construct their own protocols around how the data should be collected, and what features should or should not be included. These protocols will be shaped by: (a) Practical and physical factors such as the quality of an operator's eyesight, whether or not it is easy for them to repeatedly crouch down to get a closer view and stand up to move around, spatial co-ordination that affects the ease with which they cover the scanline, and the time available to gather the data; (b) Inherent cognitive or personality-related factors.

As an example, some participants focussed only on more pronounced fractures, ignoring, for example, smaller subsidiary fractures, closed or filled fractures, or thin 'hairline' fractures intersecting the scanline. This behaviour was particularly common where a large or clear fracture is present; the participant reports only the dominant feature. As one participant exclaimed during group discussion "*What do these tiny things matter - if you have a massive fracture?*". However, this viewpoint was not shared by all participants: others raised the importance of the spatial distribution of small fractures either as indicators of strain incompatibility, or as the locus of flow at fracture intersections. It is clear that decisions about "what feature counts" and whether a feature has geological origins are subjective judgements. Shipton et al. (*in press*) and Gibson et al. (2016) discuss the concept of Mental Models in the geosciences: a mental model is a simplified internal representations of some external event or process. We suggest that our participant's mental model of the processes that they are measuring may guide their attention to particular features, and so obscure or censor the network that they record. The mental model, and therefore the features – or scale of features - observed, may also be influenced also by the intended application for collected data (Shipton et al., 2019), or the conceptual model that the participant is working to (Shiple and Tikoff, 2016).

While one may expect mental models be shaped by the experience levels of operators, this is not observed in our dataset. Scheiber et al. (2015) studied different participants' observations from a single LiDAR dataset, and found no correlation between experience and the reported number of bedrock lineaments. Similar to our work, Scheiber et al. (2015) found that participants who reported the largest number of lineaments observed the greatest number of small features, and these small features often did not follow the main orientation trends seen in the data. Biological studies also find no evidence for a relationship between level of experience and the detail or observations (e.g. Dickinson et al., 2010; Dunham et al., 2004).

We suggest that the cognitive style of the participant is more important than experience in how a participant interprets the studied media; the fracture network. Cognitive style refers to how an individual perceives, thinks, solves problems, learns, makes decisions and interacts with others (Witkin and Goodenough, 1977). The work of Carl Jung (2016, *original work published 1924*), particularly the use of the Myers-Briggs Type Indicator (Myers, 1962) to assess cognitive style, underpins much of this field. Jung's theory outlines three facets of cognitive style, each with end-member preferences (Myers et al., 1998): *Perception* dictates whether a person is either meaning-oriented (*intuitive*) or detail-oriented (*sensory*); *Judgement* dictates whether a person makes decisions based on analytical and logical means (*thinking*) or through a set of personal values (*feeling*); and *Environment* dictates whether a person reacts to immediate and objective conditions (*extrovert*) or by looking inward to their internal and subjective reactions (*introvert*) when reacting to their environment. On top of these three facets, people often have an innate preference for either *perception* or *judgement* trains of thought such that a perception person has a tendency to use sensing and intuition orientated thought, while judgemental person uses a combination of thinking and feeling. It is well known that cognitive style can have an impact on how people both respond to stimuli and make decisions (Jung, 2016, *original work published 1924*). If a cognitive style is at odds with the task in hand, for example where an intuitive participant is required to undertake a detailed task which would be better suited to a sensory participant, a lower performance is to be expected (Chan, 1996). This has been reported in the case of auditors (Fuller and Kaplan, 2004) and air traffic controllers (Pounds and Bailey, 2001). A 'cognitive culture' is often observed in different professions and roles, where people aim to fit their cognitive style to the task or workplace environment (Armstrong et al., 2012). A misfit between cognitive style and the task tends to be associated with lower performance levels (Chilton et al., 2005).

While cognitive styles may not be clear-cut (e.g. Peterson et al., 2009), it is useful to adopt end-member styles to consider how the cognitive style of the data collector could, in theory, affect the fracture data they collect. For example, a *sensory* participant should show a high attention to detail, often observing small fractures and subtle features of the fracture network that may tend to be missed by intuitive participants. Conversely, while an *intuitive* participant may not record small features, they should update their conceptual model more frequently in response to new observations (e.g. a specific orientation of fracture is consistently mineralised), leading them to develop a more robust conceptual

model of the subsurface (Shipley and Tikoff, 2016). A *thinking* participant may collect more consistent or transparent data than participants with other cogitative styles, for example, by developing and applying a set of logical and analytical rules.

The node data collected in our study is most consistently affected by cognitive biases (Figures 3.3, 3.4 & 3.6). Detailed-orientated participants reported a greater number and percentage of y-nodes compared to i- and x-nodes. One of the underlying reasons for this was identified in the workshop discussions, where sensory-type participants described reporting the small fractures at fracture intersections, whereas intuitive-type participants reflected that they did not report these features, since they believed (i.e. interpreted) that they would not contribute to flow. Similarly, jogs in the fracture were classified systematically differently by different participants, where some considered jogs to be the termination a fracture and initiation of another fracture, whereas others considered jogs to be a slight side-step of an otherwise continuous fracture. This would have consistently affected the number of nodes reported.

Working in groups: We observed that behaviour varied considerably between groups, and that the behaviour of groups depended on the cogitative styles of individuals within that group (pairs, in most cases). For example, in one group a participant explained *“[when we started working together] I very quickly ...realised that [their partner] cares about tiny features, so, together we cared about tiny features...but I was aware that if I was working on my own, I would have done it differently”*. This group evidently consisted of participants with different levels of detail-orientated behaviour, and the participant who individually displayed a less sensory cogitative style tended towards the level of their partner. This is perhaps an example of herding behaviour (c.f. reference), often herding towards a more detailed approach. Another participant reflected *“I didn't find we [their group] were talking about 'does this fracture count?'. Instead, we were discussing whether something was a Y-Y or an X, or where exactly a fracture goes or where it terminates and so on”*. This group appears to be made up of two in intuitive-type participants, and worked well together discussing the meaning behind the fracture network.

The very knowledge that you are working together might be effective in itself. As one participant articulated *“the very knowledge that you are working with someone changes your approach. You want to engage together and so you need to defend or explain your choice, which makes you more alert to what you are doing and why”*. This suggests that for

fracture analysis a group comprising of different cognitive styles could be advantageous in terms of capturing the range of perspectives and potential interpretation styles. Fracture network analysis is not simple; it requires not only the identification of fracture traces, but also a consideration of how these fractures traces from a network (Peacock and Sanderson, 2018). Parallels may be drawn to the findings of Cheng et al. (2003), who found that when participants were asked to complete a complex accounting task, groups comprised of different cogitative styles outperformed homogenous groups. That said, working in mixed groups can be a cause of conflict and introduce errors due to a negative effect on the ability to reach a consensus in the decision making process (Aggarwal and Woolley, 2013). In our study, some participants felt that working as a group slowed down the data collection process to a problematic degree. However, this was only observed in WS1; the sampling time was comparable for individuals and groups in WS2 (Figure 3.3, Table 3.5).

Interestingly, there are many different interpretations of what 'working together' means, or shapes that working together takes. While for many, this meant working through the scanline together, others elected to divvy-up the window or scanline, working separately and combining their results at the end, or for one person to be the data gatherer, and the other the data recorder (i.e. the scribe). For the latter two models of working, the potential benefits of discursive or deliberative group work (i.e. rationalising and laying bare thought processes) will not be leveraged.

Projecting into areas of limited exposure. The effect of subjective bias on the required length of linear scanlines, radius of circular scanlines and area of sample windows will have particular consequences in areas of limited exposure, where a detail-orientated operator may not be able to collect enough data to statistically represent the fracture network. In the discussions following WS1, several participants reflected that where exposure was limited or obscured, they did not attempt to interpret where the fracture went, nor the type of fracture intersection, since this was straying too far from quantitative observation into more qualitative interpretation. Other participants, however, did interpret the network despite these difficulties, which increased the number of nodes that they reported and decreased the number of illogical 'floating' nodes. Clearly some felt it was most appropriate to interpret in the face of uncertainty, so as not to discount nodes that could be logically inferred, while others felt that this would be over-interpretation. Both viewpoints have internally consistant reasoning, but will produce very different outcomes in terms of fracture network characteristics to be applied to analyses of fluid flow or rock strength.

In some cases, these uncertainties could easily be overcome in the field. For example, where a fracture was obscured by shadow or seaweed. Some field participants described 'feeling' for the trace of a fracture with fingers or pencils when obscured (e.g. by seaweed), or difficult to see. Some also describe inferring fracture trace by extrapolating from the exposed traces, triangulated by observing the general fracture trends. Such 'exposure bias' is recognised when studying fault zones, where, by their nature, the fault rocks are often preferentially obscured and therefore good continuous exposures of fault zones are very rare (Shipton et al., *in press*).

The scale of observation: In the workshops, participants were provided with a 2D 'birds eye' view of the full circle being sampled. In the field, only the tallest operator will be able to observe the full circle, while all others would have a more limited field of view. In the field, the participant can potentially crouch down and 'get their eye in' to the detail within a complex fracture network. The ability to adjust the scale of observation during data collection in the field is most likely the reason for more nodes reported in the field than in the workshop for the same circular window (Figure 3.10). Similarly, it is important that the same scale of observation is maintained when using remote sensing methods. For example, it is important that an operator does not zoom into areas of interest, unless they do so systematically.

Using pre-set data cut-offs: It is clear that a meaningful quantitative analysis of fractures requires a certain degree of consistency. This is particularly relevant for combining or comparing data collected by a number of individuals, including for meta-analyses. Participants in WS1 discussed whether their collected data could be more readily compared or combined if a minimum trace length cut-off was applied to the data. However, no consensus could be reached about the scale of or style of the cut-off to be applied because (i) it would not be an accurate representation for flow and/or rock strength; and (ii) more attention should not be paid to simpler, larger, and more isolated structures that could have almost no flow or mechanical significance. The use of size cut-offs has been used in scanline studies which investigate aperture size distribution (e.g. Hooker et al., 2014; Ortega et al., 2006). Fracture trace length however differs from aperture studies in that what you are measuring (the number of fractures) is not a clearly defined parameter (i.e. aperture size) but instead highly subjective. This stems from the fact that most opening mode fractures show evidence of growth through the linkage of several smaller fractures,

and, due to the fractal nature of fractures, a single fracture tends to be comprised of several smaller fractures (e.g. Bonnet et al., 2001), and so the fracture count is dependent on the scale of observation. We observe similar effect in our dataset, where participants differ in their interpretations of where a fracture starts and ends, and whether fractures with jogs should be classified as one continuous feature or multiple fractures.

Another knock-on effect of having no data cut-off is that the derived statistics for *fracture intensity* or *fracture density* from reported data can return wildly differing results (Ortega et al., 2006). From our findings, it is clear people 'self-censor' according to a minimum trace length, and this minimum cut-off is variable in scale. That said, we find that the range in reported values decreases towards 10 to 15% of the diameter of a circular scanlines or window sampling. For example, for Circle 8 data (S8), the range in the number of reported fractures is 36, however, when fractures <5 cm trace length are removed the range falls to 19. The range stabilises if only fractures >10 cm length are considered. This effect is amplified for fracture density, which is calculated using the number of reported fractures. The raw density statistics range by a factor of 3 (23 to 69 f/A), however, as you apply cut-off's to the data the values decrease and converge so that when all fractures less than 10 cm length are removed, the difference between minimum and maximum values reduces to 1.3 (18 to 25 f/A). This suggests that it should be possible, depending on the aim of the study, to apply a cut-off to the minimum trace length included in the dataset, however, it is vital that this approach is reported, otherwise the data reported will not be replicable.

3.7.3 Recommendations for reducing subjective bias

We encourage reflective critique of the fracture data collection process, including identification of potential uncertainties when collecting new data, and when collating or comparing fracture statistics from different field studies. Drawing on our results, we propose the following approaches to assess, reduce, and report the potential subjective bias in the data that geoscientists collect:

1) Understand your style of data collection: It is vital that when collecting fracture data, either in the field or from photographs (or e.g. remote sensing), that the 'go to' style of data collection is understood; i.e. detail-orientated vs data volume orientated approaches. In relatively homogenous fracture networks a detailed operator will characterise a network quicker as less circle is required (i.e. detail-orientated will be preferable). In areas of regional heterogeneity, however, it is better to undertake more circles covering larger

fractures (i.e. be more data-orientated). Finally, but most importantly it is vital that we report our own biases and methods used to reduce bias in the field reports, to enable replicability and comparison of studies.

2) *Select your fracture data collection methods to limit subjective bias:* While all methods of collecting fracture data are susceptible to subjective bias, we find that window sampling is the least effected. The approach does not take much longer than topology sampling (the time taken is on par with topology sampling when working in groups, and <1.6 times as long as topology sampling when working individually,). Thus, we recommend that, where possible, a window-sampling approach is adopted to collect fracture data. In addition, regardless of which approach is adopted (circular, window, linear), the fracture network should be traced out; either on a printed photograph/tablet or with chalk on the outcrop. Doing so for at least some of the sample windows would allow participants to examine their own biases in how they classify fractures, and critique their collection approach. Since we find that the window radius, to some extent, governs the size of the fractures observed and reported by different individuals, we recommend that, if using circular scanlines, the radius of the circle is kept the same across a sample area since we find that the circle radius, to some extent, governs the size of the fractures observed and reported. However we recognise that this could be problematic in areas of drastically different fracture intensities where a 'valid' circle size for one sample location would not collect valid data at other locations.

3) *Define what fracture features to include early on:* Prior to the collection of field data, or as the first step of field data collection, the sampling strategy should be reflected upon and agreed, in line with the goals of the study and the characteristics of the locality. For example, in fluid flow studies it is vital that information for all *connected* fractures are included in the dataset, in which case, the location of small fractures that contribute to the network becomes key: simply stating this may induce people to focus more on the small features (c.f. Macrae et al., 2016). The spatial distribution, not just the relative percentage, of fracture terminations within a network should be assessed and recorded when reporting fracture statistics. In the case where small fractures may be important, then it is important that all the observed fractures are collected, however, sub-sets based on fracture trace length should be used when comparing data. One could take the approach that everything should be collected and only after collection should the data potentially be censored for the

purpose of further analysis (e.g. to investigate the intensity of fractures above a certain trace length). However, not every sampling campaign necessarily needs the same level of detail, and so adopting this approach could lead to the collection of a large amount of unnecessary data as a function of campaign goals. If the level of detail collected is superfluous to the needs of the study, the overall data quality could suffer in terms of the extent of outcrop studied (i.e. the number of detailed sample windows completed over a given area is less than the number that would have been completed if the level of detail relevant to the study was collected).

4) Agree how to address data collection in areas of limited exposure: We recommend that operators take steps to ensure that the fracture network they collect is complete (i.e. all node types have the correct number of branches and the counts of parameters are checked) and consistent with the network observed in areas of full exposure. This could be achieved through the extrapolation of trends from outside the sample area, or through ensuring the consistency of the network within the sample area (e.g. are EW trending joints consistently connected to NS joints by y-nodes?). It is important that areas of no exposure (see Fig. 7d) are interpreted as best possible, otherwise estimates of trace length and connectivity will be unrepresentative of the network. This approach is also important as it enables the operator to gain further insight into the development of the fracture network: for example, a better understanding of the age relationships between fracture traces (Procter and Sanderson, 2017). If this is completed as the first step of fieldwork, sources of counting errors can be identified and minimised. Regardless, the sampling or counting error identified should be communicated as part of the data reporting.

5) Where possible, collecting fracture data from field exposures is preferable to interpreting field photographs: We find that there is less variability in fracture data collected by different participants when data is collected in the field, rather than collected from field photographs. Field-based observations have a number of advantages over photo-based approaches: the operator can change position and distance for more complex fractures, remove obstructing material, adjust so that something isn't in shadow, physically feel for the fracture, check if a feature rubs off, or if it is continuous into another plane of the outcrop. A further advantage of collecting data in the field is the ability to look outside the sample area, to ensure that the fracture network within the sample area is consistent with the wider network, and to enable kinematic data to be collected. A caveat to this

recommendation is that in the field the quality of observations can be negatively affected by environmental factors (e.g. rain, cold, heat etc.) which are not encountered during analysis undertaken in the office. Recording such factors and the likely effect on one's field approach is good practice.

6) Working as a group: Working as a group is preferable to working individually to collect fracture data, since we find less variability and fewer inconsistent nodes in data collected as groups. However, group work should be considered a collaborative and dialogic process, where participants discuss their rationale or reasoning before, during and after data gathering, as opposed to divvying up tasks to be completed individually in a team. In the former, working together allows for the identification and reconciliation of differences in interpretational approach, while improving the mechanics of the data gathering, thereby reducing the potential for subjective bias by increasing the detail of observations. The quality of the data collected will be more consistent as a result. In line with this, a group comprised of different cognitive types is preferable. In particular, sensory-type operators should be paired with intuitive-type operators, and encouraged to work collaboratively to tease out whether and how the detail observed by sensory participant is identified and interpreted. The level of geological experience is not relevant to consider when selecting groups, but the relationship dynamics within the group should be managed such that the less experienced individuals feel comfortable to actively discuss with those more experienced than them, rather than simply consent to their views or defer to their judgement.

If data are to be collected separately and then combined, then the sampling behaviour of members of the team should be assessed prior to data collection to establish if data from the individuals can indeed be meaningfully combined. The sampling strategy should be conceived such that the minimum number of moderate-scale, obvious, fractures should be captured (i.e. when using a circular approach, the radius should capture 20-30 terminations of the major fracture sets), with the small fractures still recorded. If conducting collaborative fieldwork, where operators are working individually to collect data from different sampling sites, the team must first characterise their own biases, then agree on a unified approach and classification system, the process of determining sample location and dimensions, and what to do when, e.g. a particular fracture intersection is obscured. It is

important to characterise the way participants differentiate fracture terminations and distribution of reported trace lengths.

7) Define a data cut-off: Because all fractures larger than 10 to 15% of the circle diameter are typically well defined by all data gatherers, all data above this size can be confidently compared between operators with different fracture judgements. The circle radius should be set and reported on prior to the start of the collection of field data. It is vital that the scanline is large enough to cover enough fractures for the least detailed-orientated member of a group to still collect sufficient number of fractures. We recommend that the scale of observation is kept consistent throughout the survey and if a minimum fracture trace length cut-off is chosen that it is clearly reported in field reports and publications.

The procedure could be further improved, and tested through either (a) using a set of calibration scanlines prior to data collection to test personal biases and familiarise the operator with the technique or (b) have a scanline, or sample area which is used as a marker and completed regularly throughout data collection procedure to test replicability, as also advised by Peacock et al., (*in press*). While the above procedure outlined above is undoubtedly helpful and goes some way to providing consistency in fracture data collection, it also does not take into account that behaviours may change through time (e.g. Scheiber et al., (2015)). Such changes may be due to such things as experience of the data gathering procedure, experience of trends in the fracture network being classified, subsequent training (e.g. the introduction of minimum trace length cut-offs) or when undertaking fracture data collection with differing survey goals (e.g. paleo-stress analysis vs fluid flow studied). Due to this the procedure should be repeated regularly and assigned to 'single events' such as a day in the field or a single data collection session.

8) Communicate the steps taken to manage bias in data collection: Steps one to seven should be communicated as part of data reporting and publication.

3.7.4 Wider geoscientific implications

While this work concentrates on a 'field-based approach', which uses several 'data points' (sampling areas) to collect data from outcrop, many of our findings are also relevant to the collection of data from broad scale approaches such as UAV or remote sensing derived maps. With the advent of digital-image analysis techniques and UAV technology, it can

seem preferable to perform digital fracture mapping, however, uncertainties regarding, say, hairline fractures, potential weathering features, or vegetation obscuring the fracture network can be more easily explored by direct field observations. While one may expect marginal error, which is a function of the sample size, to be reduced by digital fracture mapping, since digital mapping allows for a much larger number of (and area of) fractures to be sampled in a given time. We instead suggest this to not be the case because each participant is in effect using their own method to identify and classify features on the digital image being studied, many of the subjective biases that we observed in our work will be applicable to remote mapping methods. This corroborates work by Scheiber et al. (2015), who investigated the number of lineaments identified by six participants interpreting the same LiDAR dataset (at the same resolution). Extreme variability was observed between participants, who counted between 74 and 607 lineament traces (COV = 1.61). Indeed, concern about consistencies in image interpretation was raised in early work on remote imagery; Huntington and Raiche (1978) suggested that inter-operator variability in the interpretation of lineaments from LANDSAT imagery could be so significant that it may seem as if different scenes with different geologies had been interpreted.

In this work, we have demonstrated, for the first time, the clear need for geoscientists to develop consistent and transparent protocols for collecting field data that is scientifically rigorous. We find that the type and scale of subjective biases that affect how we identify, classify, and report on fracture characteristics are independent of experience, and appear to be related to personal character traits. It is vital that the geoscientific community become more aware of the potential for subjective bias, the subsequent effect on scientific uncertainty, and options to manage biases. Indeed, we feel that these issues should be discussed openly from the very first time that students collect field data. Training schemes and procedures should be developed that not only consider the relative differences between methods (as in Watkins et al., 2015) but also the inherent human factors which effect data collection. These schemes will differ based on the specific aims of the study, however, approaches to manage subjective uncertainty in data must be communicated openly so as to enable the study's findings to be replicable, and to facilitate comparison with other field data.

In fact, we propose that a series of reasoned recommendations or protocols derived from and adopted by the scientific community could prove valuable to streamline the data

collection process and reduce the uncertainty in observation-based sciences. The recommendations for field-based fracture data collection may be different to those for remote sensing images. Any such workflow should not be so prescriptive as to be inhibitive, or to limit the scope of study, however, should be supportive enough such that the results obtained by the adopted method are replicable. Since the type and scale of subjective bias is independent of the level of experience or expertise, a suitable workflow should enable crowd sourcing or citizen science to be a useful medium for fracture data collection and analysis in such a way that is commonplace in ecological studies (Dickinson et al., 2010). Indeed, our work has implications beyond the geoscience discipline; for example, to garner maximum potential from Big Data, these subjective uncertainties and any protocols to manage them must be reported. However, our work also demonstrates the clear need for further work in this field, to test the effects of subjective or operator bias on the collection of fracture data, both in the field and using maps generated from remote sensing, in addition to investigating the role of subjective bias in other forms of geological data and beyond.

3.8 Conclusions

In Arthur Conan Doyle's *Silver Blaze* (1892), Sherlock Holmes states "I only saw it because I was looking for it". We observe that this behaviour may be common in geoscience data collection and has the potential to impart subjective biases in the data collected, introducing uncertainty in the geological information derived from these data and potentially affecting the ability to replicate studies. We demonstrate that geologists' own subjective biases influences the data they collect, and, as a result, different participants collect different fracture data from the same scanline or sample area. This has consequent effect on the fracture statistics that are derived from these data and that are used to inform geological models. Although we find that participants can collect a range of data, we observe internal consistency in the classification of and number of fractures gathered by each participant. This consistency is not related to geological expertise or experience, nor the time taken to complete the scanline, so we propose that the underlying control on the subjective bias relates to the individual's personal characteristics (detailed vs pragmatic) and also the process that the data will inform (bulk fluid flow? Scale of relevant observation?). Major fracture sets tend to be captured by all participants, and so the subjective bias mostly affects the smaller-scale fracture features. We find that the effect of

subjective bias on the fracture statistics derived from the observed fracture attributes can be large, and that trace length and fracture density are the parameters that are most susceptible to subjective bias.

The subjective biases in how features are identified, classified, and reported have implications for how data should be collected and collated. Firstly, for the characteristics of a fracture network to be statistically valid, a circular scanline should aim to capture a minimum number of fractures in its area, and the radius adjusted to ensure that these conditions are met. However, to meet the necessary validity criteria, individuals who pay particular attention to small features could potentially use a circular scanline with much smaller radius (and consequently, can collect data from smaller outcrops) than individuals who tend to dismiss small fractures. Secondly, by comparing fracture data collected in the field and from field photographs, we find that if possible fracture data should be collected in the field, where the type of connections present can be examined in more detail.

Drawing on the quantitative and qualitative data in this study, we propose a series of methods for managing subjective bias. As well as supporting individuals to understand – and so mitigate - their own biases, there are other practical steps that can be taken. For example, we suggest that the perceived fracture network should be drawn out, either onto printed field photos or using a tablet computer, to minimise bias by prompting the operator to consider and report the trace length distribution and network topology. Doing so also records not just the number of terminations and individual trace lengths, but also where in the scanline/are the values recorded, and also makes clearer the rationale behind the interpreted fractures. For similar reasons, we also propose that people should work collaboratively in (small) groups when gathering fracture data, and preferably with people who have different personal characteristics to them. A series of protocols could be developed to streamline fracture data collection and reduce uncertainties introduced by subjective biases, but, ultimately, the steps taken to manage bias in data collection should be communicated as standard during data reporting and publication.

This study is the first to quantitatively illuminate and discuss the scale of and potential causes of subjective bias in the collection of geological field data. As the implications of our findings has relevance for a range of observation-based sciences beyond geoscience, from digital mapping to Big Data, our study is, ultimately, a call for further work in this area.

Chapter 4: The role of lithology and bed scale heterogeneity on fracture trace length and topology. A case study of the UK Carboniferous Coal Measures.

Billy. J. Andrews^{1*}, Zoë Cumberpatch², Zoe Shipton¹, Richard Lord¹

¹Department of Civil and Environmental Engineering, University of Strathclyde, 75 Montrose Street, Glasgow, G1 1XJ, UK

²SedResQ, School of Earth and Environmental Sciences, University of Manchester, 176 Oxford Rd, Manchester, M13 9QQ

4.1 Rationale

The interaction with stratigraphic layering and fracture networks is well known, and many studies have investigated the relationships between bedding and joints. Many interbedded clastic successions however contain abundant sub-bed scale heterogeneities that include sedimentary structures (e.g. channels, coals and rootlets) or discontinuous sandstone and mudstone interbedded laminations. During fieldwork with BJA and ZC the relationship between small, sub-bed scale, sedimentary features and the joint network at Whitley bay, Northumberland (UK) was recognised. Following the award of a Geological Society research grant additional fieldwork enabled the sedimentary succession and mechanical stratigraphy to be classified at both a bed- and sub-bed-scale. This was then used as a framework to investigate the geometrical and topological properties of joints and how these relate to lithology and sub-bed scale heterogeneity. BJA prepared the text and figures in the chapter, with all authors involved in the editing process.

We find that unlike binary mechanically layered sequences (e.g. sandstone/shale or limestone/marls), the complex sedimentary architecture observed in fluvial deltaic sequences cause joints to usually terminate within beds. A total of six litho-mechanical facies were found, which displayed characteristic properties including: the variability in joint strike and dip; joint height; bed-parallel joint length; and topology. Rebound values display a weak correlation with grain size, with sub-bed scale heterogeneities causing large variabilities to be observed within beds and sub-bed units. These small-scale sedimentary heterogeneities may act as mechanical boundaries, restricting joint propagation, or strength inclusions leading to the initiation of joints. We suggest because sedimentary

architecture can be predicted and sampled through vertical boreholes, while fractures are typically poorly sampled, that sedimentary information can be used to inform likely fracture properties. This is of particular interest to several industry applications including the extraction of natural gas from the Southern North Sea and the ability to de-risk shallow mine geothermal projects.

4.1 Introduction

The interaction of sedimentology and structural geology (e.g. faults and fractures) can combine to complicate a hydrocarbon reservoir, aquifer of Carbon Capture and Storage (CCS) reservoir, mining operation or geothermal project. It is common knowledge that stratigraphic layering effects the way rocks deform through folding (Currie et al., 1962; Chester, 2003; Edmunds et al., 2006); faulting (Fischer and Jackson, 1999; Ferrill and Morris, 2008; Ferrill et al., 2017), and opening mode fractures (joints and veins) (Bai and Pollard, 2000; Ortega et al., 2006; Laubach et al., 2009; McGinnis et al., 2017). A large body of work, driven primarily by the oil and gas industry, has focussed on the interaction of deformation and large scale lithological variations. For example, seismic or gravity data sets have been used to investigate the interaction of large-scale faulting and sedimentary relationships (e.g. Jackson et al., (2002); Leeder et al., (2005)). However, densely spaced faults, fractures, and sub-seismic scale heterogeneities can combine to complicate subsurface datasets (Jolley et al., 2010). These features are often below seismic resolution (typically ~30 m) and poorly sampled by cored wells (e.g. Yielding et al., (1996)).

One way to address this shortcoming is the use of field analogues to collect field data, that can then be used to populate subsurface models (e.g. reservoir models or discrete fracture networks). In fractured reservoirs it is important to quantify the orientation, abundance, connectivity, length, fill (mineralised/presence of gouge) and aperture of fractures within the network in order to help with subsurface prediction. In mechanically layered sedimentary sequences, fracture attributes are strongly layer-dependent and a fracture stratigraphy develops (Helgeson and Aydin, 1991; Afşar et al., 2014; McGinnis et al., 2017). Mechanical stratigraphy is defined as “the rock mechanical properties, layer thickness, and frictional properties of mechanical boundaries which make up the rock sequence” (Ferrill et al., 2017). Mechanically stratified lithologies often develop a fracture stratigraphy whereby layer-specific fracture networks develop that display characteristic fracture style (e.g. dip, curvature etc.), trace length distributions, and intensity of fracturing for each layer (e.g.

bed) of the succession (Laubach et al., 2009). Layer-specific properties vary depending on several factors including the mechanical properties of lithologies which make up the succession, the thickness of bedding, and the interface strength between beds (Laubach et al., 2009).

The role that sub bed-scale sedimentary heterogeneity plays on fracture networks remains poorly understood. This study attempts to improve this by comparing fracture attributes (in particular fracture trace length and network topology) with detailed sedimentary observations in two planes of observation (bed-parallel and section view) and at two scales (bed- and sub-bed). Although we find a strong correlation between mechanical and fracture stratigraphy, we argue that in fluvial-deltaic near-shore sequences fracture networks are controlled by a combination of both lithology and sub bed scale sedimentary features, as opposed to bed thickness alone. With appropriate knowledge of the basin history, it could be possible that predictions of fracture network characteristics (e.g. fracture height) for inputs to subsurface models can be improved through the use of sedimentological information, which is often better constrained. We also argue that small, sub-bed scale heterogeneities (e.g. mud-draped ripples and channel coals) play an important role in the connectivity and trace length of fractures, and that data on sedimentology could be used to inform likely parameters of a fracture network at depth.

4.2 Geological setting

To understand the role lithology and sub-bed scale sedimentology plays on the fracture networks in the field area, it is important to have an understanding of the stratigraphy and depositional history. During the Carboniferous the UK passed northward across the equator, which left predominantly arid deposits during early and late Carboniferous times, with an equatorial climate in-between (Scotese and McKerrow, 1990). Much of this rock record remains due to the development of several late Devonian to early Carboniferous, E-W trending grabens and half-grabens (Cope et al., 1992). These basins formed in response to back-arc extension within the Laurussian plate in response to the subduction of the Theic oceanic plate (Leeder, 1982; Leeder, 1988), with the location and style of rifting strongly controlled by pre-existing crustal structures (Chadwick and Holliday, 1991; Chadwick et al., 1995).

The field site at Whitley Bay is located within the Northumberland Basin (Figure 4.1), a 50 km wide, ENE-WSW trending, half graben which formed in response to the extensional

reactivation of the underlying Iapetus Suture during the mid-late Carboniferous (Johnson, 1984; Chadwick et al., 1995). The majority of deposition occurred during the early Diantian (Johnson, 1984; Chadwick et al., 1993), associated with the deposition of up to 5 km of syn-tectonic sediments (Johnson, 1984; Kimbell et al., 1989; Chadwick et al., 1995). This was followed by minor-faulting and thermal subsidence which continued throughout the Namurian and Westphalian (Chadwick et al., 1993; Chadwick et al., 1995). The Pennine Coal Measures exposed in the Northumberland basin reach ~830 m in thickness and display repeated successions of upper and lower delta plain deposits and interspaced peat beds (Fielding, 1984; Collier, 1989).

Shallowly dipping (5° to 8° to the west) lithologies of Duckmantian (Westphalian B) Middle Coal Measures are exposed in the cliff and wave cut platform at Whitley Bay along a roughly 850 m long coastal section. The lithologies are comprised of fossiliferous and barren shales (55 to 50%), thinly (cm-dm) bedded sandstones and siltstones (48% to 40%), and seat earth and coals (<5%) (Fielding, 1982; Christopher R. Fielding, 1984; Fielding, 1985; Jackson et al., 1985; Lawrence and Jackson, 1986). The depositional environment is interpreted as a broad flat deltaic plain which was cut by multiple distributary channels (Christopher R. Fielding, 1984; Fielding, 1985; Jackson et al., 1985). The rocks exposed at Whitley Bay have high percentage of organic rich layers (~5% in many beds) and exhibit extensive sub-bed scale heterogeneities and along strike variation, particularly in siltstone and fine sandstone units. Such sedimentary heterogeneities include channel coals, rootlets, mud-draped ripples, channelised sandstone bodies and rip-up clasts.

Deformation at the field site is dominated by several faults with centimeter to meter offset, two larger offset faults (Hartley Steps fault zone (HSFZ) and Crag Point Fault Zone (CPFZ) (Jones and Dearman, 1967; De Paola et al., 2005; Færseth et al., 2007)), and two sub-vertical (> 75° dip) joint sets. The area of influence of the two largest faults, were avoided for the purposes of this study. Fracture data collection was limited to opening mode joints, and occasionally fractures related to small offset faults. Joint sets can be split into two sets, one trending generally N-S and another E-W, with some local divergence in trend near minor structures and within incompetent lithologies. This field site is an ideal location to study the interaction of fracture stratigraphy, lithology, and sub-bed scale sedimentary heterogeneity for the following reasons: the shallow dip of bedding; exposures in both plan

view and cross section; abundance of sub-bed scale heterogeneities; simple deformation history; and the well-developed mechanical and fracture stratigraphy.

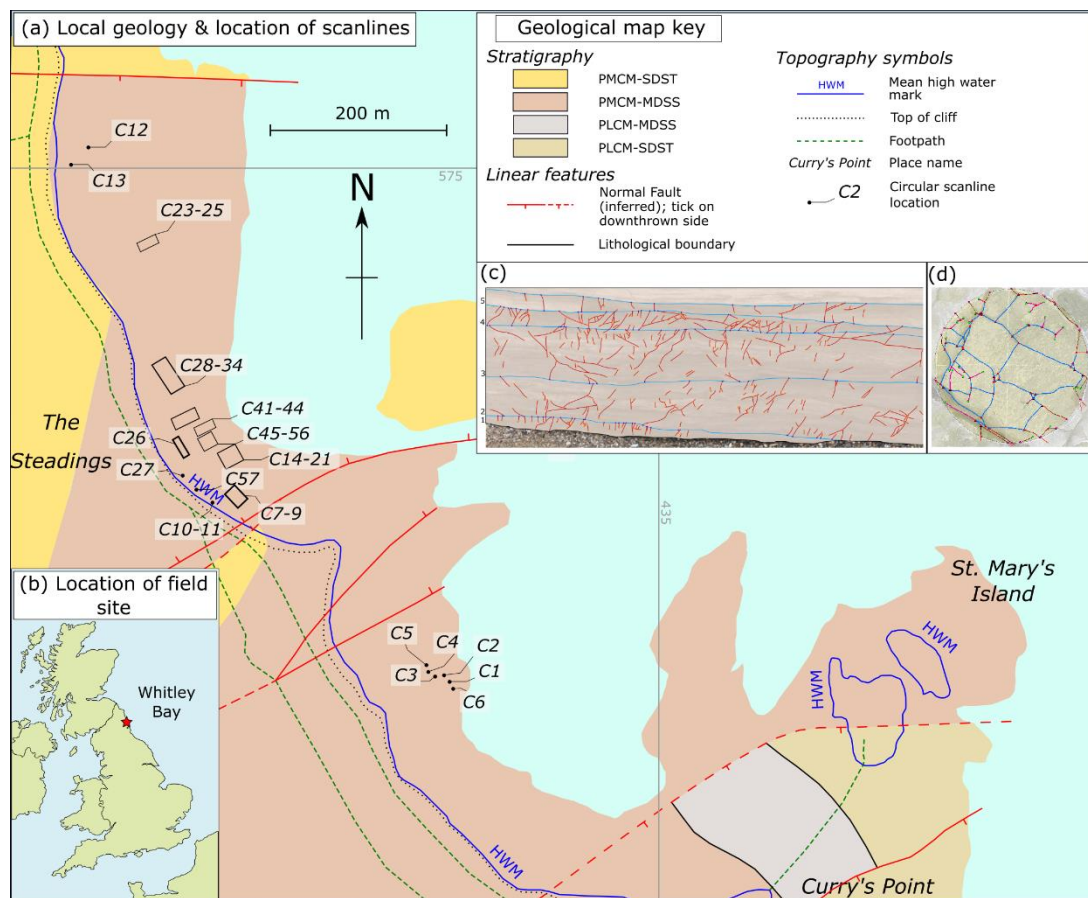


Figure 4.1: Location map, adapted from Andrews et al. (2019) highlighting (a) the local geology and (b) the location of the study area, located near Whitley Bay, Northumberland (UK). Grid lines are annotated with UK national grid numbers. Field photographs of (c) section view (bed-scale) fracture map (S1) and (d) bed-parallel view experiment (Cx) are also shown. The geological map is modified from Geological Map Data BGS © UKRI (2018), where stratigraphy is as follows: PLCM-SDST = Pennine Lower Coal Measures – Sandstone; PLCM-MDSS = Pennine Lower Coal Measures – mudstone, siltstone and sandstone; Pennine Middle Coal Measures – sandstone; PLCM-MDSS = Pennine Middle Coal Measures – mudstone, siltstone and sandstone. For detailed stratigraphy see Figure 4.2.

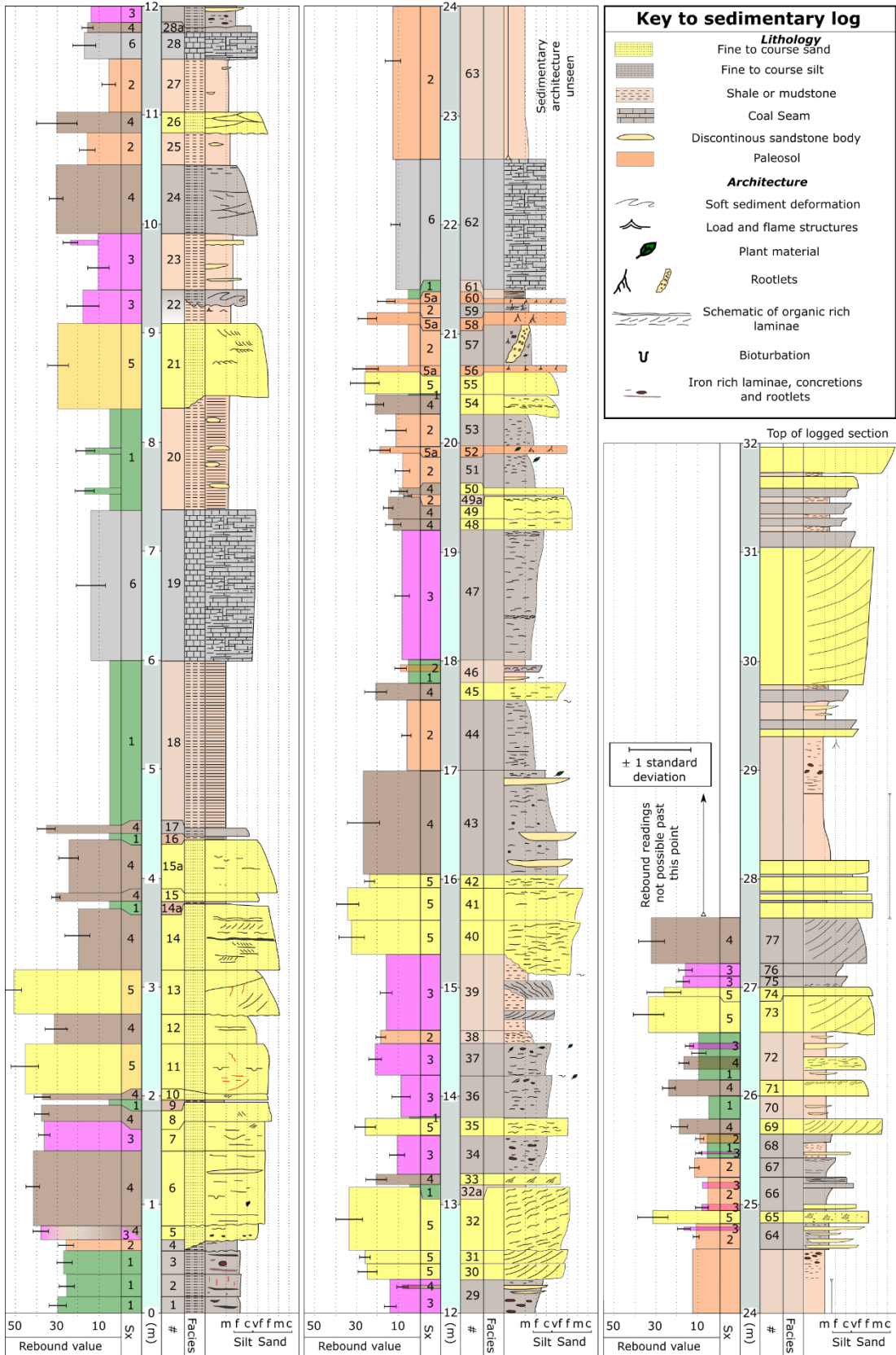


Figure 4.2 (previous page): Litho-stratigraphic and rebound profiles as measured for the bed-scale observations. Colour for mean mechanical rebound values match S_x . Examples of sub-bed scale sedimentary logs and rebound profiles 21/1 and 21/4 are provided in the appendix to this chapter.

4.3 Methods

4.3.1 Network Topology

The characterisation of fracture networks from field analogues typically involves the collection of data using scanlines, which may be linear (Priest and Hudson, 1981; Priest, 1993; Marrett et al., 2018) or circular (Mauldon et al., 2001; Rohrbaugh et al., 2002), or through mapping of fracture traces (Wu and D. Pollard, 1995). Fracture length, orientation, and spacing are commonly measured along with abutting relationships. An alternative is to use the topological approach developed by Sanderson & Nixon (2015), coupled with trace mapping, to extract topological and geometric data. Topology is the analysis of a fault or fracture network through the dimensionless properties which characterise the spatial relationship between fractures (Sanderson and Nixon, 2015; Procter and Sanderson, 2017; Sanderson et al., 2018). Topology describes a fault or fracture network as a series of branches and nodes. A branch is a fracture trace with a node at each end which may either: a) terminate into rock as i-nodes (unconnected terminations); (b) abut against another fracture as a y-node or; (c) cross another branch as an x-node. The ratio of node and branch types can be plotted on a triangular diagram (Manzocchi, 2002; Sanderson and Nixon, 2015) and used to calculate the percentage of connected branches (P_c).

Traditional node notation (Figure 4.3a), does not enable direct correlation of abutting and termination relationships with changes in lithology and bed-scale heterogeneities. In order to further classify the fracture network and capture the effect of sedimentary heterogeneity i- and y- nodes were split according to whether they occurred at the top (It, Yt), base (Ib, Yb) or inside (Ii, Yi) a sedimentary layer. This enabled networks to be classified using i- and y-node triangles, in addition to traditional node and branch triangles.

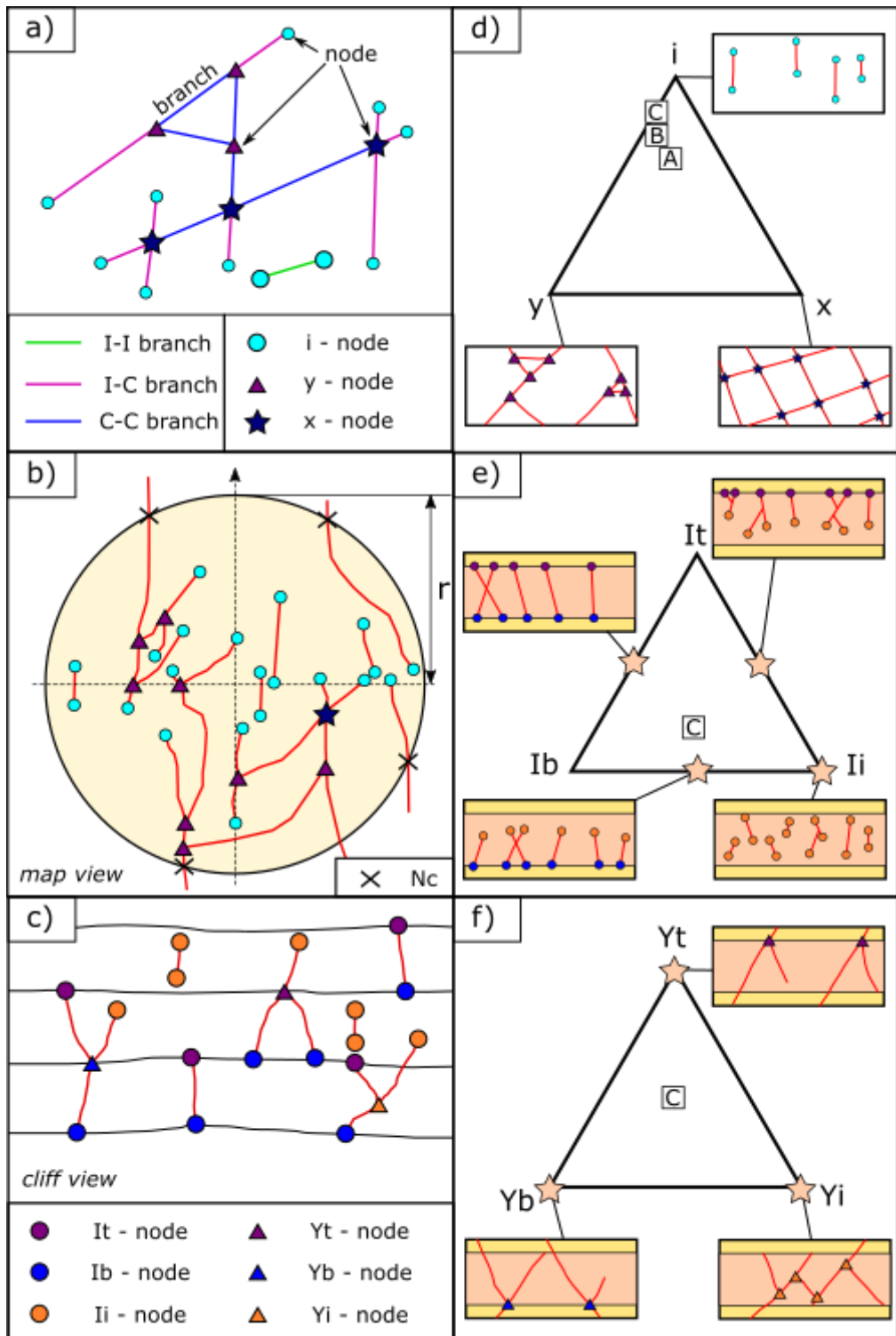


Figure 4.3: Topological sampling notation: (a) Standard topological notation after Sanderson and Nixon (2015); (b) topological sampling within a circular scanline, following the methodology of Procter and Sanderson (2017); (c) amended node notation used in this study; (d) node-triangle, showing end-member fracture networks and the position (a), (b), and (c) would plot; (e) i-node and (f) y-node triangles, showing typical 'end-member' cases and the position fracture map (c) would plot.

4.3.2 Field procedure

4.3.2.1 Sedimentary logging and mechanical stratigraphy

Within this study two scales of observation were used: 'bed-scale' and 'sub-bed scale'. For bed-scale experiments sedimentary units are classified as being within two obvious boundaries between different sedimentary event beds at a decimetre scale. Sub-bed scale classifies sedimentary units as distinct sedimentary layering (e.g. thin clay-rich laminations) or structures (e.g. mud-draped ripples, rip up clasts etc.), which may or may not be laterally extensive (e.g. discontinuous lenticular bodies). At bed and sub-bed scale, sedimentary logs and mechanical stratigraphy were taken at decimetre scale and centimetre scale respectively. Based on field observations, a litho-mechanical facies scheme (Table 4.1) was created and used as a framework for bed-scale observations. These facies were derived to sub-divide fracture data and as such, represent obvious mechanical and lithological difference rather than a depositional facies *sensu stricto*. For example, multiple sedimentary processes and depositional sub-environments could be responsible for the formation of the same litho-mechanical facies; and multiple mechanical facies can arise within a unit deposited within a single depositional environment. At a sub-bed scale facies were not assigned due to many features not displaying along-strike continuity. Instead features were compared according to their grain size, mechanical strength and dominant sedimentary structures.

To define mechanical stratigraphy we used an N-type Schmidt hammer (Aydin and Basu, 2005) to measure present day in-situ elastic rebound properties of the rock mass (hereafter rebound) for each stratigraphic layer (e.g. Ferrill & Morris 2008). Following the method of Morris et al. (2009), measurements were undertaken on sub-vertical rock faces away from areas of fault-related damage, eliminating the need for corrections due to variations caused by gravity. Each sample included a minimum of 10 rebound readings within the unit of interest. Wherever possible readings were undertaken within a 25 cm² patch of a single bed exposure. However, for sub-bed scale logs where units in question were often thinner than 25 cm measurements were taken along a bed-parallel profile and care was taken to avoid bed partings and fractures. Although rebound has been correlated by previous authors to unconfined compressive strength and Young's modulus (Katz et al., 2000; Aydin and Basu, 2005) we present the data in its raw form as rebound values (R-values). The rock properties will have changed during post-Carboniferous uplift and deformation. However R-value

profiles provide a valuable proxy for the relative stiffness of the sedimentary layering units and the ability for the unit to resist deformation (Ferrill and Morris, 2008).

S _x	Description
S ₁	Mudstone: Fissile, homogenous with occasional channel coals and iron concretions. Few sedimentary structures. Very dark grey in colour and often organic rich.
S ₂	Siltstone: Typically, paler than S ₁ with grains visible. Occasional ripples present, however, the beds are typically laminated or massive with occasional fine sand lenses or mud laminations/drapes.
S ₃	Sandy mudstone: less than 50% sandstone within the unit. Heterolithic bedding, flaser and lenticular bedding. Lots of interbedding and moderate to poor sorting. Beds contain generally muddy sandstone layers or lenses of poorly sorted sandstone.
S ₄	Muddy sandstone (or mudstone and sandstone): <40% mud, mud draped ripples and organics, small (cm-scale) burrows. Ripples, climbing ripples, scour marks common. Lenticular bedding present.
S ₅	Sandstone: trough cross bedding, distributed organics present. Typically, less than 20% mud and generally fine to medium grained. Paleocurrents observed through point bars and (sinuous) channels.
S _{5a}	Seat Earth: medium to coarse grained paleosol, often containing rootlets and logs.
S ₆	Coal: Has a shiny lustre, orthogonal fracture pattern spaced on a cm-scale (cleats) and is bituminous in rank.

Table 4.1. Litho-mechanical facies scheme used as a framework for bed-scale and bed-parallel fracture maps.

4.3.2.2 Fracture mapping

In order to compare fracture networks from different sites, it is important that the same scale of observation is maintained throughout the data collection process (Scheiber et al., 2015; Andrews et al., 2019). Two scales of observation were taken here to compare the mechanical stratigraphy at the bed- scale and sub-bed scales. However, the derived fracture statistics from both scales were not directly compared. Similarly, it is not possible to compare sub-bed scale fracture observations to the bed-scale sedimentary logs as the

litho-facies scheme does not capture sub-bed scale sedimentary heterogeneity. Andrews et al. (2019) demonstrated that different geologists collect fracture data differently from the same outcrop, such that a 'detail-orientated' geologist will collect a greater number of fractures, many of which will have a small trace length, compared to a 'data-orientated' operator. To limit the effect of subjective bias in our dataset, and enable replicability in our results, we follow the following steps:

1. All fracture data is collected by the lead author, who is identified as a 'detail-orientated' data collector (Andrews et al., 2019). This ensures consistency in the data collected, and because of the detailed nature of the data small fractures were captured, enabling the effect of small sub-bed scale heterogeneities on the fracture network to be investigated.
2. All fracture data were collected using window sampling undertaken in the field, which enables the ground truthing of connections and fracture terminations and has been found to be least effected by subjective bias (Andrews et al., 2019). Window sampling was undertaken at a bed- and sub-bed scale by drawing fracture traces directly onto field photographs, either using printed A3 (29.7 x 42.0 cm) photographs or a vector graphics program on the Apple iPad Pro. To investigate the sedimentary facies in the bed-parallel view, 'experiments' were set up using an adapted method based on Procter and Sanderson (2017). The aim was to complete all fracture analysis using 1 m diameter circles. The fracture network was drawn out onto a field photograph using an Apple iPad Pro. The location and orientation of fractures intersecting the circle's circumference (n-points) and topological sampling of nodes within the circle were recorded. For this study aperture is not investigated as we believe it is not representative of the subsurface due to aperture being drastically increased through coastal weathering processes. Occasionally, 1 m diameter circles were not possible as the outcrop was too narrow to allow this or the fracture network was too sparse to collect a representative sample (Mauldon et al., 2001; Procter and Sanderson, 2017). When this was the case the diameter of the circle was adjusted so a minimum of 20 fracture terminations were present within the sample area.
3. For section view analysis at both bed- and sub-bed scales, the sedimentary boundaries which were defined during sedimentary logging, were correlated across

field photographs (using either an iPad Pro or A3 printed photographs), and fractures drawn out.

4.3.2.3 Post fieldwork analysis

The fracture maps created in the field were imported, scaled to true size, and digitised in ArcGIS. Topological sampling (Figure 4.3) was undertaken using a combination of NetworkGT (Nyberg et al., 2018) and manual i-node and y-node classification. Topological and trace length data were exported into MS Excel separately for each sedimentary units (beds or sub-bed units). Due to the orientation of the cliff line (NW-SE), fractures investigated in this study belong to the steeply dipping E-W trending set, and have not been split into sub-sets. Data from bed-scale fracture maps and ‘experiments’ were analysed using the litho-mechanical facies scheme (Table 4.1) as a framework. Sub-bed scale analysis was undertaken for each location separately and used the grain size, rebound values and sedimentary structures for each sedimentary horizon as a framework to compare results.

4.4 Results

4.4.1 Mechanical stratigraphy

Bed scale	
Sx	R-values
S1	<10 (\bar{x} = 6.5)
S2	<10 to 20 (\bar{x} = 11.3)
S3	7.7 to 31.6 (\bar{x} = 16.1)
S4	8.9 to 34.7 (\bar{x} = 23.9)
S5	23.5 to 46.6 (\bar{x} = 31.1)
S5a	15.2 to 25.5 (\bar{x} = 21.0)
S6	11.2 to 16.4 (\bar{x} = 13.6)

Table 4.2: Rebound properties of identified litho-facies.

Where mechanical stratigraphy was assessed at bed scale, rebound values are affected by both grain size and the litho-facies the bed belongs to (Figure 4.4a). As grain size increases, rebound values also increase with a moderate linear correlation of $R^2 = 0.52$. For example, for clay-grade lithologies rebound values ranged from <10 to 17.3 (mean = 6.8), while values ranged from 12.3 to 46.6 (mean = 27.2) for medium sand. The range of rebound values for a specific bed can be both high or low (Figure 4.5a), with greater scatter

observed in medium grain-size lithologies (Phi ranging from 3 to 6). When beds are characterised using the sedimentary facies scheme outlined in Table 4.1, it was found that mean and range of rebound values for a specific 'experiment' were dependant on the sedimentary classification. Overall, bed-scale mechanical stratigraphy displays a systematic increase with grain size, however, there is a large degree of scatter in the data.

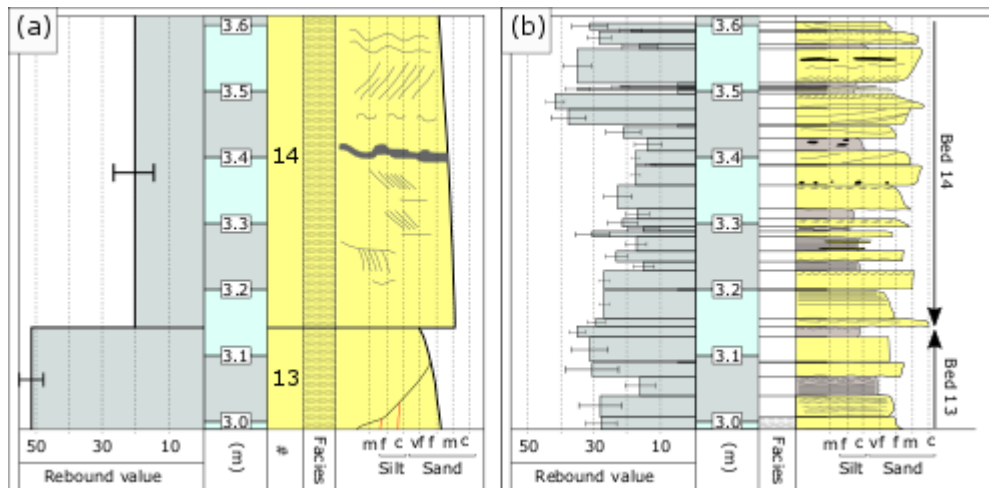


Figure 4.4: A comparison of bed- and sub-bed scale sedimentary logs and mechanical stratigraphy: a) A section of the stratigraphy covered by the bed-scale logging (see Figure 4.2) and included parts of Beds 13 and 14; b) The same section of stratigraphy logged at a cm-scale resolution with mechanical stratigraphy undertaken for each sub-bed scale sedimentary unit.

When cm-scale logging was undertaken, it was found that what is defined as a bed in fact consists of multiple identifiable sedimentary layers. This is illustrated in a section of sedimentary log where only one event horizon is recorded on a bed scale (Figure 4.4a) compared to 33 horizons when logged at a cm-scale (Figure 4.4b). At a cm-scale, although the general fining up trend can be observed throughout Bed 14, some of the coarsest beds are in fact found near the top of the section (around 3.5 m).

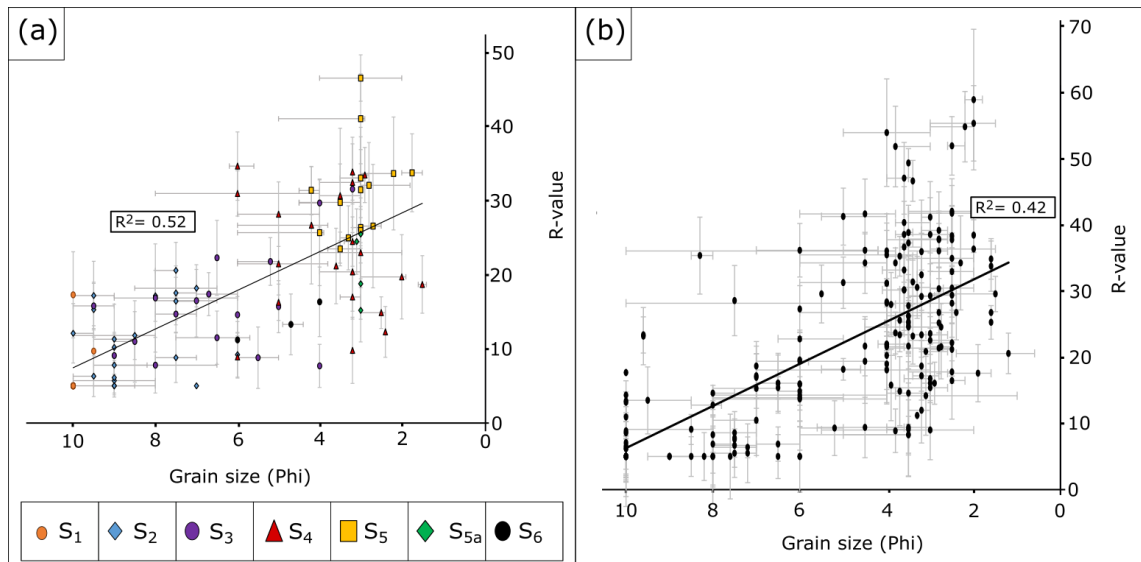


Figure 4.5: Graphs of rebound value against grain size (presented as Phi) for a) bed-scale presented by the lithofacies introduced in Table 4.1 and b) sub-bed scale experiments. Linear coefficient of determination (R^2) are presented for each graph.

When the mechanical stratigraphy was measured at a sub-bed scale, associated with cm-scale logging, a weak positive correlation was also observed between grain size and rebound values ($R^2 = 0.42$; Figure 4.5b). The correlation is lower than at a bed-scale, and considerable scatter at grain-sizes between Phi = 6 and Phi = 3 was observed. For example, for Phi = 3.5 to 3.6 rebound values ranged from 8.3 up to 47.1. Scatter is observed due to the dominant sedimentary structures present within the beds (e.g. mud-draped ripples or channel coals (Figure 4.4). Variability in R-values from a single sample location is marginally lower when sub-bed scale measurements are taken (average CV of 0.22 for sub-bed scale and 0.25 for bed-scale).

4.4.2 Fracture data

Joints at Whitley Bay typically have steep dips and form two primary sets (trending ESE and NNE respectively) along with several off-trend joints in incompetent lithologies (Figure 4.6 & 4.7). Joint strike values in S_1 display little clustering, with all strikes containing at least 3% of measured fractures, and the maximum orientation (130° to 140°) only containing 8% of the measured fractures. As grain size increases (S_2 to S_4) the peaks in the data become more distinct, with some orientations not containing any data. In S_5 the two joint sets are clearly visible, with only 1 to 2% of fractures in the strike histogram present in bins that do not match the main trend (Figure 4.7). The fractures in S_6 (Coal) is strongly affected by the ENE and NW trending face and butt cleats. The NNE trending set is also clearly visible in S_6 ,

which constitutes ~12% of measured fractures. Dip also differed between different sedimentary facies (Figure 4.7). For example, joint dips in S5 ranged from 40° to 90° (median = 84°) compared to S1 where dips ranged from 18° to 89° (median = 72°). The variability in dip also varies between sedimentary facies, with S2 and S3 displaying higher variability (QCV = 0.21 and QCV = 0.22 respectively) than the other facies (e.g. S4, QCV = 0.11). In all lithologies apart from S5 shallowly dipping (<60°) joints were observed, with field observations showing these usually occurring off the primary trends.

The style of fracturing (joint curvature, age relationships, and trace/branch length distributions) in map-view scanlines also changes with the lithofacies observation (Figure 4.6a).

- **S1:** Joints typically form an interconnected mesh with individual strands displaying curvature between nodes (Figure 4.6). This leads to the widespread variability in strike values recorded in the field. Age relationships are difficult to deduce, with E and NNE trending joints abutting against each other suggesting they formed concurrently. Trace length is typically low and shows a negatively skewed distribution with the most abundant bin (0.05 m to 0.1 m) containing 26% of joints (Figure 4.7a). Branch length similarly shows a negatively skewed distribution, with the 87% of branches between 0.025 and 0.1 m long (Figure 4.7a).
- **S2:** Joints also display a degree of curvature, however, to a lesser degree than S1 and the primary trends become visible (Figure 4.6). Although both sets locally abut against each other, typically the ENE trending joints pre-date those trending NNW which often form ladder joints. Trace length distributions are similar to that observed in S1 (mode = 0.05 to 0.1 m) (Figure 4.7b), however, the branch length distributions for S2 are more skewed (5.37 compared to 3.10).
- **S3:** Joints in S3 doesn't show curvature, which explains why the main joint sets are clear in the strike data (Figure 4.5). Abutting relationships suggest ENE trending joints pre-date the NS set, however, later stage ~EW trending features are observed abutting against NS joints where joints meet. Fracture trace lengths are typically longer than S1 and S2, with the mode occurring at 0.15 to 0.20 m (17%) (Figure 4.7b), and are typically less negatively skewed. Branch length is low (median = 0.05 m) with the distribution only displaying moderate skewness (2.00).

- **S4:** Joints display little curvature; however, the fracture pattern is characterised by several small-trace length features which form at the intersection of longer fractures. Cross cutting relationships place the ESE trending set as pre-dating the NNE set, with the later small fractures forming last. The small features at fracture intersections cause S4 to be dominated by small fractures, with 64% of fractures less than 0.2 m and 29% less than 0.1 m. The large joints are also observed through the peaks in the trace length histograms for several experiments (Figure XX). Branch lengths display a bimodal distribution (Figure 4.7b) with a main peak between 0.025 m and 0.5 m (21%) controlled by small branches at fracture intersections and a subsidiary peak at 0.20 m to 0.225 m (6%) where large joints connect.
- **S5:** Joints in S5 display a degree of curvature particularly in the EW orientation (Figure 4.6) which likely explains the spread in strike values collected in the field (Figure 4.7). Three sets are identified, an early EW set which is followed by a NS trending set. Finally, an oblique set (typically striking NW) is observed which abuts against both sets. Fracture spacing is considerably higher in S5, which required 2 m diameter sample windows to be used, with the length of fractures also larger than other lithofacies (Figure 4.6 & 4.7). Trace lengths display close to a normal distribution (average skewness = 1.47), with the most abundant trace length being between 0.35 and 0.4 m (11%). In contrast, branch lengths are highly skewed (4.94) with 22% of branches less than 0.025 m. This is caused by the high connectivity of the network, the three joint sets, and the abundance of small features at joint intersections.
- **S6:** S6 is characterised by a dense network of interconnected fractures which are arranged into 'fracture corridors' (c.f. Gabrielsen & Braathen (2014)) (Figure 4.6). Although pre-existing cleats were not recorded in the fracture mapping, many of the cleats showed reactivation, leading to the two sharp peaks in strike collected in the field (Figure 4.7). Late NNE joints are recorded, which abut against all other sets. The trace-lengths are only moderately skewed (2.5) and low, with no joints recorded over 0.2 m and 90% of branches occurred below 0.025 m.

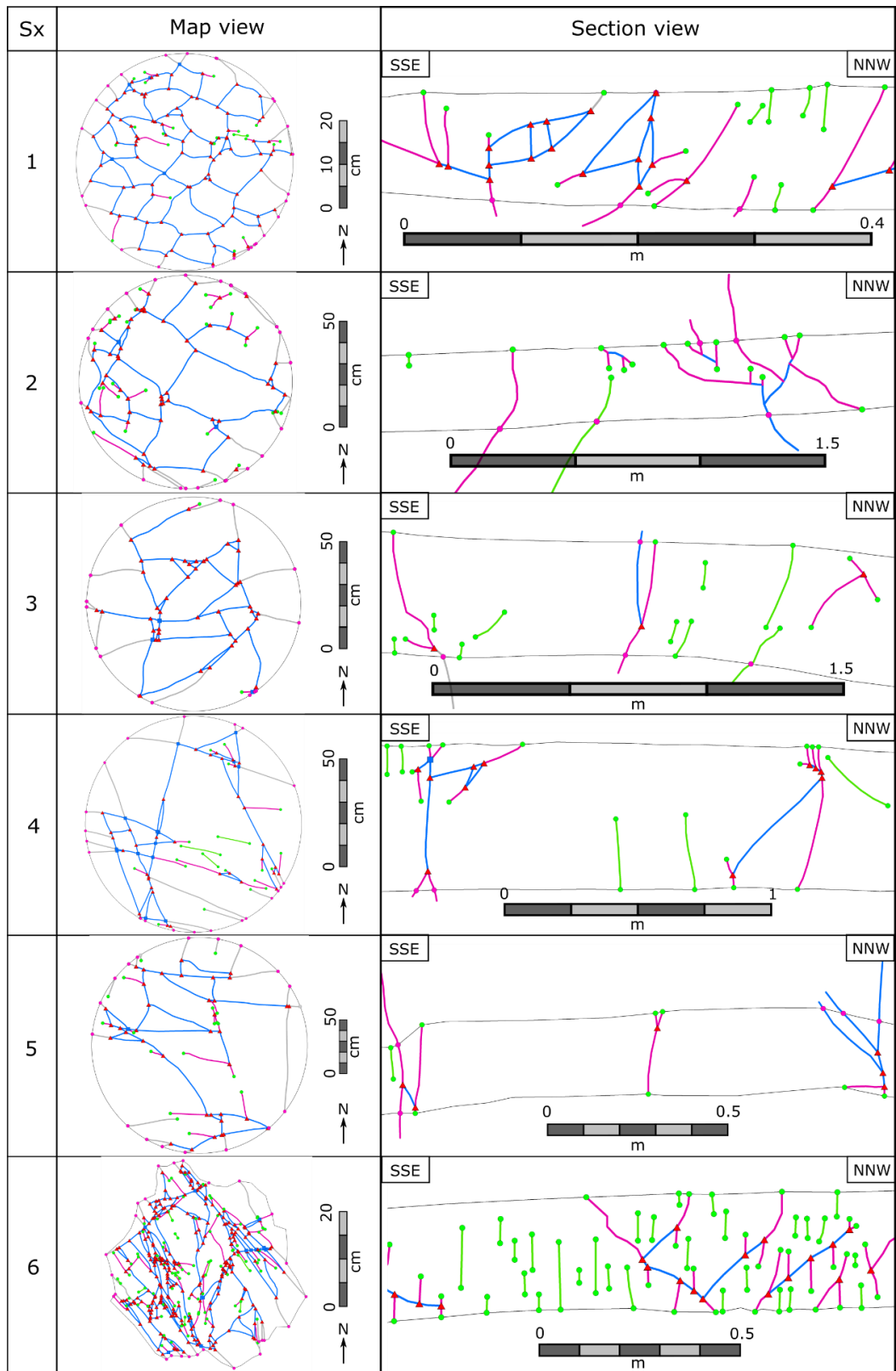


Figure 4.6: Example fracture maps for both map- and section- view. Data is presented by lithofacies and displays the standard topological sampling introduced in Figure 4.2.

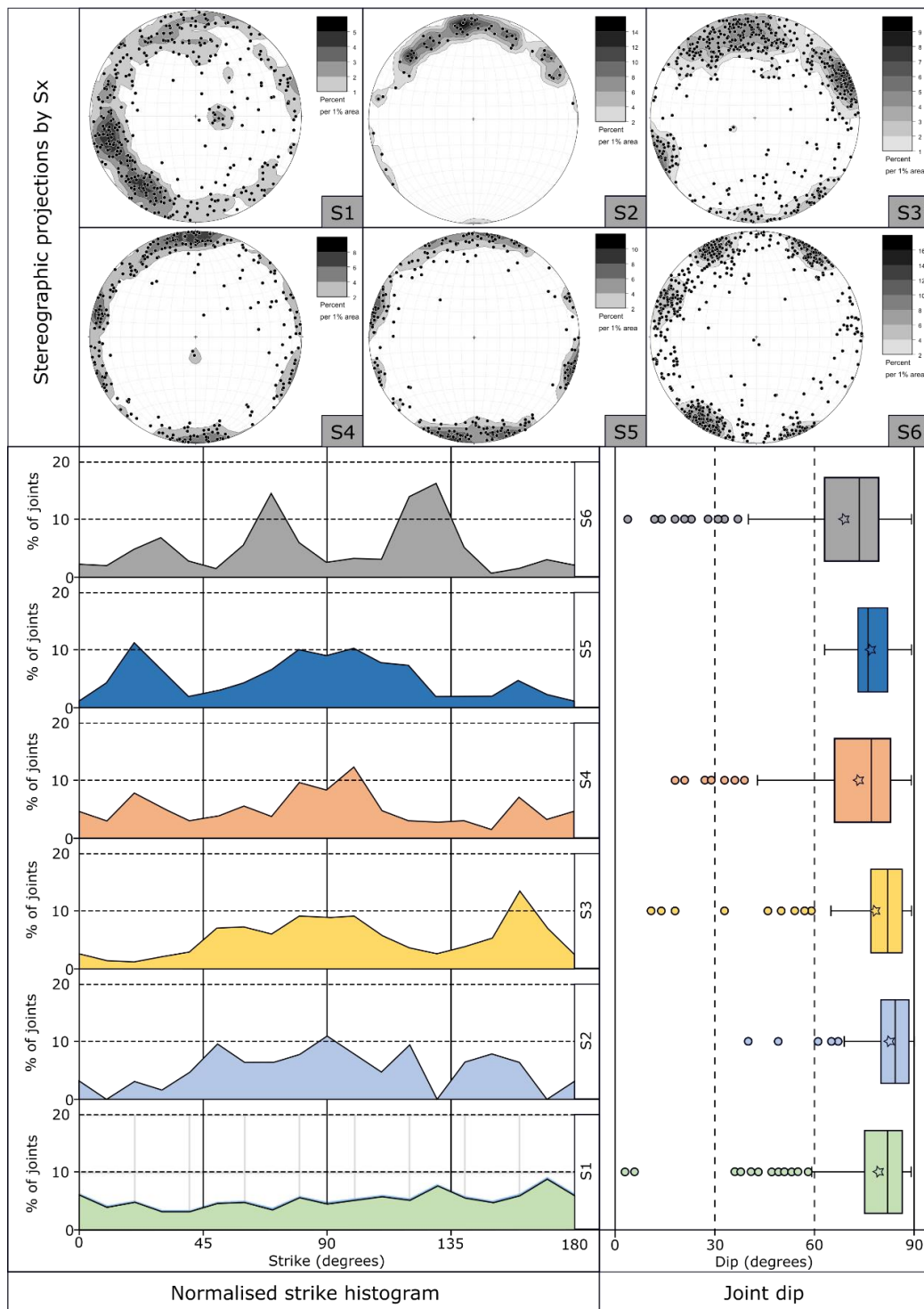


Figure 4.7: Joint dip, strike and trace length for bed parallel and bed-perpendicular experiments. Data is presented by lithofacies (Sx). Dip and strike data are presented using equal area stereographic projections created using Stereonet 10.1.1 (Allmendinger et al. 2013; Cardozo and Allmendinger, 2013). Data is contoured by 1% area with the value of each contour provided next to each stereonet. Strike data is presented using normalised histograms with a bin-width of 10°. Dip data is presented using box and whisker diagrams.

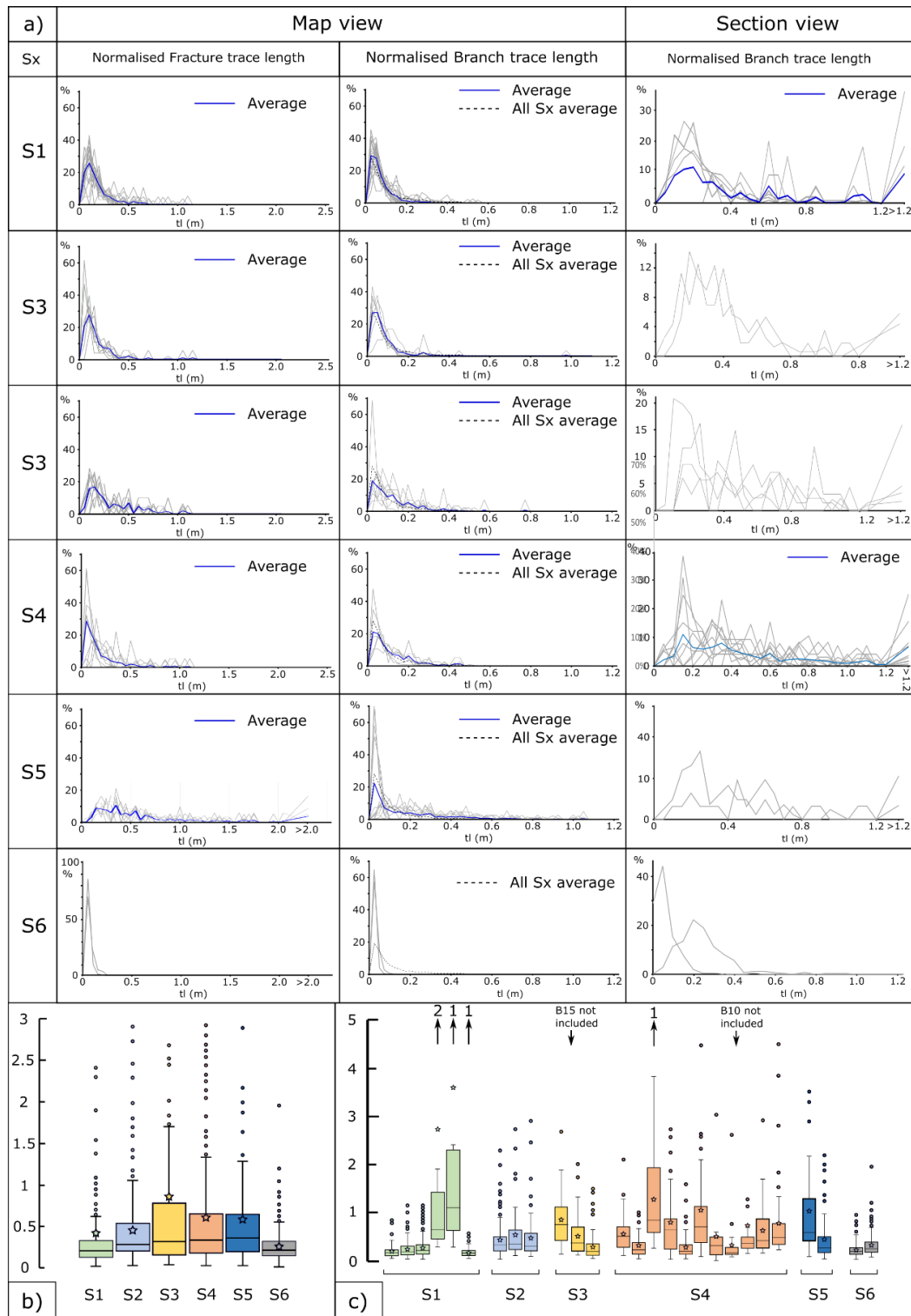


Figure 4.8: Trace length data. a) normalised trace length and branch length histograms for map-view experiments, and branch length histograms for section view. Blue lines represent the average value of all experiments for that bin. Box and whisker plots for the ratio of branch length and bed-thickness presented b) by litho-facies and c) for each experiment. Experiments where the bed-thickness is low (c. 5 cm) did not typically show bed-bound branches, and are not included in this figure.

The fracture patterns and network characteristics observed in map-view are distinctly different to those in section view (Figure 4.6 & 4.7b). In section view the mechanical contrasts imparted by the mechanical stratigraphy caused joints to become vertically restricted, leading to a different set of properties. Due to the orientation of the coastal outcrops (~N/S), section view maps capture joints from the EW trending set. For section view 'experiments', a visual description of the joint network is provided prior to discussing the characteristics of branches were considered and are discussed for each litho-facies below.

- **S1:** Although through-going joints exist in S1, it is far more common for joints to be localised within a thin zone (sub-bed unit) where fractures terminate against the top and base of the thin zone (Figure 4.6). Connections are rarely observed and when they are, they occur along a localised area and instead isolated joints are common. Branch lengths tend to be low, with 35% below 0.25 m. Branches typically terminated within the bed (97.2%), with an average branch length of 35% of bed thickness (Figure 4.8). The exception to this is the 5 cm thick Bed 16, which due to its thickness was dominated (8 out of 11) by through-going features.
- **S2:** Unlike S1, several joints were observed abutting against pre-existing features, and the number of fracture terminations within the bed were lower. Branch length was higher than S1, with the majority of branches between 0.2 and 0.3 cm (22%); however, branches over 0.7 m were rare (18 %). Similar to S1, branches typically terminated within the bed (92%), however, had a higher average branch length of 45% of bed thickness (Figure 4.8).
- **S3:** Joints are typically bound by the bed-boundary and laterally extensive horizons which cut through the bed (see half-way up the bed in Figure 4.6). The apparent dip of individual joints occasionally either steepens or shallows. A large amount of scatter is observed in the branch length data with the averaged normalised trace lengths representing a normal distribution (Skewness = 0.98). However, B23 displays a moderate skewness (2), and more data from this lithofacies is required to better understand the branch length histograms. Similar to S1, branches typically terminated within the bed (83.2%), with a higher average trace length of 86% of bed thickness (Figure 4.8). The 6 cm thick Bed 15 is also dominated (17 out of 19) by

through-going features and when this bed is discounted from the data the percentage of bed-bound branches increases (90%) and the average branch length reduces to 43% of bed thickness.

- **S4:** The pattern of joining of S4 is similar to that of S3, however, there is a smaller number of internal features that cause joints to abut, which tend to occur near the top of beds (Figure 4.6). Branch traces are planar, rarely connect to other branches, and display steep, or moderate apparent dips which is also observed in the field data (Figure 4.5). Branch trace length displays moderate skewness (1.96), peaking at 0.15 to 0.2 m (11%). Four peaks are observed, which correlate to the thickness of beds or sub-bed sedimentary packages (Figure 4.6 & 4.8). Branches typically terminated within the bed (87.3%), however, the average branch length is higher at 62% of bed thickness (Figure 4.8).
- **S5:** The fracture patterns observed in S5 match very closely those observed in S4, however, the spacing of fractures is higher and more through-going fractures are observed (Figure 4.6 & 4.8). Branch length peaks between 0.2 and 0.3 m (20%) (Figure 4.8), with 16% of fractures cutting through the bed-boundary and the average branch trace length is 59.3% of the bed thickness.
- **S6:** Joints in S6 are either steep and isolated, or display a high trace length and shallow apparent dip (Figure 4.6). Similar to in map-view the majority of branch traces are small (<0.3 m) and less than 6% of branches longer than bed thickness. The average branch length is 26% of bed thickness.

4.4.3 Network topology

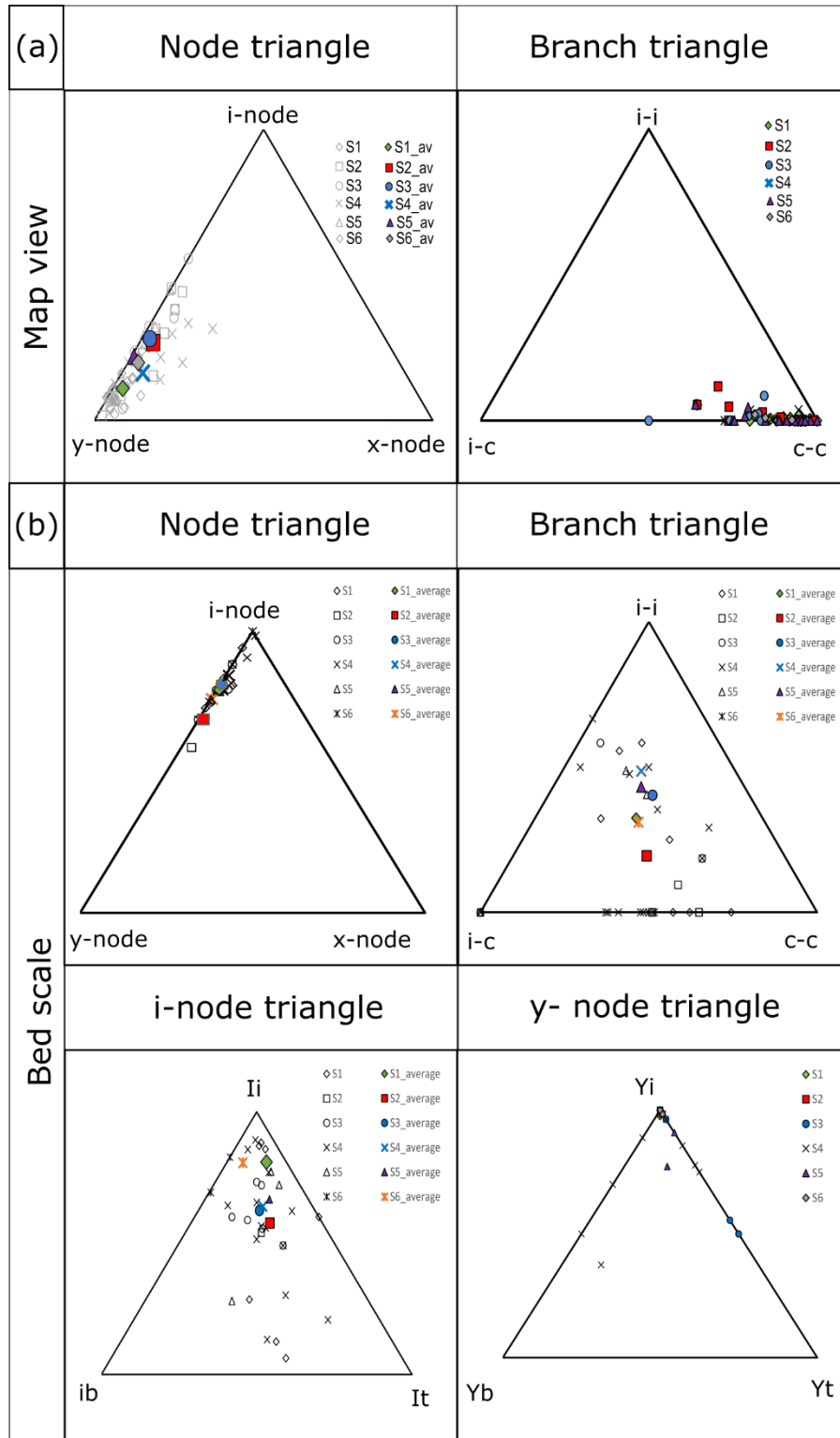


Figure 4.2: Topological data presented by litho-facies. Results are presented for (a) map-view and (b) section view experiments. An explanation of each triangle is provided in Figure 4.3.

Topology was used to assess the connectivity of the joint networks in both bed-parallel and bed-perpendicular view (Figure 4.9). In map view most node data plots close to the y-node axis on the i-node y-node ti-line, with x-nodes rarely observed (Figure 4.9a). When data were grouped by litho-facies there was significant overlap in results, however, it was observed that S6 on average contained a higher percentage of y-nodes, and S2 and S3 a lower percentage compared to the rest of the facies. The data-points from S4 which plot towards x-nodes represent thin beds of iron stone which display increased fracture intensity compared to the surrounding lithologies. Fully connected branches (C-C) dominate fracture networks in all litho-facies, however, S2 and S3 display the greatest percentage of partly connected branches (I-C). Isolated branches are rarely observed in map-view experiments. The connectivity (P_c) ranges from 0.88 for S2 and S3, up to 0.96 for S1, with partially connected branches occurring in both orientations.

Compared to map-view, connectivity in bed-perpendicular view is considerably lower, with average values of P_c ranging from $P_c = 0.36$ for S3 and S4, up to $P_c = 0.54$ for S2. Similarly, to map-view, node data lies along the i-node to y-node ti-line; however, i-node dominates (69% to 54% of nodes) (Figure 4.9b). Little difference is observed between litho-facies, however, S2 displays a greater proportion of y-nodes (30%) compared to the other classifications (19.5%) (Figure 4.9). The location of branch data on the branch triangle varies from close to a point on the I-I to I-C ti-line with ~66% isolated branches, to a point on the C-C to I-C ti-line which contains 70% fully connected branches. Several beds from S2, S3 and S4 display no isolated branches, with I-C branches dominating S4. The average positions of the beds in branch-triangle space shows S2 to be most connected, followed by S6 which show similar branch properties. S4 displays the lowest connectivity and plots closest to the I-I vertex, even though several beds only contain fully connected branches. This highlights the high variability observed between fracture networks in different beds for S4.

When the location of i- and y-nodes were assessed (Figure 4.9b), overall trends and lithofacies specific trends were identified. In the majority of beds y-nodes occurred within the bed (Y_i), with a high proportion of y-nodes only occurring at the base and top of some S3 and S4 beds. These beds display a low total number of y-nodes (e.g. Bed 7), where large trace length fractures branch at the mechanical contrast between S3 and S4. Typically, it is considered that bed-bound joints dominate (e.g. Laubach et al., 2009), which would plot

halfway along the It-lb ti-line in i-node triangle space (Figure 4.9). We find however, that beds plotting here are rare, and instead i-nodes occur within beds (Figure 4.9). This is highlighted in S1 and S6 where 81% of mapped joints occur within both lithofacies. This is also observed in the section view and is likely controlled by the presence of cleats in S6 and the large number of sub-bed heterogeneities in S1 (e.g. iron nodules). S2 contains the most bed-bound jointing, with 57% of i-nodes occurring at a bed boundary. Where joints occur at a bed-boundary, a greater amount terminate at the top of the bed, with the ratio of It to lb ranging from 1.6 in S3 to 2.3 in S1.

4.4.4 Sub-bed scale observations

Sedimentary logging is often undertaken at a decimetre scale which captures the laterally continuous sedimentary features. Beds are typically classified as being between two obvious boundaries between event horizons. However, within a single bed many sedimentary structures (e.g. ripples) and layering (e.g. thin clay-rich laminations) are present which can act as a mechanical barrier. We use two examples where cm-scale logging is correlated to fracture maps to investigate this further (Figure 4.10), before commenting on general trends observed throughout the study area.

4.4.4.1 Example 1: Fine sands with abundant channel coals (Figure 4.9a)

The lithology at this location is comprised of interbedded siltstone, fine to medium sandstone, and semi-continuous thin coal laminations. At a bed-scale this section was classified as Bed 13 (S5) into Bed 14 (S4), however, at a cm-scale a total of 24 sedimentary units were identified, which ranged in rebound values from <10 to 29.3 (Figure 4.10a). Fractures in this location are controlled by a nearby small offset strike slip fault (090°/70° S; 08°/068°) which can be seen slightly offsetting stratigraphy in the bottom right of the figure. The number of 'bed-bound' fractures observed at this scale were higher than at a bed-scale, illustrating the importance of small scale sedimentary features in controlling fracture trace length. For example, most fractures terminate at the boundary between the 2.5 cm thick SSt unit and the overlying laminated siltstone.

Several sedimentary structures are observed to effect the termination of fractures, in particular the presence of organics which occur either within the bed or as channel coals on the lee side of ripples. This can be observed by comparing the lowest logged bed, which contains organic draped ripples and laminations to the relatively organic free muddy-sandstone present between 8 and 10 cm. Both beds have a similar rebound value (19 ± 3.8

and 16.8 ± 6.4), however, the number of fractures terminating within Bed 1 is far more than in the organic free bed. The location where fractures terminate is primarily controlled by the presence of the <1 cm thick zone of ripples, which typically have channel coals present. Ripples are also present in the organic poor bed, however, they are sand and red-silt rich and do not contain organic drapes. Small, discontinuous sandstone pods, which are commonly observed in weak siltstone beds, display increased pod-bound fracturing. Fracturing appears to increase near the edge of the pods where the thickness decreases, a feature which is also observed on larger channelised bodies.

4.4.4.2 Example 2: Seat earth and underlying organic rich shale (Figure 4.9b)

This section includes two beds of seat-earth (S5a), which due to the limited number of outcrops has not been investigated to the same degree as the other lithofacies and captures beds 58 to 61 of the bed-scale log. Even at this scale of logging, the majority of fractures are found to terminate within beds, with a median trace length of 1.61 cm. The majority of joints were bound by thin sandstone stringers found within seat-earth beds, or siltstone interbeds, whose thickness ranged from 0.5 cm up to 2 cm and led to the formation of bed-bound joints. The presence of rootlets, iron nodules, and logs are common in these lithologies, and can act to localise joint formation. Where logs are found, for example, to the right of Figure 4.9b, the logs themselves typically become fractured, forming 'bed-bound' fractures which terminate at the top and base of the log. Diagenetic halos are present within this sample area and causes the buff coloured discoloration observed around through-going fractures. The presence of sandstone stringers control the width and location of these zones, with the alteration considerably thinner where mud- and silt-stone dominates.

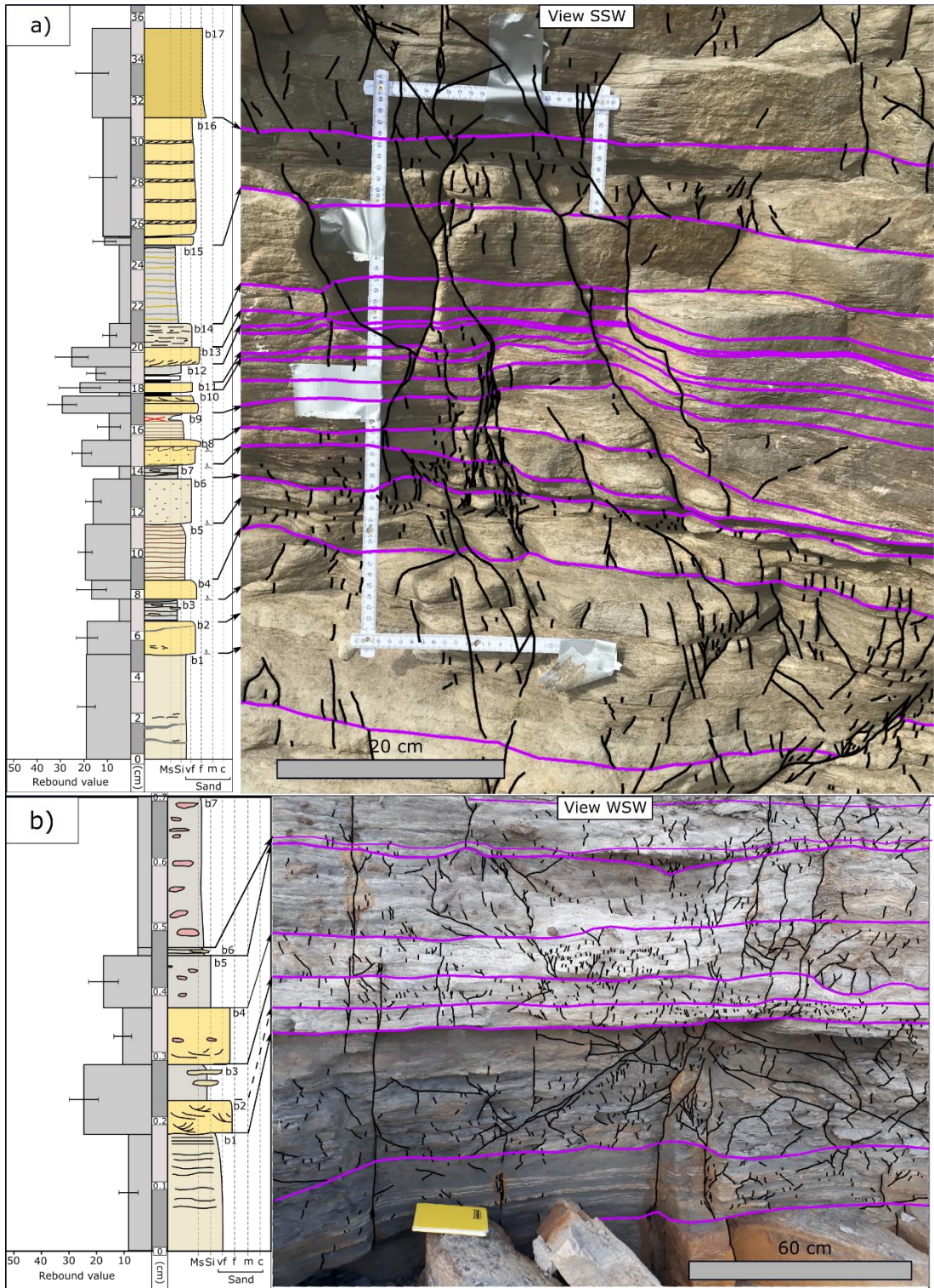


Figure 4.9: Example fracture maps linked to mechanical stratigraphy. Rebound values represent the mean for the specific sub-bed unit, with error bars representing plus and minus one standard deviation. Detailed sedimentary information for both logs are provided in the appendix to this chapter.

4.4.4.3 General observations

The examples in Figure 4.10 demonstrate that the mechanical contrasts, which lead to the arrest of fractures, are often found at a scale well below that used for capturing the sedimentology of a unit (bed-scale). Similar observations were observed in many other aspects of the field area (Figure 4.11), with the key sedimentary controls found to include:

Pre-existing cleat network: In coal (S6) the presence of the pre-existing cleat network imparts two sets of mechanical weaknesses into the coal. This controls the presence, orientation, and intensity of fractures which form (Figure 4.5 and 4.6). Where fracture intensity is high, cleats become reactivated and often filled with a buff orange carbonate (probably Ankerite) (Figure 4.11e).

Tips of channelised bodies: Channelised bodies, which are typically comprised of a clean relatively high porosity sandstone are commonly found throughout the succession (Figure Xx). These bodies typically show bed-bound fracturing, which increases in intensity towards the tip in cross sectional view (Figure 4.11f).

Increased fracturing at the intersection of fractures at the top of clean sandstones: The top of sandstone beds (e.g. clean channelised bodies) the intensity and style of jointing changes at fracture intersections. For example, in Figure 4.11c the E-W trending feature displays an angular fracture pattern, which is particularly evident to the left of the image. At the intersection of the primary features a large number of y-nodes are observed, which is also observed in many S5 bed-parallel fracture maps. These form as ‘tetrahedral zones’ (c.f. Peacock et al., (2019)), and meet to form a single feature as you move into the bed (e.g. Figure 4.10f).

Presence of organics: Organic fragments and organic rich layers, which may be observed either distributed throughout beds (e.g. Bed 6 in Figure 4.2), as laterally continuous thin coal bands (Figure 4.11d), or as discontinuous channel coals (Figure 4.11h) and organic-draped ripples (Figure 4.11b). In all cases organics strongly effect the fracture patterns observed, causing joints to either: i) terminate against the organic layer (Figure 4.10a and Figure 4.11a, b, d, & g); ii) propagate along the channel coal (e.g. Figure 4.11h) or; iii) localise fractures when organics are distributed within the bed (e.g. Figure 4.10a).

Sandstone stringers: Laterally discontinuous sandstone stringers, or pods, were often observed in fine-grain size lithologies (see sedimentary logs in Figure 4.2 & the appendix).

The presence of a competent lithology surrounded by incompetent lithologies leads to the development of bed-bound fracture networks, which display a high bed-parallel connectivity (Figure 4.10a, Figure 4.11a, and lower beds of Figure 4.11d).

Soft sediment deformation & undulating bedding: Where soft sediment deformation (e.g. load and flame structures) and undulating bedding was present, joints were often observed to form at the peak of a flame or undulation (e.g. Figure 4.11g). This is also observed with the beds of seat earth (Figure 4.10b), where the undulous nature of the paleo-sol causes the nucleation and arrest of fractures.

Iron concretions and plant material within mudstone and siltstone beds: Below coal-beds it is common to observe a large number of iron-concretions and plant material (e.g. rootlets and logs) (Figure 4.2). These act to impart a mechanical heterogeneity within the bed and can cause the localisation of deformation (faults & fractures; Figure 4.10b). The inclusions themselves can also become highly fractured (see log in Figure 4.10b), in a similar manner to channelised bodies.

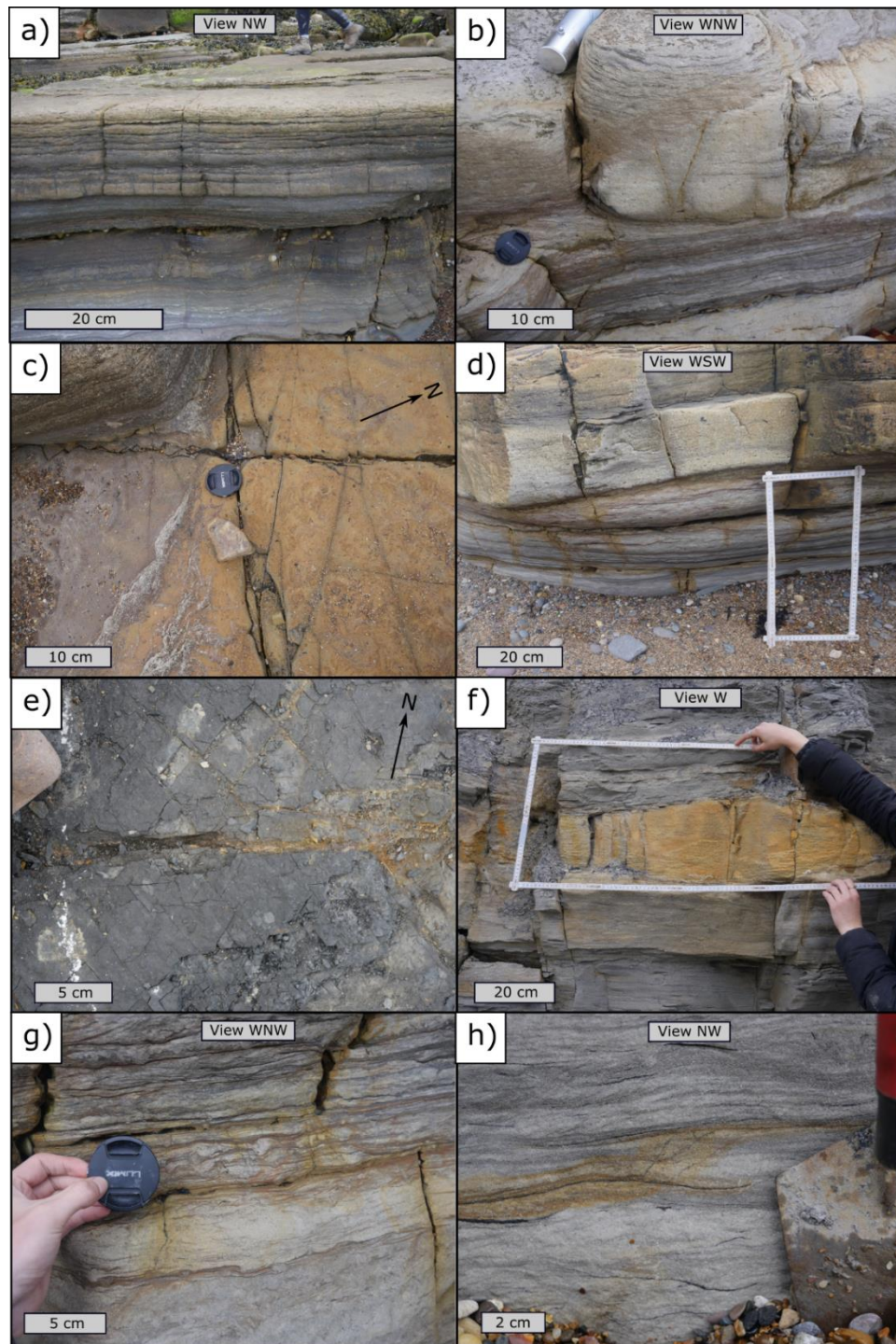


Figure 4.10: Field photographs of key sedimentary features: a) bed- and sub-bed bound joints cutting S3 (base) and S4 (top) near C3. b) Conjugate joints cutting the tip of a channelled sandstone body south of S6. c) Interacting joints on the bedding plane of S4 (CC4). d) Alteration halos surrounding channel coals, organic draped ripples and joints south of C6. e) Mineralised joints and cleats within the High Main Seam near C10. f) Joints increasing near the edge of a course channelled sandstone body north of C28. g) Interaction of ripples, soft-sediment deformation, jointing and lithology with alteration halos. h) Interaction of channel coal 'partings' with alteration halos.

4.5 Discussion

4.5.1 Effect of the plane of observation: Section view changes in mechanical strength

The plane of observation makes a large difference to measured fracture network characteristics, with networks in map view displaying considerably higher connectivity when compared to section view. Much of the analysis of fracture networks has been undertaken in a single plane, either using vertical profiles (e.g. cliffs) (Underwood et al., 2003; Hooker et al., 2013; McGinnis et al., 2017), mapping out fracture sets on sub-horizontal or shallowly dipping bedding planes (Zeeb et al., 2013; Watkins et al., 2015; Healy et al., 2017), or even via effectively linear borehole data (Mauldon and Mauldon, 1997; Dershowitz et al., 2000; Olson et al., 2009). Previous work has mainly concentrated on the geometrical properties of joint sets (Dershowitz and Einstein, 1988; Zeeb et al., 2013; Healy et al., 2017) and the spatial relationship between features within the network (i.e. topology) (Sanderson and Nixon, 2015; Procter and Sanderson, 2017; Sanderson et al., 2018; Nyberg et al., 2018). Several authors have highlighted the importance of considering the 3D nature of the fracture network when collecting fracture data (Dershowitz and Einstein, 1988; Priest, 1993; Dershowitz et al., 2000; Mauldon et al., 2001), however, direct 3D sampling is confined mainly to the seismic imaging of fault zones (Beidinger and Decker, 2011; Jackson and Rotevatn, 2013; Torabi, Alaei, et al., 2019) or CT scanning of hand specimens (Busse et al., 2017; Romano et al., 2019). While some recent work has attempted to use photogrammetry to better understand the 3D properties of joint networks (Bisdom et al., 2017; Napolitano and Glisic, 2019), fracture networks are still predominantly analysed in 2D (Nyberg et al., 2018; Peacock and Sanderson, 2018; Sanderson et al., 2018). Little work has been undertaken which looks at the relative ratio between the sample planes, or how the height of fractures varies up section (Hooker et al., 2013).

The lithofacies cut by joint networks at Whitley Bay were found to affect the style and properties of fracture networks in both map and section view (Figures 4.5, 4.7, 4.8). In map view, it is the grain-size and presence of pre-existing weaknesses such as joints and cleats which controls fracture properties. In fine grained lithologies (i.e. S1 and S2), fractures often displayed a degree of curvature (Figure 4.5) which affects the strike distribution in the orientation data (Figure 4.6). This is in contrast to competent lithologies (S4 and S5) where distinct orientation peaks are clearly observed (Figure 4.6). Curved joints form where there

is a local perturbation of the stress that may be caused by multiple mechanisms including: the intersection of joints as they grow towards each other (Pollard and Aydin, 1988); rotation of stress surrounding faults (Peacock, 2001; Faulkner et al., 2006); and the intersection of wing cracks (Wilkins et al., 2001). Small-scale sedimentary structures may also effect the initiation location and propagation of joints (Bahat and Engelder, 1984; Eidelman and Reches, 1992; McConaughy and Engelder, 2001). McConaughy and Engelder (2001) found that sedimentary structures (e.g. burrows) often acted as the nucleus for new fractures, with some features causing the initiation of multiple fracture planes. Similar relationships have also been observed in welded ignimbrites, where Moon (1993) found shards in the groundmass acting to localise strain. Such features (e.g. iron concretions, rootlets and channel coals) are commonly observed within S1 and S2 and would lead to a high intensity of joints, which then interact and lead to the curved traces in map view. The intersection of joints within S5 display increased fracture intensity with individual traces displaying curved traces (Figure 4.11c). When viewed in cross section these features become a single feature towards the centre of the bed (Figure 4.10f). Peacock et al. (2019) noted similar features where joints approach each other at Somerset, UK, which they termed 'tetrahedron structures'. These are widely observed in mechanically layered sequences and are likely caused by the stress change across the mechanical contrast imparted by an incompetent lithology (siltstone or shale) overlying the competent sandstone (S5).

The stratigraphy at Whitley Bay includes sandstones, siltstones, seat earths and coal that imparts a well-developed mechanical stratigraphy into the succession (Figure 4.2). A moderate correlation exists between grainsize and rebound values at a bed-scale ($R^2 = 0.52$; Figure 4.4), however, the correlation is weaker at a sub-bed scale ($R^2 = 0.42$). When the section shown in Figure 4.4 is logged at a sub-bed scale, the fining up trend observed at a bed scale is not clearly present. This is partly due to the sub-bed scale capturing discontinuous features (such as mud-draped ripples or clay-rich partings), the top of Bed 14 not included in the comparison leading the overall trend being obscured, and spatial heterogeneity in the quantity and thickness of sand-rich channels that are only observed when sedimentology is investigated at such a fine scale. Following the method of Morris et al. (2009) rebound values taken at a bed-scale were undertaken within a 25 cm² circle and away from bed partings. This was not possible for sub-bed scale measurements due to the thin nature of the sedimentary units, which could act to increase variability in the rebound

values. The scale of observation and in particular the level of detail recorded by data gatherers has been noted to effect observation style in many other disciplines. For example, Scheiber et al., (2015) and Andrews et al., (2019) found that the fracture statistics extracted from lineament mapping depended on what scale of observation was used by data-gather.

For mechanically layered sequences it is often assumed that the vertical growth of joints is explicitly controlled by bed thickness (Ladeira and Price, 1981; Narr and Suppe, 1991; Soden et al., 2014). Joints form primarily in competent lithologies and rarely propagate into incompetent beds (Laubach et al., 2009). As layer-parallel strain is applied, fractures develop between existing fractures (termed sequential infilling), until no new joints may form and the bed becomes 'fracture saturated' (Wu and Pollard, 1995; Bai and Pollard, 2000). A primary control on fracture saturation is the thickness of the mechanical layer being stretched, which is typically assumed to be bedding (Ladeira and Price, 1981; Huang and Angelier, 1989; Narr and Suppe, 1991). This has led to bed-thickness representing a key aspect of models used to predict the growth and patterns of an evolving fracture network (e.g. Pollard and Aydin (1988); Olson (2004)). However, Hooker et al. (2013) highlight that bed-bound fractures represent an end-member case, and instead fractures may form as: a) perfectly bed-bounded; b) top-bounded; c) hierarchical; or d) unbound, depending on the location and distribution of fracture tips.

Bed-bound fractures were rarely observed at Whitley Bay and instead fractures typically terminate within the bed (Figure 4.6 & 4.8). Within fluvial deltaic sequences it is common to observe many sub-bed scale sedimentary features (e.g. mud-draped ripples, load and flame structures, and discontinuous mud-laminations) (Fielding, 1982; Fielding, 1985; Besly and Fielding, 1989; Thomas, 2013). Many of these features occur at a sub-bed scale, controlling some of the differences in the rebound values observed when mechanical stratigraphy was undertaken alongside cm scale logging (Figure 4.4b, 4.10). We found that the presence of organic rich layers, organic fragments (e.g. rip-up clasts), iron nodules, channel coals, and sandstone stringers strongly effected the height of joints and fault related fractures (Figures 4.10, 4.11). Small scale sedimentary features have been shown to effect the initiation of joints (McConaughy and Engelder, 2001), and complicate fault and fracture patterns in beds with a large number of heterogeneities (Cilona et al., 2016). During sedimentary logging these units are often clumped together as 'heterolithics', however, the detailed mechanical

stratigraphy profiles suggest that this is an over-simplification. It is important to note the mechanical strength, thickness, and extent of small features, along with quantifying the nature of the sedimentary structures observed.

We find mechanical stratigraphy to be a useful tool for informing the likely joint patterns found at Whitley Bay, however, care needs to be taken when applying this technique as the mechanical properties of a rock mass can change during diagenesis (Shackleton et al., 2005; Laubach et al., 2009; Hammer et al., 2010; Lavenu and Lamarche, 2018). For example, Lavenu and Lamarche (2018) found that early jointing was not effected by stratigraphic layering and large trace length, thorough-going features were observed. Instead it was only fractures relating to later tectonic events which were influenced by mechanical stratigraphy. This highlights the fact that mechanical stratigraphy and fracture stratigraphy can both coincide, show little relation to each other, and/or display a temporal evolution (Laubach et al., 2009; Laubach et al., 2018). For UK Carboniferous Coal Measures, fracture stratigraphy will likely match the mechanical stratigraphy due to the rapid burial of Carboniferous basins which only reached relatively shallow depths (e.g. 3km for the Midland Valley of Scotland (Monaghan, 2014)). This will have caused the mechanical stratigraphy to have been developed early during basin evolution, with properties potentially locally altered by later fault related fluid flow (Knipe, 1993).

The presence and orientation of small features within a rock mass has been shown to effect the strength and deformation style of several lithologies (Banks-Sills and Schwartz, 2002; Y.W. Li et al., 2016; Bubeck et al., 2017). Bubeck et al. (2017) found that the shape and aspect ratio of pores within porous lavas controlled the perturbation of stress throughout the sample. At Whitley Bay, isolated weak (channel coals) and strong (siderite nodules) inclusions are present throughout many fine grained lithologies with the location and orientation effecting the location of fractures. Where weaknesses are planar, it is the orientation of the plane relative to the applied stress which is a major control on rock strength and whether failure will occur (Hobbs, 1964; Ajalloeian and Lashkaripour, 2000; Whittles et al., 2002; Y.W. Li et al., 2016). For example, coal is weakest when cleats are orientated at an angle of 45° and strongest when orthogonal to an applied stress (Y.W. Li et al., 2016). Ripple laminations, which typically form at an angle between 10° and 30° will be more prone to shear-failure and less favourably orientated for the development of joints

leading to the observed termination of features against these features (e.g. Figure 4.10 & 4.11).

The use of branch properties, as opposed to fracture trace length, in the analysis of fracture networks has been shown by Sanderson and Nixon (2015) to reduce the effect of censoring, which can greatly effect derived fracture statistics (Zeeb et al., 2013). Branch data can also be combined with node-data, along with the spatial position of node data to inform on the style and connectivity of the joint network (see Figures 4.9). We find that while fracture trace length is elongated in a bed-parallel direction, branch length is typically elongated in the bed-perpendicular direction (Table 4.3). The ratio between bed-perpendicular and bed-parallel branch length varies depending on lithofacies (Table 4.3) with values ranging from 1.25 for S1 up to 7 for S6. This ratio is controlled by the vertical restriction of fractures caused by the mechanical contrasts, and the number and intensity of joint sets in the given lithology. It was found that branches in the bed-parallel view were more varied (QCV= 1.2 to 1.9) compared to the bed-perpendicular view (QCV = 0.8 to 1.4). This suggests that the height of fractures, which is controlled by systematic variability in sedimentology, will be easier to predict than bed-parallel branch length.

Sx	Bed-parallel branches (a)				Bed-perpendicular branches (b)				Aspect ratio b:a
	Median (m)	QCV	Skew.	\bar{x} Pc	Median bl	QCV	Skew.	\bar{x} Pc	
1	0.04	1.3	3.1	0.96	0.05	1.0	16	0.41	1.25
2	0.04	1.2	5.4	0.88	0.06	1.4	3.7	0.54	1.5
3	0.05	1.9	2.0	0.88	0.13	1.3	2.2	0.36	2.6
4	0.04	1.9	2.3	0.94	0.10	1.3	6.3	0.36	2.5
5	0.02	1.5	4.9	0.91	0.12	1.2	2.0	0.45	6
6	0.01	1.4	2.5	0.92	0.07	0.8	2.6	0.48	7

Table 4.3: Branch aspect ratio

4.5.2 The effect of mechanical stratigraphy and sub-bed scale sandstone bodies on fluid flow.

Joints and fault-related fractures play an important role in the flow of groundwater in deltaic sequences with bed-parallel flow dominant (Ferrill et al., 2014; Dochartaigh et al., 2015). Because of the presence of laterally continuous low-permeability layering, whether there will be up-section flow will depend on the presence of through-going fractures, which

we find to be a function of both lithology and bed thickness. For example, in beds which are less than 5 cm thick, through-going fractures dominate. However, in the majority of beds sub-bed scale mechanical contrasts lead to i-nodes forming within the bed (Figure 4.8). In map-view all lithofacies display high connectivity ($P_c = 0.88$ to 0.96), suggesting that bed-parallel flow would be favoured in these lithologies.

The orientation of fractures relative to the regional stress state has been shown to affect which fractures are open to flow (Cherubini et al., 2014). The collection of fracture data from field analogues is often biased towards competent lithologies (e.g. sandstone and limestones), with incompetent lithologies such as shale often under-sampled. We demonstrate that both the strike and dip of joints vary considerably between different lithofacies (Figure 4.6). This is particularly the case in beds that display low mechanical strength and fine grain size, with joints in S1 and S2 formed in a far greater range of orientations than from regional trends. Fracture flow is particularly important in shale reservoirs (e.g. Jardine et al. (1999)) and the variability in joint orientations could lead to the development of unexpected flow pathways.

At Whitley Bay evidence of paleo fluid flow can be found through: i) calcite mineralisation of coarse sandstone beds; ii) ankerite mineralisation of fractures and cleats in coal; and iii) diagenetic alteration halos. Calcite mineralisation is only found in the proximity to fault zones within the clean sandstones (S5). Similar to many other tectonic settings (e.g. Bristol Channel, Somerset (Peacock, 2001)), the mineralisation is associated with strike-slip faulting, with these joints potentially becoming reactivated during fault slip. Ankerite mineralisation of coal is often observed both in proximity to, and away from faults. Mineralisation occurs along the E trending fracture set and the NW trending face-cleats which display evidence of reactivation.

Diagenetic halos are observed at multiple locations throughout the outcrop, and are typically confined to heterolithic beds (S3 and S4) and seat earth (S5). The method of formation of diagenetic halos are difficult to deduce with some authors suggesting they form in response to sub-surface fluid flow (Taylor et al., 1999; Eichhubl et al., 2009) and other suggesting near-surface groundwater processes (Nriagu and Dell, 1974; Johnson and Huntoon, 1994; Whitaker and Smart, 1997). Regardless of the type of fluid these halos provide evidence of flow pathways through the succession and can be used to investigate which fractures that were conductive to flow (e.g. Taylor et al., (1999)). In the lithologies

surrounding and including seat earth (Figure 4.10b), alteration is observed surrounding steeply dipping through-going fractures. Alteration is more commonly observed where fractures intersect sandstone stringers. Where an alteration front is observed in both sandstone and fine-lithologies, the width is higher within the sandstone and a 'butterfly' alteration pattern is developed (see the fraction to the top left of Figure 4.10b).

Diagenetic halos in S4 are observed not only around fractures, but also along sedimentary beds (Figure 4.11d, g and h). For example, in Figure 4.11d alteration halos around sub-vertical joints are connected by laterally continuous thin (<1.5 cm) coal interbeds within the heterolithic beds towards the base of the outcrop. In Figure 4.11g a similar arrangement is observed, coupled with a 'butterfly' alteration pattern, and alteration surrounding organic rich ripples. In Figure 4.11h alteration jumps from one laterally discontinuous channel coal to another through several moderately dipping organic partings.

The diagenetic halos at Whitley Bay demonstrate the importance of considering not only the connectivity of the fracture network, but also the relative permeability and connectivity of potential sedimentary controlled fluid pathways. McCay et al., (2019) observed similar trends when undertaking detailed field mapping of paleo fluid-flow networks in shales. They found that fluid flow episodes occurred through a combined network of fractures or joints and thin sand-rich turbidites, and without the presence of both elements flow would not be possible. The presence of channel coals at Whitley Bay provides a similar 'sedimentary' element to the fluid flow network.

4.5.3 Use of field data for assessing sub-surface fracture patterns

Discrete Fracture Networks (DFNs) are often used in order to predict the sub-surface fluid flow (Min et al., 2004; Bigi et al., 2015; Romano et al., 2017) and strength of a fractured rock mass (Jing and Hudson, 2002; Harthong et al., 2012). To populate these models several fracture parameters need to be classified which include trace length (mean and distribution), fracture abundance (intensity and density), and connectivity. However, the direct sampling of fault and fractures from the sub-surface is challenging and typically limited to the 1D fracture analysis of core. Joints, which are open-mode (Mode 1) fractures that form at 90° to the minimum applied stress (σ_3) (Pollard and Segall, 1987), commonly form at a high angle to bedding. The orientation of joints combined with vertical drilling leads to the under sampling of sub-vertical joint sets.

This is highlighted in the research borehole GGC01 which was cored as part of the £9 million UK Geoenergy Observation (UKGEOS) project to de-risk mine geothermal projects (Monaghan et al., 2017). The reported data are available in the intermediate data release (Kearsey et al., 2019), with the relevant findings reported here. While the stratigraphy was well documented, with features such as bed-boundaries, dip of bedding, lithology, sedimentary features, and grain size recorded, only 97 discontinuous (discounting coal cleats) structures were identified in 160 m of core. These features included 38 veins, 18 non-mineralised joints, 28 slip surfaces, 10 faults and 3 other features, with their location unevenly distributed and controlled by stratigraphic layering. This is in contrast to outcrop exposures of Carboniferous lithologies in the Midland Valley of Scotland where competent lithologies often display penetrative joint patterns (e.g. Sandstones and Limestones exposed at Spireslack SCM (Leslie, Browne, et al., 2016; Healy et al., 2017)).

At Whitley Bay we demonstrate that lithology and sub-bed scale heterogeneity strongly effects the fracture properties of the network in both bed-parallel and bed-perpendicular view. Small-scale sedimentary features are often relatively laterally extensive, and orientated roughly perpendicular to the direction of drilling which enables them to be sampled in core. For example, in borehole GGC01 features such as 5 cm wide siderite nodules, continuous mussel bands, *Diplocraterian* burrows, and mud-drapes were recorded (Kearsey et al., 2019). The abundance of sedimentary information available through core, coupled with comparisons to modern day processes, has enabled predictive models to be proposed for several environments (e.g. deep-water succession (Shanmugam et al., 1996; Garland et al., 1999; Porter et al., 2006), ramp carbonates (Al-Awadi et al., 2017), and deltaics (Nordahl et al., 2006; Hamilton et al., 2014)). For example, Nordahl et al (2006) used observations of sedimentary structures (e.g. combined-flow ripple cross laminations) at a mm-scale and time-series analysis to produce a predictive model for the sand and mud content in heterolithic ripple-laminated deposits. Due to the importance of such features in controlling fracture propagation, the ability to predict the spacing of particular sedimentary structures could lead to better understanding of probable fracture height in such lithologies. The use of core has also enabled the prediction of sedimentary facies and how lithology and sedimentary structures vary throughout a basin (e.g. Shanmugam et al., 1996).

Our work suggests that within a specific depositional setting it is possible to predict the typical topological and geometrical properties of a fracture network based on sedimentary information. It should be possible to apply a 'mechanical facies' to a lithofacies with a reasonable amount of confidence, which will capture some of the sedimentary variability observed within each lithofacies. Using the data from Whitley Bay, a set of typical network properties (Table 4.4) could be added to individual beds either recorded through core or predicted through subsurface geomodels, enabling the typical height of fractures to be deduced.

Due to inherent difficulties in directly sampling sub-surface fracture patterns, and our ability to produce complex sedimentological models, it is clear that the identification of links between stratigraphic layering and fracture attributes is key to enable extrapolation of the fracture network into areas which are not directly sampled (e.g. sparse outcrop, under-sampled or the subsurface) (Narr, 1991; Morettini et al., 2005; Laubach et al., 2009).

4.6 Conclusions

Geoscientists, like many scientists become highly specialised and data collection methods become too focused on the collection of specific types of data, that separate completely isolated strands of geoscience develops? [i.e. structural geologists that don't understand sedimentary processes and vice versa). This study highlights the power of interdisciplinary research through combining detailed sedimentology with fracture mapping to provide insights into the fundamental controls on fracture characteristics. We find that lithology and sub-bed scale heterogeneities combine to strongly effect the style and properties of a fracture network. This enables beds to be split into mechanical facies with distinctive properties. These properties vary depending on whether fractures are observed in the bed-parallel or bed-perpendicular plane. In the bed-parallel view networks are typically well connected, however, in section view joints terminate within the bed. This is particularly the case for heterolithic sequences such as S3 and S4, and the characteristic height of fractures correlated to the percentage of bed-thickness in all but the thinnest beds. Within coal-bearing successions, there are an abundance of weak laminations and sedimentary structures (e.g. coal-drapes or mud-draped ripples) leading to the termination of joints within the bed.

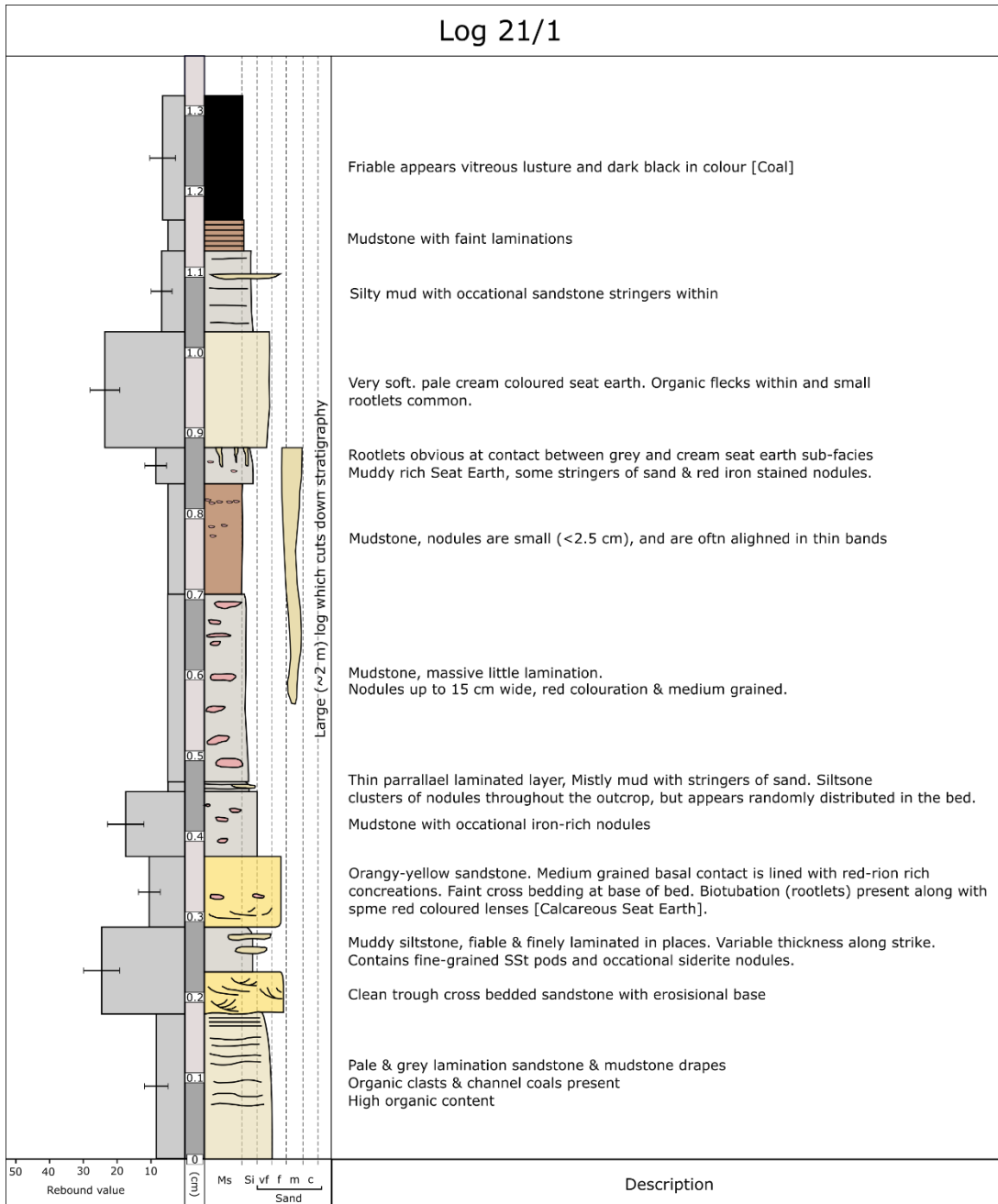
We suggest that because the lithology and sedimentary architecture of a target resource (e.g. hydrocarbon play or geothermal target) can be reliably sampled and/or predicted, that

sedimentary information combined with knowledge of the regional stress field can inform probable fracture properties. In particular, the height of fractures, which is related to the presence and frequency of sub-bed scale heterogeneities, should also be predictable. With recent advances in the modelling of sedimentary processes, the combination of detailed sedimentological logging, and fracture mapping has the potential to improve our understanding of sub-surface fracture networks not just in coal-bearing sequences, but in a wide range of sedimentary settings. The ability to predict sub-seismic fracturing, in particular how penetrative a fracture set is (i.e. fracture height), is key to understanding sub-surface fluid flow. The clay-rich nature of the lithologies at Whitley Bay suggest such successions could be targeted as a regional seal for hydrocarbon or CO₂ reservoirs. However, depending on the fractures leakage pathways could develop leading to the loss of resource or surface leakage of stored CO₂. This work represents an initial attempt to utilise detailed sedimentary logging to inform fracture development and represents a potential workflow to inform the deformation style of mechanically stratified, fracture-controlled plays (e.g. Southern North Sea gas fields).

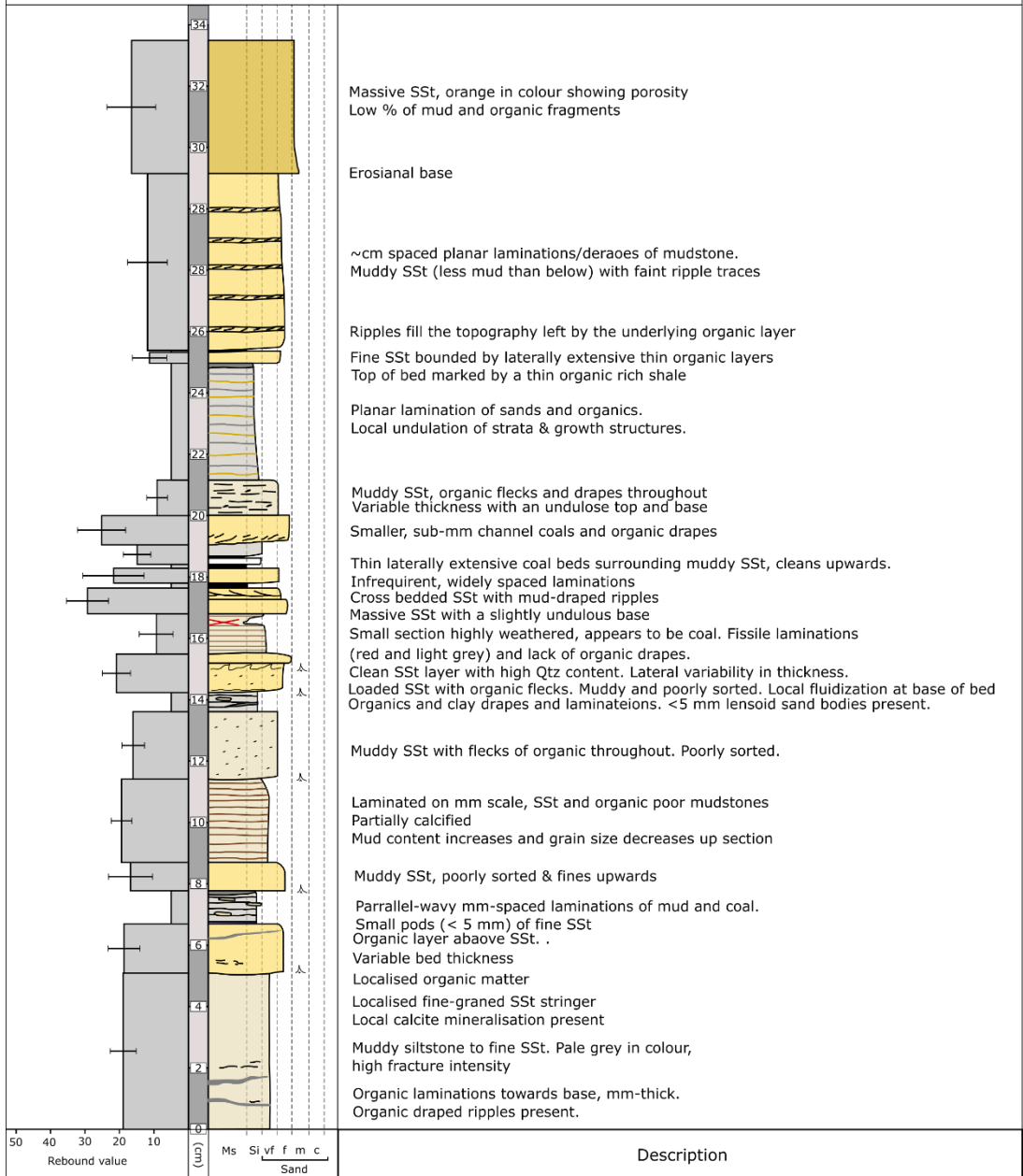
Sx	R-values	Joint Strike	Sub-bed scale features	A.R.	Trace (tl) and branch length (bl) characteristics.		Topology & connectivity
1	<10 (\bar{x} = 6.5)	Highly variable with several curved fractures and no clear orientation trends.	Laterally extensive sub-bed features (e.g. laminations or elongated siltstone pods) cause features to terminate within bed. Iron concretions common which localised small tl, well connected fractures. Fining/coarsening up sequence cause features to curve.	1.25	Map	Low TL, with 87% of branches below 0.1 m.	2:1 y-node : i-node ratio [Pc = 0.96]
					Section	Low TL and strongly negatively skewed distribution and few through-going fractures. Features terminate against sub-bed scale features within the bed (97%). Average bl 0.35	I-nodes within the bed dominate. y-nodes internal to bed. [Pc = 0.41]
2	<10 to 20 (\bar{x} = 11.3)	Trends visible, however, most joints display a high degree of curvature.	Where S4 or S5 are loaded into S2, fractures are localised towards the point of the flame and into the overlying bed. Rootlets and channel coals often localise joint formation.	1.5	Map	Low TL, with majority of branches below 0.1 m. Highly negatively skewed [5.4].	2:1 y-node : i-node ratio [Pc 0.88]
					Section	Branches rarely exceeded 0.7 m (majority between 0.2 and 0.3 m). 92% terminate within bed. TL 45% of bed thickness.	i-nodes dominate, typically at bed boundaries (57%). Greatest proportion of y-nodes, y-nodes internal to bed [Pc = 0.54]
3	7.7 to 31.6 (\bar{x} = 16.1)	Well defined peaks, which match the regional fracture trends.	High percentage of organics (e.g. organic draped ripples) act to both localise, and terminate joints. Sandstone stringer control vertical restriction of joints and width of alteration zones.	2.6	Map	less skewed tl distributions, low median bl of 0.05 m.	Y-note dominant [Pc = 0.88]
					Section	Large BL features branch at mechanical boundaries. Features dip steepens or shallows up section. 83% features terminate within the bed with average bl 86% of bed thickness.	I-nodes within the bed dominate. Y-nodes may occur at the base and top of bed. [Pc = 0.36]
4	8.9 to 34.7 (\bar{x} = 23.9)	Well defined peaks, which match the regional fracture trends.	Where S4 loads into S2, joints form at the tip of flames and propagate into S4. Ripples terminate joints where organic/mud is present, however, silt-draped ripples have little effect. Distributed organic fragments and rip-up clasts may localise jointing and increase intensity.	2.5	Map	Dominated by fractures below 0.2 m (29%). Large tl joints controlled by abutting relationships.	Y-note dominant, Ironstone layers contain abundant x-nodes. [Pc = 0.86]
					Section	Large BL features branch at mechanical boundaries near top of bed. Planar joint traces. Bl correlates to sub-bed packages & 87% terminate within the bed with average bl of 62% bed thickness.	I-C dominate & highest number of I-I. Y-nodes may occur at the top and base of bed. [Pc = 0.36]
5	23.5 to 46.6 (\bar{x} = 31.1)	Sparsely spaced joint sets, which display a reasonably match to regional trends. Some curvature observed in fracture off-trend fractures.	Due to the low clay content of ripple laminations, joints rarely interact with sub-bed features. Joints localised at the tips where channels pinch, and where fractures interact at the top of beds.	6	Map	TL normally distributed (1.47) around 0.35 to 0.4 m. Bl negatively skewed with 22% of branches below 2.5 cm.	Y-note dominant. [Pc = 0.91]
					Section	Similar to S4 but more features that are thoroughgoing (16% fractures). Average bl 59.3% of bed thickness.	I-nodes within the bed dominate. y-nodes internal to bed. [Pc = 0.45]
6	11.2 to 16.4 (\bar{x} = 13.6)	Joint strike matches that, or slightly rotates that of the cleat network.	Fractures strongly interact with cleats, which control the orientation and trace length of joints in both planes of observation.	7	Map	Fracture orientation and trace length (both planes of observation) strongly affected by bed partings and pre-existing cleat network. Fractures occur as fracture corridors in map view.	Predominantly y-nodes interacting with cleats. [Pc = 0.92]
					Section		Nearly all i-nodes occur within the bed. y-nodes internal to bed [Pc = 0.48]

Table 4.4: Summary of typical joint properties. Note: there are not enough data points to fully classify S5a.

Appendix: Sub-bed scale sedimentary logs



Log 21/4



Chapter 5: The role of pre-existing jointing on damage zone evolution and faulting style of thin competent layers in mechanically stratified sequences, a case study from the limestone coal formation at Spireslack SCM.

B. J. Andrews¹, Z. K. Shipton¹, R. Lord¹, L. McKay¹

¹Department of Civil and Environmental Engineering, University of Strathclyde, 75 Montrose Street, Glasgow, G1 1XJ, UK

5.1 Abstract

Fault and fracture networks play an important role in sub-surface fluid flow, and can act to enhance, retard or compartmentalise groundwater flow. In multi-layered sequences, the internal structure and growth of faults is not only controlled by fault throw, but also the mechanical properties of lithology cut by the fault. This chapter uses geological fieldwork, combined with fault and fracture mapping, to investigate the internal structure and faulting behaviour of the mechanically stratified Limestone Coal Formation and surrounding lithologies exposed at Spireslack SCM (Surface Coal Mine). We find that the development of fault rock, and complexity of a fault zone is dependent on: a) whether a fault is self-juxtaposed or cuts multiple lithologies; b) the presence and behaviour of shale, which can lead to significant bed-rotation and the formation of fault-core lenses; and c) whether pre-existing weakness (e.g. joints) are present at the time of faulting. Pre-existing joint networks in the McDonald Limestone, and cleats in the McDonald Coal, control both fault growth and the fluid flow evolution of these lithologies. We demonstrate the importance of integrating fieldwork with lineament mapping, and consider how flow properties of a network are effected by mineralisation and regional stress states. Fieldwork was undertaken for this chapter by BJA and LM, fracture mapping undertaken by BJA. The text and figures were prepared by BJS, with all authors involved in the editing process.

5.2 Introduction

The mechanical properties, thickness, and interface properties of lithologies in the succession combine to influence the style of deformation (e.g. Ferrill *et al.* (2017)). The effect of 'mechanical stratigraphy' on faulting, in particular normal faulting, has been studied for sand-shale sequences (e.g. van der Zee & Urai (2005); Schmatz *et al.* (2010)), interbedded limestones and marls (e.g. Ferrill & Morris (2003), (2008); Long & Imber (2011); Ferrill *et al.* (2012)), and ignimbrites (Soden and Shipton, 2013). The dip of a fault depends on the lithology being cut, such that strands in competent layers display steeper dips than those in incompetent layers (Ferrill and Morris, 2008). The ratio of competent to incompetent lithologies affects the observed fault style and displacement profiles (Ferrill and Morris, 2008; Ferrill *et al.*, 2017). Folding is commonly observed where incompetent layers dominate, with thin competent lithologies displaying fault-related folding (Ferrill and Morris, 2008; Lăpădat *et al.*, 2017). Fault growth is often vertically restricted and strands terminate in incompetent lithologies, leading to faults with high aspect ratios orientated parallel to the strike of bedding (e.g. Nicol *et al.* (1996); Soliva & Benedicto (2005); Roche *et al.* (2013)).

Fluvial-deltaic sequences are characterised by cyclical sequences containing limestone, sandstone, siltstone, seat-earth, shale and coal (Thomas, 2013). The competent lithologies in the sequence (limestones and sandstones), commonly contain joints, similar to many sedimentary rocks. Coal is a unique sedimentary rock with a distinctive blocky texture due to the presence of two roughly perpendicular fracture sets called cleats (Laubach *et al.*, 1998). Joints and cleats can represent pre-existing weakness which can affect the location, orientation and length of faults (e.g. Peacock (2001); Walsh *et al.* (2002)). The impact of weaknesses on fault growth depends on the orientation of a weakness relative to the growing fault and the stress ratio (Peacock, 2001; Rebecca J. Lunn *et al.*, 2008; Peacock and Sanderson, 2018). The presence of pre-existing weaknesses has also been shown to affect the development of fault rock. For example, Soden & Shipton (2013) showed that layer and joint spacing in ignimbrites effected the aspect ratio of clasts found within the fault core.

The relationship between faulting and mechanical stratigraphy can be used to predict structural style for normal faults (Ferrill *et al.*, 2017). While the role of mechanical stratigraphy on normal faults have received considerable attention, relatively few studies have focused on strike slip faults (Sylvester, 1988; Gross *et al.*, 1997; Nemser and Cowan,

2009). Strike-slip faults play an important role in the deformation of the upper-crust (e.g. Sylvester (1988)), and many basins display evidence of transtension (e.g. The Midland Valley of Scotland (Ritchie et al., 2003) and the Northumberland Trough (De Paola et al., 2005) in the UK). With the abundance of small-offset strike-slip faults in these basins, it is of increasing importance to be able to predict the behaviour of such structures. This will have applications for hydrocarbon extraction (e.g. Gamson *et al.* (1993); Shuichang *et al.* (2009)), shallow geothermal projects (e.g. Malolepszy (2003)), carbon capture and storage (Solomon, 2007) and geotechnical engineering (Donnelly, 2006).

This chapter utilises exceptional exposures of the Limestone Coal Formation exposed at Spireslack SCM (Surface Coal Mine), Scotland, to investigate the effect of lithology and pre-existing structures on the growth of strike-slip faults. Field mapping at a 1: 1,000 scale was undertaken onto field photographs to identify the key structures and kinematics. Fault and fracture mapping onto high resolution photomontages of the high-wall and dip-slope were then used to investigate the interaction of faults and fractures with lithology and pre-existing joint sets. High offset faults are thin (<0.3 m), display a complex deformation pattern, and locally branch entraining lenses of sandstone. We find that pre-existing joints and lithology strongly effect the growth and fluid flow history of small offset, self-juxtaposed, faults.

5.3 Geological setting

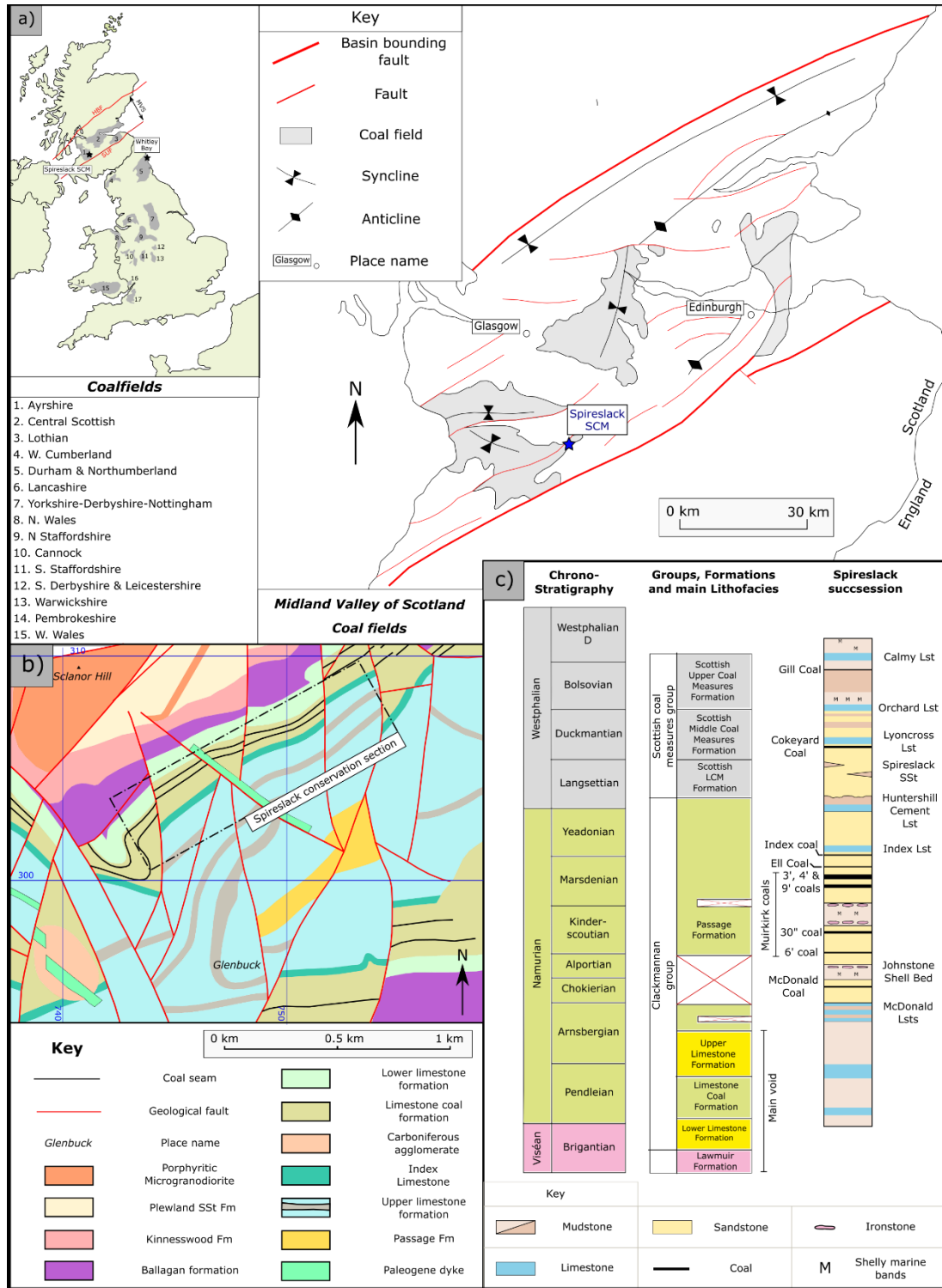


Figure 5.1: Location map: a) Map of UK coalfields (adapted from Donnelly (2006)) showing the location of Spireslack SCM and Structural features of the Midland Valley of Scotland; b) Regional geology of Spireslack open cast coal mine (after Ellen et al. (2019)); c) Regional stratigraphy of Spireslack SCM (after Ellen et al. (2019)).

The Midland Valley of Scotland (MVS) is one of many basins, including the Northumberland Basin to the South, that opened during late Devonian to Early Carboniferous times in response to back-arc extension within the Laurussian Plate (Leeder, 1982; Leeder, 1988). This was followed by a period of thermal subsidence which continued throughout Namurian and Westphalian times (Leeder, 1982) leading to the deposition and preservation of thick coal measures across much of the UK. The location and style of rifting was strongly controlled by pre-existing Caledonian structures (e.g. the Iapetus suture) (Soper et al., 1987). The fill of these basins varied both spatially and through geological time and was controlled through a combination of movement along basin bounding faults, marine incursions, and location of regional highs (Cope et al., 1992).

The MVS is a 90 Km wide 150 km long, ENE-trending graben which runs parallel to and is bounded by two major tectonic lineaments, the Southern Upland Fault (SUF) to the south and Highland Boundary Fault (HBF) to the north (Figure 5.1) (Bluck, 1984). Carboniferous rocks occur in a number of basins with axes that are oblique to the main trend of the MVS (e.g. Central Scottish Coalfield; Francis (1991)). These basins can reach over 6 km in thickness (Dean et al., 2011), however, they are often obscured by Quaternary deposits. The MVS is separated from Carboniferous basins to the south (e.g. the Northumberland Trough) by the Southern Uplands Block and the Scottish Highlands to the North which both represent emergent areas during much of the Carboniferous period (Cope et al., 1992). Faults with localised associated folding within the MVS have a complex history of reactivation caused by a sinistral strike-/oblique-slip during the Tournaisian and dextral strike-/oblique-slip during Viséan to Westphalian times (Browne and Monro, 1987; Rippon et al., 1996; Ritchie et al., 2003; Underhill et al., 2008). These regional-scale faults, combined with fracture systems, combine to influence groundwater flow (Rippon et al., 1996; Dochartaigh, 2004; O Dochartaigh, 2009).

5.3.1 Spireslack SCM

The decline of open cast coal extraction in Scotland has led to the availability of several disused open cast coal mines for geological study (Leslie, Browne, et al., 2016). One example is Spireslack SCM (Figure 5.1), located at the now abandoned coal mining village of Glenbuck, South Ayrshire (Scotland). Spireslack SCM provides an exceptional exposure of Carboniferous rocks through a 1-km long void with a 20° - 40° southerly dipping dip-slope along bedding planes and an <130 m high working face. The stratigraphy, which can be

easily traced across the high wall, includes a continuous succession of Viséan to Namurian strata which includes a complete section through the Limestone Coal Formation (Figure 5.1c), one of the most economically important coal bearing successions in Scotland (Ellen et al., 2016; Ellen et al., 2019). Bituminous coal is found in cyclical fluviio-deltaic sequences which outcrop across much of the dip-slope and high wall, bounded by the Upper and Lower Limestone Formations. The Lower Limestone Formation represents more marine-influenced facies including extensive, fossil-rich limestone units (e.g. The McDonald Limestone) (Davis, 1972). Above the Limestone Coal Formation is an outcrop of the Spireslack Sandstone comprising of one channelised, and two tabular, sandstone beds (Ellen et al., 2019).

Clearly visible offsetting this stratigraphy are several fault zones with shallow slip vectors and variably complex internal structures. In addition to the faults, at least 5 Paleogene basaltic dykes are observed, which Leslie *et al.* (2016) suggest intrude along pre-existing faults. Rocks exposed at Spireslack SCM form part of the Southern Limb of the upright, WSW-ENE trending Muirkirk syncline which formed in response to mid- to late-Carboniferous sinistral transpression (Davis, 1972; Leslie, Browne, et al., 2016). Leslie *et al.* (2016) attribute the faulting and folding observed at Spireslack SCM to this deformation phase, and have observed no evidence of the later widespread dextral- stress state (e.g. Underhill *et al.* (2008)).

5.4 Methods

5.4.1 Field mapping

Geological mapping of the dip-slopes was carried out capturing all units between the sandstones and shales below the McDonald Limestones and the sandstone bed above the Muirkirk 6' Coal (Figure 5.1, 5.3). Mapping was undertaken at a 1: 1,000 scale onto printed Bing (2017) aerial photography. All faults with >0.2 m offset were recorded. Printed field photographs were used to collect more detailed observations at several key sites.

5.4.2 Analysis of fault and fracture networks

To classify the properties of a fault and fracture network it is important to understand the geometrical and topological relationships and combine this with basic geological descriptions, age relationships, and fracture kinematics (Sanderson and Nixon, 2015; Sanderson et al., 2018; Peacock and Sanderson, 2018). Fractures typically form as a number

of distinct sets with similar fracture properties (Singhal and Gupta, 2010; Gutierrez and Youn, 2015). Fracture sets can be classified on either age and/or orientation (Peacock and Sanderson, 2018). The properties of individual sets, and the network as a whole can then be investigated to understand regional tectonics, fluid flow properties, and/or mechanics of a rock mass (Hooker et al., 2011; Bigi et al., 2015; Lei et al., 2017; Peacock and Sanderson, 2018).

For the purposes of fracture modelling (e.g. the creation of discrete fracture networks to model up-scaled permeability (e.g. Chesnaux *et al.* (2009); Bigi *et al.* (2013); Romano *et al.* (2017)), fracture trace length and trace length distribution are important characteristics to extract from the network (e.g. Priest (1993); Watkins *et al.* (2015); Andrews *et al.* (2019)). Challenges in interpreting the trace lengths of individual fractures include: the scale of observation (Zeeb et al., 2013; Scheiber et al., 2015); the classification of fracture intersections (Peacock *et al.* 2019.; Ortega & Marrett 2000); the presence of fracture fill (Olson et al., 2009); and the subjective biases and interpretation style of the user interpreting the network (Peacock *et al.* 2019.; Scheiber *et al.* 2015; Andrews *et al.* 2019). Fracture intensity (I) is the number of fractures normalised based on the size of the sample line or area and is often referred to as P_{10} or P_{20} (Dershowitz and Einstein, 1988; Sanderson and Nixon, 2015).

Fracture topology describes a fault or fracture network as a series of branches and nodes (e.g. Manzocchi (2002); Sanderson & Nixon (2015),(2018)). A branch is a fracture trace with a node at each end. Nodes can occur where a fracture: terminates into rock (i-node); abuts against another fracture (y-node); or crosses another fracture (x-node). The proportion of different node types (i, y, and x) can be plotted on a triangular diagram for the purposes of characterising and quantifying the connectivity of the network (Manzocchi, 2002; Sanderson and Nixon, 2015). In this work we interpret fault and fractures as orientation sets and report fracture/branch trace length (tl), 2D fracture intensity (I), and the percentage of connected branches (P_c). The chronology of the fault and fracture network is investigated at several locations within the sample areas to ensure consistency in interpretation.

5.4.2.1 Mapping procedure

Fault and fracture mapping were undertaken using two data-sets: (a) a UAV derived photo-montage of the McDonald Limestone bedding plane collected by Dave Healy of Aberdeen

University; and (b) an auto rectified photomontage of the high wall collected by the British Geological Survey. Interpretation areas were selected from the dip-slope and high wall for further analysis to understand the geometrical and topological properties, and cross cutting relationships of fault strands and joint sets. The interpretation areas were scaled in ArcGIS with mapping being undertaken by the lead author at a scale of 1:30 for the dip-slope and 1:50 for the high wall. Lineament mapping was undertaken by the same operator, at the same scale, to limit the effect of subjective bias on the data collected (Scheiber et al., 2015; Andrews et al., 2019).

5.4.2.2 Network analysis

Once the faults and fractures were digitised, a visual assessment of the network was undertaken followed by network analysis using the open source ArcGIS toolbox NetworkGT (Nyberg et al., 2018) using the following workflow:

1. *Defining sets*: A number of ‘interpretation boxes’ were added to the ArcGIS file (with three along both the dip-slope and high wall) as a shape file and the orientation of faults and the fractures within them analysed. Based on this analysis fracture traces were organised into ‘orientation sets’ using the ‘sets’ function. Sets were selected based on length-weighted rose diagrams with 5° bin widths. The digitised fault and fracture data sets were then combined, using the merge function in ArcGIS, and all three data sets were investigated separately.
2. *Branch & Nodes*: The topology of the network was extracted using the ‘Branch and Node’ tool, which splits the fracture trace poly-line file into individual branches, and assigns nodes as a separate point-files (Nyberg et al., 2018). The resulting network was visually checked for errors (e.g. incorrectly assigned nodes) and manually adjusted in ArcGIS to remove spurious nodes and branches. Data were then exported to excel for further analysis.
3. *Network analysis*: For each network, the following data was extracted;
 - a. *Network connectivity*: This was carried out for each network, with the data not split into sets. The node and branch proportions were visually assessed using a triangular diagram (c.f. Sanderson & Nixon (2015)). The percentage of connected branches was then calculated using Equation 1.

$$P_c = \frac{(3N_y + 4N_x)}{(N_i + 3N_y + 4N_x)} \quad (\text{Equation 1})$$

b. *Trace length*: The trace length of digitised networks and sets within each sample area were assessed using trace length distributions (Priest and Hudson, 1981; Andrews et al., 2019), with the minimum, maximum, and median trace length values used to compare analysis. Because trace length distributions were negatively skewed, the Quartile Coefficient of Variance (QCV; Equation 2) was used to compare the degree of variability within each sample.

$$QCV = \frac{Q3-Q1}{Q2} \quad (\text{Equation 2})$$

c. *Censored fractures*: The percentage of censored fractures is important, with data sets containing a high proportion of censored fractures leading to the under-estimation of trace length parameters (Zeeb et al., 2013). The percentage of censored branches as calculated by Equation 3.

$$C_b = \frac{\text{number of censored branches}}{\text{total number of branches}} \times 100 \quad (\text{Equation 3})$$

d. *2D fracture intensity*: We compare the intensity of the networks and sets within the network using 2D fracture intensity (P21; Dershowitz & Einstein (1988); Rohrbaugh et al. (2002)). This is calculated using Equation 4.

$$P21 = \frac{\sum tl}{\text{Area}} \quad (\text{Equation 4})$$

5.5 Results

5.5.1. General fracture observations

Fractures at Spireslack SCM typically occurs in two orthogonal directions (typically NS and EW) that vary throughout the site and we classify them as either joints, shear fractures, or fault-related fractures. We describe in detail the fracture network style and properties (including mineralisation) for fracture patterns in the McDonald Limestone and Muirkirk 6' Coal, before briefly summarising the style of fracturing observed in other lithologies.

Joints in the McDonald Limestone, away from faulting form two orthogonal sets of barren joints, trending roughly NE-SW and NNW-SSE. Orientation of these sets vary, with up to 20° of strike rotation observed throughout the site. Cross cutting relationships show that there are multiple 'age sets' (Figure 5.2a), with NE-SW joints forming initially, followed by sparsely spaced NE-SW joints. Then more NE-SW joints, which abut against the pre-existing

NNW-SSE trending joints. Finally, a dense network of NS joints abuts against both sets of EW trending joints.

In the limestone the majority of joints are barren, some display calcite mineralisation (Figure 5.2b). Mineralisation occurs in the vicinity of, and along, faults. As shown in Figure 5.2b, mineralisation typically occurs along the second NW trending set, with pre-existing joints that are not in this orientation remaining barren. Mineralisation occurs as two styles: 1) amorphous, where no growth structures are present and occasional fragments of limestone can be observed within the mineralised zone (referred to as matrix supported breccia), or 2) with syntaxial growth textures suggesting both sinistral and dextral motion during mineralisation. Within a few meters of faults, composite veins are commonly observed, with multiple stages of growth and reactivation of the fracture (Figure 5.2c).

Fractures in the coal layers are commonly filled with a buff-orange coloured mineralisation, interpreted as ankerite (iron rich carbonate) (Figure 5.2d-f). Fractures in coal occur as:

- *Coal cleats*: Ubiquitous in all coals. Spacing (typically <2 cm at Spireslack SCM) is dependent on bed-thickness, coal quality and the presence of clastic material (e.g. shale partings) (Laubach et al., 1998).
- *Mineralised shear fractures*: Form as planar ankerite veins, whose thickness is related to the length of the fracture. Typically, 2 to 15 cm in length, but increase to over a meter as apparent shear offset increases. Fractures less than 15 cm long abut against EW trending cleats, with trace length restricted by cleat spacing.
- *En-echelon arrays*: En-echelon veins of ankerite are observed, displaying both sinistral and dextral motion (Figure 5.2d). Dextral strands occur both simultaneously to, and later than, sinistral arrays.
- *Barren shear fractures*: In addition to the cleat-network, fractures with trace lengths typically between 5 to 15 cm are present which abut against all other fractures. Unlike other fracture types, these are often curved and may propagate from the tip of pre-existing mineralised shear fractures (Figure 5.2d).

A complex evolution of fractures is often observed in the Muirkirk 6' coal. In Figure 5.2d dextral offset en-echelon vein arrays (red) may be observed cross cutting earlier sinistral sets (blue), with the former abutting against mineralised shear fractures. Barren shear fractures then abut against both sets displaying a curvature indicative of a dextral stress

state. The barren shear fractures likely formed at the same time as the dextral en-echelon vein array, however, they were not connected to a source of mineral rich fluids. In Figure 5.2e, multiple phases of mineralisation and reactivation of veins for later slip can be observed. Veinlets of ankerite both abut against, and cut through the calcite vein associated with a nearby small (<5 cm) offset fault. Brecciation of coal and calcite is also observed, with undisrupted ankerite veinlets cutting through the breccia. This requires to a minimum of three stages of deformation:

- 1) Ankerite veinlets formed along the NS striking face-cleats.
- 2) Faulting lead to the development of coal breccia and calcite veining which either cut across or abutted against pre-existing structures.
- 3) Brecciation of the calcite vein and coal led to the development of a chaotic fault breccia. The breccia contains angular clasts of coal and calcite within an amorphous calcite matrix.
- 4) Finally, there was a return to ankerite mineralisation, with dextral en-echelon arrays which developed alongside locally barren tip-damage zones.

These observations allow a conceptual model of growth of initial deformation and associated mineralisation occurred over a wide zone of en-echelon arrays (Figure 5.2d), which was strongly influenced by the pre-existing cleat network (Figure 5.2e). En-echelon arrays then began to interact, leading to the development of localised mineralised shear fractures (Figure 5.2f). As the trace-length of the shear fracture increased, as did thickness of the zone leading to the formation of a dense array of small offset (<1 cm) strands which interacted through the development of relay-zones. A later dextral stress state, occasionally reactivated features (Figure 5.2e) and lead to another phase of en-echelon veins (Figure 5.2c), which also locally developed into mineralised shear fractures.

The rest of the lithologies in the sequence display a strongly developed fracture stratigraphy (c.f. Laubach *et al.* (2009)). The McDonald Seat Earth exposed in the western panel (Figure 5.3a) lacks a well-developed joint pattern. Instead fracturing was only observed in relation to small offset strike slip faults which cut the dip-slope (Figure 5.4a,b). Fractures are only found in close proximity to fault strands either forming sub-parallel to fault strands in the hanging wall block, or oblique to the fault strands in relay zones and fault tips. These fractures commonly display small sinistral and dextral offsets (mm to cm)

and are typically barren, although occasionally showing pyrite along the fracture plane. Sandstones displayed bed-bound joint-sets in a similar manner to the McDonald Limestone, however, there was limited bed-parallel exposure to explore the age and orientation of sets in sandstone lithologies. Where seat-earth is observed in the high wall, in contrast to the dip-slope, a well-developed bed-bound fracture network was observed. This suggests that mine-related stresses have caused deformation of these lithologies, the fracture network has been altered by both subsurface and surface mining activities (see Chapter 7).

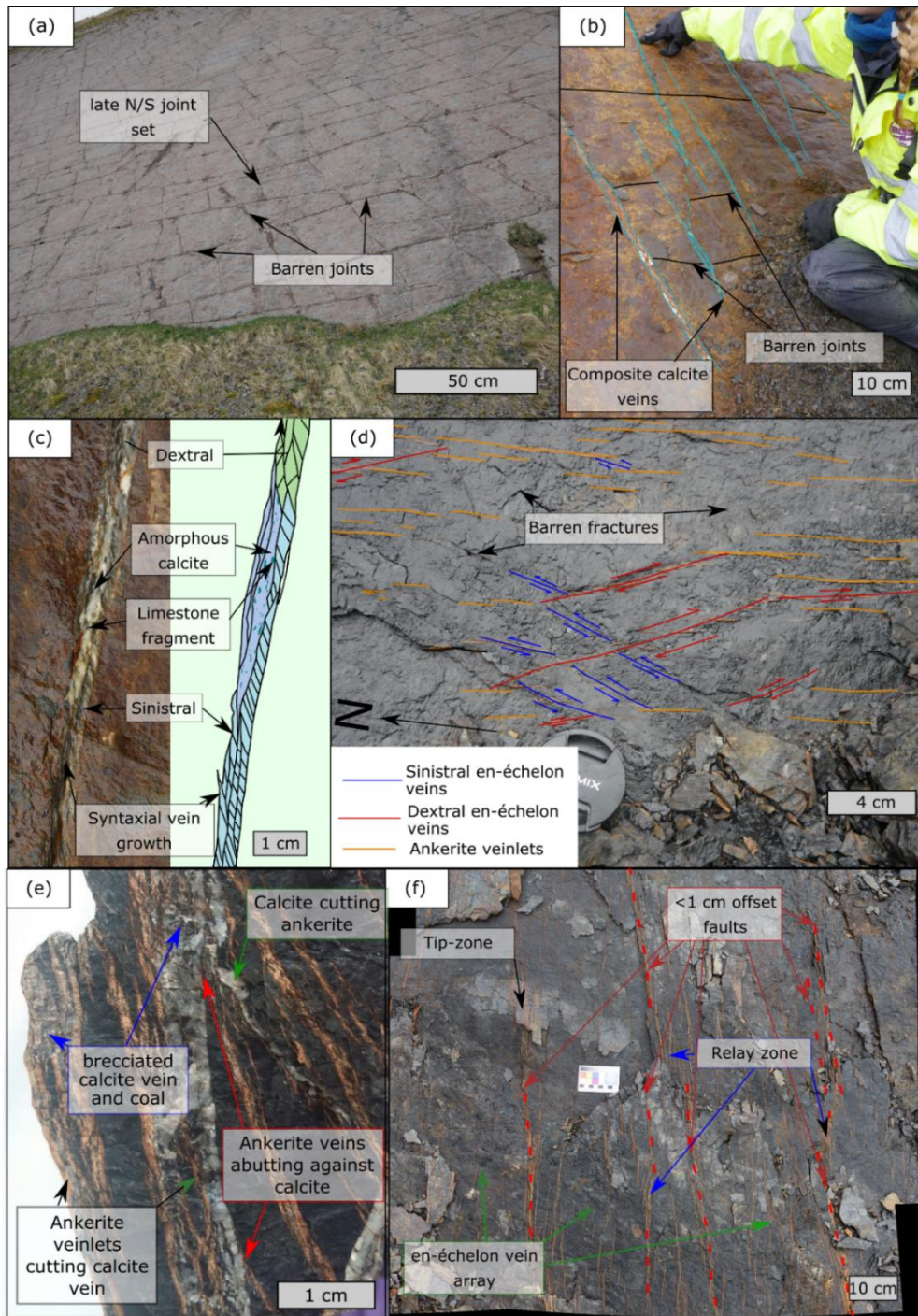


Figure 5.2: Typical fracture properties for McDonald Limestone & McDonald Coal: a) barren joints observed away from faults across the southerly dipping (c. 40°) McDonald Limestone bedding plane; b) Mineralised N-S trending calcite veins, offsetting abutting E-W ladder joints on the bedding plane of the McDonald Limestone; c) annotated field photograph and interpretation of a multi-phase composite calcite vein exposed in the vicinity to a small offset fault along the McDonald Limestone Pavement; d) bedding plane exposure of mineralised fractures present within the Muirkirk 6' coal; e) annotated hand specimen displaying the vein relationships present during the faulting of the Muirkirk 6' coal; and f) the larger-scale mineralisation pattern as you move towards small offset faults in the Muirkirk 6' coal.

5.5.2 Fault observations

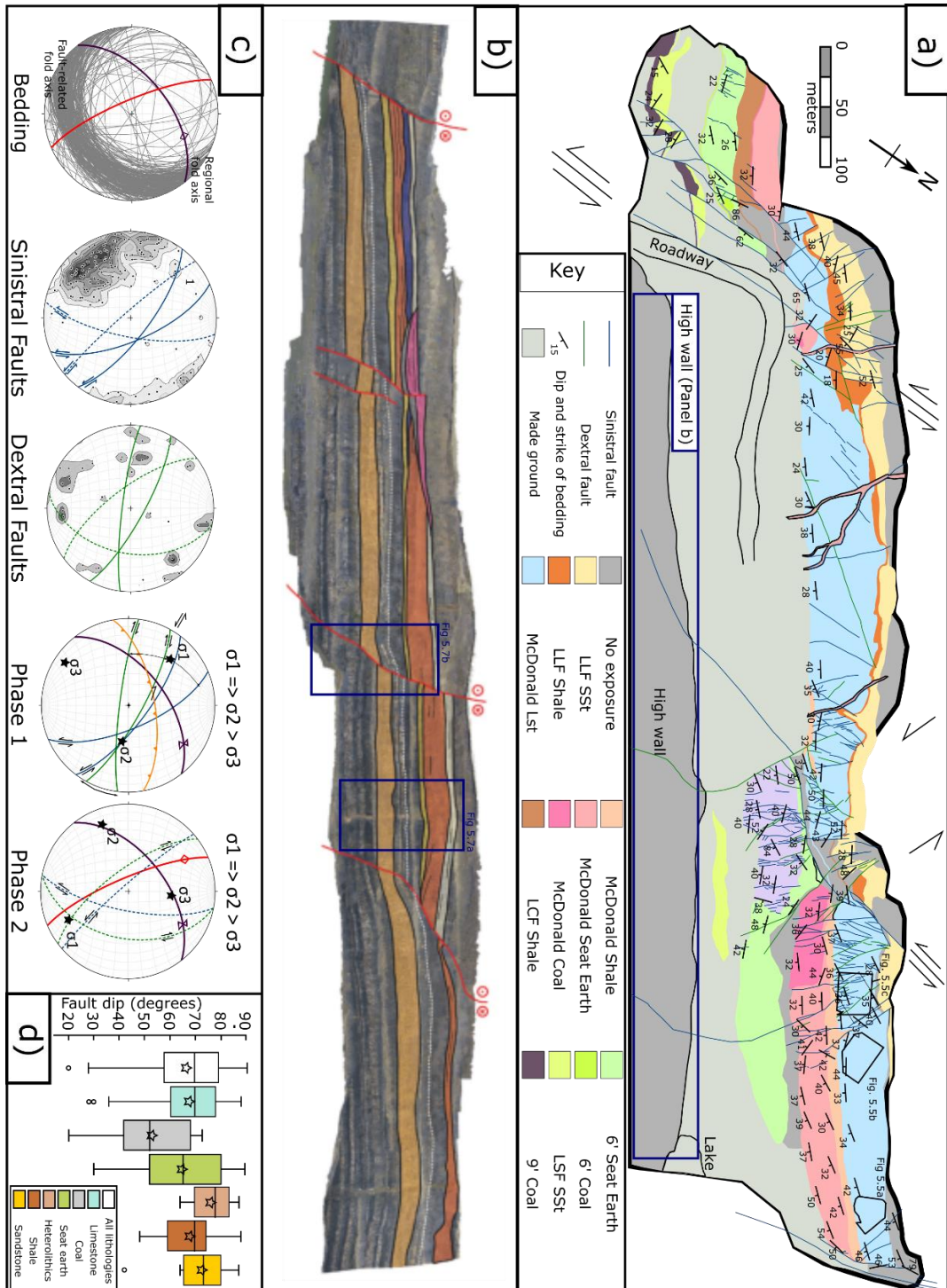


Figure 5.3: Geological map of Spireslack SCM: a) Geological map undertaken as part of this study, displaying the locations of the detailed map-view fracture maps shown in Figure 5.5; b) Annotated photogrammetry of the high wall displaying the key stratigraphic horizons and faults (Ellen et al., 2019); c) Fault kinematics by lithology, stereographic projections are created using Stereonet 10.1 and contours represent 1% area; and d) box and whisker plots for fault dip by lithology.

5.5.2.1 Fault kinematics

Several steeply dipping faults with low angle slickenfibers (5° to 30°) were mapped at Spireslack SCM (Figure 5.3). Fault offset ranges from cm-scale, where displacement is limited to specific lithology (self-juxtaposed), up to the largest offset fault (c. 120 m true offset according to Ellen *et al.* (2016)) which cuts the east of the site. Most faults belong to a sinistral offset set (75%), which formed simultaneously to ~NE trending dextral faults. Additionally, a later set of sinistral faults, whose offset ranges from cm to meters, with related dextral faults, offset the earlier sinistral fault set. Fault strike varies across the main void (Figure 5.3c), with a NS trend observed in the east and west of the site and a NW-SE trend observed in the centre. Fault dip depends on the lithology cut by the fault: dips in the McDonald Limestone range from 40° to 90° (mean = 67°), however, in coal they range from 20° to 73° (mean = 49°). In the shale interbeds layer bound bed-parallel thrusts (e.g. $040^{\circ}/70^{\circ}$ SE) with centimetre to meter offsets and associated folding can be picked out by their offset of ironstone layers (Figure 5.4d). The McDonald Seat Earth to the west of the site displays dip-slip slickenfibers (50° to 60°), only in faults with offset below 1 m.

Only large offset fault strands can be traced between beds (e.g. the 5 m offset fault cutting the western panel; Figure 5.3), apart from where large packages of sandstone are found (e.g. the Spireslack Sandstone). For lithologically restricted faults, trace length is typically low, with strands abutting either into rock or another fault strand in less than 15 m. Faults are well connected, with isolated fault strands only observed where strain is low.

The majority of faulting at Spireslack SCM fits a sinistral-offset strain-ellipse (Figure 5.3c). In this model the early dextral faults represent R' radial shears, with normal faulting of the McDonald Seat Earth, thrusting in the shale and radial shears of the major fault strands which bound the workings developing in the centre of the void. The folding of bedding, which dips towards the south, matches a fold axis of $042^{\circ}/80^{\circ}$ N and is likely to have been developed in association with the regional Muirkirk syncline under the same stress state. Faulting that cuts the earlier structures (e.g. the oblique sinistral fault and minor dextral fault strands) does not fit within this strain ellipse, and likely formed under a later dextral strain. In addition to the two phases of strike slip tectonics, Paleogene dykes are observed exploiting pre-existing NW trending fault strands. These locally display pods of edge brecciation similar to that developed along faults in limestone, and show dip-slip lineations suggesting there could have been a late stage of normal faulting.

5.5.2.2 Self-juxtaposed faults:

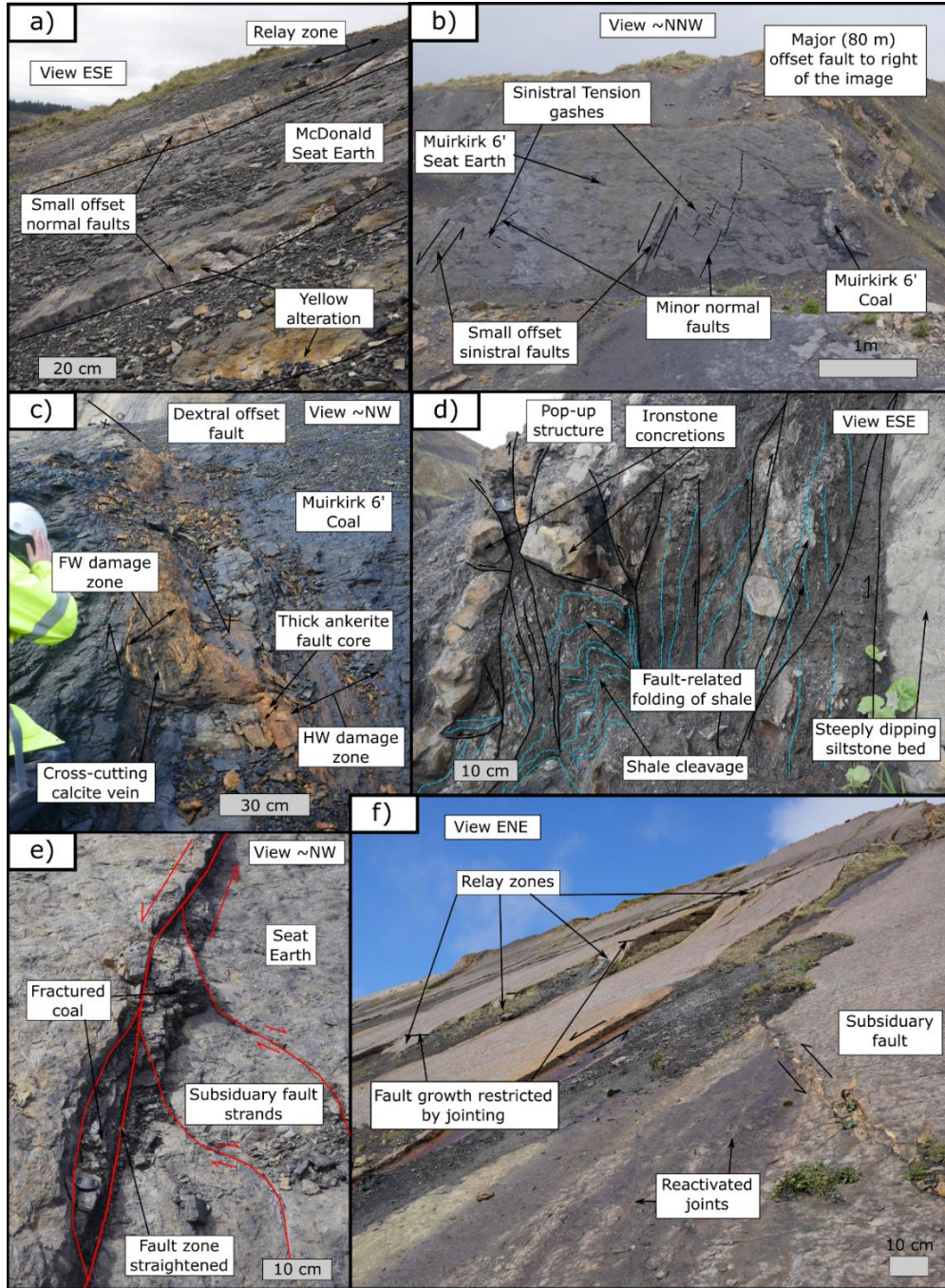


Figure 5.4: Characteristic observations of Self Juxtaposed Faults (SJFs): a) Small-offset (c. 15 cm) fault strands and relay structures, and b) tension gashes and small offset normal faults exposed within the McDonald Seat Earth in seat-earth exposed to the far west of Spireslack SCM; c) symmetric damage zone and thick zone of ankerite mineralisation along a c. 40 cm offset dextral offset fault cutting the Muirkirk 6' Coal; d) bed-parallel thrusts and folding developed within the shale which underlies the McDonald Limestone to the NE of the site; e) the development of small pods of fractured McDonald Coal along a small offset sinistral fault exposed to the SW of the site; f) the interaction between faults and joints along the southerly dipping bedding plane of the McDonald Limestone.

Self-Juxtaposed Faults (SJFs), with offset below 3 m, form either isolated strands (e.g. west of the void), or a network of both sinistral and dextral strands (e.g. near the centre of the void) (Figure 5.3). 3D exposures of SJFs cutting the MacDonald Limestone, MacDonald Seat Earth and Muirkirk 6' Coal are present on the dip-slope. SJFs in shale are only observed where overlying competent lithologies have been weathered out (e.g. near the large fault to the east of the void). SJFs cutting sandstone are poorly exposed on the dip-slope and only observed in the damage zones of larger faults in the high wall, discussed in Section 5.4.2.4. The internal structure of SJFs depends on the lithology which the fault strand cuts (Figure 5.4, Table 5.1).

Lithology	SJF characteristics
McDonald Seat Earth	Segment linkage, folding, and increased fracturing between strands led to the development of a highly asymmetric damage zone (Figure 5.4a & 5.4f). Fault strands are often barren, only displaying yellow alteration and occasionally pyrite.
McDonald Limestone	SJFs, associated relay zones, and nearby NS trending joint sets, are mineralised (calcite), display high displacement to length ratios (2.2 to 2.8), and show extensive folding of the surrounding lithologies (Figure 5.4f). Strands often abut against favorably orientated pre-existing joints (see Section 5.5.2.3).
Coal	Fault strands are characterised by a fault core comprising of a 5 to 20 cm thick zone of ankerite, with occasional calcite mineralisation, brecciated coal and pyrite (Figure 5.4c). The fault core is discontinuous along strike, with displacement transferring to other strands after 1 to 5 meters (Figure 5.2c). The gentle folding of the bed between strands is taken up by a symmetric zone of damage consisting of increased fracturing, en-echelon veining and mineralised shear fractures. The structures represent a continuation of the processes discussed in Section 5.4.1.1.
Shale	Fault strands are rarely observed. High angle thrusts (40° to 60°) dominate, with bed parallel folding picked out by ironstone concretions (Figure 5.4d), which themselves can display internal deformation (tension gashes). Near SJFs a cleavage is developed sub-parallel to the fault plane, which combined with slickenfibers on competent bedding planes suggests bed-parallel slip.

Table 5.1: Self Juxtaposed Fault (SJF) characteristics.

5.5.2.3 Interaction between joints and faults within the MacDonald Limestone

The style of the fault and fracture network exposed in the MacDonald Limestone changes across the site (Figure 5.3). Overall, the network is well connected and dominated by x- and y- nodes, with i-nodes only observed where faults terminate into rock and transfer displacement to another strand. The interaction of faults and joints was investigated through the use of three sample areas (indicated on Figure 5.3a). The chronology and network properties of each area are described in Table 5.2. As fault intensity increases, the

complexity of age relationships in the fault-fracture network increases. Where fault intensity is low and not favourably orientated to reactivate joints, a reasonably simple age relationship of early NE trending joints, followed by a later abutting NW set is observed. Faulting, as with all panels of Figure 5.5, abut against the larger trace-length NE trending set. When the interaction between faulting and jointing increases, either through an increase in fault intensity or joints being favourably orientated for reactivation, age relationships are complex. New joints form which developed at the same time as faulting in a rotating stress field. The fact that age relationships vary across the site suggests a highly heterogeneous stress field, which was rotated relative to locally active fault strands. An increase in fault offset also affects the intensity, trace-length and connectivity of the network.

Sample area	Sets & age relations	Trace length & intensity characteristics	Network topology & connectivity
1 Fig. 5a	Joint sets occur as two roughly perpendicular sets, an older 045° trending set and later 145° trending set. Faults are present as a separate NS trending set, which displace both joint sets, typically abut against large trace length NE trending joints, are mineralised and display sinistral syntaxial growth textures (e.g. Figure 2c). In the vicinity, and locally abutting against faults is a final stage of jointing, either associated with initial fault slip or later dextral reactivation.	The NE trending set ranges in has a larger trace length (4.10 ± 3.40 m) compared to the SE trending set (1.30 ± 1.10 m), with the latter typically abutting against the NE trending set. Trace lengths in the NS trending set range from 0.20 to 9.30 m (Median = 1.60 m), and typically abut against the NE trending set. Fault intensity is low (0.4 f/m), with moderate joint density (2.6 f/m) split into 1.3 f/m for the NE set, 1.0 f/m for the SE trending set and 0.3 f/m for obliquely aligned features.	The connectivity of the full network is high ($P_c = 0.99$) and is dominated by y nodes (76%), with X-nodes representing 23% of nodes. Field observations suggest the majority of x-nodes mapped on the drone map represent two y-nodes separated by <5 cm. The fault network is dominated by I nodes (90%) and is poorly connected ($P_c = 24\%$). The joint network is dominated by y-nodes and has a connectivity of $P_c = 95\%$.
2 Fig. 5b	Dominated by barren joints, with faults displaying a NW trend, which reactivate appropriately orientated joints and abut against NE trending joints. The age relationships are complex and show multiple generations of joints, typically orientated in a NE or NW trend, however, many joints are observed which do not fit these sets.	Faulting is slightly higher intensity than SA1 (0.5 f/m), with fault trace length varying between 0.20 and 13.20 m (median 1.20 m). Small trace length faults are found oblique to the main strand (e.g. northerly trending faults median trace length = 0.80 m). Joint intensity is 3.1 f/m with the majority of fractures belong to the NE (1.7 f/m) or NW (0.7 f/m) trending sets. Fractures off this trend typically have smaller tl (Median = 0.60 to 0.70 m) compared to the NE (median = 1.30 m) and NW (median = 1.00 m) sets.	The connectivity of the full network is high ($P_c = 0.99$) and is dominated by y nodes (88%). The fault network is dominated by I nodes (89%) and is poorly connected ($P_c = 28\%$). The joint network is dominated by y-nodes and has a connectivity of $P_c = 90\%$.
3 Fig. 5c	The complexity of joints varies considerably throughout SA3. Some areas display a simple relationship with an early ENE trending set and later NNW trending set, however, other areas display fracture corridors, which are aligned at a similar orientation to faulting, and which display multiple generations of joint formation. Faulting occurs as two sets, trending NNW, and NW. Faults typically abut against ENE trending joints, and locally cause the formation of new joints and rotation of pre-existing features.	Faulting intensity increases considerably in SA3 (1.9 f/m), with fault trace length ranging from 0.10 to 15.30 m (median = 1.40 m). The majority of faults trend between 125° and 155° (0.16 f/m) and display a higher median trace length (1.40 m) compared to other faults (1.10 m). Joint trace length is smaller in SA3 (0.50 m) compared to other sample areas (Median tl = 1.00 m and 0.80 m). Although most joint trend is NE (2.4 f/m) the NW trending set displays a wide range in orientation (125° to 155°) and 17% of joints are off axis from these trends. NE joints display a larger trace length, ranging from 0.00 to 5.50 m (median = 0.70 m) compared to other orientations (median = 0.40 m).	The connectivity of the full network is high ($P_c = 0.99$) and is dominated by y nodes (93%). The fault network is dominated by both I- (55%) and y-nodes (45%) and is moderately connected ($P_c = 71\%$). The joint network is dominated by both i- and y-nodes and has a connectivity of $P_c = 77\%$.

Table 5.6: Network characteristics for the sample areas outlined in Figure 5.5

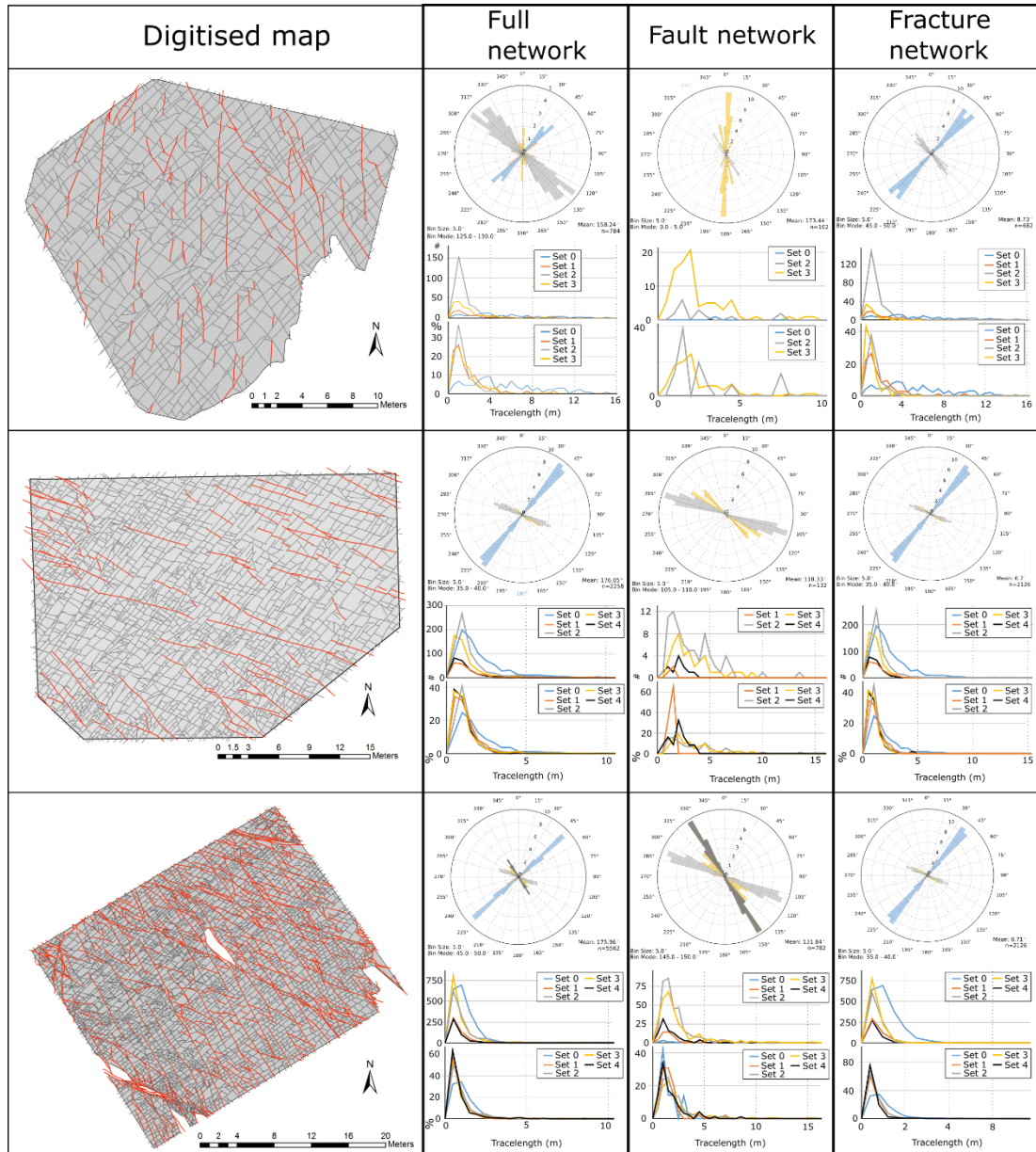


Figure 5.5: Fracture maps with increasing intensity of faulting: For each digitised map the exported fault (red lines) and fracture (dark grey lines) maps, along with the interpretation areas used for the analysis (light grey) are provided. The orientation data, colour coded by sets, is then provided using length weighted rose diagrams with 5° bin widths. Trace length is presented as trace-length histograms as well as normalised trace-length histograms with bin widths of 0.25 m. Histograms are colour coded to match the sets outlined in the orientation data.

5.5.2.4 Large offset faults

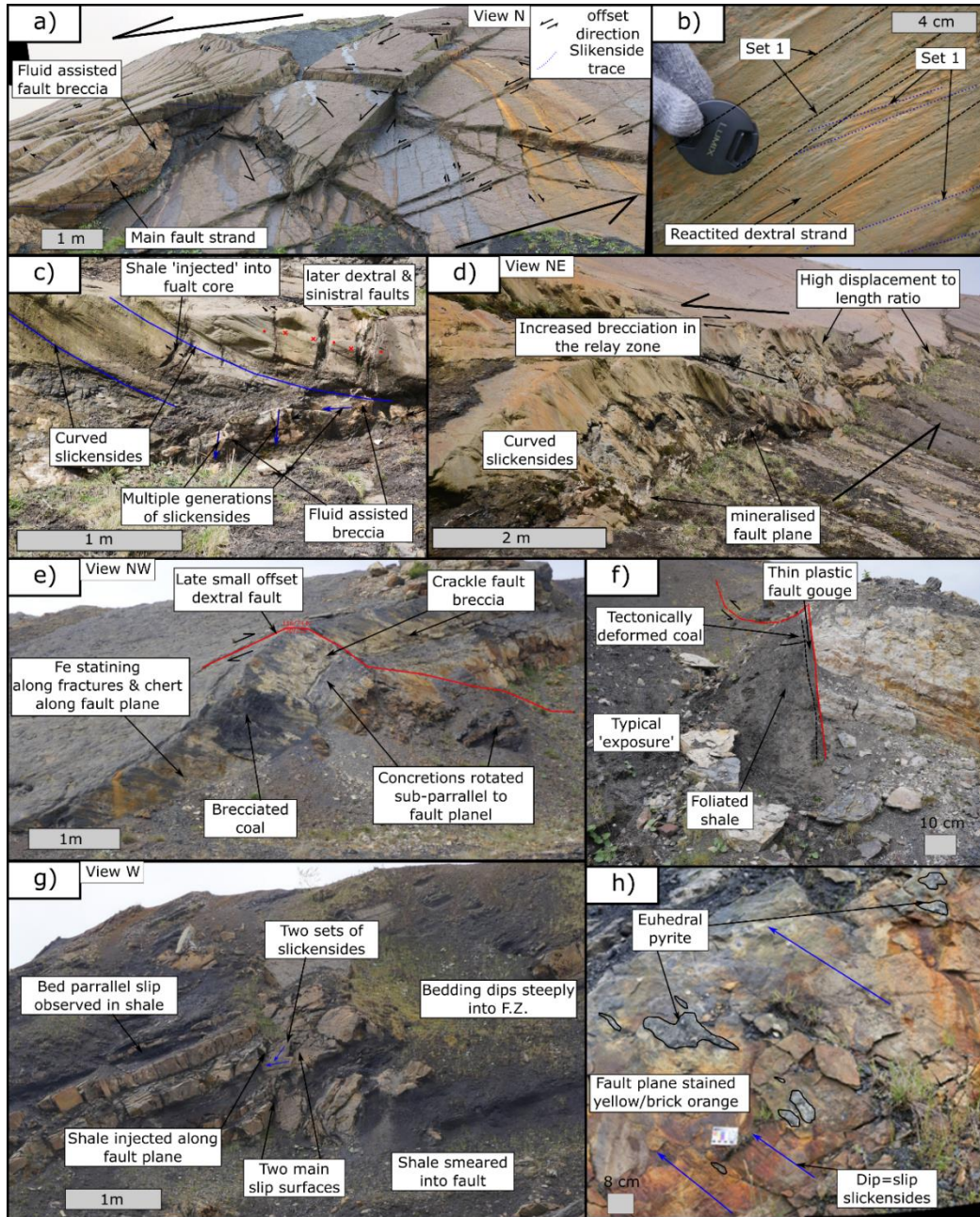


Figure 5.6: Large offset fault characteristics: a) complex fault mesh consisting of multiple strands of sinistral and dextral strike slip fault planes (offset marked with arrows) picked out by shallow striations and the offset of the McDonald Limestone bedding plane; b) field photograph of a ~3 m offset fault strand within the complex mesh which displays multiple generations of fault striations, with local dextral reactivation separating striations belonging to set 2; c) fault architecture and d) view along strike of a 3 to 5 m offset fault strand exposed along the southerly dipping bedding dip-slope; fault architecture of the same 5 m offset fault cutting e) lithologies surrounding the McDonald Seat Earth, and g) interbedded sandstones, siltstones and shales of the Lower Limestone Coal Formation; f) primary slip plane of the ~80 m offset fault which cuts the west of the site; and h) shallowly dipping, sinistral dip-slip fault plane within a ~2 m thick sandstone bed of the Limestone Coal Formation.

Faults that cut multiple lithologies show greatly increased complexity in deformation style (Figure 5.6). Fault dips still vary depending on lithology, with steeper dips observed in competent lithologies for the same fault. For example, a 4 m offset fault changes orientation from 135°/85° NE in the McDonald Limestone to 110°/72° N in the McDonald Seat Earth. This change in orientation causes bed rotation and the development of lenses, particularly in sandstones and seat-earths. Examples of larger-offset faults are provided below, with the complexity of faulting appearing to depend on the lithologies cut by the fault (Figure 5.6) and the plane of observation (i.e. map (Figure 5.3) vs high wall (Figure 5.7)).

Example 1: Fault meshes in the McDonald Limestone and surrounding lithologies

Faults cutting the McDonald Limestone with ~3 m offset lead to the development of fault meshes (Figure 5.6a). Rotation of bedding is accommodated along several fault-strands accompanied by the development of tension gashes. This caused the rotation of limestone blocks surrounded by fault strands. The thickness of individual fault cores is low (<5 cm, Figure 5.6a and 5.6b), with thickness not appearing to increase with displacement. The fault cores are mineralised, with local development of matrix-supported breccias containing angular limestone and re-worked calcite clasts. This, along with the development of Mode 1 fractures which offset previous slickenfibers (Figure 5.6c), demonstrate fault reactivation. Multiple generations of slickenfibers are developed whose dip shallows from the top to the base of the bed (Figure 5.6c, insert), providing further evidence of block rotation within the fault zone. Folding and bed parallel deformation of the under- and over-lying shale helped accommodate this rotation.

Example 2: Dip-slip faulting of sandstones and seat earths

3D exposures of faults cutting sandstone are rarely observed, however, in the center of the void there is a 3 to 5 m offset fault which cuts decimetre thick seat-earth and sandstones of the Limestone Coal Formation (Figure 5.3). The fault-plane is low-angled (100°/40° S) and displays dip-slip (40° to 55°), sinistral offset lineations. The fault plane is altered to a brick-orange colour and pyrite is locally observed (Figure 5.6). Pyrite is preserved within corrugations along the fault plane and consists of <4 cm euhedral crystals (usually <0.5 cm). Alteration and pyrite suggests sulphur-rich fluids migrated along the fault zone, with pods of crystal growth developing elongated to the slip-vector suggesting this was syn-kinematic.

Where coal is observed above seat-earth (Figure 5.4e), brecciation of coal, the development of thin zones of friable coal and the rotation of cleats relative to the orientation of the fault plane occurs.

Example 3: ~5 m offset fault cutting interbedded lithologies from the Lower Limestone Formation and Limestone Coal Formation

A c. 5 m offset, sinistral fault may be observed cutting limestones and sandstones of the Lower Limestone Formation and the McDonald Seat-Earth to the west of the void (Figure 5.3). In the McDonald Seat Earth (Figure 5.6b) fault dip changes from ~60° near the base of the outcrop to 007°/79° NE near the top and low angle lineations (e.g. 20°/107°) and offset markers indicate a sinistral offset. The main fault plane is cut by several later fractures (e.g. 116°/74° N and 292°/71° NE), which occasionally show cm-scale sinistral offset (18°/019°). Brecciated McDonald coal is found within undulations on the fault plane. In the underlying shale, several iron concretions (<10 cm) have been locally rotated and sheared in response to motion along the fault. An asymmetric damage zone is developed, with minimal deformation of the footwall and a 20 to 30 cm wide zone of higher fracture intensity developing in the hanging wall. Fractures are typically barren with only local iron mineralisation present. Bedding in the seat earth away from the the fault displays gentle (2-5m wavelength) low amplitude (~50 cm) folding with the wavelength decreasing towards the fault.

In the underlying Lower Limestone Formation, the same fault develops a complex, 2 to 3 m thick, mineralised fault zone (Figure 6c). The fault core is characterised by two mineralised slip surfaces (216°/60° W & 261°/68° NW), each with shallow (10°/080°), moderate (25°/050°) and steeply (68°/083°) dipping sets of slickenfibers developed. It is unclear which order these developed, and all apparently display a sinistral offset markers. Along the fault surface (015°/88° E) a c. 5 cm thick pod of matrix supported brecciated limestone is present in the hanging wall. Shale appears to have been locally injected into fractures that had already been mineralised with calcite. To the north of the fault, the interbedded sandstones, limestones, and shale dip steeply into the fault zone, reaching dips which match that of the fault plane (60° to 70°). In contrast, bedding to the south displays only low amplitude folding (015°/56° N; 043°/56° N).

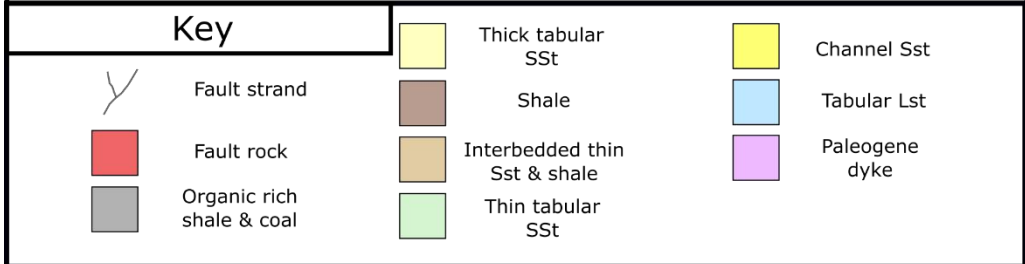
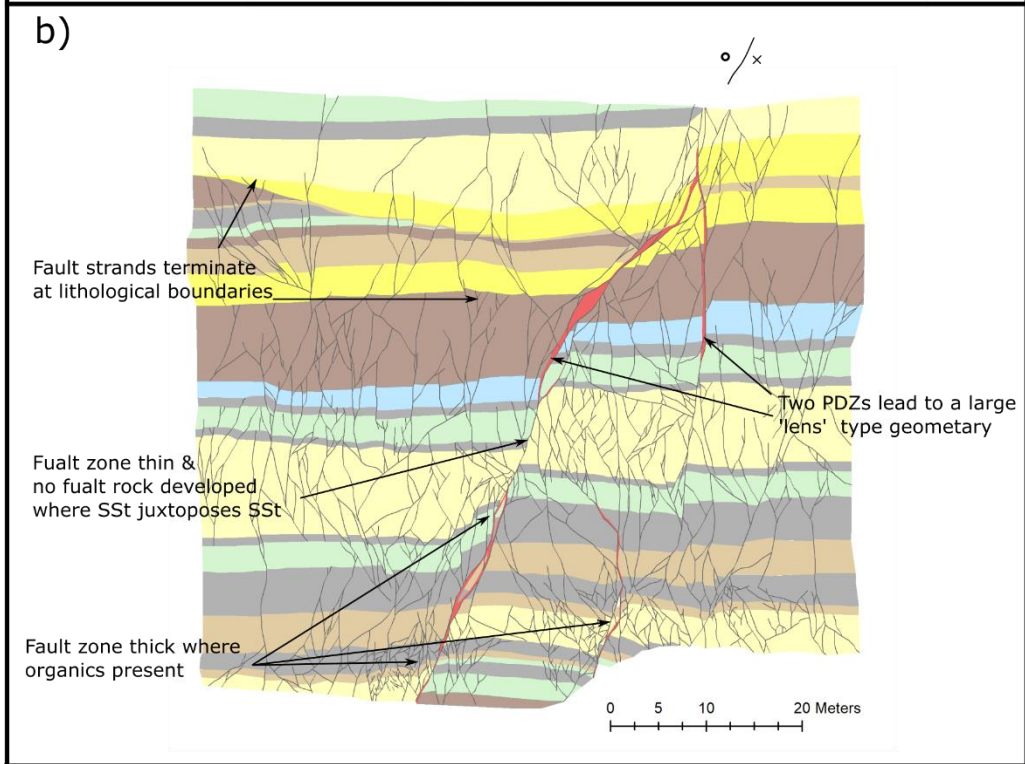
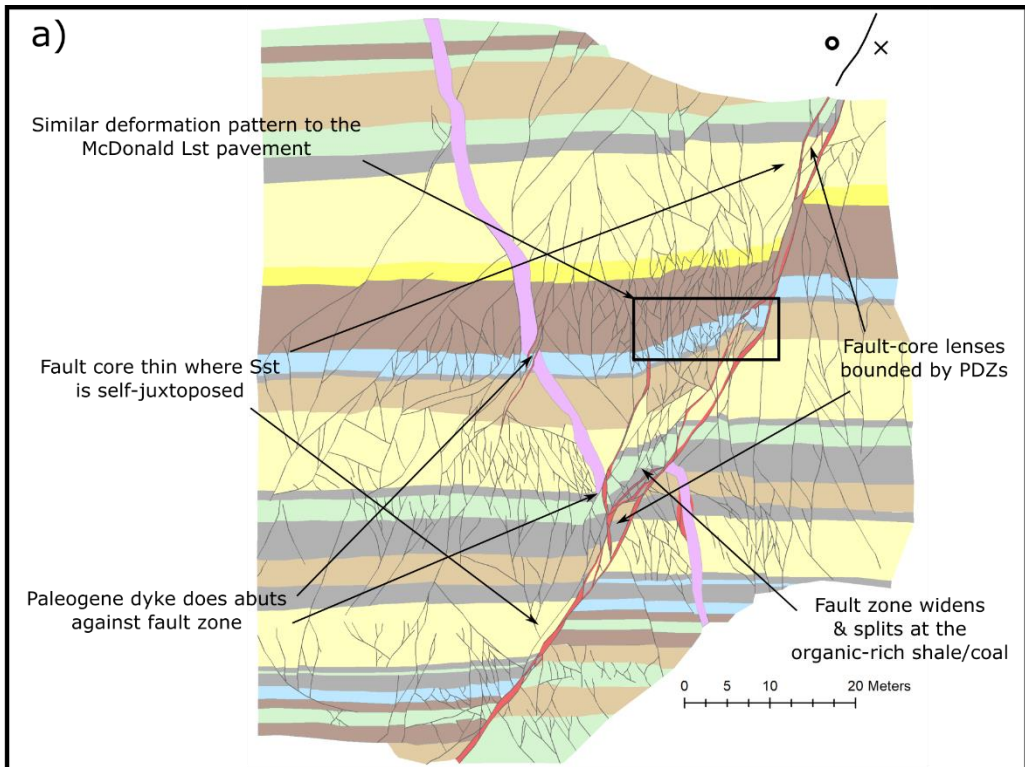


Figure 5.7 (Previous page): Digitised fault strands of sinistral faults cutting the Limestone Coal Formation exposed along the high wall: a) sinistral fault which displays between 2 and 5 m of throw and has been cut by a later Paleogene dyke which is not observed with the main PDZ; b) sinistral fault with displays between 2 and 8 m throw along two PDZs.

Example 4: 80 to 100 m offset fault cutting the full sequence

The internal structure of the 80 to 100 m offset fault, which cuts the west of the main void, is largely obscured and only observed at a single location (Figure 6e). The footwall of the fault comprises an outcrop of 6' Seat Earth, which has been highly fractured, juxtaposed against highly altered coal and folded shale with a steeply dipping cleavage. The fault core is comprised of a thin (<5 cm), clay rich zone of plastic fault gouge containing <2mm clasts of sandstone and organic fragments. The altered coal has lost its cleat-network and is noticeably harder than its unaltered equivalent, creating a spark when struck with a geological hammer. This increase in coal rank is potentially due to shear-heating (Fowler and Gayer, 1999; Li, 2001). The fault-related fractures in the surrounding seat earth are often stratabound and increase in intensity towards minor-slip zones and the fault core.

Example 6: Fault strands cutting the high wall

Fault strands cutting the high wall appear to show a simpler geometry (Figure 5.7) to those observed on the dip slope (Figure 5.6). It should be noted that because of the predominant strike slip kinematics significant out of plane displacement exists such that visible offsets represent an underestimate of true displacement. The majority of throw is taken up by a small number of fault strands, particularly in the channelised sandstones and limestones in the sequence. Individual fault strands are thin and form an interconnected network of SJFs. Fault core thickness is typically below a pixel (c 5 cm), however, on the major faults the development of fault-core lenses and undefined fault-rock can be observed. The thickness varies considerably down-dip, and while a continuous strand is observed in Figure 5.7a, in Figure b no fault rock is observed where the thick sandstone bed is self-juxtaposed.

The deformation style varies depending on the lithological juxtaposition, with the proportion of sandstone in the faulted section controlling whether fault-core lenses are developed. For example, in both panels of Figure 5.7, faults are steep (apparent dip ~70° to 80°) with displacement taken up along a single fault strand, and damage zone evolution is low in areas where thick sandstone units are juxtaposed. However, where interbedded units are juxtaposed against each other the fault zone widens to 4 m in Figure 5.7a and 4.5

to 6 m in Figure 5.7b. Within these zones beds of competent lithology are rotated away from the main fault zone and subsidiary antithetic fault strands develop which abut against the main strand. Small offset faults are more abundant in the thick tabular sandstone, interbedded and shale units, with fault stands abutting and branching at lithologically controlled mechanical boundaries.

5.6 Discussion

5.6.1 The role of lithology in faulting style: self-juxtaposed vs non-self juxtaposed faulting

The observation at Spireslack SCM suggests that initially faults only grew in competent lithologies (sandstone, seat-earths and limestones) and coals (Figures 5.3, 5.4), with fault properties (trace length, connectivity, D-L ratio and fault-rock development) that depend on the lithology being cut. This is similar to the growth of normal faults in interbedded limestones and marls (Ferrill et al., 2017), as well as 2D and 3D numerical modelling (Schöpfer et al., 2007; Schöpfer et al., 2016). Self-juxtaposed faults developed in all the competent layers at the same time and initially grew as isolated strands, before interacting with other strands from the same unit. This behaviour matches established models for fault growth (Walsh et al., 2002; Wibberley et al., 2008; Fossen and Rotevatn, 2016). Large offset faults which breach more than a single lithology, however, were strongly affected by the presence and behaviour of shale inter-beds.

Shale in the sequence behaves in a ductile manner with folds and cleavage developing (Figure 5.4d), along with enabling bed-parallel slip. In Figure 5.6g, shale is squeezed into pre-existing mineralised fractures, indicating the highly ductile nature of shale during faulting. The ductility of shale can be effected by many factors including lithology, mineral composition, organic carbon content, diagenesis, and thermal maturity (Wang and Gale, 2009). Burial depth is a major controlling factor for many of these properties and it is important to consider both the current and past burial depth (Yuan et al., 2017). As shale is buried and compressive stresses increase, the ratio of pre-consolidation stress and compaction related stresses control the behaviour of shales and mud rocks. Where lithologies are normally-consolidated (pre-consolidation stresses < burial stresses) ductile behaviour is observed (Yuan et al., 2017), however, where over-consolidation (pre-consolidation stresses > burial stresses) occurs shales deform in a brittle manner (Nygård et al., 2006). As a general rule, shales are ductile during burial, and brittle during exhumation.

While estimates vary across the MVS, it is suggested the limestone coal formation has a maximum burial depth of <3,000 m at around c. 60 Ma (Monaghan, 2014). Ductile behaviour of the shales at the time of faulting suggests that faulting was active during burial, rather than uplift, enabling faults to initiate as isolated strands in competent lithologies. When faults cut multiple lithologies shales accommodate the rotation of bedding leading to rotated blocks and multiple generations of curved slickensides.

Faulted coal at the site can remain relatively undeformed, or developed a thin zone of ankerite mineralisation, apart from in large offset faults. This differs from the published literature, where tectonically deformed coals, occurring as soft-coal bands, are often associated with normal faults (Ju et al., 2012; Godyń, 2016; Li et al., 2018), or bed-parallel slip in compressive environments (Frodsham and Gayer, 1999; Li, 2001). Soft coal bands often display a range of brittle and ductile features, for example S-C type cleavages, minor thrusts and folding (Li, 2001), all of which act to degrade the quality of the coal. Soft-coal bands were also not developed in the far east of the site, where archival photographs show coal was extracted from an area where bedding steepened to $\sim 70^\circ$ (Leslie, Browne, et al., 2016; Ellen et al., 2016).

The fault core of the large offset faults often contain pods of coal present as un-mineralised chaotic fault breccia (Figure 5.6e). These deposits form in asperities along the fault zone, which get cut as the fault straightens (Sagy et al., 2007). Asperities, formed by corrugations along the fault zone, have been identified both in the field (Wright and Turner, 2006; Sagy et al., 2007) and from seismic data (e.g. Lohr *et al.* (2008)). Asperities typically form aligned parallel to fault slip (Hancock and Barka, 1987), which is also observed in fault zones at Spireslack SCM.

The behaviour of coal in larger faults (Figure 5.6) differs from small offset faults (figure 5.4) in that no mineralisation is observed. Where coal was observed overlying seat-earth (Figure 5.4e), coal was rotated, brecciated and thin zones of friable coal developed, suggesting that coal becomes entrained into the fault core as a rotated block, similar to a fault-core lenses (Gabrielsen et al., 2016). This suggests that while SJFs can be used to understand fault growth up to a certain point, once multiple lithologies are cut the processes change such that SJFs are not representative of large offset faults.

5.6.2 Jointing and the effect of pre-existing weaknesses on deformation style and fault growth

The mechanically stratified succession at Spireslack SCM has led to the development of a fracture stratigraphy (Laubach et al., 2009). Orthogonal joint sets are developed in the MacDonald Limestone (Figure 5.2a), cleats in the MacDonald coal (Figure 5.2d) and bed-bound joints within the sandstone layers. While only two orientation sets are observed within the MacDonald limestone, the use of abutting relationships show these formed as 4 'age sets'. Similar observations are reported for other sites (Sanderson, 2015; Peacock et al., 2018), with fractures which appear to form in the same orientation, in fact occurred in response to separate deformation events. Another way in which multiple age sets can develop is where the intermediate (σ_2) and minimum (σ_3) principle stresses are nearly identical, and can therefore easily switch between each other (Caputo, 1995; Caputo and Hancock, 1998). The difference between principle stresses changes the mechanical response of the layer (Healy et al., 2006; Moir, 2010; Moir et al., 2010), with the dip and dilatancy of fractures varying depending on the difference between (σ_2) and (σ_3) (Haimson and Chang, 2000; Chang and Haimson, 2000).

The joints at Spireslack SCM formed prior to faulting with the sparsely spaced joint set likely forming in response to far-field stress fields during burial, and later sets related to the early stages of folding associated with the Muirkirk Syncline. This folding, and later faulting is attributed to the mid-to late Carboniferous sinistrally transpressive deformation event which effected this part of the MVS (Leslie, Browne, et al., 2016). The late-stage dextral event, which was not identified in the work of Leslie *et al.* (2016), locally reactivates these structures and is attributed to the Upper Carboniferous stress fields which strongly control deformation to the east of the MVS (Underhill et al., 2008). This stress field also reactivates cleats within the coal (Figure 5.2 d, e & f), and locally causes kink-bands to develop. The Paleogene dykes, which intruded along pre-existing NE to N trending faults, display a minor amount of reactivation, with brecciation and dip-slip lineation's developed along the margins. This suggests that late stage extension, orientated to enable the reactivation of NE trending structures occurred since the Paleogene, possibly linked to isostatic rebound or the opening of the North, or Irish Seas.

The presence of joints in the McDonald Limestone, and cleats within the Muirkirk 6' Coal influence the internal structure and fault growth in these lithologies (Figure 5.4, 5.6). In

both lithologies multiple sets of pre-existing weaknesses existed at the time of faulting, however, it was only those orientated roughly orthogonal to fault trend which caused fault strands to terminate (Figure 5.4). Coal cleats in the Muirkirk 6' Coal both show evidence of reactivation (forming mineralised shear fractures and en-echelon arrays), and may act to restrict the growth of these features. Although small-offset fault strands display evidence of reactivation (e.g. brecciated coal, calcite and ankerite), further displacement is often taken up by the formation of new shear fractures. Mineralisation of the cleats causes the strain-hardening of the coal with pre-existing weaknesses (cleats) becoming mineralised strength inclusions. During the dextral deformation stage new mineralised fractures formed, and tip-damage zones developed from the end of shear fractures that had developed during the sinistral phase.

While joint sets in the McDonald Limestone may become rotated close to fault strands, no increase in fracture intensity is observed and a typical core-damage zone structure is not developed (e.g. Caine *et al.* (1996); Gudmundsson *et al.* (2010); Bense *et al.* (2013)). Mineralisation (primarily calcite) increases towards the fault core, with fault cores in the McDonald limestone comprising of multiple generation of slickensides, mineralisation and calcite matrix chaotic fault breccias (Figure 5.6a, c). Similar observations of the interaction of jointing and faulting have been made in the Liassic limestone (Somerset, UK) (Peacock, 2001; Peacock and Sanderson, 2018). Veins have been reported surrounding normal and strike-slip faults in the area (Caputo and Hancock, 1999), with joint frequency not increasing towards faults (Peacock, 2001), but instead changing orientation towards the fault (Bourne and Willemsse, 2001). While similar orientations are observed, Spireslack SCM differs in that the joint-sets in Somerset occurred post-faulting, with faults in Somerset formed without the presence of pre-existing weaknesses (Peacock, 2001). While some rotation of individual joints occurs towards the east of the site, the majority of joints remain planar and instead acted as planes of weaknesses which became reactivated to accommodate fault slip.

The rotation of the joints is in part related to the bulk rotation of competent beds into fault zones which is observed both along the dip-slope and high wall. As discussed above, this rotation is accommodated along shale inter-beds, and can lead to the re-orientation of joint sets. In Figure 5.5, the folding of the McDonald Limestone can lead to joints which would not usually be favourably orientated to become reactivated. Displacement on large offset

faults, such as those observed in the high wall, is typically localised onto a small number of principal displacement zones (Figure 5.7). This indicates that while jointing strongly impacts early fault parameters, once a fault reaches a certain displacement, small scale features such as joints have only a minor effect on fault growth. The effect of joints on the early growth characteristics of faults is discussed by Wilkins *et al.* (2001), who found faulted joints to develop little fault rock, and to have considerably smaller distance/length ratios that would be expected for faults which do not cut jointed lithologies. Pre-existing joint-sets restrict fault-growth for SJFs through the formation of faulted joints (Wilkins *et al.*, 2001; Peacock, 2001; Soden *et al.*, 2014), with lithology becoming the major control once faults breach multiple layers (Nicol *et al.*, 1996; Wilkins and Gross, 2002; Soliva and Benedicto, 2005). This behaviour is not observed in the McDonald Seat Earth, where jointing is not present. Instead fault strands grow as single strands, which interact with other strands to form tip-damage zones and relay zones where displacement transfers between fault strands (Fossen and Rotevatn, 2016).

5.6.3 Effect on flow pathways:

Mineralisation along fault planes within coal (Figure 5.4), limestone (Figure 5.4 & 5.6), sandstone (Figure 5.6), and to a lesser extent seat-earth (Figure 5.4 & 5.6), provides evidence of up-section flow. Fault-related veins display one or more crack-seal events (Figure 5.4) indicating vertical flow was related to fault assisted opening of dilatational zones leading to the connection of pre-existing fractures (Ferrill and Morris, 2003; Laubach *et al.*, 2009; Ferrill *et al.*, 2014). The multiple events suggest pathways only remain open for a small amount of time and close following fault slip (*c.f.* Sibson 1990, 1992). Faults in the McDonald Limestone behave in a similar way to other faults in carbonates with primary slip surfaces becoming sealed following slip (*e.g.* Billi *et al.* (2003)).

Fault-related mineralisation in both limestones and coals would act to reduce connectivity, and hence permeability, of the network (Figure 5.8). From the timing relationships, at the time of faulting, the majority of the network existed, however, only joints/cleats orientated favourably for reactivation became mineralised. Following mineralisation, these fractures became sealed and closed to future fluid flow. During faulting, the connectivity of the network on the McDonald Limestone bedding plane varies depending on the intensity of faulting (Table 5.3). Fault-assisted fluid flow in areas of low fault intensity (0.4 f/m^2 ; Figure 5.5a) was primarily confined to a sparse network of partially connected NS trending, poorly

connected ($P_c = 0.24$) fault strands. Where faulting of a similar intensity (0.5 f/m) is orientated favourably to reactivate joints (SA2), the connectivity remains low ($P_c = 0.28$), however, fault trace length is greater due to the orientation and spacing of pre-existing joints. When faulting intensity is high (1.9 f/m), the connectivity of faults is high ($P_c = 0.71$), and both sets of joints become reactivated. Because multiple sets of joints may restrict the growth of faults, trace length of individual fault strands is low and strain is taken up by many small offset faults.

		Network parameter	Sample area		
			SA1	SA2	SA3
a) Combined network	#lines		784	2258	5562
	D (F/m ²)		3.1	3.5	5.9
	P _c		1.00	0.99	0.96
	Tl (m)	Min	0.09	0.02	0.04
		Max	14.71	13.16	15.33
		Median	1.12	0.90	0.51
b) Fault network	#lines		102	132	782
	D (F/m ²)		0.4	0.5	1.9
	P _c		0.24	0.28	0.71
	Tl (m)	Min	0.22	0.21	0.10
		Max	9.33	13.16	15.33
		Median	1.62	2.34	1.36
c) Joint network	#lines		682	2126	4778
	D (F/m ²)		2.6	3.1	3.9
	P _c		0.96	0.90	0.77
	Tl (m)	Min	0.09	0.02	0.04
		Max	14.71	10.33	5.49
		Median	1.53	0.86	0.46

Table 5.32: Overview of network properties for: a) the combined fault and fracture network; b) the mineralised fault network; and c) the joint network which does not display mineralisation or reactivation during faulting.

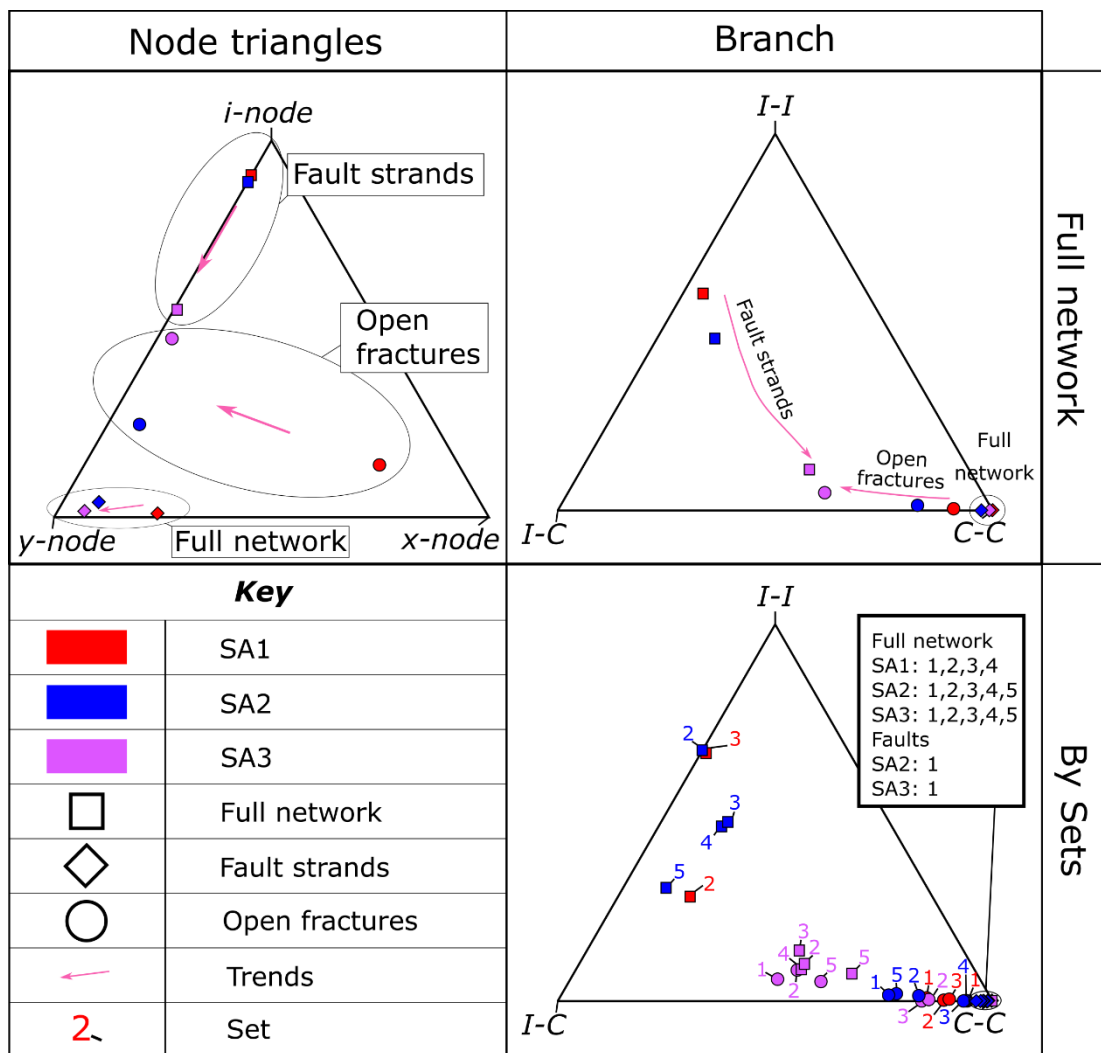


Figure 5.8: Network topology data. Node and branch triangle (after Sanderson & Nixon (2015)) are presented for the full-network, mineralised fault strands, and open joints, for each of the three sample areas shown in Figure 5.5. Branch data is then presented by sets, as outlined in figure 5.5, to investigate the directionality of network connectivity.

Faulting caused the development of several new joints, with joint intensity increasing from 2.6 in SA1 where limited fault-related jointing is observed, 3.9 f/m where fault intensity is high. The joint network initially remains well connected ($P_c = 0.96$), however, as joints become reactivated connectivity drops to $P_c = 0.90$. In SA3, where fault intensity has increased to 1.9 f/m, the connectivity of the joint network drops to $P_c = 0.77$. It is also important to consider the orientation of the feature when considering fluid-flow properties of the network. For example, while faults typically have a low to medium number of connections per branch (Figure 5), those orientated between 060° and 100° plot close to the C-C vertex of the branch triangle. This is also observed for joint sets, with those trending to the NW being the most connected.

The evidence of transient fluid flow in both the McDonald Limestone and Muirkirk 6' Coal highlights the importance of understanding the evolution of a fault and fracture network when assessing the geological and fluid-flow history of a particular site (Peacock & Sanderson, 2018). If fracture data was collected using the high-resolution imagery alone, and not combined with field evidence, all fractures might be assumed to have been open to flow. This would lead to a significant over-estimation of the permeability of the network. For example, in SA3 the connectivity of all lineaments is $P_c = 0.96$, however, when only joints which have not been reactivated by faulting are considered this drops to $P_c = 0.77$. In this case the trace length, which represents one of the most important parameters in fracture modelling (Min et al., 2004; Lei et al., 2017) would also be overestimated, with mineralised fault strands displaying a larger median trace length of 1.36 m. The presence of mineralisation only within particularly orientated joint or cleat sets also highlights the importance of stress state on hydraulic properties of fractures (Cherubini et al., 2014). While no data exists to quantify the magnitude of modern day stresses in Scotland (Comerford et al., 2018), the stress orientations have been suggest as roughly EW trending extension (Baptie, 2010), and a NNW trending maximum compressive stress (Heidbach et al., 2008). This would act to further reduce the modern day connectivity of the network through aperture reduction of large trace length ENE to NE trending joint sets.

5.7 Conclusions

The exceptional exposures of the Limestone Coal Formation exposed at Spireslack SCM enabled the effect of lithology and pre-existing structures on the internal structure, fluid flow properties, and growth faults to be investigated. We find that the internal structure of fault strands is strongly affected by a) the lithology being faulted, b) whether multiple lithologies are cut by the fault or not, c) the presence and behaviour of shale interbeds, and d) the presence of pre-existing weaknesses. The geological evolution of Spireslack SCM displays a complex relationship of folding, brittle deformation and stages of mineralisation. Unlike –previous authors we find that locally structures are affected by a late stage dextral stress field, which is commonly observed within the Midland Valley of Scotland.

Faults in the McDonald Limestone and Muirkirk 6' Coal are strongly affected by the presence of the pre-existing joint and cleat network. In both cases this causes the restriction of fault growth, with individual strands abutting against favourably orientated structures. The mineralisation of the cleat network in the Muirkirk 6' Coal leads to an

increase in the strength of the coal seam, with later reactivation effected by the presence of mineralised cleats. In the McDonald Limestone, strain hardening is not observed, however, because fault planes become mineralised the permeability of the rock mass decreases as fault intensity increases. Our work demonstrates the importance of considering not just the lithologies being faulted, but also whether pre-existing weaknesses are present. Where this is the case fault-growth will be restricted and the connectivity of a network can drastically change through time following mineralisation and/or changes in stress directions. This needs to be considered when using field analogues to predict sub-surface fluid flow and lineament mapping should always be integrated with fieldwork.

Chapter 6: The internal structure of faults cutting coal bearing successions: A case study using the Northumberland Basin.

6.1 Rationale

This chapter investigates how the internal structure of fault zones develop in coal-bearing sediments through geological mapping and detailed observations at a number of scales (1:2,000, 1:100, 1:10, and 1:1). Fieldwork was undertaken at two field sites (Howick and Whitley Bay) within the Northumberland Basin chosen for their exceptional exposures of faulted Carboniferous Coal Measures. The fieldwork finds that the footwall fault strand is systematically more planar, both in map and section view, and that this strand often developed a wide zone of fault rock (cataclasite, fault-breccia, and fault-gouge). The zone immediately towards the hanging wall is characterised by the development of fault-core lenses and several subsidiary faults, whose strike is typically either 15° or 30° to that of the main fault strand. The footwall often displays very little deformation. However, at Howick a zone like that observed in the hanging wall is observed. The minor strands are often characterised by discontinuous fault-rock growth including pods of matrix-supported breccias with calcite cement, which, coupled with the distribution and orientation of veining and alteration, suggests that off-fault fluid flow is common through the hanging wall damage zone. The orientation and sense of shear of mapped features, which is consistent over four orders of magnitude, fits within a dextral strike-slip strain ellipse and suggests that aspects of the tectonic evolution of the basin remain unknown.

6.2 Introduction

Characterising and quantifying the properties of fault zones is vital if we are to understand sub-surface fluid-flow properties and the strength of a rock mass. Fault zones typically contain a high strain fault core, which accommodates the majority of displacement, which may be further concentrated onto a principal displacement zone (PDZ). This is usually surrounded by a damage zone (Caine et al., 1996; Childs et al., 2009; Faulkner et al., 2010) of comparatively low strain typically consisting of subsidiary faulting, veining, fracturing and folding (Caine et al., 1996; Kim et al., 2004; Faulkner et al., 2010). The intensity of damage typically increases towards the fault core (Kim et al., 2004; Faulkner et al., 2011) and where fault strands interact (Walsh and Watterson, 1988; Peacock and Zhang, 1994; Watterson et al., 1998).

The fault core of shallow faults may comprise of various fault rocks including: a) clay-rich fault gouge; b) fault-breccia; c) cataclasite; d) shale smear; e) and/or lenses or clasts of relatively undeformed host rock (Sibson, 1977; Woodcock and Mort, 2008). Fault breccia and cataclasite form through the entrainment and progressive shearing of the host rock (Collettini et al., 2009; Molnár et al., 2014). This causes the fault zone to widen as material gets incorporated into the PDZ (Bastesen and Braathen, 2010; Torabi, Alaei, et al., 2019; Torabi, Johannessen, et al., 2019). Breccias may also form through the fluid-assisted brecciation of competent lithologies off axis to the main fault strand (Jébrak, 1997; Woodcock and Mort, 2008; Peacock et al., 2018). Where clay rich lithologies are present (e.g. shale), or displacement is high, thin (cm scale) zones of foliated fault gouge develop (Collettini et al., 2009; Bastesen and Braathen, 2010). In shale rich lithologies folding commonly develops accompanied with lenses of unaltered, or fractured, host rock become entrained into the fault-core (Berg and Skar, 2005; Torabi and Berg, 2011; Gabrielsen et al., 2016) and shale smears form (Færseth et al., 2007).

Fault thickness may range across several orders of magnitude and represents a poorly constrained but important fault parameter when modelling sub-surface fluid flow. Fault core thickness is affected by the lithologies cut by the fault, fault type, and displacement along the fault (Sibson, 1977; Shipton et al., 2005; Van der Zee et al., 2008; Torabi and Berg, 2011; Torabi, Johannessen, et al., 2019). The thickness, type, and distribution and fault-rock lithologies in the fault core is strongly affected by lithological juxtapositions along the fault (Sibson, 1977; Chester and Chester, 1998; Agosta and Aydin, 2006; De Paola et al., 2008; Walker et al., 2013; Bullock et al., 2014). For example, in interbedded sandstone-shale lithologies it is common to develop shale smears in succession with high proportions of shale relative to sandstone (Lindsay et al., 1993; Aydin and Eyal, 2002; Færseth, 2006; Færseth et al., 2007)

Several authors suggested that fault-core thickness displays a power-law relationship with the maximum displacement along a fault (i.e. $T = aD^n$) (Evans, 1990; Bastesen and Braathen, 2010; Torabi, Johannessen, et al., 2019). Field observations have shown fault-core thicknesses can vary considerably both along-strike and down dip on a single fault plane (Kolyukhin and Torabi, 2012; De Rosa et al., 2018; McKay et al., 2019). Using traditional T-D relationships masks this variability (Shipton et al., 2006; R.J. Lunn et al., 2008), and can also be influenced by how a geologist defines the fault core (Torabi,

Johannessen, et al., 2019; Shipton et al., 2019). Heterogeneity is also seen in the observed fault-rock lithologies and their spatial relationships (e.g. (Faulkner et al., 2003; Hooker et al., 2014; De Rosa et al., 2018; McKay et al., 2019). For example, Sagy and Brodsky (2009) found that geometrical and lithological heterogeneities could lead to the rotation of fault rock geometries towards the trend of local fault strands.

Riedel shear relationships are commonly observed in minor features associated with strike-slip faults (i.e. veining, subsidiary folding etc.) (e.g. Tchalenko and Ambraseys, 1970; Schandelmeier and Richter, 1991; Cunningham 1993) and in high strain zones within the fault core (Power and Tullis, 1989; Otsuki et al., 2003; De Paola et al., 2008; Smith et al., 2011). A Riedel shear system associated with dextral strike slip faulting (Tchalenko, 1970; Wilcox et al., 1981; Bartlett et al., 1981):

- Synthetic shears orientated 15° clockwise relative to the trend of the PDZ termed R-shears.
- Synthetic shears orientated 15° counter-clockwise relative to the trend of the PDZ termed P-shears.
- Antithetic shears orientated 75° clockwise relative to the trend of the PDZ termed R'-shears.
- Synthetic shears that form parallel to the PDZ termed Y-shears.
- Tension fractures (joints) orientated 45° clockwise to the PDZ termed T-fractures.

Following on from the work presented on chapter 4 and 5, this chapter examines how the internal structure of faults cutting coal measures develops as faults grow. Detailed geological mapping and structural logs are used to classify the fault-rock lithologies and the distribution of these lithologies, within several fault zones at two field sites in the Northumberland Trough (Whitley Bay and Howick).

6.3 Methods of data collection

6.3.1 Faults used in this study

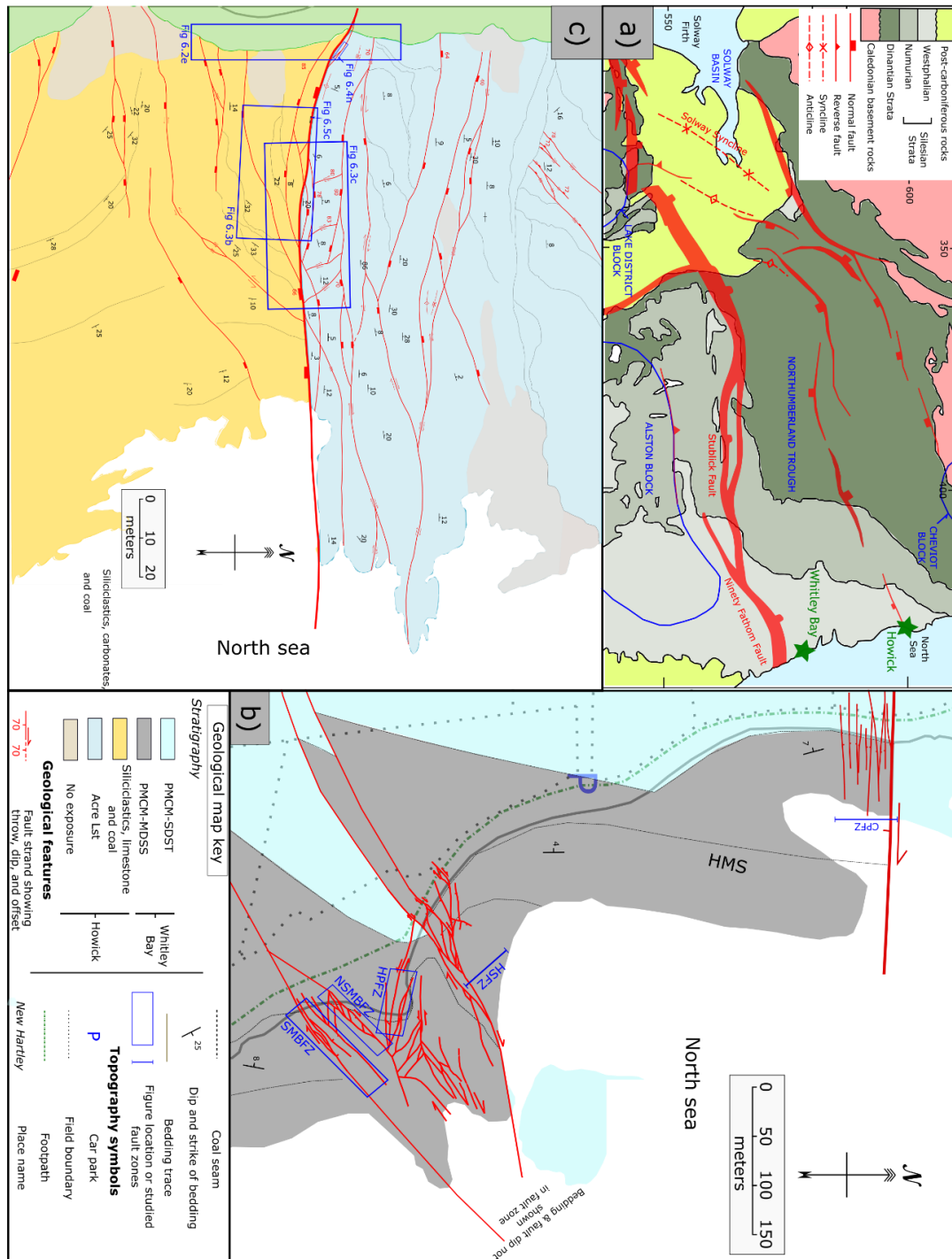


Figure 6.1: Regional and local geology: a) Key structure and distribution of Carboniferous lithologies within the Northumberland Trough (after (Chadwick et al., 1995); re-mapping undertaken as part of this study for b) Howick and c) Whitley Bay highlighting key structures and areas of detailed study.

	Fault zone	Acronym	Key features	Lithologies cut
Howick	FW fault strands (20 m cumulative throw)	HFWF	Limited along strike variability. Steep fault strands. Fault anastomose promoting fault-core lenses to form sub-parallel to HMFZ. High wavelength folding of bedding. Shallow angle lineations (<20°).	Acre Limestone and Calcareous shales.
	Main fault strands (100 m + cumulative throw)	HMFZ	Planar PDZ with fault-rock typically developed. Lens development common. Intense folding of bedding with wavelengths between 2 m and 10 m. Strike-slip and dip-slip fault strands observed.	
	HW wall fault strands (40 m cumulative throw)	HHWF	Fault strands vary in strike orientation. Gentle folding of bedding, which decreases away from HMFZ. Lens development decreases away from HMFZ. Complex interacting fault strands observed in section view.	Thinly bedded (5 to 20 cm) siliciclastic fluvio-deltaic sequence including the Parrot Coal.
Whitley Bay	Crag Point Fault Zone (20 m cumulative throw*)	CPFZ	Multiple EW trending fault strands. Dip-slip to strike-slip lineations (10° to 25°) PDZ and FW damage zone considered for this study.	dm bedded channelised sandstone and interbedded fluvio-deltaic sequence. (Including sandstone, siltstone, shale, seat-earth and coals).
	Hartley Steps Fault Zone (17 m cumulative throw)	HSFZ	PDZ bounded by two NE-trending, steeply dipping fault strands joined by a dip-slip fault with fault-gouge developed along it. Well-developed HW damage zone.	
	Hartley Point Fault Zone (5 m cumulative throw)	HPFZ	SE-trending anastomosing fault zone with dip-slip and sinistral fault strands	
	North of St. Mary's Bay Fault Zone (2 m cumulative throw)	NSMBFZ	NE-trending dextral fault zone with the PDZ forming a 2 to 3 m high cliff section. Well-developed fault core and HW damage zone.	
	St. Mary's Bay Fault Zone (3 to 5 m cumulative throw)	SMBFZ	PDZ is obscured in section view, however, exposed in map view. NE-trending fault zone with a very well developed HW damage zone (>20 m).	

Table 6.1: Summary of fault-zones characterised in this chapter. *The throw for CPFZ refers to the strands investigated in this study and not the overall throw on the fault zone (estimated at c 200 m (Jones and Dearman, 1967)).

Data were collected from six fault zones (Table 6.1) exposed at Whitley Bay and Howick (Northumberland, UK). The faults contained individual fault strands ranging from <2 cm to 25 m offset (Figure 6.1; Table 6.1). An introduction to the geology and basin history is provided in Chapters 1 and 4, with the detailed stratigraphy surrounding the HMS outlined in Chapter 7. The location of detailed maps undertaken at Howick are highlighted on the geological map made as part of this study. Howick data are presented based on whether they were collected in the footwall, main fault strand, or hanging wall. Whitley Bay fault strand data are presented based in the fault zone they belong to (Figure 6.1c). The coastal sections studied represent world class outcrops of UK Carboniferous Coal Measures and have been assigned sites of special scientific interest (SSSI). This combined with the ease of access, exceptional cliff and map-view exposures, and well characterised stratigraphic succession makes this the ideal location to investigate fault development in these lithologies, though SSSI status does mean that samples cannot be taken for microstructural analysis.

6.3.2 Field mapping & structural logs:

Fault zones were investigated using the following methods:

- 1) 1:1,000 scale geological mapping onto printed aerial photography to classify the large-scale structure of fault zones;
- 2) fault and fracture mapping of cliff sections to investigate down-dip heterogeneity and the role of stratigraphy on fault style;
- 3) structural logs using the method of McKay et al (2019), whereby a series of transects perpendicular to fault strike are undertaken capturing fault rock lithology and structure (e.g. veining, shear fractures, fault kinematics);
- 4) cm- to dm-scale grid mapping onto graph paper of the NSMBFZ and key strands identified during mapping.

Fault breccias were described using the terminology of (Woodcock and Mort, 2008) (Chapter 1; Table 1.1), with clay-rich fault gouge described using the BS5930 (BSi, 2015) standard for the description of soils. Where clasts were present within fault rocks, the long (a) and short (b) axis was measured along with the orientation of the long axis. It is usually not possible to observe clasts in 3D, and therefore the 2D long axis was used to measure the dip and dip-direction of clasts in the field. This enables the comparison of field and map data.

6.3.3 Post-fieldwork data analysis

Following fieldwork, maps and structural logs were imported into ArcGIS and scaled for further analysis. The area of fault-rock polygons were compared to investigate the distribution of fault-rock lithologies. The orientation of linear features which include fault-strands, foliations, and calcite veins, were assessed using 'sets' function in the ArcGIS toolbox NetworkGT (Nyberg et al., 2018). This adds an orientation column to the attribute column in ArcGIS, which can then be extracted to Excel and compared to the orientation of the fault plane being investigated.

Several elongated features such as clasts, lenses, and breccia pods were identified. Clasts and lenses were digitised by lithology (i.e. organic fragments/coal, sandstone, siltstone, shale) and split into new polygon layers depending on the fault core facies in which they occur (high strain zone, foliated gouge, breccia, calcite breccia etc.). The area of polygons within each layer were exported in to Excel. The minimum bounding geometry tool in ArcGIS was then used to add a layer containing the best fit 'rectangle by width', which returned the length and width of the rectangle (used as a proxy for a and b axis). Following this, the aspect ratio, equivalent circular area, and the orientation of the long axis was calculated. Breccia pods were digitised, with the area covered by the pods exported depending on whether they were a 'typical fault-breccia' or a 'calcite matrix-supported breccia'. For this study 'typical fault-breccia' is defined as a lithology with angular to sub-angular clasts in a fine-grained matrix with both constituents comprised of fragmented host rock (Woodcock and Mort, 2008; Mort and Woodcock, 2008). The area, orientation, and aspect ratio were assessed in the same manner as lenses and clasts.

6.4 Results

6.4.1 Fault kinematics

Across both sites, fault dip was typically high with fault strand dips ranging from 50° to sub-vertical (Figure 6.2). A strong correlation between dip and both the lithology cut by the fault and proximity to the main strand was observed. Competent lithologies, such as sandstones and limestones typically display dips in excess of 70°, while siltstones and shales show much lower dips (35° to 60°). Through-going faults that cut coal are only observed on strands larger than c. 25 cm, with smaller faults terminating within the coal seam as conjugate mineralised shear fractures, similar to what was observed at Spireslack SCM (See

Chapter 5; Figure 5.4). Fault data are presented in Figure 6.2, with the key features summarised in Table 6.2.

Fault		Key features	Fractures	Bedding
Howick	HFWF	EW and NE trending fault sets are observed. The EW set displays shallow angle lineations (15° to 30°), with fault dip highly variable. The NE trending set develops both shallow angle and dip-slip lineations and forms at an angle of 70° to the main strand.	Fracture data not collected	Bedding displays gentle folding with a fold axis orientated sub-parallel to the strike of HMFZ.
	HMFZ	PDZs Trend EW (mean = 082°), with subsidiary strands striking SE and ENE. Low angle lineations typical. Conjugate subsidiary strands at a high angle to PDZs are also observed with steeper lineations (55° to 60°).	Conjugate sets or fracture corridors form at 55 to 75° and 15° to 25° to PDZs.	Rotated towards the fault, with beds close to the fault zone matching the dip and strike of the major structure
	HHWF	Orientations match that observed in HFWF.	Fracture data not collected	Bedding is folded along a fold axis orientated 60° to HMFZ.
Whitley Bay	CPFZ	Majority of strands trend ESE and display lineations below 25°. A subsidiary set of S-dipping fault strands display dip-slip lineations.	Three sets observed (ESE, NNW and ENE). NNW and ENE sets are regional joints.	Bedding rotated along a fold axis parallel to the strike of CPFZ, with maximum dip reaching that of the main strand.
	HSFZ	ENE trending main strand, with strands also observed at 20° and 70° to this. Lineations are predominantly low angle, however, dip-slip lineations are present on the NE and SE trending faults.	Fractures form roughly parallel to observed fault trends.	Bedding rotated around a fold axis orientated EW.
	HPFZ	Two sets observed, one trending ENE, and another trending SW. The SW is the primary set, however, the fault plane was often obscured. Lineations are between 15° and 30°.	Trends strike the same as observed faults, however, dip towards the fault.	Little rotation of bedding, with steeper beds only observed along the SE trending fault.
	NSMBFZ	Primarily trends NE and displays shallow angle lineations ranging from 4 to 30°.	Occur at angles of 30° and 75° to the main fault strand.	Bedding rotated into the fault by up to 40°
	SMBFZ	Three sets observed trending NS, NE and EW, with each set displaying conjugate sets.	Three sets observed (EW, NW and ENE).	Bedding rotated relative to the NE trending fault plane.

Table 6.2: Summary of fault, fracture, and bedding data presented for each fault zone.

	Fault strand	Fracture	Bedding	
HMFZ				Howick
HWF		Fracture data not collected		
HHWF				
CPFZ				Whitley Bay
HSFZ				
HPFZ				
NSMBFZ				
SMBFZ				

Figure 6.2 (Previous page): Stereographic projections of fault, fracture, and bedding data presented by fault zone. Stereographic projections were created using Stereonet 10.1 (Allmendinger et al., 2013; Cardozo and Allmendinger, 2013).

6.4.2 Fault zone structure

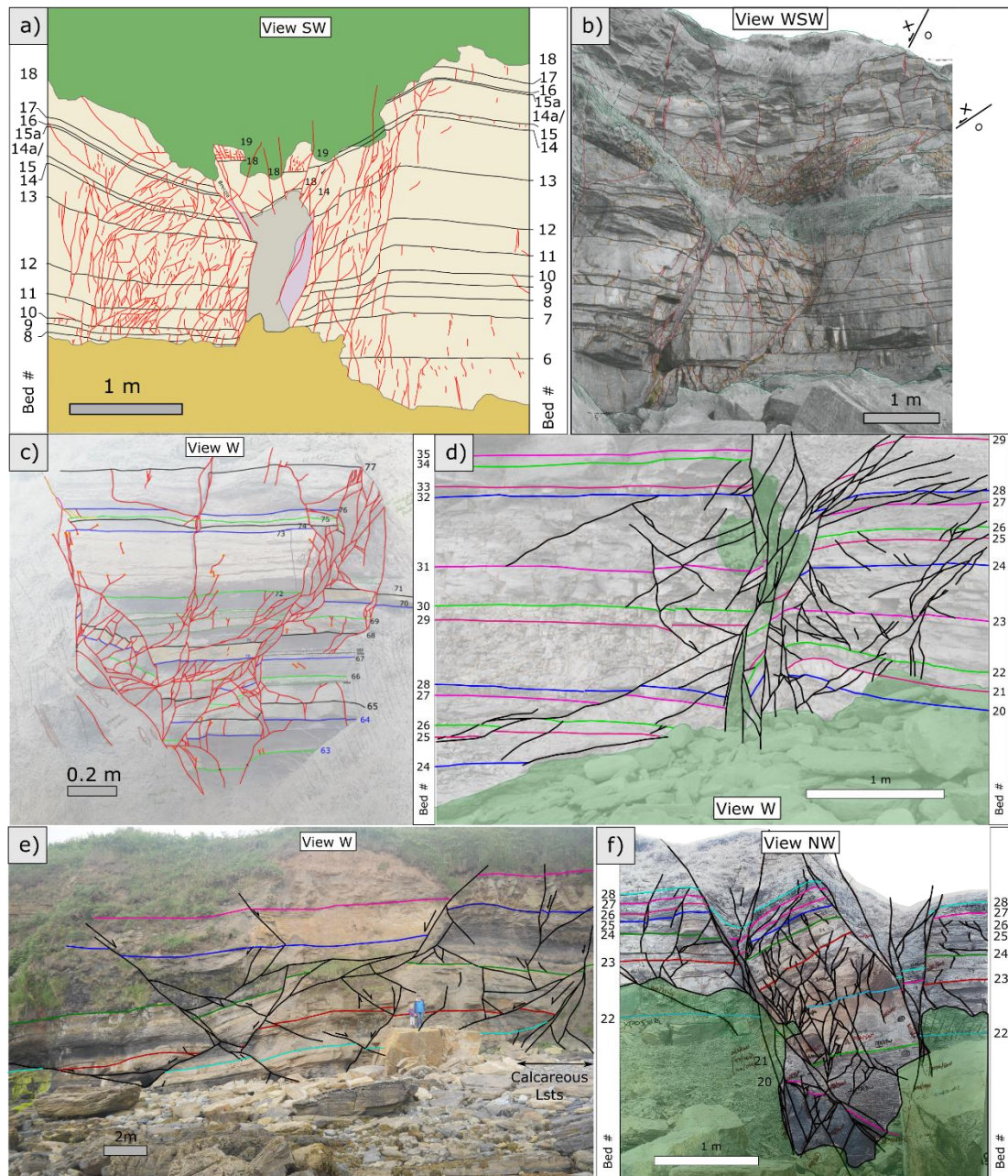


Figure 6.3: Annotated features of faults (horizon numbers for faults at Whitley Bay correlate to bed numbers used in Chapter 4): a) dextral offset fault cutting sandstone-rich lithologies at Whitley Bay displaying an asymmetric damage zone; b) and c) dextral offset fault strands cutting interbedded lithologies exposed at Whitley Bay; d) interaction between dip-slip and dextral fault strands within the Hartley Steps Fault Zone, Whitley Bay; e) HW fault strands at Howick cutting interbedded silicilastics, carbonates and coal; f) small offset splay of the CPFZ.

Faults exposed at Whitley Bay and Howick rarely occur as a single strand but instead as several anastomosing faults with complex patterns that interact with the stratigraphy (Figure 6.3). Fault strike may vary along strike for a single fault, and while large faults match the regional trend, small offset faults often occur obliquely to this. This promotes block-rotation and the entrainment of fault-core lenses bounded by fault strands. For example, the HSFZ at Whitley Bay (Figure 6.1 & 6.2) occurs as three primary strands striking E-W at the cliff line, however, out to sea strike rotates to the SE and splays interact with HPFZ and NSMBFZ.

In section view, faults display either: a) strongly asymmetric damage zones with few fault strands cutting the footwall sediments and a large damage zone developed in the hanging wall (Figure 6.2a, e); b) two or more anastomosing fault strands, which bound zones of undeformed or fractured host rock that can usually be defined as fault-core lenses (Figure b, c). In cases where fault-core lenses can not be defined, the zone is instead bound by two or more fault strands that may or may not terminate at mechanical boundaries (e.g. bedding). Where fault strands interact, a complex zone of damage is developed. This is observed in a number of settings including:

- where fault strands with shallow apparent dip interact with steeply dipping strike-slip faults (Figure 6.2d).
- where two dip slip fault strands interact (Figure 6.2e).
- where two oppositely dipping dip-slip strands meet and cause a 'triangular' damage zone to develop (Figure 6.2f).

The termination, branching, and dip of fault strands is greatly affected by the lithologies cut by the fault, with complexity showing little correlation to displacement. For example, Figure 6.3b and 6.3c show faults with similar deformation patterns, however they have throws of <0.3 m and 1.5 m respectively. This is likely due to the greater proportion of incompetent beds in Figure 6.3c. However, the difference may also partly be due to out of plane motion as both faults display shallow angle lineations. Lithology controls fault structure at all scales, from the larger offsets observed at Howick (Figure 6.2e), to cm scale fault strands associated with the CPFZ (Figure 6.2f). Where shale and organic layers dominate: a) there is a greater degree of lens development; b) faults splay, with a greater number of strands observed in heterolithic beds; c) greater heterogeneity in the fault thickness is observed;

and d) fault strands often terminate at the boundary between shale rich layers and overlying sandstone beds.

Along PDZs and major fault strands (>1 m throw) a semi-continuous zone of fault rock is often developed (breccia, cataclasite, and/or gouge), followed by up to tens of meters perpendicular to the PDZ (in map view) where fault-core lenses are developed. Within this fault rocks, higher strain strands occur at an oblique angle to the primary PDZ and match a Riedel shear strain ellipse for right lateral shear. Additionally, a number of map-specific features were identified as summarised below:

- *St. Mary's Bay Fault (Figure 6.4a)*: Three PDZs are identified, each with fault rock developed including fault gouge and pods of matrix supported fault-breccia that occur where the fault strike changes. Fault core lenses are aligned parallel or slightly oblique (15° to 20°) to the PDZ with slip planes observed between individual lenses.
- *Subsidiary fault strand cutting limestone and siliciclastics at Howick (Figure 6.4b)*: the zone is bounded by two PDZs, each accommodating the majority of the throw along the fault. Between these, exposures is often poor, however it is possible to identify several sandstone, siltstone, and locally organic rich shale/coal lenses. Long axis orientation rarely deviates more than 15° from the PDZ and the edge of lenses may display brecciation and shallow angle striations (6° to 15°). Towards the SE shale thins from 3.5 m, to 0.4 m, with the dip also increasing from 40° to sub-vertical. Although some thinning can be explained by the change in dip, the thickness of the undeformed shale bed exceeds 1 m suggesting structural thinning.
- *Main fault strand, Howick (Figure 6.4c)*: Across the studied section the PDZ only varies in strike by 20° and this occurs along small scale (meter scale) undulations. The PDZ displays a laterally continuous zone of fault rock comprising of fault-gouge and breccia which ranged in thickness from 0.2 to 0.6 m. Away from the PDZ is a zone of lens development with variable thickness (7 to 12.5 m), with lenses separated by anastomosing fault strands. The average orientation of these strands match that of the main strand, however, individual strands may form as much as 45° away from the strike of the main strand.

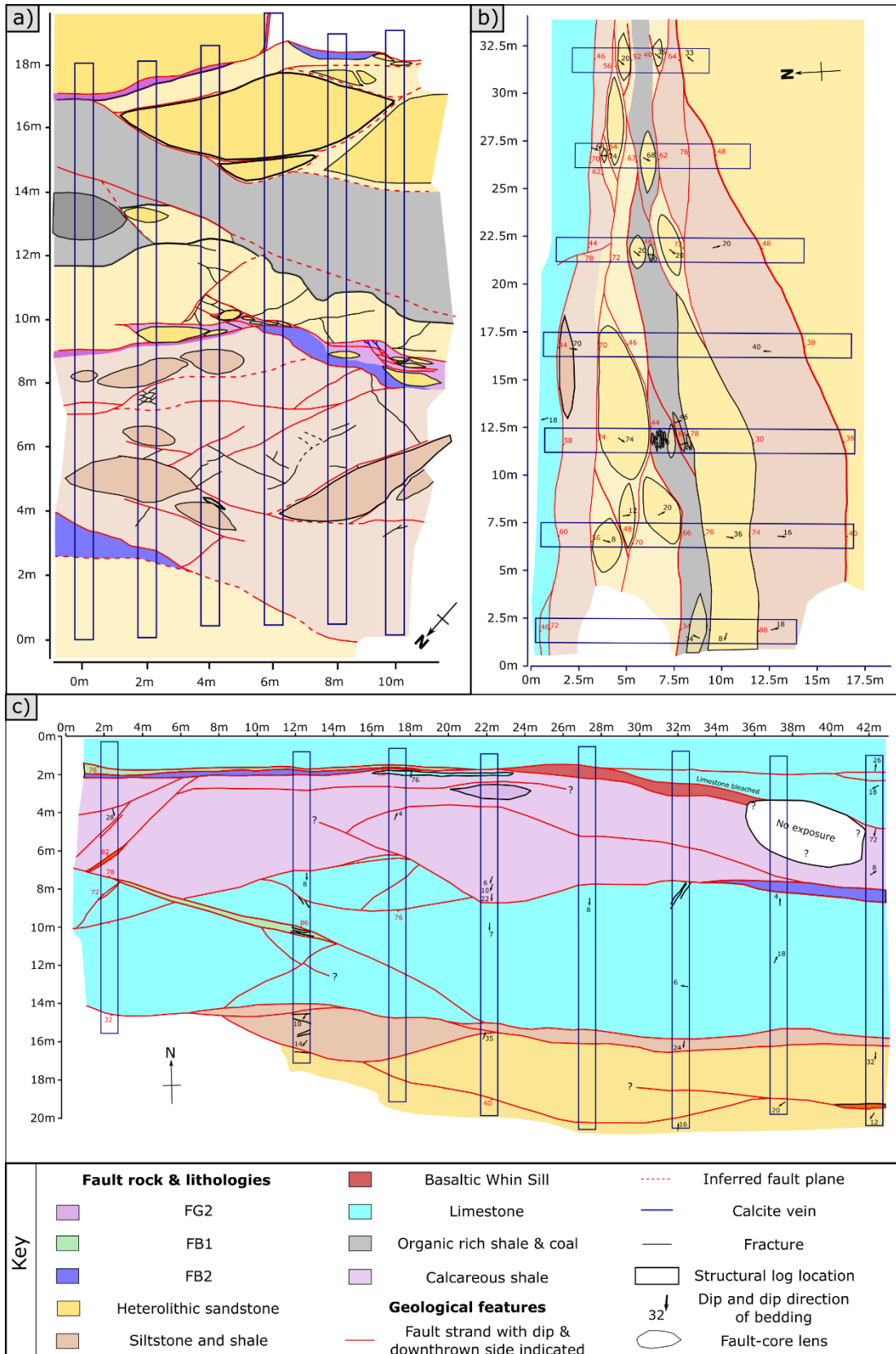


Figure 6.4 (Previous page): Structural logs of the fault core. Areas outlined in blue were logged in detail and detailed orientation data collected. Fault unit boundaries were correlated between these logs, using printed field photos to ensure that the geometries are honoured. a) SMBZ which cuts interbedded heterolithic sandstones, siltstones, shale and coal; b) Howick Strand 1 which separates limestones of the Acre Limestone in the FW from silicilasts in the HW; and c) Howick Strand 2 which cuts across many of the FW fault strands observed at Howick.

Significant variability in fault dip and strike are observed in both planes of observation with lithology strongly affecting fault zone characteristics. However, several differences exist between map- and section-view, even along the same fault. In map view extensive lens development is observed, however, in section view it is unclear what constitutes a minor fault splay, and what constitutes a fault-core lens. This could be a weathering effect such that strands are preferentially weathered, or that fault-core lenses display very high down-dip aspect ratios (which is difficult to quantify due to poor section view exposure in lens-developing lithologies). Another difference is that while the stratigraphy is observed in section view, it is rare to find fault-rock, shale, and coal in the same map view exposure. This will affect the thickness measurements for a fault zone. For example, along the main strand at Howick several discrete fault strands are observed in section view; however, in map view thickness measurements are taken on sandstone beds and are therefore taken between the two primary slip planes.

6.4.3 Fault rock lithologies

Several fault rock lithologies have been identified including fault gouge, cataclasite, clast-supported fault breccia, matrix-supported fault-breccia, alteration of coal, and fault-core lenses (Figures 6.5 to 6.8). Additionally, slip-planes often nucleate within organic rich shales, with lineations developing along the boundary between channel coals and shale (Figure 6.5a).



Figure 6.5: Fault rock lithologies: a) Fault-core lens and radial shear development along HPFZ; b) alteration of the High Main Seam and local development of tectonically deformed coal along HPFZ; c) lineations developed between channel coals and organic rich shale in the vicinity of SMBFZ.

Fault-core lenses

Fault-core lenses are observed along the majority of fault planes and range in 2D area from less than a cm² (Figure 6.4k) to several meters² (Figure 6.5a and Figure 2.6). Lenses are elongated down dip and along strike, with long axis orientated parallel, or slightly oblique to the PDZ and may be composed of sandstone, limestone, siltstone, and coal. Lenses rarely display multiple lithologies, at least at the field scale and it is likely that they are entrained along mechanical boundaries within the stratigraphy. Sandstone and limestone lenses are most commonly observed (other lithologies are preferentially weathered) and the rotation of competent bedding surrounded by shale is observed close to PDZs. Large lenses may be cut by several minor faults orientated oblique to the PDZ that subdivide lens into sub-lenses. Minor slip planes and the edge of lenses often display brecciation and the development of fault rocks including matrix-supported breccia, clast-supported breccia, cataclasite, and veining (calcite and quartz). Aspect ratio increases close to PDZs and is accompanied by a reduction in area. Locally (e.g. along the St. Mary's Point fault zone), fault-core lenses progress into cataclasite along strike (Figure 6.5a).

Cataclasite

Cataclasite occurs either as pods along PDZs, or as thin bands along minor faults cutting sandstone or limestone. Cataclasites contain 0.5 to 1 mm, rounded to sub-rounded, clasts of limestone/sandstone, siltstone, and organics fragments. Less than 5% of clasts exceed 5 mm, with those that do elongated parallel to the strike of the fault where cataclasite is developed. The smallest clasts are always observed along the footwall. Cataclasite bands may cut across PDZs or fault breccias. Organic fragments are often observed within these zones as sub-rounded 1 to 2 mm clasts elongated parallel to the slip direction or angular clasts bounded by cleats and bed-partings.

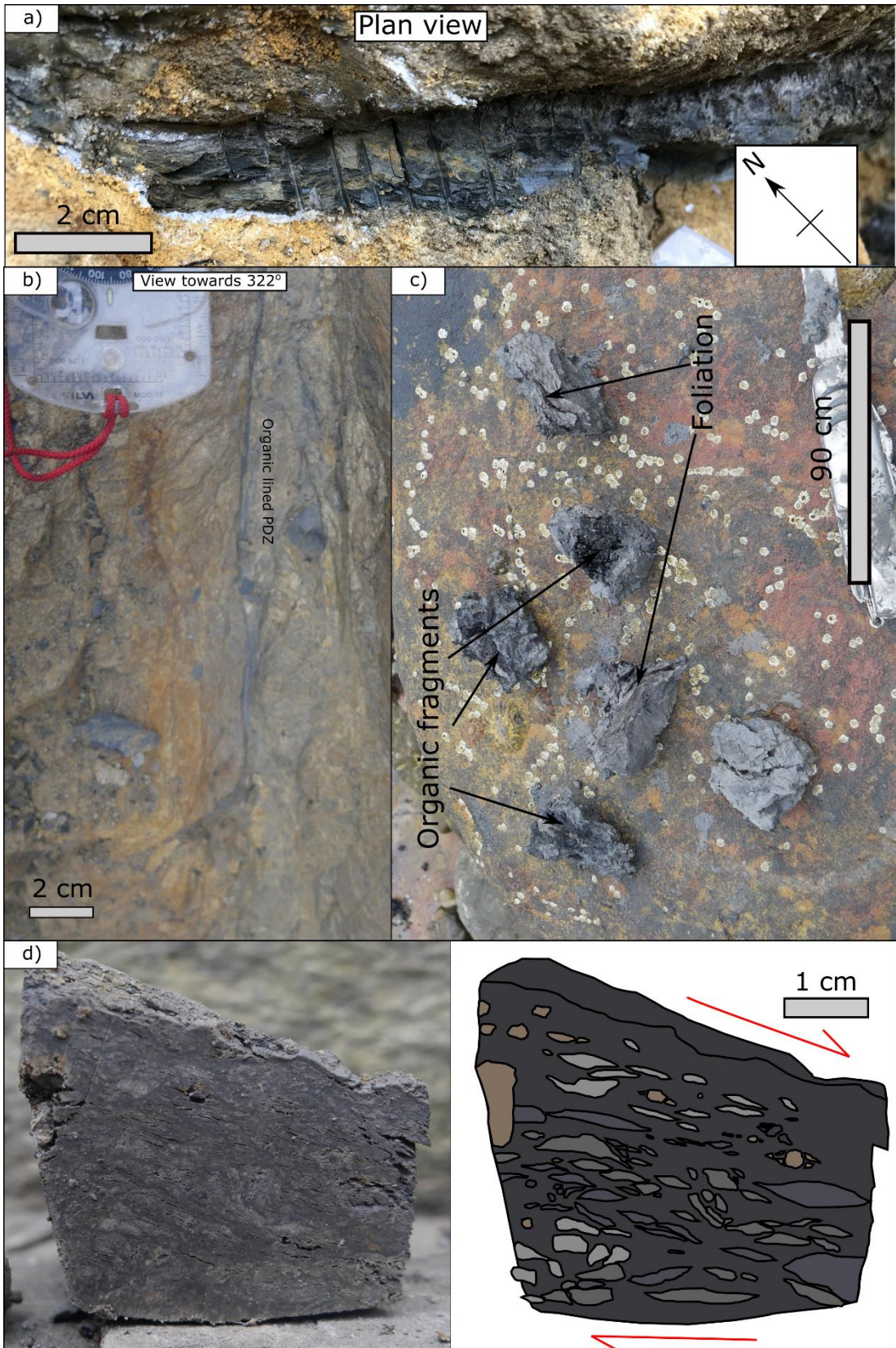


Figure 6.6 (Previous page): Fault gouge: a) FG1 developed along NSMBFZ; b) FG3 developed within heterolithics close to SMBFZ; c) fragments of FG1 and FG2 found within rock-pools along the CPFZ; d) FG2 and interpretation of key structures developed within HSFZ.

Fault gouge

Fault gouge is common on faults with throws above 0.5 m that cut clay-rich lithologies.

While the thickness of the gouge zone can highly variable, a near-continuous zone of 1 to 5 cm thick fault-gouge is observed along PDZs where shale is cut (e.g. CPFZ and HSFZ). Three types of fault gouge have been identified:

- *FG1: Plastic fault gouge (Figure 6.6a)*: FG1 occurs within 2 to 4 cm of the PDZ of faults with throw above 1.5 m (e.g. NStMB and HSFZ) and is light grey to off white in colour. FG1 displays high plasticity such that it sticks to fingers when wet and crumbles when dry which is indicative of a high clay content. FG1 is soft to very soft and either contains extremely closely spaced foliations (0.5 to 1.5 mm) or no clear foliations at a field scale. Clasts, which range in size from 0.5 mm up to 1.5 cm, are elongated parallel or sub-parallel to the PDZ. Clasts may consist of sandstone, siltstone, shale, coal, or pods of cataclasite. Sandstone clasts often display alteration to either: a) off-white coloration and associated with a decrease in mechanical strength such that it is easily scratched with a knife; or b) brick orange that occurs as sub-rounded clasts with increased hardness. Where coal or organics are observed they are found as pods of friable coal (see Chapter 2 for terminology) aligned parallel to foliation (Figure 6.4m).
- *FG2: Foliated plastic fault gouge (Figure 6.6c & d)*: FG2 is observed along the majority of large offset faults cutting shale-rich lithologies and reach <10 cm in thickness (See Figure 6.5). FG2 is light to dark grey with moderate plasticity, however it does not crumble when dry and retains its structure. FG is firm to soft, with a closely spaced foliation (0.5 to 2 mm) picked out by dark-grey organic layers. Foliations display an anastomosing geometry around pods of cataclasis and lensoidal clasts. Along the foliations organic fragments (<1 mm) are commonly observed and are likely the cause of the dark grey coloration. Clasts may be shale, siltstone, or sandstone with no large clasts of organics observed. Clasts are rounded to sub-rounded with tails of disaggregated small clasts elongated parallel or sub-parallel to the PDZ.
- *FG3: Organic-rich gouge (Figure 6.6b)*: FG3 is found along faults with small throw (0.01 to 0.80 m) cutting heterolithic lithologies with a high organic content. FC3 is

black and occurs as planar bands whose thicknesses does not exceed 2 mm. FG3 may be slightly granular to touch and disaggregates in water suggesting a fine-silt grain size. It displays a firm to stiff consistency and displays no visible discontinuities or clasts.

Alteration of coal and development of TDCs (Figure 6.5b)

Where small offset faults cut coal and/or shale, coal may either become mineralised or altered. Mineralisation is typically ankerite that utilises the cleat network, in the same manner as that described at Spireslack SCM (Chapter 5). Where present, alteration occurs in zones parallel to the PDZ and is bounded by tectonically deformed coal (TDC). However, due to the coloration and the fact that this is only observed within the HPFZ near abandoned pillar and stall mine workings (described in Chapter 7) it is likely that the discoloration and alteration is mine-water related. TDCs are rarely developed, and where they are observed thicknesses do not exceed 10 cm and only occur where the High Main Seam is cut by faults with throws above 1.5 m.

Fault breccias

Where competent lithologies are juxtaposed against each other, three types of fault breccia commonly form. These rarely display along-strike continuity but instead form as pods whose long-axis length ranged from <10 cm up to > 5 m (Figure 6.2 & 6.4).

FB1: Rounded to sub-rounded crackle breccia (Figure 6.7)

FB1 is the most commonly observed fault breccia, occurring as pods along PDZs and between fault-core lenses. Within siliciclastic lithologies the matrix comprises of silt to fine sand, well to moderately sorted grains of predominantly quartz and subsidiary clay and organic fragments. Clasts are typically rounded to sub-rounded, with occasional sub-angular clasts present towards the edge of the pod and display high variability in clast grain size. Clast long axes are only weakly aligned with the PDZ, with clasts orientated perpendicular to the fault strand observed. Clasts commonly display alteration to bleached white, which is not observed in the host rock. Strength also decreases such that it can easily be scratched with a knife. The matrix may develop a foliation, whereby planes of fine material (silt to v. fine sand) are aligned sub-parallel to the PDZ and cut through the breccia, being deflected by large clasts. When a breccia was investigated using the XCT at the University of

Strathclyde it was found that organic fragments typically pick out thin foliations, with organic fragments also surrounding rounded to sub-rounded clasts (Figure 6.7d)

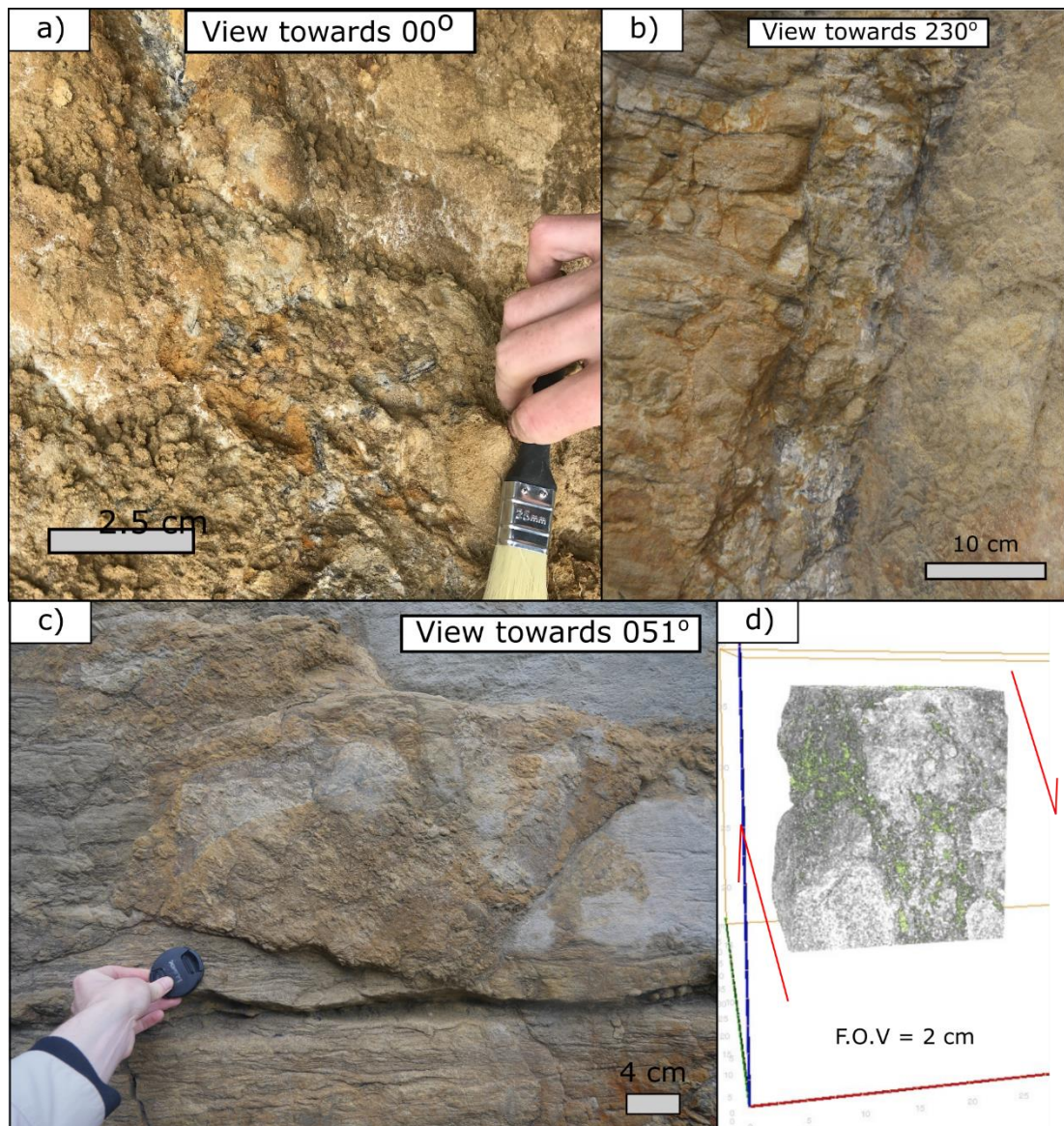


Figure 6.7: FB1: a) FB1 developed along the main strand of CPFZ; b) highly altered layered fault-rocks (FG3, Cataclasite, FB1 and fault-core lenses) associated with a minor splay cutting heterolithics near SMBFZ; c) altered pod of FB1 along HSFZ with dip-slip lineations developed along the HW; d) xCT image showing the density contrasts and highlighting the distribution of organic contents (green).

In limestones (e.g. the main fault plane at Howick) the matrix comprises of fine to medium grade crushed limestone and oolitic fragments, which support clasts of disaggregated host rock. Limestone clasts are sub-rounded to sub-angular and typically display a long axis orientated parallel to the local edge orientation of the breccia pod. Where a large zone of

brecciation is developed (e.g. the main strand of CPFZ), several pods with distinct properties are observed.

FB2: Matrix-supported calcite breccia (Figure 6.8c & d)

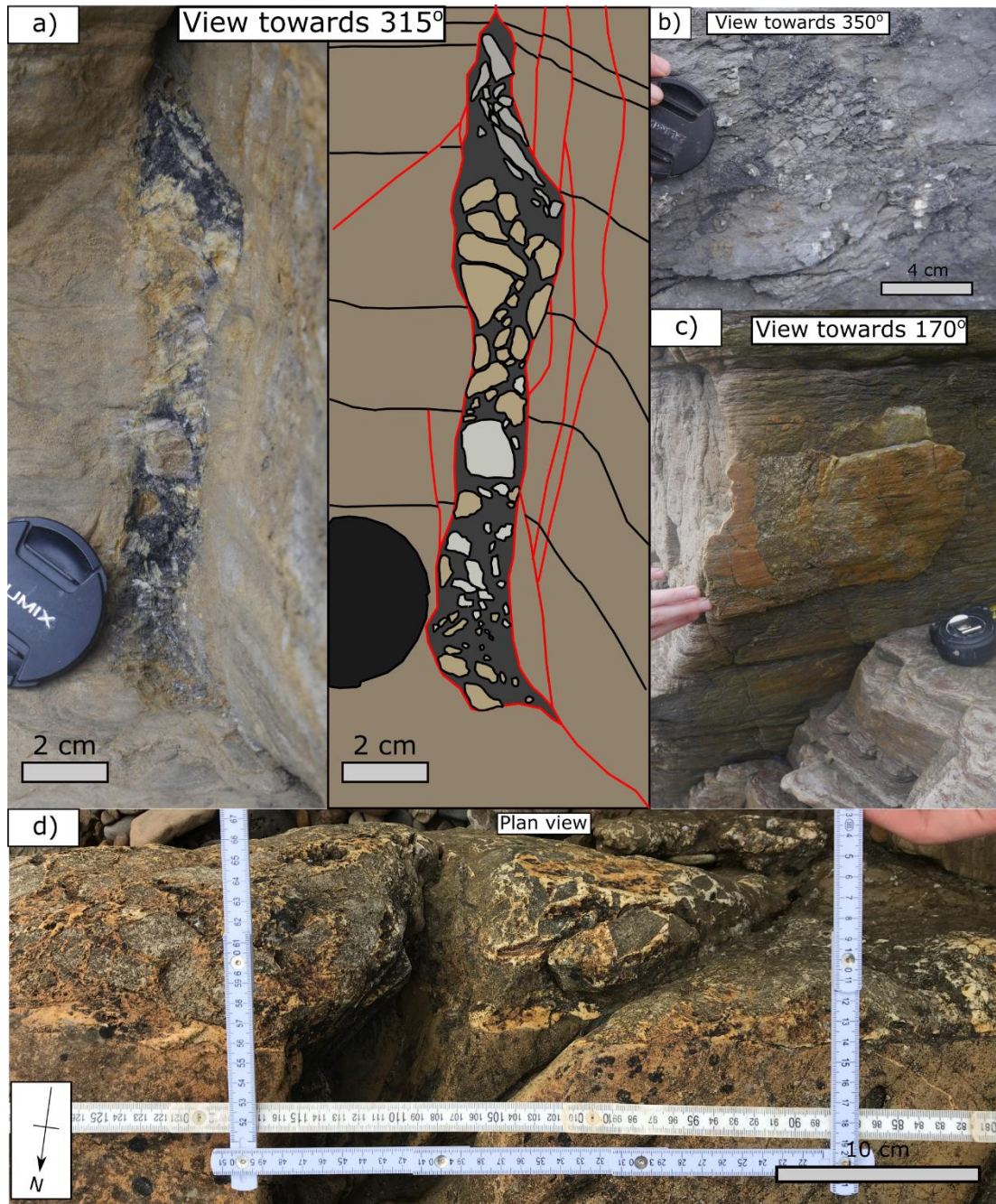


Figure 6.8: FB2 and FB3: a) pod of FB3 which forms along a y-shear to the HSFZ which displays no apparent offset; b) FB3 along a y-shear associated with the HMFZ where the organic rich shale matrix has been coalified; c) FB2 associated with SMBFZ which displays shallow angle lineations along slip surfaces which bound the breccia; d) Pod of FB2 found along a T-shear associated with the NSMBFZ.

FB2 commonly forms within sandstone and limestone as isolated pods on moderate offset (throw > 0.2 m) faults off the main PDZ. The matrix is comprised of macrocrystalline calcite with crystal size ranging from 0.5 mm up for 3 cm. No internal structure was observed in the matrix, including no preferential crystal growth directions. Clasts are randomly orientated, angular to sub-angular, and can be visually pieced back together (mosaic breccia). Clast size may increase towards the centre of the pod, with the tip of pods displaying small (<3 cm) tetrahedral clasts of sandstone/limestone. At locations where the fault hosts FB2, the PDZ is often bounded by a 1-2 cm thick mineralised slip plane, with either no clasts, or clasts below 0.2 cm in diameter. These may also be observed to occasionally cut through a matrix-supported breccia, separating two zones with marked differences in clast size that indicating multiple events. The slip plane often displays slickenfibers and/or lineations indicating strike slip motion (Figure 6.8c).

FB3: Organic-matrix supported chaotic to mesoic breccia (Figure 6.8a, b)

At several locations in Whitley Bay isolated pods of majority matrix-supported breccia develop with an organic rich matrix (Figure 6.8a). These occur when faults cut heteorolithic units consisting of between 10% and 15% organic rich layers which include abundant channel coals and organic draped ripples. FB3 displays sub-angular to angular clasts of fine-sandstone to siltstone, with bedding indicating the block rotation of clasts within the breccia. No clear preferential orientation is observed, with clast rotation occurring both towards and away from the PDZ. The matrix consists of between 90% and 95% organic content from visual inspection, which comes away as a fine powder when touched. The remaining 5% to 10% consists of randomly distributed, sub-mm, quartz and ironstone fragments. The matrix wraps around clasts, contains no internal structure, and often thins to a fine strand of FC1 or cataclasite along strike.

At Howick a strand parallel to the main fault which displays no throw, but evidence of sinistral strike slip contains a 1 to 2 cm thick organic rich breccia zone (Figure 6.8b). The matrix of the breccia is comprised of very hard, coalified organics interpreted as a meta-anthracite. This matrix surrounds angular limestone clasts which show weak to no orientation. Similar to Whitley Bay the clasts are bounded by the organic-rich matrix and have been rotated both away, and towards the PDZ.

6.4.4 Fault-strand maps

6.4.4.1 Heterogeneity along a single fault strand: NSMBFZ

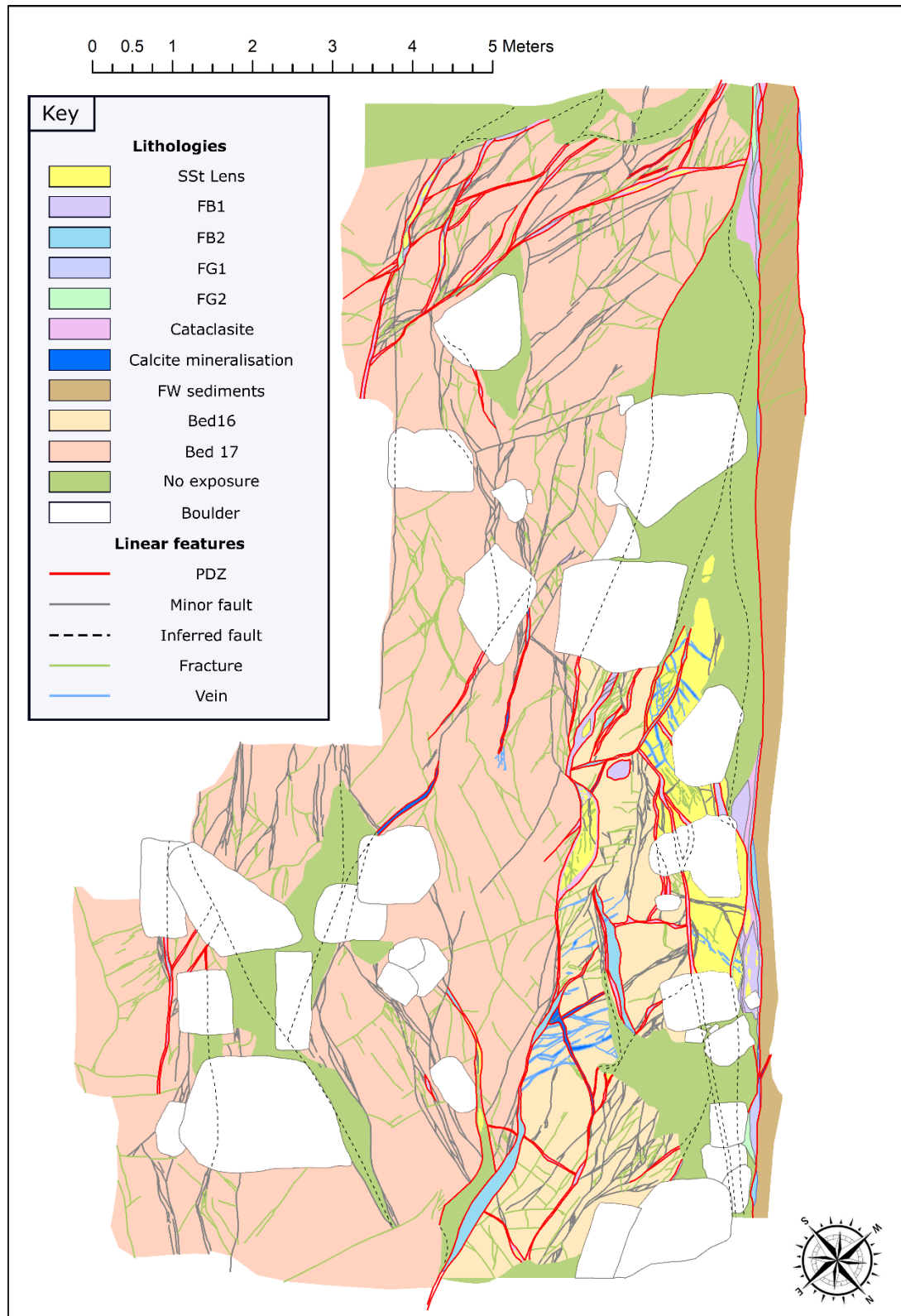


Figure 6.9 (Previous page): Fault map for NSMBFZ (plan view) undertaken using 0.5 m grid mapping. The map was created using a 50 cm² grid laid out over the outcrop, with key features mapped onto graph paper. The mapped area displays little topography and the bedding planes for beds 16 and 17 are at the same level.

50 cm² grid mapping of NSMBFZ enabled the distribution of fault-rock, minor fault-strands, fractures, and mineralisation to be investigated along the strike of a single fault (Figure 6.9). The zone is bounded by a major PDZ that makes up the NW of the outcrop (1.2 m throw) and a sub-parallel minor PDZ (<10 cm throw) to the SE. Several PDZs displaying offsets up to 80 cm develop at angles of $\pm 12^\circ$ to 20° and $+70^\circ$ to 78° . Similar orientations are observed within minor faults, with fractures and veins also striking at a high angle ($+40^\circ$ to 55°) to the main fault strand.

PDZs display anastomosing patterns that bound elongated sandstone lenses. Close to the PDZ and within Bed 16, the aspect ratio is higher than away from the PDZ, with 2D area also increasing with distance from the PDZ. However, this is not the case in the SW of the map where a mesh of minor slip surfaces in Bed 16 results in high aspect ratio and low 2D area lenses. Lenses in Bed 16 display internal deformation including minor faults and mineralisation. Lenses break down, from the lens which makes up the exposure of Bed 16, to <0.5 m lenses near tip of lenses.

Fault rock is extensively developed along PDZs and is thickest immediately adjacent to the main fault strand. The following fault-rock types are developed:

- FG1: Only developed as a <5 cm thick, laterally continuous band along the main fault strand.
- FG2: Found along the main fault strand, as well as the 0.8 m PDZ which bounds Bed 16, and the sub-parallel PDZ which makes up the SE of the mapped section.
- Cataclasite: Forms thin (typically < 2cm) laterally continuous bands along the majority of PDZs. Strand thickness can vary considerably for a single strand and may either terminate at, convert into, or bound pods of fault breccia.
- FB1: Developed as elongated pods with long axis orientated sub-parallel to the nearest PDZ. Pods are largest in the vicinity to the PDZ and may include small (<0.5 cm) sandstone lenses.
- FB2: Typically developed on PDZs orientated at 70° to the main strand where fault strands display a jog. For example, the EW trending PDZ displays two pods of FB2, developed at jogs and suggesting sinistral motion. Along the rest of the PDZ

cataclasite is developed, suggesting FB2 represents point-source vertical fluid flow. Thickness of FB2 varies considerably both within individual pods, and between pods with maximum pod thicknesses ranging from 5 to 22 cm.

- Mineralised fault plane: Typically developed at 45° to 55° to the main fault strand, with local divergence along connected northerly striking faults. Shallow angle (<20°) and/or dip-slip (45° to 55°) lineations may develop along the edge of mineralised zones and no internal growth structures are observed.

6.4.4.2 Section view fault zone characteristics.

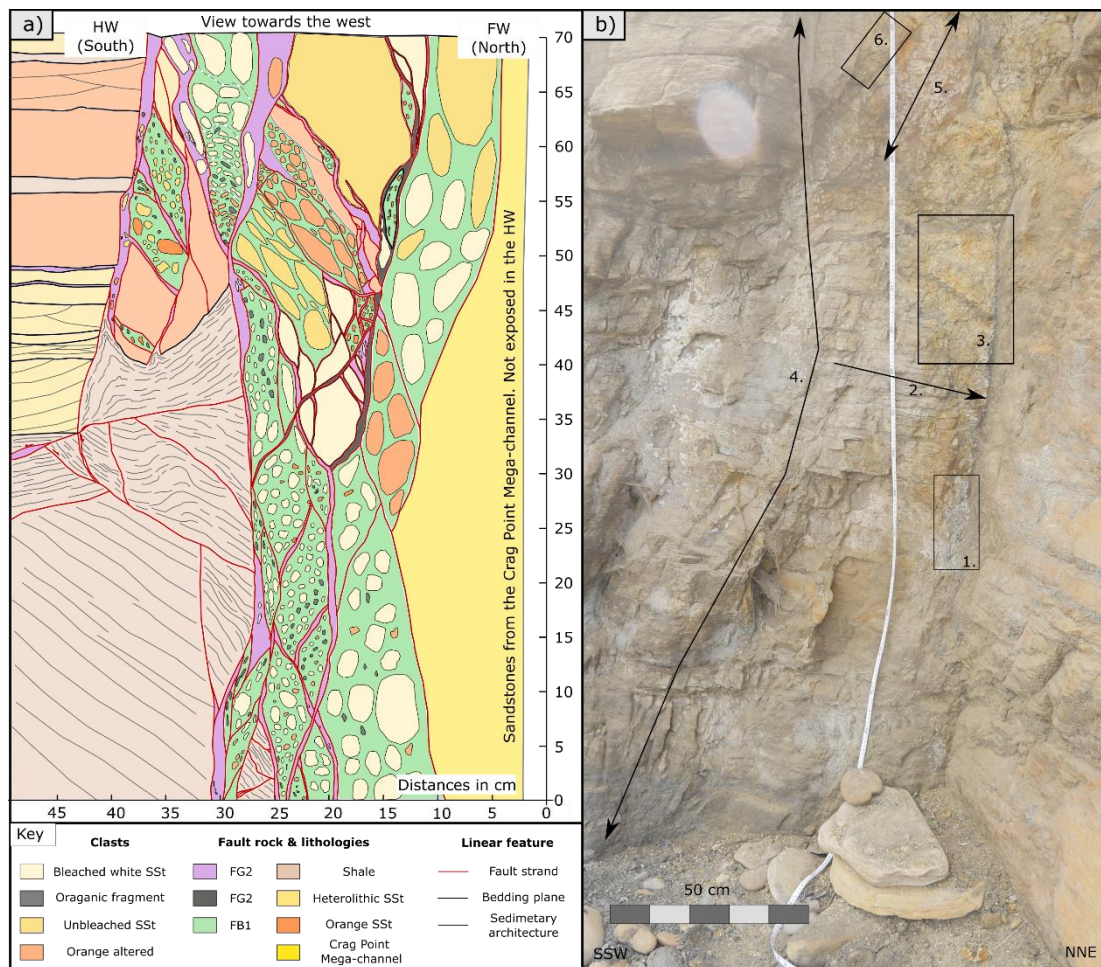


Figure 6.10: Section view of fault strands: a) fault-map of the CPFZ main strand outlining the distribution of fault-rock and fault-related fractures. The map was undertaken by laying a vertical tape measure over the outcrop (similar to observed in panel b) with features drawn onto graph paper. Clasts represent true clast geometry and highlight the high degree of rounding within this breccia zone; b) field photograph of a splay associated with SMBFZ. Numbers relate to the features discussed in the main text.

Fault with ~80 cm throw associated with SMBFZ (Figure 6.10b)

The fault zone displays the alteration of fine- to medium-grained sandstone to an off-white to bleached-white colour. When viewed at a distance, the discolouration extends between this structure and the fault immediately to the north bounding a 2 m wide zone. The altered sandstone is considerably weaker than the undeformed host rock and discolouration appears again after 5 to 10 minutes after a surface is scratched clean with a knife. It likely represents pyrite oxidation, with pyrite emplaced through sulphur rich fluids which migrated along the fault zone. Additionally, the following key observations were made, with the location of each highlighted on Figure 6.10b:

- 1) *Pod of clast-supported breccia*: Foliated clay to silt matrix with bleached fine sand particles. Foliations picked out by white clasts aligned parallel to the PDZ. Clasts have typically lost any hint of bedding, however, small organic clasts are still be observed. A large clast with remnants of bedding is rotated to dip shallowly towards the south (8° apparent dip). Clast size varies from long:short axis of 28mm:10mm to individual sand particles. Foliations curve and the breccia pod tapers off up- and down-dip (length = 250 mm, width = 35 mm). The pod is bounded on both sides by a 2 to 3 mm thick, dark grey band of FG1.
- 2) *Disaggregated bedding towards the PDZ*: Faults with minor throws (2 to 3 mm) chop up bedding towards the PDZ until bedding is disaggregated along the PDZ. 65mm by 12 mm sandstone 'clasts' develop that are elongated parallel to the PDZ. At this location the PDZ displays a very thin (hairline) zone of FG1. Above this zone is another clast-supported breccia with a maximum thickness of 22 mm that contains bleached white clasts (2 to 8 mm) aligned parallel to the PDZ.
- 3) *Organic-lined shear fractures*: An organic-rich layer is cut by several shear fractures lined with organic material. The layer has been folded between the fractures. The organic-lined fractures bound an area of fine-medium sandstone with a reddish colour which appears less altered and is clearly harder.
- 4) *Hanging wall side of the fault*: The hanging wall side of the fault is more variable and no planar, through-going slip planes are observed. This area is cut by several synthetic, organic-coated, shear fractures. The organic-lined fractures do not cause the consistent stepping down of bedding but instead display inconsistent slip senses displaying variable sense of motions.

- 5) *Competent, red-silt rippled sandstone*: Reddish medium sandstone, well cemented, with no porosity observed with a hand lens (<5%) and orange specks developed on a fresh surface. Apparent dip of bedding is flat-lying, and the layer contains fewer fractures than the lighter sandstone. Fractures do not propagate into the surrounding lithologies. The undeformed host rock is characterised by red silt occurring along ripples, with less jointing also observed away from faults.
- 6) *Orange wedge of breccia*: This zone of breccia is similar to (3), however, has been fractured and lost its cohesion (comes away as a powder when touched). A web of fractures, with no clear orientation sets causes bedding to become disaggregated. An isolated patch of 'wispy' organics is present at the intersection of small slip-planes. The orientation of the slip-plane that bounds the breccia varies from 020°/60° S at the base, to 176°/66° E in the middle, and 026°/62° S at the top.

Breccia pods along the main strands of CPFZ (Figure 6.10a)

Where CPFZ is observed in the cliff to the north of Whitley Bay, a 25 to 35 cm thick PDZ juxtaposes sandstones, siltstones and shales in the hanging wall against channelised sandstones in the footwall. The zone is characterised by multiple breccia pods, with grain size varying from 0.5 cm to 8 cm. Pods are elongated oblique to the PDZ and separated by synthetic and antithetic high strain zones. The high strain zones comprise of cataclasite, gouge, and/or small pods of fine-grained FB1. PDZ thickness widens towards the top of the mapped area where sandstones are juxtaposed against sandstones (35 to 45 cm) compared to the base where shale is juxtaposed against sandstone (12 to 20 cm). Deformation style varies in three separate zones as described below:

- *Zone 1: Sandstone juxtaposed against sandstone*: A wide zone (35 to 45 cm) consisting of anastomosing PDZ which develop FG2, FG3, and pods of FB1 which dip towards the PDZ. Rotation of HW blocks into the fault zone is also observed. Clasts display high aspect ratios and dip towards the PDZ.
- *Zone 2: Sandstone juxtaposed against shale*: Z2 is thinner than Z1, ranging in thickness from 12 to 20 cm. Fault-rock lithology systematically changes from the FW to HW in the following order: 1) FB1 with large, rounded to sub-rounded clasts orientated sub-parallel to the main strand; 2) Thin (<2 cm) FG2 band; 3) 8 to 13 cm thick zone consisting of FB1 pods with small sub-rounded to sub-angular, low aspect ratio clasts bounded by anastomosing PDZs with FG2 developed.

- Zone 3: The boundary between Zones 1 and 2: Gradual increase in fault-core thickness up section. Additionally, shale in the HW displays folding and minor faults and is locally injected along the PDZ which bounds the HW if Z1.

6.4.4.3 Fault gouge maps

NStMB fault zone (Figure 6.11a):

Located along the PDZ of NSMBFZ where fine to medium sandstones in the footwall are juxtaposed against heterolithic beds. The mapped section is dominated by high-strain zones comprising of FG1 and FG2, surrounding pods of FB1. The footwall strand is bounded by a continuous <0.5 to 3 cm thick band of FG1 that contains elongated pods of cataclasite and fine-sandstone clasts. Cataclasite consists of sub-mm clasts of sandstone, siltstone, and organic fragments that display aspect ratios of 1 to 1.8. Clasts within the high strain zone are disaggregated and/or altered to a dark-orange colour. Disaggregated clasts, such as the one to the far right of the image, have 'tails' of small clasts in strain shadows surrounding the main clast. Foliation within FG1 wraps around pods and clasts.

Pods of FB1 are present as close as <0.5 cm to the footwall fault strand and increase in size moving away from the PDZ. Unlike cataclasite, breccia pods are irregular and bounded, or cut, by thin zones of FG1. Breccia clasts are sub-rounded to sub-angular, with some small angular clasts present. Large clasts occur in the centre of breccia pods and show slight elongation parallel to the PDZ. Small clasts are randomly orientated and wrap around larger clasts.

HSFZ normal fault strand (Figure 6.11b):

The mapped area is located on an 8-10 m offset dip-slip strand of HSFZ which juxtaposes a lens of interbedded siltstones and shale in the footwall, and sandstones in the hanging wall. The zone is bounded by two PDZs; a fairly straight hanging wall strand, and an oblique footwall strand which causes the section to thicken from 8 cm to 20 cm. Both PDZs have 0.5 to 2 cm thick high strain zone, primarily consisting of FG1 with occasional pods of cataclasite. Small clasts are common within these zones and are elongated parallel, or slightly oblique to the PDZ. While organic fragments are rarely observed throughout the rest of the mapped section, they are common within high strain zones. Towards the top of the mapped section, a pod of FB1 is observed whose orientation matches that of the bedding in the adjacent lens.

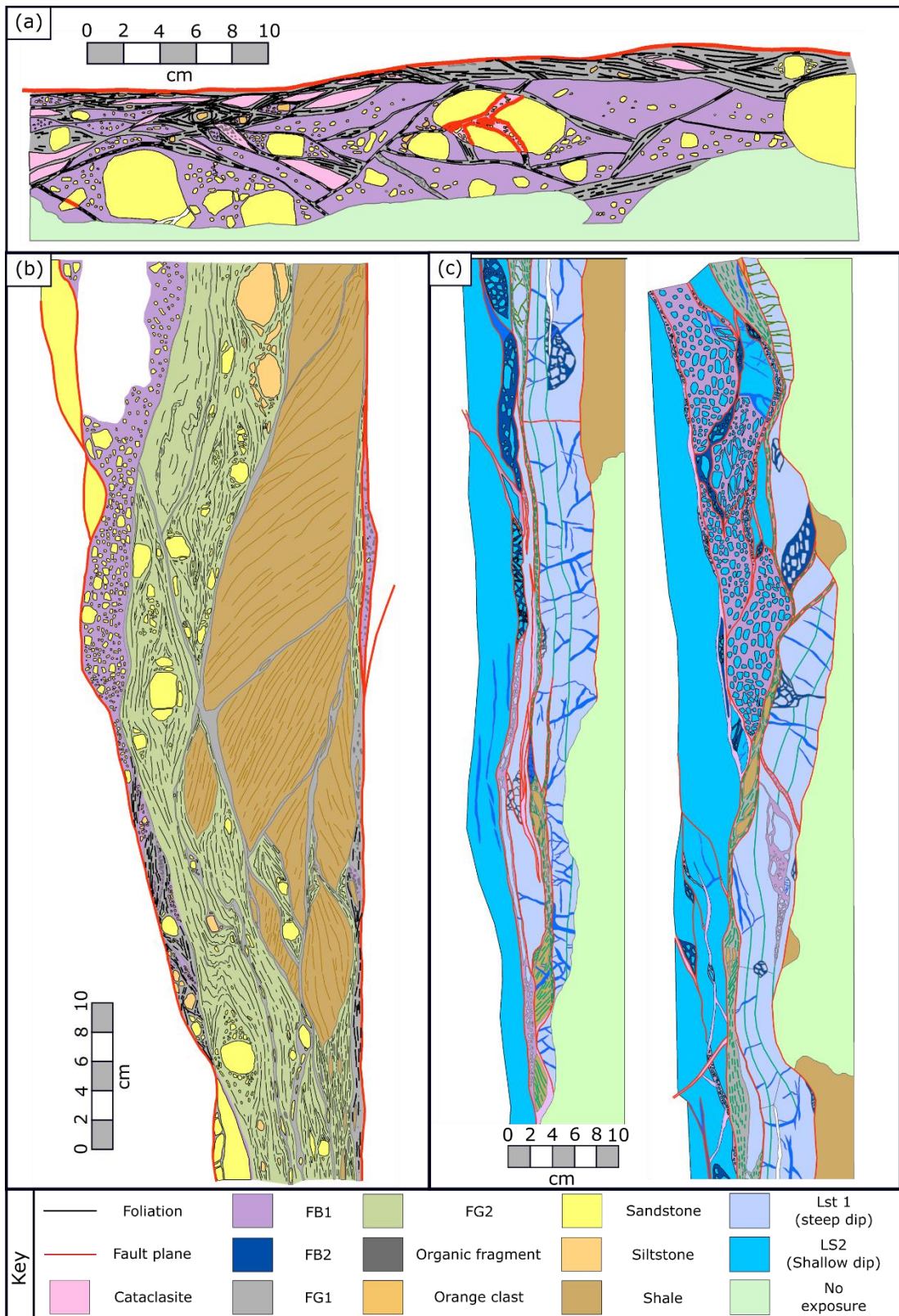


Figure 6.11: Fault gouge maps undertaken using 5cm² scale grid mapping: a) small section of the main fault strand of North St Mary's Bay Fault Zone (location shown on Figure 6.1); b) Section of the dip-slip strand of the HSFZ; and c) a section of the main strand of major fault at Howick.

Between PDZs is a 4 to 8 cm thick zone of FG2, cut by several high-strain zones. Clasts of sandstone, siltstone, and shale are common and occur as sub-rounded clasts surrounded by 'tails' of angular to sub-angular clasts aligned sub-parallel to the PDZ or nearby high strain zone. Close to the hanging wall a <20 cm shale clast is cut by several high strain zones which develop FG1. Bedding within the clast is aligned oblique to the PDZ with sections of clast rotated relative to each other.

Foliation within FG1 and FG2 display several features including:

- Increased intensity towards the hanging wall fault strand, accompanied by high aspect ratio clasts.
- Foliation deflected around clasts and rotated towards high strain zones which cut FG2.
- Foliation becomes folded either: a) where clasts are in close proximity to each other; or b) in the bottom left if the map where a plane of damage occurs, possibly associated with a high strain zones which cuts the shale clast.

Howick fault strand (Figure 6.11c):

The mapped area is located along a footwall strand associated with HMFZ that juxtaposes steeply dipping limestones (LS1) and shales against shallowly dipping limestones (LS2) in the hanging wall. The fault strand is dominated by breccia development, with subsidiary development of a FG1 and cataclysite. FG1 is found along the hanging wall fault strand, is light grey and contains clasts of shale which are elongated parallel to the local strike. Foliation follows the strike of the hanging wall fault strand, however, is deflected by shale clasts. Cataclysite occurs along bedding planes within the steeply dipping limestone or along small offset fault strands cutting both limestones.

Both FB1 and FB2 are observed along the mapped section, in both LS1 and LS2. The spatial distribution of these varies along strike and they often occur as pods. Within FB2 clasts display little elongation and in some cases may be 'fitted back together'. This is not the case for FB1, which displays sub-rounded to rounded clasts elongated parallel, or slightly oblique to the PDZ. Clasts may be rotated within the breccia pod to match the strike of bounding fault planes. Single fault strands can develop both FB1 and FB2.

Calcite mineralisation is common occurring perpendicular to bedding in LS1 and parallel to fault strike in the vicinity to the hanging wall PDZ in LS2. Mineralisation can not be trace across the PDZ, however, occasionally clasts display calcite veining. Mineralisation is far more abundant within LS1 compared to LS2.

General trends:

Although the fault maps intersect different lithologies, several common features are observed in all three maps (Figure 6.11, Table 6.3). This suggests that processes occur within multi-layered sequences that are not controlled by lithology. In particular, the formation of lensoid geometries that form parallel or sub-parallel to the main fault strand and the presence of a thin high strain zone along PDZs and Riedel shears. Although FB2 was only observed in Figure 6.6c, it is commonly observed along other faults including NSMBFZ (Figure 6.9).

Characteristic	Figure 6.11a	Figure 6.11b	Figure 6.11c
Highly plastic fault gouge along high-strain zones	✓	✓	✓
Straight principal slip planes and off-axis minor slip planes	✓	✓**	✓***
Foliated fault gouge	✓	✓	✓
Sub-rounded clasts surrounded by 'tails' of small clasts	✓*	✓	✓
Cataclasite pods	✓	✗	✗
Cataclasite along minor slip planes	✗	✓	✓
Organic fragments within high strain zones	✓	✓	✗
Clast-supported, rounded to sub-rounded fault breccia which occurs as pods	✓	✓	✓
Matrix supported breccia with a calcite matrix	✗	✗	✓
Folding and deflection of foliations surrounded clasts and high-strain zones.	✓	✓	✓

Table 6.3 (previous page): Characteristic properties of fault-core maps. *Sub rounded clasts are only observed within the high strain zone close to the footwall fault strand. **The hanging wall fault strand of HSFZ is straight, however, the footwall displays several undulations. ***Footwall strand not mapped, however, displays a planar appearance at a field-map scale.

6.5 Discussion

6.5.1: Fault and fault-rock orientation: implications for the Northumberland Basin

Fieldwork at Whitley Bay and Howick found that fault-strands in coal measures do not develop as isolated planar strands, but instead consist of multiple anastomosing faults with complex interaction patterns with stratigraphy and other fault strands. Fault zones at both sites strike either E-W, or NE-SW, with multiple sets of smaller faults observed within a single fault zone (Figure 6.1, 6.3, 6.4). When the trace length of the smaller faults is considered it was found that the largest small faults formed either: a) sub-parallel to the main trend; b) orientated at an angle of 15° to 30°; or c) 60° to the local PDZ (Figure 6.12a). Fault mapping indicates that small faults abut against those orientated sub-parallel to the PDZ. This matches previous findings that small-trace length faults in coal measures are restricted laterally (Childs et al., 1996; Nicol et al., 1996; Crider and Peacock, 2004; Soliva and Benedicto, 2005) and orientated oblique to and abut against local PDZ (Huggins et al., 1995; Waldron, 2004; Waldron, 2005).

The background fracture populations were not studied in detail at Howick, however, close to PDZs fractures appear to be sub-parallel to the trend of the PDZ and not match trends observed away from the fault zone. Out of all the fault zones studied at Whitley Bay, joints are only recorded in the proximity to CPFZ. Assuming strike-slip geometries these joints display the regional trend and favourably orientated ENE trending joints are not reactivated suggesting that jointing occurred post-faulting. At other faults (SMB, NSMB, HPFZ and HSFZ) no background joints are observed, and instead fractures form either sub-parallel to the local PDZ, or between 40 to 50° to the trend of the local PDZ.

When the orientation of the measured faults (Figure 6.12) is compared the fault patterns associated with dextral strike slip faulting (Figure 6.12a) clear parallels may be drawn. For example, at the field-scale (Figure 6.12b) CPFZ represents the large-scale 'regional' structure, and PDZ of the scale-dependent strain ellipse. The southern bounding PDZ is likely made up by a regional fault which cuts St. Mary's Island immediately south of the area mapped for this study. This fault is marked as a normal-offset fault and exposure is very poor. The fault plane dips steeper than 75°, and comparisons with the other faults and

lineations observed on them suggest it may be a strike slip fault. HPFZ, which displays sinistral offset, is orientated such that it represents a Y-shear relative to CPFZ, with both SMBFZ and NSMBFZ representing P-shears. HSFZ, which contains both steep strike-slip strands and a prominent dip-slip strand also represents an P-shear, with the normal strand favourably orientated as a T-fracture relative to the CPFZ. Additionally, the fracture data match the expected orientation for R- and T-shears. The dip of bedding and long axes of lenses also match Riedel shear geometries. At a larger scale, HSFZ, HPFZ, NSMBFZ, and SMBFZ can be combined to represent a regional P-shear linking CPFZ and the fault that cuts St. Mary's Island.

The geometrical relationships of structural logs (1:100), grid-mapping (1:10) and cm-scale mapping (1:1) can also be correlated to Riedel shear geometries. In all cases appropriately orientated R-, P-, Y-, and R'-shears, along with opening mode fractures and veins which match T-fractures. Where lens data are incorporated, the long axis is found to be aligned slightly off axis to these strands (typically c. 15°). The dip of the bedding within lenses matches the orientation for wrench folding. Within a single fault zone (e.g. NSMBFZ; Figure 6.4d) the orientation of PDZs and fault rock may also be matched to the strain ellipse. The analysis of fault orientation, lineation data, and lens/clast orientations across four orders of magnitude suggest that both Howick and Whitley Bay developed within a dextral strike slip regime, with a relatively minor component of dip-slip.

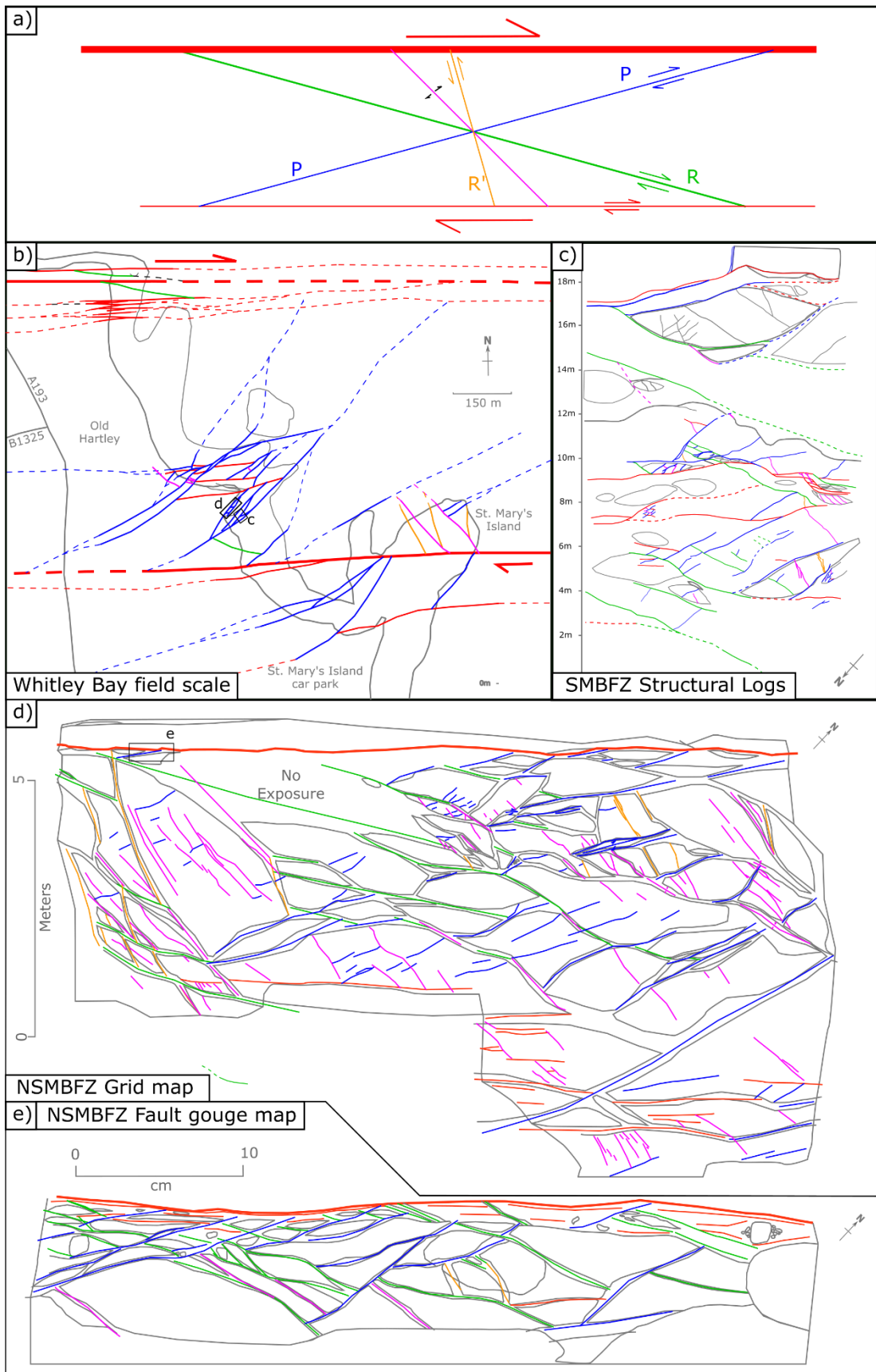


Figure 6.12 (previous page): Riedel shear geometries observed over four orders of magnitude at Whitley Bay. a) Typical riedel shear geometries, with the colour of each component carried on to the simplified maps. Simplified fault maps for: b) field-scale geological mapping undertaken for this study and expanded to include key faults cutting St. Mary's Island; c) SMBFZ structural log; and NSMBFZ d) grid map and e) fault core. For full maps please refer to Figures 6.1c, 6.4a, 6.6 and 6.8.

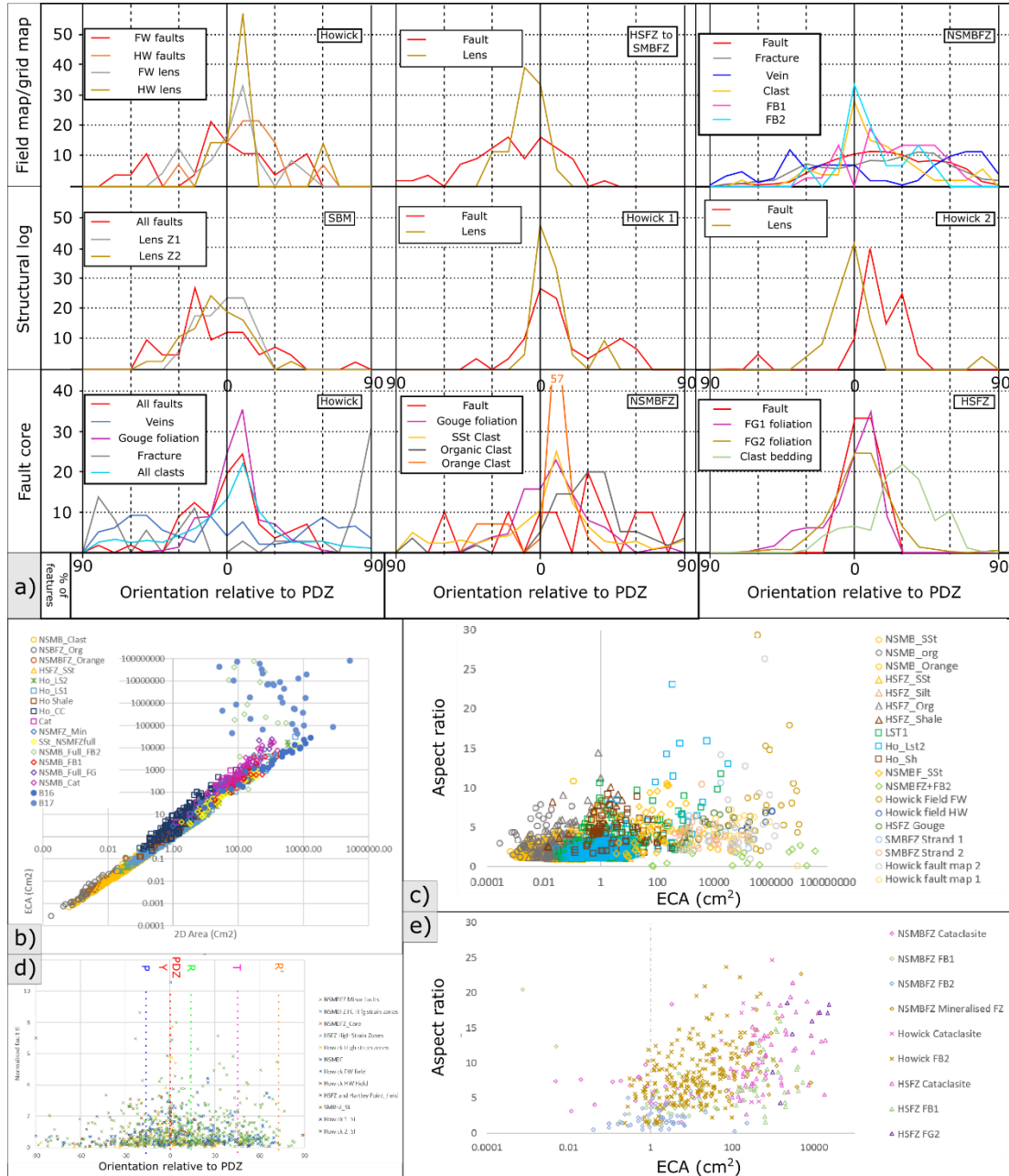


Figure 6.13: Clast and lens orientation and relationships between aspect ratio and clast area: a) normalised orientation histograms for lenses, clasts, and linear features; b) comparison between 2D area exported from ArcGIS and the Equivalent Circular Area (ECA); c) relationship between aspect ratio and ECA for lenses and clasts; d) Normalised trace length by orientation; e) Aspect ratio by ECA for fault-rock lithologies.

The majority of faulting in the Northumberland trough has been attributed to late-Carboniferous thermal subsidence, which led to widespread faulting throughout the basin (Chadwick et al., 1993; Chadwick et al., 1995; De Paola et al., 2005). During this time the basin was still subsiding, which causes shale in the sequence to behave in a ductile manner (Wang and Gale, 2009; Yuan et al., 2017). This enables the block rotation of competent lithologies, causes faults to splay, and promotes the development of fault-core lenses. While parts of the basin have been reactivated during the variscan orogeny (Chadwick et al., 1995; De Paola et al., 2005), no evidence of reactivation was found at either site.

Re-mapping of the Whitley Bay coastal section suggests the area records the interaction between the CPFZ and the EW trending fault which cuts St Mary's Island. While dip-slip offsets are recorded along a strand of the HSFZ, this too fits within an overall dextral strike slip system, with no strain partitioning required. HSFZ has been long been identified as a normal fault (e.g. Jones & Dearman (1967) and used as a type example for the development of shale smears (Færseth et al., 2007) and fault-core lenses (Gabrielsen et al., 2016) within normal faults.

While dip-slip motion at Howick has been previously reported (De Paola et al., 2005), the presence of a strike slip system at Whitley Bay was unexpected. De Paola *et al.* (2005) highlights the effect of transtension on the development of the Northumberland Trough and as part of this work recognised some strike-slip faults in the area (e.g. NSMBFZ). The kinematic data presented by De Paola *et al.* (2005), is in agreement with with the orientations found in this study and includes data from the fault which cuts St. Mary's Island. However, De Paola *et al.* (2005) considers fault zones in isolation, and no faults were mapped at Hartley Point. The data presented in this chapter suggests that strike slip faulting, in particular large-scale systems, remains under-reported in the Northumberland Trough, which could have important implications for the basin evolution.

The previous interpretations of the Whitley Bay are likely caused by: a) the shallow dipping nature of the stratigraphy limiting strike-slip offset markers; b) the regional interest in the fault throw from coal mining operations; c) the lack of detailed, multi-scale studies at the field area; and d) exposure bias (c.f. Shipton *et al.* (2019)) towards section view outcrops. Additionally, lineations are only rarely observed and are often limited to mineralised sections of competent lithologies. This means that the orientation of structures relative to

each other needs to be considered when assessing the regional kinematics of faults cutting these lithologies.

Shipton et al., (2019) found that a geologist's mental model can impart strong biases on the collection of fault data. Subjective bias has also been highlighted in other areas of geology including fracture data collection (Scheiber et al., 2015; Andrews et al., 2019; D C P Peacock et al., 2019) and seismic interpretation (Bond *et al.* 2007, 2015 *and references therein*). Important factors which can lead to subjective bias in data collection include (Wilson et al., 2019; Shipton et al., 2019): a) lack of standardised methods used during fieldwork; b) the scale of observation; c) the experience and specialism of the geologist collecting the data; and d) the time and weather conditions during fieldwork.

Unlike fracture analysis, where interpretation changes with a change in the scale of observation (Scheiber et al., 2015; Andrews et al., 2019), similar relative orientation relationships to local features are observed over 4 orders of magnitude in this study. However, the orientation of these features differs such that although a dextral sense of shear can be inferred in all bar R' Reidel shears, under-sampling could lead to a misinterpretation of the regional tectonic setting. The standardisation of geological mapping is difficult, particularly due to the subjective nature of field interpretations, site specific considerations (e.g. tides), and effect exposure bias. The quality and quantity of data collected will also be strongly affected by the weather conditions and other 'human factors' (Wilson et al., 2019; Shipton et al., 2019). While undergraduate students are routinely encouraged to record these, such practices are rarely continued into research and it does not reach field reports or publications. This will likely affect the replicability of studies (Wilson et al., 2019) and more work is required to quantify the effect of such biases in field geology.

Experience bias is an important consideration in data collection. For example, Bond *et al.* (2007) found participants were more likely to interpret a 2D synthetic seismic image based on their field of expertise, particularly those working in extensional and salt-influenced basins (i.e. geologist who work in extensional environments often interpreted normal faults in the section) and only 23% of participants returned the correct geological interpretation. Because faults are often studied in section view (i.e. cliffs) where throw is clearly visible, it is more likely that the interpretation will be a normal fault unless kinematic data is

collected. This is further complicated in siliciclastic sediments where fault lineations are poorly developed, and are mainly restricted to competent layers.

The interpretation of purely normal faults without any dip-slip or strike slip component is likely to be widespread. Using a google scholar search for 'Strike slip fault*' (About 21,500 results) and 'normal fault' (About 46,700 results) in combination with 'interbedded sand and shale' returned 2.17 times as many hits for normal faults compared to strike slip. Due to the ability to develop multiple kinematics either through transtension (De Paola et al., 2005), or strike slip faulting alone, the 'experience bias' of field geologists and geologists working with seismic data towards normal faults could lead to incorrect, or unnecessarily complex basin history models. Another bias towards normal faults is that strike-slip faults are typically steep ($>70^\circ$) (Sylvester, 1988), meaning they will be poorly sampled in vertical boreholes, and hard to image in seismic.

6.5.2 Fault architecture and localisation of strain.

Faults at both study sites display asymmetry, with significantly less damage in the footwall compared to the hanging wall (Figure 6.1, 6.3 & 6.4). The PDZ was characterised by a laterally continuous zone whereby fault rock is developed. The footwall damage zone is typically small and comprises of subsidiary fault strands whose strike is sub-parallel to the PDZ. At Howick these act to entrain a number of high aspect ratio (>3.5) lenses bounded by mineralised fault planes. Additionally, several sinistral strands connect dextral strands and lead to the development of fault-core lenses orientated at a high angle to the main strand. Such deformation is rarely observed at Whitley Bay, where footwall damage is very limited. At both sites the hanging wall damage zone is far more extensive and includes the development of fault-core lenses, the rotation of bedding towards the fault, and faults that display a high degree of curvature and fit a dextral strike-slip strain ellipse (Figure 6.1, 6.12).

In section view fault-strands typically branch and/or terminate at the boundary between shale and sandstone/limestone, or within coal seams (Figure 6.3). The vertical restriction of faults in coal-measures is well known, with small offset fault strands only present within a single cyclothem (Huggins et al., 1995; Nicol et al., 1996; Soliva and Benedicto, 2005). The termination of faults at sand-shale mechanical boundaries is widely studied (Wilkins and Gross, 2002; Long and Imber, 2011; Ferrill et al., 2017). One of the key controls is the mechanical contrast between mechanical layers, and the strength of that boundary (Schöpfer et al., 2006; Ferrill and Morris, 2008). Coal is typically considered a weak lithology

(Chapter 2), however, faults rarely terminate at the boundary between coal and the surrounding lithologies and instead conjugate fractures develop that interact with the cleat network. For large offset faults, coal becomes brecciated and entrained into the fault zone as fault-core lenses, suggesting that although coal is mechanically weak it behaves as a brittle lithology.

Similarly to jointing (See Chapter 4), small offset faults are strongly affected by sub-bed scale features. Cm-scale vertical restriction is observed. The fault-zone is considerably thicker in heterolithic beds. For example, in Figure 6.10b the fault architecture for units with thin shale and organic interbeds displayed a wider zone of damage, with several mm-scale faults acting to disaggregate bedding and form small (cm -scale) fault-core lenses. In contrast, where homogenous siltstone is observed the fault zone is considerably thinner. This is also observed along the main strand of CPFZ (Figure 6.10a). The vertical restriction and branching of faults is at a scale far below bed- or cyclothem-scale. The widening of the damage zone will be promoted by the presence of strength contrasts within the stratigraphic succession (McConaughy and Engelder, 2001; Cilona et al., 2016), which in fluvio-deltaic sequences occurs at a sub-bed scale (Fielding, 1982; Christopher R. Fielding, 1984; Fielding, 1985; Besly and Fielding, 1989). Sub-bed structures cause vertical restriction and complication of fault structure at several scales (Chapter 4).

The majority of throw on faults in the field areas is taken up along thin (0.5 to 18 cm) PDZs that develop either parallel to the main strand or as Riedel shears. This can lead to over 50% of cumulative throw occurring along damage zone strands, and not along the main PDZ. The main PDZ for a particular scale of observation is through going and contains a thin (<5 cm) zone of foliated fault gouge (FG1 and FG2). As you move away from the PDZ, a band, or pods of cataclasite, fault breccia, and/or high aspect ratio fault-core lenses may be observed orientated sub-parallel to the PDZ. Away from the main strand only major PDZs (for the scale of observation) develop fault gouge or high strain zones and instead display Riedel shear orientations with thin cataclasite bands and pods of fault breccia, which often bound fault-core lenses. Breccia pods are nearly always surrounded on at least one side by a thin cataclasite band. Overall, the aspect ratio of clasts and lenses increases and area decreases (Figure 6.13) towards the PDZ (Figure 6.14), and a distinctive layered fault structure is observed at all scales of observation (Figure 6.1, 6.4, 6.9 & 6.11). However, this

is most marked at the small scale (fault-core maps) and does not affect clasts within cataclasite, which instead become rounded (Figure 6.11).

The development of a 'layered fault zone structure', whereby distinct zones are observed which change thickness and properties both along strike and down dip, is a common feature of fault zones (e.g. Collettini *et al.* (2009); Sagy & Brodsky (2009); Bullock *et al.* (2014); McKay *et al.* (2019)). The majority of displacement is accommodated along a thin PDZ which typically does not exceed 20 cm (Schulz and Evans, 2000; Sibson, 2003). Along the main strand plastic fault-gouge with foliations orientated sub-parallel to the main fault strand is often found. Collettini *et al.* (2009) found that the presence of foliations within fault gouge greatly decreased its mechanical strength relative to powdered samples, acting to further localise deformation along the PDZ. Thin bands or pods of cataclasite are also commonly observed immediately next to fault-gouge (Sagy and Brodsky, 2009; Bullock *et al.*, 2014), which is also observed at Whitley Bay and Howick. Along the fault plane, regular elliptical asperities develop that are elongated parallel to the slip of the fault (Power *et al.*, 1987; Peacock, 2001; Sagy *et al.*, 2007; Sagy and Brodsky, 2009). These asperities may affect the local thickness of fault rock (Sagy and Brodsky, 2009; De Rosa *et al.*, 2018) and the entrainment of host-rock into the fault core (Sagy *et al.*, 2007). As fault strands grow the wavelength of asperities increases as the amplitude remains constant or slightly decreases such that small offset faults display a rough fault trace while larger offset faults are simplified (Sagy *et al.*, 2007; Sagy and Brodsky, 2009).

The anastomosing nature of fault strands (Figures 6.1, 6.3, 6.4), and rotation of bedding towards fault PDZs (Figure 6.1 & 6.2) leads to the entrainment of fault-core lenses into the fault core. Fault-core lenses and clasts within breccias are observed to have Equivalent circular areas which span nearly 6 orders of magnitude and typically display aspect ratios below 10 (Figure 6.13). As ECA decreases below 1 cm² the aspect ratio of sandstone and limestone lenses decreases. In fault-core maps this can be attributed to the break-down of the lensoid shape, with tails of small clasts developed consisting of angular fragments aligned oblique to the PDZ. High aspect ratio lenses were found to represent lenses that had been broken down, with a hierarchical nature of lenses observed in the maps. Gabrielson *et al.* (2016) showed this process whereby master lenses orientated sub-parallel to the PDZ can be cut by high angle Riedal shears to form subsequent 'secondary' or 'tertiary' lenses whose long axis is orientated at a high angle to the PDZ. Lenses may

eventually be broken down to form FB1: for example, the breakdown of LS2 in Figure 6.11. The reduction of aspect ratio below 1 cm^2 marks a change from high-aspect lens and clasts deformed by through-going slip planes, to the development of small clasts with low aspect ratios through rotation. This will lead to the development of cataclasite localised along fault planes.

The transition from fracture-processes, which form fault core lenses and fault breccia, to cataclastic flow has been identified by several authors (e.g. Jefferies *et al.* (2006); Sagy & Brodsky (2009)). This process leads to the fractal relationships observed in clast area towards faults over several orders of magnitude (Molnár *et al.*, 2014). The data collected at Whitley Bay and Howick suggest this can be extended to lens formation, and also applied to the relationship between aspect ratio and distance from the PDZ at the scale of observation. The process leads to the progressive deformation from fracturing, through lens formation, to the development of cataclasite and fault gouge (Sammis *et al.*, 1987; Molnár *et al.*, 2014).

While FB1 may form through the process described above, whereby pods are orientated parallel to the orientation of the previous lens until the breccia is itself broken down to form cataclasite bands (Sagy *et al.*, 2007; Sagy and Brodsky, 2009), FB1 is also commonly observed where faults jog (e.g. Figure 6.9). Strands at fault jogs display significant variability in thickness (up to an order of magnitude) and fault-rock lithology, however, unlike previous studies this cannot be linked to fault throw (Shipton *et al.*, 2006; Bastesen and Braathen, 2010) or lithological juxtapositions (Peacock, 2001; Bullock *et al.*, 2014; Laubach *et al.*, 2014). For breccias to form, there needs to be dilatational stresses to enable the rotation and expansion of clasts (Woodcock and Mort, 2008). To form breccias, space needs to be created to enable the disaggregation of clasts (Woodcock and Mort, 2008; Mort and Woodcock, 2008), with voids commonly being observed in tensional parts of the fault system (e.g. Wright *et al.* (2009)). In the study area pods are often orientated such that the long axis is orientated parallel to T-shears, where dilation is possible. These processes cause fault-rocks, including breccias, to rarely display random orientations, but instead fit a shear strain ellipse which matches that of the major structure for the scale of observation. For Whitley Bay, the orientation of structures within the fault core provide further evidence of the regional dextral strike slip system.

The same features are not be observed for organic clasts, with even very small clasts displaying aspect ratios which range between 2 and 8. When these clasts are investigated in the fault maps (Figure 6.13) it is observed that they become orientated parallel to local PDZs or cataclasite bands. Coal and organic fragments are abundant within these lithologies and may contribute up to 9% of the succession, however, in fault-core maps they are only observed either: a) lining small offset faults; b) as small clasts within FG1 and cataclasites; c) as fault core lenses; or d) as small pods of friable coal within FG2. Additionally organics are locally found to form the matrix for matrix-supported chaotic breccia with cm scale angular sandstone clasts (Figure 6.11). The lithologies on either side of this zone have <3% organic fragments, however, the matrix contains between 20 to 25% organics. Because coal has weak mechanical properties and inherent planes of weaknesses (cleats), it will be easy to entrain fragments into the fault core without the need for grinding. This enables aspect ratios to remain high, even in areas of high strain. The localisation of organics along PDZs also suggests that organics are highly mobile within the fault zone may become injected along fault planes in a similar manner to that observed with shale (Van Der Zee et al., 2003; Smeraglia et al., 2017). This process likely explains the formation of FB3.

FB2, which is characterised by angular clasts with low aspect ratios within a calcite matrix, is commonly observed along a number of faults. To form FB2 you require a pulse of high fluid pressure (Pf). Peacock *et al.* (2019a) proposed that the centroid effect (e.g. Finkbeiner and Zoback (2001); Bruce & Bowers (2002)) could be the mechanism behind the formation of such 'fluid-assisted breccias', which are common in strike-slip environments (Tarasewicz et al., 2005; Nixon et al., 2011). The centroid effect occurs when the fluid stored within porous lithologies follows the Pf-depth path, while low permeability lithologies (e.g. shales) follow that of the rock leading to the development local Pf gradients.

The lithologies at Whitley Bay consist of thinly bedded sandstones, which typically have porosity between 8% and 10% interbedded with siltstones, shale, seat-earths and coal (See Chapter 4). The presence of low-permeability interbeds limits vertical groundwater flow in these lithologies, and will promote Pf gradients to form through the centroid effect. Where a vertical connection can be made between areas of high and low Pf, for example through faulting, the brecciation and near instantaneous mineralisation of formation waters occurs as pressure decreases (Sibson, 1996; David C. P. Peacock et al., 2019). At Whitley Bay, the location of FB2 is not random, and instead pods are often found at jogs along R-shears

(Figure 6.10, 6.12). This leads to the short axis, or thickest point of the pod, to be aligned parallel to the extension direction expected for a dextral strike-slip fault zone (Figure 6.12a). The Riedel shear orientations associated with strike-slip fault zones could provide favourable pathways during faulting for the hydraulic connection of lithologies which have a high Pf gradient between them.

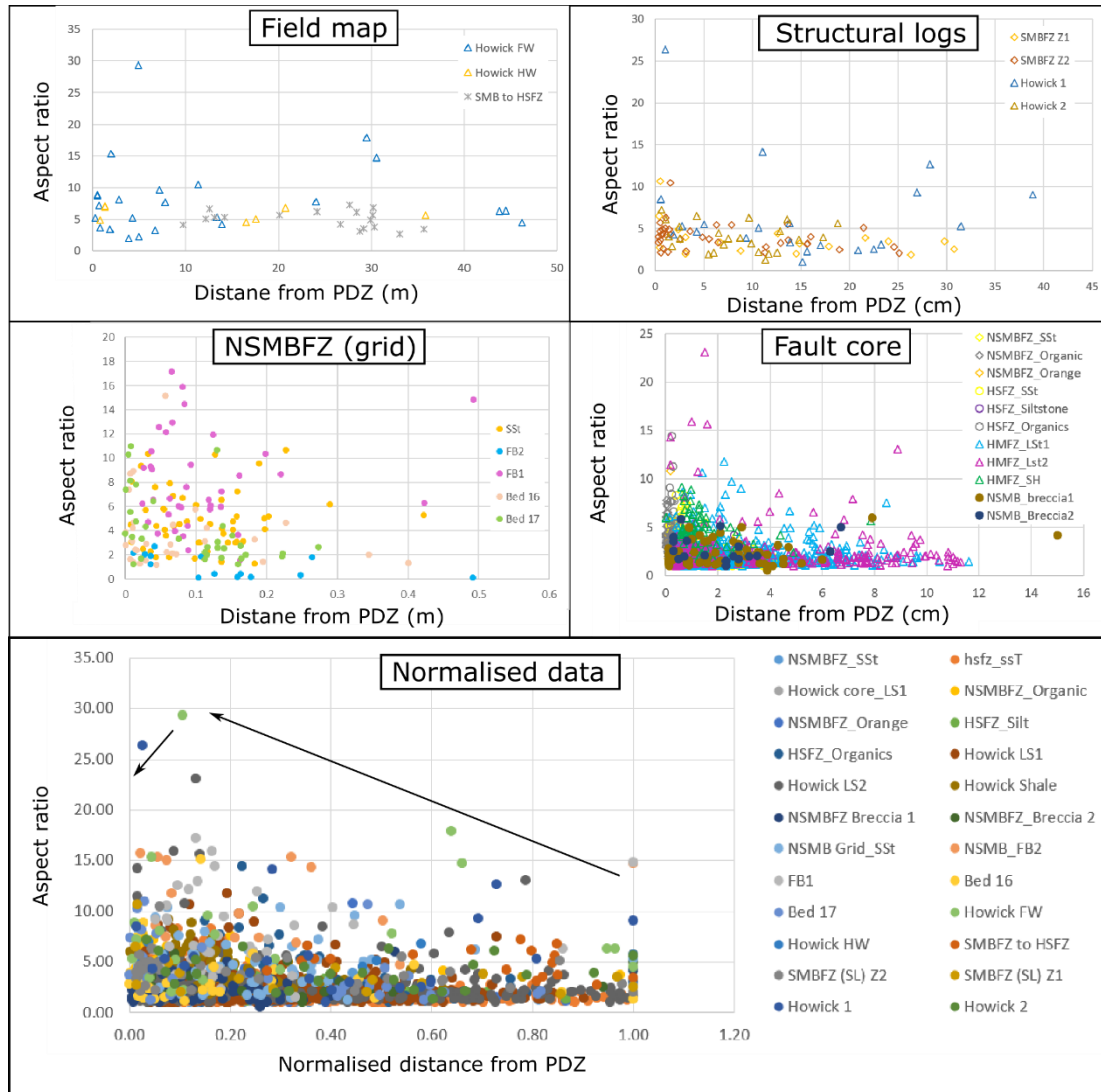


Figure 6.14: Clast aspect ratio compared to the distance from the main PDZ for that scale of observation.

6.6 Concluding remarks

Through geological mapping over four orders of magnitude, the internal structure of faults cutting coal measures was investigated. Faults rarely occurred as a single strand but instead formed a systematic zone of anastomosing fault strands which fits with a strike slip strain ellipse. Although several fault-rock lithologies were identified, fault-zones display an asymmetric internal structure over all mapped scales with damage greater in the hanging wall. Fault-rocks displayed a layered relationship, which was observed across all scales consisting of a planar PDZ, which often developed clay-rich fault gouges, followed by pods of cataclasite, fault breccia, and fault-core lenses. Aspect ratio was found to increase towards the PDZ for a given scale of observation for clasts/lenses above 1 cm^2 , however, below this the grinding of clasts causes aspect ratio to decrease.

Throughout all scales it is clear that the orientation of fault-rock and subsidiary strands observed at both field sites is not random, but instead fit a Riedel shear geometry whose orientation is controlled by the major feature for that scale of observation. Many of the recent findings for fault-zone processes were also observed during this study, however, little to no correlation between fault-rock lithologies, fault-core thickness, and throw was identified. This could be due to the large error bars on the apparent true displacement of strike-slip faults cutting shallowly dipping sediments, or that geometrical heterogeneities and development of asperities along fault strands are more important within these lithologies. The effect of small-scale strength inclusions caused by sub-bed scale sedimentary heterogeneity (e.g. mud-draped ripples) will lead to the development of abundant strength concentrations within the host rock and lead to the development of a heterogeneous stress field. The development of T-shears and wide-damage zones within heterolithic units will likely promote the formation of fluid-assisted breccias.

Chapter 7: The lithology, internal structure and deformation style of collapsed pillar and stall coal mines: Implications for shallow mine geothermal.

B. J. Andrews¹, Z. K. Shipton¹, Z. A. Cumberpatch², R. Lord¹

1) Department of Civil and Environmental Engineering

2) SedResQ, Basin Studies Group, University of Manchester

7.1 Rationale

Abandoned pillar and stall mine workings are present in the subsurface across much of the UK, and while deep coal mining ended in 2015, flooded workings have the potential to provide an aquifer for shallow geothermal development projects. To understand the potential of such sites, it is important to classify the permeability structure of the flooded mine and the connectivity to the overlying lithologies, which may act as pathways for heat loss. We use two sites (Spireslack SCM (Surface Coal Mine) and Whitley Bay) where pillar and stall workings have been exposed through later open cast extraction and coastal erosion to investigate the internal structure and surrounding deformation pattern of collapsed mine workings. We first classify the deformation of the overlying lithologies through fault and fracture mapping of a high-resolution auto-rectified photo montage followed by the field classification of the internal structure. We found that pillar and stall workings collapse through a series of stages, which gradually decrease the permeability of the system leaving a clay-rich anthropogenic sedimentary layer consisting of a chaotic assemblages of collapse breccias and mudstones. Our data also suggests workings do not collapse as individual events but that sections near pillars may remain open to flow for years after the rest of the workings have collapsed.

7.2 Introduction

The mining of coal in the UK, along with other parts of the world, helped kick-start the Industrial revolution and played a significant role in shaping the country's economic development. Since the 1970's to 1980's the extraction of coal has drastically declined, with subsurface mining in Scotland ceasing in 2002 (Leslie, Browne, et al., 2016). This has left a huge number of abandoned workings, with some estimates as high as 70,000 (Deb and Choi, 2006), many of which are located in highly populated areas built to support the collieries and associated industries. Following mining operations, workings flood as groundwater return to pre-mining levels (Burke and Younger, 2000; Malolepszy, 2003; Yu et al., 2006; Culshaw et al., 2013; Gee et al., 2017) and subsidence occurs as sub-surface voids collapse (Bell, 1988; Bruyn and Bell, 1999). Raising water levels can also lead to widespread pollution of ground and surface waters due to acid mine-water drainage (Younger, 1995; Younger et al., 2002; Bell and Donnelly, 2006).

The UK has a long history of coal mining (Table 7.1), and while techniques varied throughout time, the pillar and stall method was widely implemented (Helm et al., 2013). Using this method coal was extracted from 'stalls', or 'rooms', supported by pit-props (Daunton, 1981) and pillars wherein, 30 to 70% of coal remained unworked (Figure 7.1) (Wardell and Wood, 1965; Garrard and Taylor, 1988). Later pillar and stall workings (Table 7.1), such as those at Spireslack SCM (Surface Coal Mine), used a regular pattern of 1.8 to 4.5 m wide pillars (termed stoops in Scotland) which are square in cross section (Figure 7.1d) (Healy and Head, 1984). The geographic location of early workings is often unknown (Table 7.1), and difficult to locate (Bell, 1986; Bell, 1988). It should therefore be expected that pillar and stall workings, particularly in the North East of England, exist where seams exist close to the surface.

Date	UK wide	The Great Northern Coalfield (GNC)	Glenbuck, Ayrshire
Pre-1200	Extracted by shallow pits or adits (shallowly dipping tunnels) ^{1,2} .	Workings of the high Main Seam (HMS) date from roman times ⁸ .	
1200s	Widespread coal mining began increasing up to, including and following the Industrial revolution.	Early shallow workings (<7 to 10 m) primarily using adits from the coast/valley side, with bell pits also used ⁹	
1300s	Bell-pits (Figure 7.1a) became widespread ^{2,3} .		
1500s	Most shallow reserves accessible by traditional methods extracted and the Pillar and Stall method began ^{2,3} (Figure 7.1d).	1550's saw the increased extraction of the HMS, with coal becoming a significant commercial interest ^{3,10,11,12} . Pillar and stall workings began in the late 16 th Century ² .	
1600s		The majority of coal close to sea-ports and above the water table extracted by the late 17 th Century ¹³ .	
1700s		Technological advances in 1710 enabled coal to be mined below the water table ¹³ .	Bell pits used to extract coal for the pig iron industry ⁵ .
1800's	Mining methods became standardised ^{1,2} (Figure 7.1b, c & e). In 1850 detailed coal mine surveys began, with abandonment plans becoming mandatory from 1872 ^{1,4} .	1800 map of sea-sale collieries does not include Whitley Bay workings ³ . 1830's to 1870s saw many large collieries opened up working the HMS (e.g. Fenwick).	1840-1850: Opening of the Grasshill colliery ⁶ , which worked the Muirkirk Nine-foot and Six foot coals ⁷ .
1900's		1993: Easington colliery closes marking the end of underground coal extraction in the GNC.	1931: Grasshill pit closes and the village of Glenbuck declines ⁶ .
2000 to 2008			The open cast workings at Spireslack SCM ⁷ .

Table 7.1: Key points in the mining history of the UK, Great Northern Coalfield and Glenbuck, Ayrshire. References; 1) Bell (1986), 2) Bruyn & Bell (1999), 3) Smails (1935), 4) Healy & Head (1984), 5) Campbell (1955), 6) Powley & Gillian (2015), 7) Leslie et al. (2016a), 8) Fielding (1982), 9) Dearman et al. (2000), 10) Page (1907), 11) Smails (1938), 12) Nef (1965), 13) Galloway (1898).

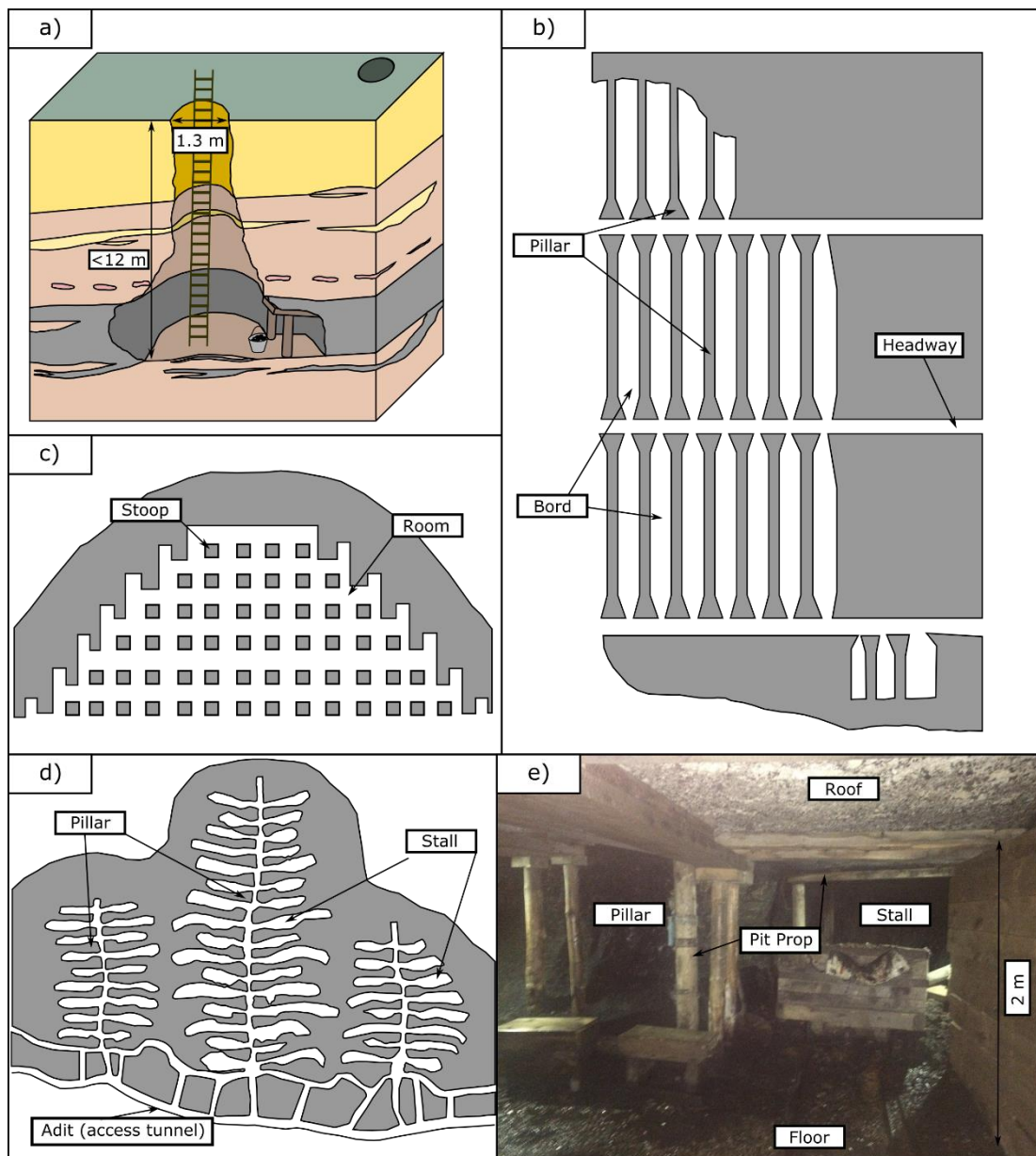


Figure 7.1: Typical UK mining methods. (b, c and d redrawn from Bruyn and Bell (1999) a) bell pit, b) Bord-and-pillar workings, Newcastle upon Tyne (17th Century), c) Stoop and room workings, Scotland (17th Century), d) Pillar and stall workings, South Wales (17th Century), e) Photograph of pillar and stall workings, Beamish open air museum.

Pillars are designed to sustain the weight of the overburden, however, following mining operations local stresses, and the spalling of the pillars, cause the roof to sag and collapse through time (Bruyn and Bell, 1999; Lokhande et al., 2005; B A Poulsen and Shen, 2013; Helm et al., 2013). This phenomenon has been shown to depend on the type and strength of the coal, ratio between seam thickness and pillar width, depth of workings and the

dimensions of the mined void (Madden and Hardmam, 1992). The presence of geological structures, such as soft coal or faults, also increases the likelihood of pillar failure (Bruyn and Bell, 1999). The failure of a single pillar will cause other pillars, particularly those in an up-dip direction, to become increasingly stressed and risk collapse causing a knock on effect until the support of the overburden is significantly reduced (Bruyn and Bell, 1999). As material falls, the stalls become clogged and deformation migrates upwards in a predictable manner (e.g. Garrard & Taylor 1988). The factors which control whether collapse occurs include: 1. the width of the unsupported span; 2. the thickness and dip of the seams; 3. the height of the workings; 4. the depth of overburden; 5. the nature and discontinuities within the overburden; and 6. the ground water regime. Pillar collapse and roof spalling, which can occur many years after mining operations have ceased (Carter *et al.* 1981; Salmi *et al.* 2019a, b) can lead to widespread subsidence (Gee *et al.*, 2017) often occurring as individual events over relatively short time scales (days to weeks) (Carter *et al.*, 1981; Marino and Gamble, 1986).

While the UK's coal mining legacy is often seen as negative, the abundance of flooded workings provides a potential for low-temperature mine geothermal projects (Malolepszy *et al.*, 2005; Watzlaf and Ackman, 2006; O Dochartaigh, 2009; Monaghan *et al.*, 2017). Shallow mine geothermal projects work by the removal of warm groundwater from flooded workings using heat pumps, and extracting heat through a geothermal recovery loop (Sanner, 2001; Lund, 2001). Systems can either be closed, where heat exchangers are installed at the base of boreholes and heat transported using heat exchanges, or open where groundwater is pumped to the surface where the heat is extracted, before being re-injected to the aquifer (Sanner, 2001; Hamm and Sabet, 2010). For coal-mine geothermal an open system is preferable (Hamm and Sabet, 2010) due to the relatively low temperatures (14 to 50°C; Jardón, 2010), and the potential for 10s of million cubic feet of groundwater in a single mine (Malolepszy, 2003). In addition to geothermal heat extraction, mining voids can act as a heat storage location for heat generated through industry, which can be extracted when required (i.e. the winter) (Sanner, 2001; Hamm and Sabet, 2010; Patsa *et al.*, 2015). The geothermal potential of abandoned coal mines has been widely investigated (e.g. Burke 2002; Malolepszy 2003; Malolepszy *et al.* 2005; Van Tongeren & Laenen 2005; McLoughlin 2006; Watzlaf & Ackman 2006; Loredó *et al.* 2011, 2017; Comerford *et al.* 2018) and the UK has recently invested £9 million into a Geoenergy

Observatory, located in Glasgow (Scotland), to help de-risk geological uncertainty in mine geothermal (Monaghan et al., 2017).

Whether a coal mine has the potential to be developed into a geothermal target is dependent on a number of site-specific factors (Malolepszy, 2003; Malolepszy et al., 2005):

- **Background geology and hydrogeology:** The stratigraphic succession is often dominated by low permeability lithofacies (C.R. Fielding, 1984) and structure (e.g. joint networks; (MacDonald et al., 2005)) that combine to control how water levels rise and fluctuate after mining operations. In most cases, groundwater returns to pre-worked levels over a period of 10 years (Malolepszy, 2003).
- **Geothermics of the mine:** As workings become deeper, the temperature of the formation increases, typically between 17 and 45°C/Km (Malolepszy, 2003). Local temperature anomalies may also arise due to the oxidation of pyrite commonly found in mudstones and marine bands (Jessop, 1995).
- **Water capacity of the workings:** The water capacity of a mine, or mine reservoir, can be very large (C Loredó et al., 2017; Menéndez et al., 2019), however, there are several features which can reduce the volume and permeability of this void. For a productive site, the relative permeability between the workings and surrounding lithologies is important (Hamm and Sabet, 2010). Immediately after working, this void-space will have a near infinite permeability, however through time and collapse, the volume and permeability will decrease (C Loredó et al., 2017).
- **Post-mining conditions:** How, and when, a mine becomes flooded, and the connectivity to active workings through shafts, will affect the flow properties of the mine (Malolepszy, 2003). Conditions can then be altered through the extraction of groundwater and can lead to the reactivation of faults (e.g. (Donnelly, 2006)) and/or the collapse of pillars (Sizer and Gill, 2000).

To understand the internal structure and leakage pathways, and hence improve estimations of the water capacity of pillar and stall workings, we investigate two surface exposures of workings (Spireslack SCM and Whitley Bay). We aim to quantify the damage above collapsed workings through the fault and fracture mapping of the high wall at Spireslack SCM. We then investigate the internal structure of the workings at Whitley Bay using a detailed sedimentological approach. We suggest that collapsed pillar and stall workings should be considered a clay-rich anthropogenic sedimentary layer, overlain by a highly

connected fault and fracture network that will combine to complicate groundwater flow in shallow mine geothermal projects.

7.3 Geological history

Carboniferous rocks cover much of the UK (Figure 7.2a) and are preserved within several late-Devonian to early Carboniferous, east-west trending basins formed in response to back-arc extension (Leeder, 1982; Soper et al., 1987; Leeder, 1988; Cope et al., 1992). During the Carboniferous the UK drifted northward across the equator, leaving a distinct pattern in the stratigraphic record of arid deposits in the early and late Carboniferous (e.g. red continental alluvial deposits), and equatorial lithofacies between (Scotese and McKerrow, 1990). Sedimentation, subsidence and paleo-source direction varied both temporally and spatially, controlled by the location of upland, emergent areas (Waters et al., 2007; Cope., 1992), and motion along basin bounding faults (Johnson, 1984; Bluck, 1984; Chadwick et al., 1995). The majority of rifting occurred during early Viséan times, where Millstone grit, and coal-bearing lacustrine lithofacies (e.g. The Limestone Coal Formation) dominated the North of England and the Midland Valley of Scotland (MVS) respectively (Cope et al., 1992; Browne et al., 1999; Underhill et al., 2008). In Namurian times rifting was followed in the North of England and Scotland by a period of uplift, which formed a widespread unconformity and separated the two depocenters (Cope et al., 1992). By Westphalian times rifting had ceased and had been replaced by thermal subsidence (Leeder, 1982) leading to the deposition of thick peat swamps, which become converted to coal during diagenesis, across shallow delta plains (Christopher R. Fielding, 1984; Fielding, 1985).

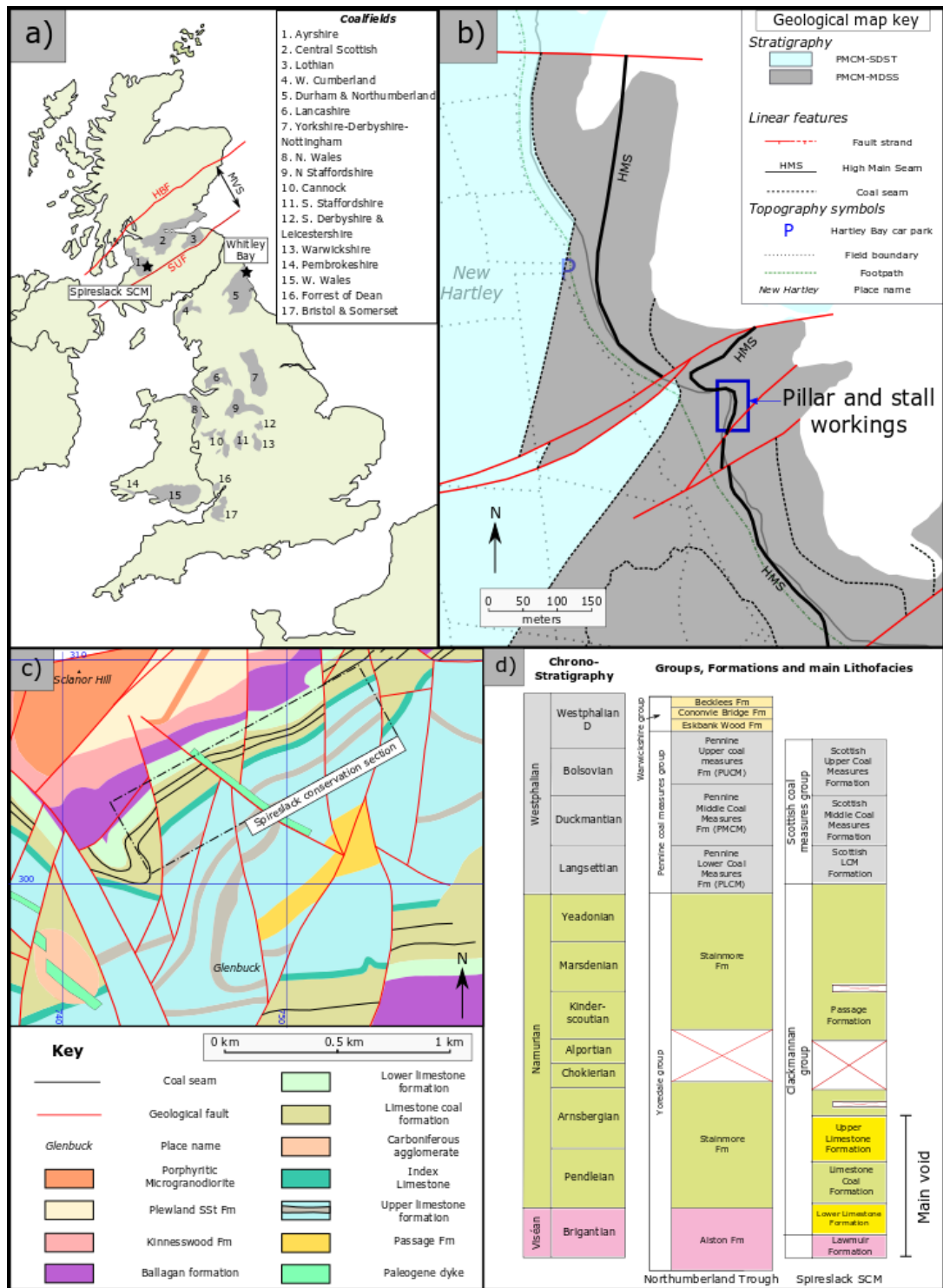


Figure 7.2: Geological setting. a) location of field sites and UK coal fields (after (Donnelly et al., 2008)), b) geology surrounding the workings at Whitley Bay (The map is modified from Geological Map Data BGS@UKRI (2018)), c) geology of Spirestack SCM and surrounding area (after (Ellen et al., 2019)), d) Chrono-stratigraphy, formations and lithofacies of both field sites (Chadwick et al., 1995; Browne et al., 1999).

Spireslack SCM:

Spireslack SCM, is located in the Muirkirk coal field, a sub-basin of the Midland Valley of Scotland (MVS). The MVS is a 90 km wide, 150 km long, ENE-trending graben bounded to the south by the Southern Upland Fault and the north by the Highland Boundary Fault (Figure 7.2a; Bluck (1984). Carboniferous rocks, reaching 6 km in thickness in places (Dean et al., 2011), occur in several basins where axis are oblique to the main trend of the MVS (e.g. Central Scottish Coalfield; (Francis, 1991). Following deposition, the MVS has been subject to a complex history of deformation leading to the development of low amplitude folds (e.g. the Muirkirk syncline) and both strike slip and normal faulting (Ritchie et al., 2003; Underhill et al., 2008; Leslie, Millward, et al., 2016).

Units which underlie the coal bearing successions (the Lower Limestone Formation, Figure 7.2d) consists of a series of 0.5 to 0.7 m thick, laterally extensive, marine limestone (e.g. the Housie (McDonald) Limestones (Ellen et al., 2016)), interbedded with shales up to 1.2 m thick (Browne et al., 1999; Ellen et al., 2016). Above this is the Limestone Coal formation, a series of upward-coarsening, upward-fining cycles of mudstone (40%), siltstone (20%), sandstone (c. 30%), seat-earth (c. 2%) and coal (8%) are observed. At Spireslack SCM this formation reaches 95 m in thickness and includes seven, mostly bituminous, coal seams including the 1.9 to 2.1 m thick Muirkirk Nine Foot Coal (NFC) (Davis, 1972; Leslie, Browne, et al., 2016; Ellen et al., 2016). The workings of these seams from the Grasshill colliery (see Table 7.1) have been exposed by the open-cast operations and may be seen exposed in the high wall. Above the coal bearing horizons, is the Upper Limestone formation with the base marked by the Spierslack Sandstone which comprises of two fluvial sandstone channel sets, and an upper fluvio-estuarine succession (Ellen et al., 2019).

Whitley Bay

Coastal erosion has exposed a series of abandoned underground workings on the headland just north of St Mary's lighthouse, Whitley Bay (England). Whitley Bay is located in the Northumberland Trough, a 50 km wide, ENE-WSW trending, half graben which formed in response to the extensional reactivation of the Iapetus Suture during the mid to late Carboniferous (Johnson, 1984; Chadwick and Holliday, 1991; Chadwick et al., 1995). The thickest coal seams (<2 m), many of which are workable; (Smails, 1935; Fielding, 1982)), are almost exclusively confined to the Middle Coal Measures which reach 450 m thick in places

(Smails, 1935; Leeder, 1974; C.R. Fielding, 1984). All rocks exposed at Whitley Bay are from the Pennine Middle Coal measures (Figure 7.2d).

The cyclical fluvial-deltaic lithofacies at Whitley Bay were deposited on a broad, flat deltaic plain with numerous distributary channels (Christopher R. Fielding, 1984; Fielding, 1985; Jackson et al., 1985). Lithologies consist of fossiliferous and barren mudstones (50 to 55%), siltstones and sandstones (40 to 48%) and coals, which nearly always occur above seat-earths (<5%) (Fielding, 1982; Christopher R. Fielding, 1984; Fielding, 1985; Jackson et al., 1985; Lawrence and Jackson, 1986). The coals are of variable quality, typically bituminous in rank and of a household, or steam quality (Smails, 1935; Lawrence and Jackson, 1986). Exceptional exposures of Middle Coal Measure lithologies, including the High Main Seam (HMS), are observed along a 1.2 Km coastal section North of St. Mary's Lighthouse, Whitley Bay [British National Grid NZ 364 756; Figure 7.2b; See Chapter 4, Figure 4.2, for detailed stratigraphy]. The High Main Seam (HMS) is highly variable in thickness (average 2 m, Fielding, 1982) and quality (Christopher R. Fielding, 1984; Jackson et al., 1985; Lawrence and Jackson, 1986; Murchison and Pearson, 2000) with shale partings commonly present (Fielding, 1982). Immediately below the HMS thin 'stringers' of coal are often found, which are locally workable (Fielding, 1982). Based on the history of the coalfield (Table 7.1), and the shallow depth above the water table, we suggest the workings exposed at Whitley Bay were extracted somewhere between 1550 and 1710 AD.

7.4 Methods

7.4.1. Fracture mapping (*Spireslack SCM*)

A section of the high wall at Spireslack SCM including workings of the Muirkirk NFC are analysed to investigate faults and fractures in the mine workings overburden. A high-resolution photomontage, with pixel resolution of 5 cm, was imported into ArcGIS, and scaled to field scale. Fault, fracture and bed-boundary mapping was then undertaken at a scale of 1:50. Mapping was undertaken by the same operator and at the same scale to limit the effect of subjective bias (Andrews et al., 2019). To understand the fault and fracture networks, it is important to understand the geometrical, and topological relationships of individual fault and fractures to each other (Sanderson and Nixon, 2015; Sanderson and Nixon, 2018; Peacock and Sanderson, 2018). This is typically done by assessing the fracture intensity, network connectivity, trace length distributions and fracture orientation (Watkins et al., 2015; Andrews et al., 2019).

Fault and fracture analysis was undertaken using the open-source Arc-toolbox NetworkGT (Nyberg et al., 2018). First the orientation of polylines was calculated using the sets function in NetworkGT, with set 1 (0° to 90°) representing apparent dips to the left (ENE) and set 2 (90° to 180°) apparent dips to the right (WSW), and converted to dip by subtracting 90°. Although these represent apparent dips, because the open cast workings were excavated along the bedding plane, and mine-related fractures form perpendicular to the direction of the workings we suggest the digitised values are close to the true dip values observed in a bed perpendicular section. To investigate how fault intensity and trace length vary up-section, 34 horizontal linear scanlines were undertaken every 2.5 m, using the 'sample line' feature in NetworkGT on digitised sample lines (Nyberg et al., 2018). Similar to typical linear scanline methods (e.g. (Priest and Hudson, 1981; Priest, 1993), the position, and spacing from previous fracture was recorded along with the length (extracted manually) and apparent dip of the individual fault strands. Because dips do not fall into distinct sets, all fault and fractures were considered together, however, cross cutting relationships were investigated to deduce age relationships. Fault offsets were investigated by digitising the offset along faults between mapped horizons, with the apparent dip, and length (throw) of each horizon considered separately. The length, number and apparent dip of each section of the mapped horizons cut by faults was exported to investigate the role of folding/bed rotation in the deformation. Fractures above ~5 cm are visible in the more competent lithologies (coal pillars, sandstone, seat-earth), and the length, connectivity and orientation of the branches of the combined fault and fracture networks were considered for each bed.

7.4.2. Field investigation (Whitley Bay)

The pillar and stall workings at Whitley Bay were classified using a sedimentological approach. High-resolution sedimentary logs of 9 vertical sections, spaced every meter, were completed along the workings (see Figure 7.5). Bed boundaries were taken as either a distinct change in grain-size, or matrix type, and due to the nature of the succession, such changes in grain size may be structural rather than depositional in origin. A sedimentary log through the unworked HMS at the base of Hartley Steps (British National Grid: NZ 34469 75668) was also undertaken and used as the comparative baseline for the collapse lithologies. Facies were then defined based on distinct changes in texture, grain size, stacking relationships and sedimentary structures. Collapse breccias were described using

the terminology of Woodcock & Mort (2008), whereby chaotic-, mesoic and crackle-breccias are defined based on clast size and ratio of clast to matrix. The clast type, orientation (taken as the dip of preserved bedding) and aspect ratio were recorded, along with the composition of the matrix. Muds in the sequence, which were not lithified, were described using the BS5930 (2015) standard for clay-rich soils.

In addition to the sedimentological approach, photographs (320 images) were taken of the outcrop to create a high resolution, orthorectified, photomontage (Figure 7.5a). Using the sedimentological information and location of logged sections, key bed boundaries were mapped out and stacking relationships investigated. Within the collapse breccia, a number of sub-divisions were mapped out, where subtle changes in clast orientation were observed (e.g. 45 and 82 cm in Log 1). These areas were used to help constrain the phases of collapse recorded in the sequence.

7.5 Results

7.5.1. Spireslack SCM High wall

The underground workings of the Nine Foot Coal (NFC) at Spireslack SCM cause deformation of the under- and over-lying stratigraphy (Figure 7.3). The worked seam may be observed in the bottom 3rd of the workings in Figure 7.3, and is comprised of pillars of unworked coal (dark grey), separated by collapsed stalls (purple) with the 10.8 m coal to the far right (Figure 7.3b) representing the unworked seam. Within the workings 6 pillars, ranging in width from 1.63 m to 6.26 m (mean = 3.53 m) are identified and make up 32.4% of the cross-sectional area of the workings. The other 67.6% of the workings is comprised of stalls of collapsed material, ranging in width from 3.01 m to 16.11 m (mean 7.34 m). The height of pillars is typically higher than that of the stalls (mean of 1.97 m compared to 1.49 m), with the stalls showing a greater variability between readings (CV = 0.24 for stall height compared to 0.15 for pillars).

Subsidence of layers overlying the NFC can be seen in Figure 7.3b, with gentle folds developing above stalls, which interfere with each other above bed 13 leading to the overall subsidence from right to left. This subsidence is accommodated by several faults (1,607 separate strands within the mapped area) which can be clearly seen cutting the high wall. Fault trace lengths (Figure 7.4a) tend to be low (0.5 to 1 m, Figure 7.4), with observed offsets also low (Table 7.2). The apparent dip of faults is highly variable (Figure 7.4a) and

ranges from 0.2° to 89.9° to the left (ENE) (n = 699, mean = 59.0°) and 1.1° to 89.8° to the right (WNW) (n = 910, mean = 58.8°). Although dips vary, the location of dip-changes above the NFC is systematic and related to the location of pillar and stalls (Figures 7.3a, 7.4a).

Faults dip away from pillars and towards stalls, with the apparent dip depending on the size and orientation of the pillar. Fractures range in length from 0.04 to 6.24 m (mode= 0.2 to 0.3 m, Figure 7.4b) and display a log-normal trace length distribution. Fractures typically display a steep dip (Figure 7.4b), however, locally the dip is altered by either a) faulting or b) rotation due to spalling of the edge of pillars (Figure 7.3c). Immediately below and above the workings fractures display shallower dips and increased connectivity.

Deformation patterns systematically change around the worked NFC (Figure 7.3, Table 7.2) and can be split into 4 distinct zones as summarised below (Table 7.2, Figure 7.3b).

- Zone 1: Below the seam: limited disruption of bedding is observed along shallowly dipping faults which decrease in fault length towards the NFC workings.
- Zone 2: Immediately above, and including the NFC workings: Subsidence of bedding can be observed into stalls, with bedding dipping away from pillars. Fault intensity is high, with the dip and offsets on individual strands low.
- Zone 3: Interference zone: In this zone the subsidence and faults observed in zone 2 interact with each other causing 'harmonic subsidence' (c.f. Lokhande *et al.* 2005). Fault strands steepen, displaying low to moderate offsets and decrease in intensity up-section.
- Zone 4: Localised slip: Gentle sagging of bedding is taken up by a limited number of large-trace length, moderate to high offset, fault strands.

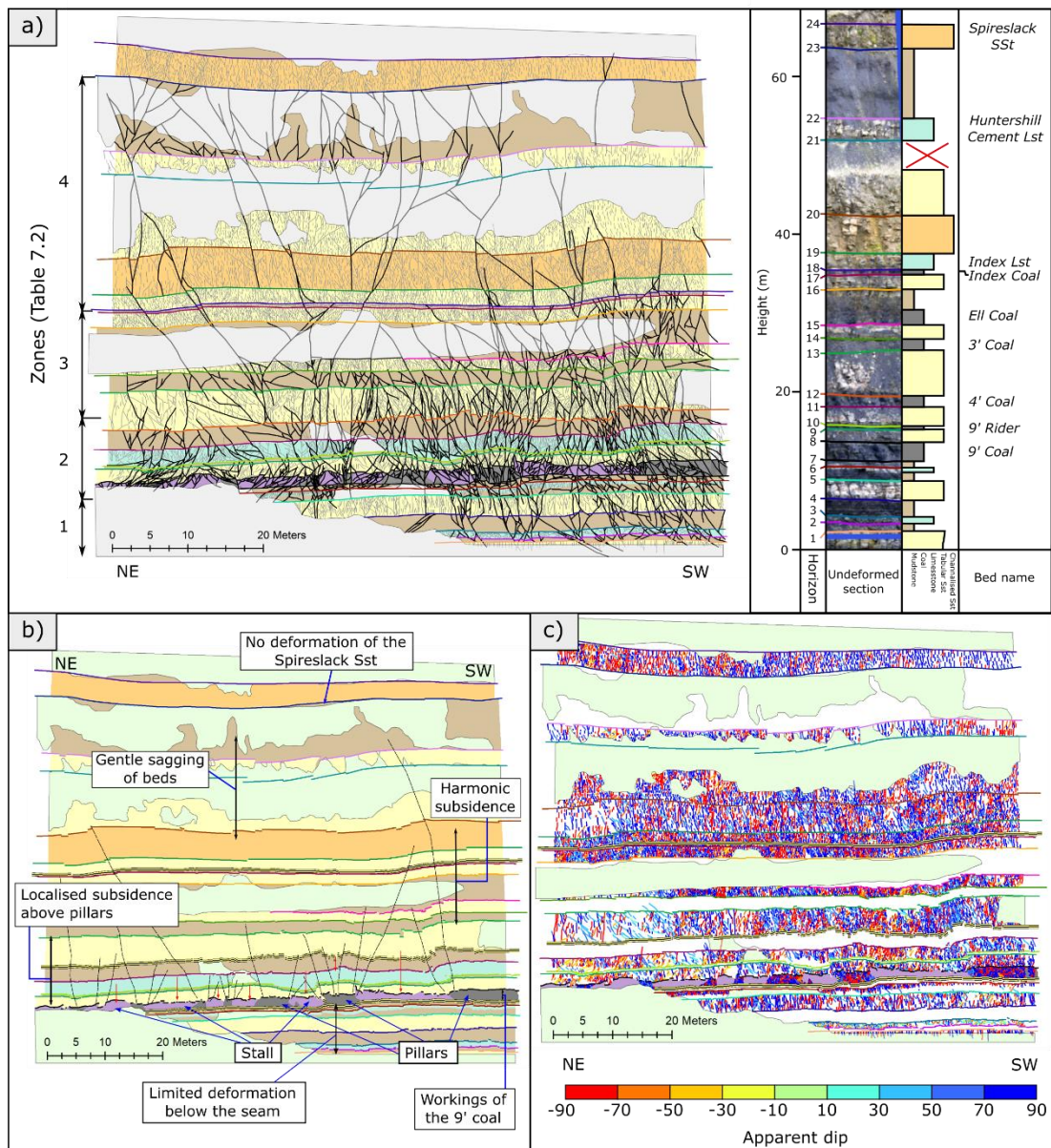


Figure 7.3: High wall deformation: a) Digitised fault and fracture network, with mapped horizons matching the schematic log; b) subsidence of beds with key deformation patterns marked, c) fractures colour coded by apparent dip.

Zone	Z1: Below the seam	Z2: Immediately above & NFC	Z3: Interference zone	Z4: Localised slip
Beds (Table 7.2)	1 to 8	9 to 13	14 to 18	18 to 23
Scanlines (Figure 7.4)	39 to 34/35	34/35 to 30	29 to 23/22	22/23 to 7/8
Subsidence pattern	Limited disruption of beds.	Subsidence of beds into the stalls between pillars is clearly evident, with each horizon dipping away from each pillar.	Subsidence above stalls interact with each other, causing 'harmonic subsidence patterns'	An overall subsidence, which increases from right to left, is taken up by a limited number of faults.
Bed dip (Table 7.3)	Dip increases towards the NFC, from 1.4° in horizon 1 to 5.7° in horizon 8.	Dip decreases from NFC to the top of this section (9.7° in horizon 9 to 5.5 in horizon 13).	Low variability in horizon dip, with a general dip around 5° (median = 5.2°).	Dip variable (0.5° to 5.4°) and dependent on lithology, with SST units displaying higher dips.
Fault intensity	Increases towards the NFC (Table 7.3, Figure 7.4a).	High (1.54 to 1.08 Fa/m) & slightly decreasing away from NFC.	Typically showing a slow decrease in intensity from 0.61 Fa/m to 0.36 Fa/m, except bed 16 which displays an intensity of 1.13 Fa/m.	Low fault intensity, reaching below 0.1 Fa/m by bed 22 & no faults observed in horizon 25.
Fault Trace length (tl)	Variable tl (10.7 m to 1.91 m), decreasing immediately below the NFC.	Low tl (1.91 to 4.56 m), increasing slightly above NFC.	Low variability, moderate tl (4.04 to 6.31 m).	Larger tl, slight dependence on lithology (5.38 to 13.57 m).
Fault offset	Low offsets (0.03 to 0.64 m, median = 0.14 m) decreasing towards NFC (Table 7.3)	Typically low offsets (median = 0.16 m), however, higher immediately above the NFC (bed 9, 0.05 to 1.64 m, median 0.22 m) and in bed 13 (0.05 to 0.88 m, median 0.21 m).	Low to moderate offset faults (median = 0.14), decreasing up-section. For example, Bed 14 has a median throw of 0.17, with bed 18 being 0.08 m.	Moderate to high offset faults (median = 0.23), variable due to lithology, with SST beds showing higher median throw (e.g. Bed 13 = 0.34 m).
Fault orientation	Shallow dipping faults, increasing towards the seam (Table 7.3).	Faults typically dip 60°, increasing to 70° above bed 12.	Dips between 65 and 70°, primarily controlled by lithology.	Dips between 65 and 70°, primarily controlled by lithology.

Table 7.2: Characteristics properties of the zones of damage above NFC workings.

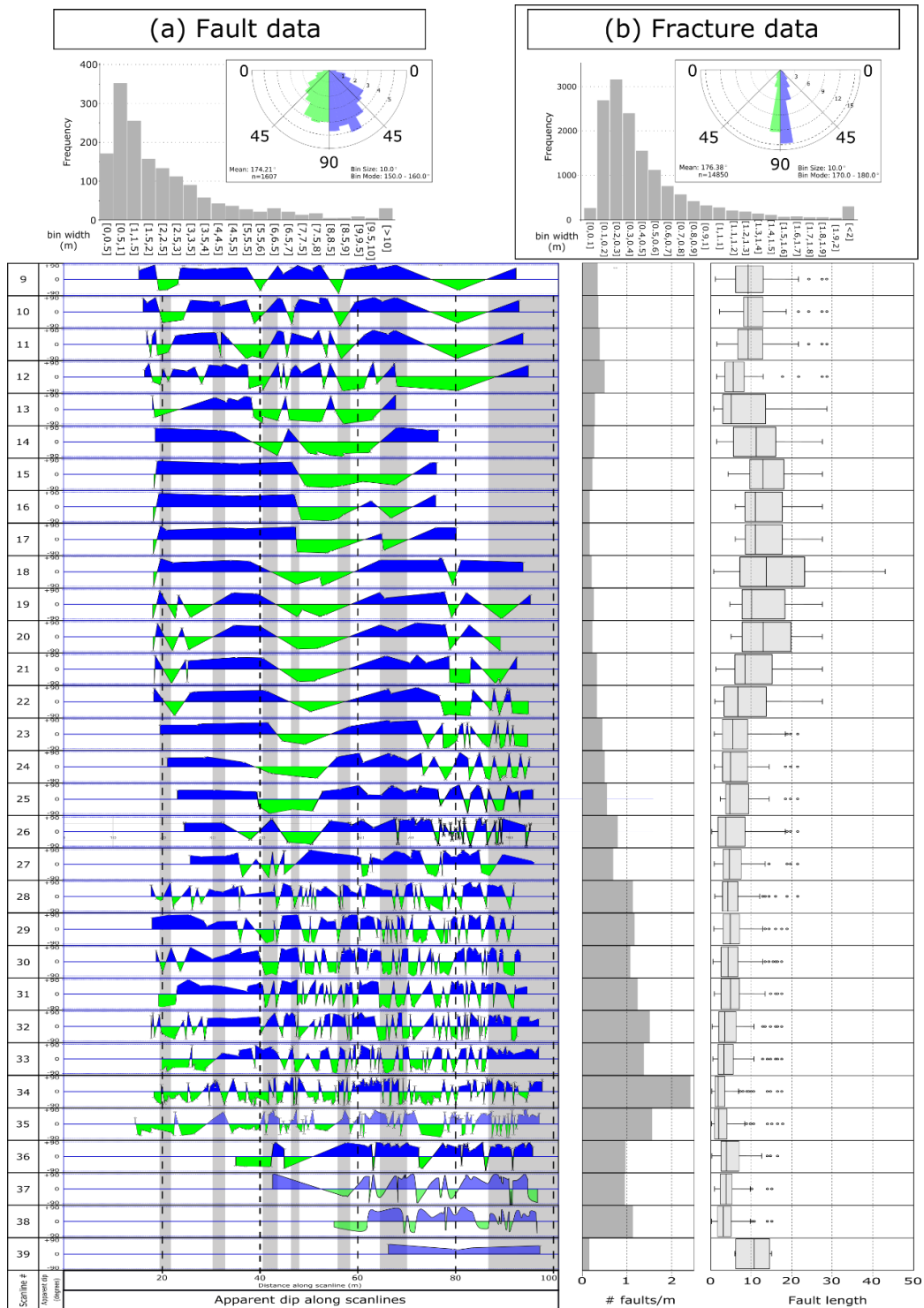


Figure 7.4: Fault (a) and fracture (b) data from the digitised high wall and scanlines undertaken along the high wall at Spireslack SCM. Fault and fracture data exported from the digitised maps include: i) trace length data presented in a trace length histogram with bin-widths of 0.5 m and 0.1 m respectively; and ii) apparent dip which is presented on length weighted rose-diagrams with bin width of 10°. Fault-data from scanlines is presented through: a) the change in apparent dip along the scanline; b) number of faults per meter observed along the scanline; and c) fault-length presented as box and whisker plots.

# Horizon	Beds				Faults									Zone
	Total length (m)	# sections	Apparent dip Mean CV		#	Intensity (F/m)	Offset			Apparent dip				
							Min	Max	Median	Min	Max	Mean	CV	
1	37.61	9	1.4	0.49	8	0.21	0.17	0.64	0.28	26.6	51.7	36.4	0.26	Zone 1
2	34.53	35	2.4	1.30	34	0.98	0.07	0.49	0.18	14.1	88.1	50.8	0.36	
3	36.44	30	5.3	1.18	31	0.85	0.05	0.44	0.14	33.7	85.3	58.0	0.26	
4	46.90	43	3.4	0.94	44	0.94	0.03	0.55	0.11	24.2	90.0	65.2	0.28	
5	60.56	45	5.0	1.01	44	0.73	0.06	0.32	0.10	41.4	90.0	70.4	0.18	
6	37.20	56	7.2	1.39	61	1.64	0.03	0.34	0.09	26.9	90.0	62.1	0.26	
7	64.94	57	5.4	1.19	57	0.88	0.02	0.36	0.09	17.9	90.0	64.0	0.29	
8	64.87	29	5.7	1.14	27	0.42	0.05	0.44	0.12	29.6	90.0	63.6	0.27	
9	77.05	94	9.7	1.07	119	1.54	0.05	1.64	0.22	14.6	89.7	59.7	0.31	Zone 2
10	82.68	85	6.3	1.05	91	1.10	0.04	0.75	0.11	30.2	88.0	64.8	0.23	
11	81.93	10 6	6.2	1.25	113	1.38	0.04	0.79	0.12	12.2	88.7	62.5	0.29	
12	82.53	85	5.7	1.32	95	1.15	0.03	0.76	0.12	20.2	90.0	71.0	0.20	
13	82.08	84	5.5	1.26	89	1.08	0.05	0.88	0.21	15.8	90.0	70.8	0.21	
14	83.99	49	6.3	1.05	51	0.61	0.08	0.73	0.17	24.6	90.0	69.9	0.19	Zone 3
15	85.64	39	5.0	0.99	40	0.47	0.08	0.44	0.15	29.8	89.2	69.2	0.23	
16	41.71	41	4.5	1.28	47	1.13	0.05	0.62	0.16	12.3	88.9	65.2	0.26	
17	83.92	39	4.9	1.00	33	0.39	0.05	0.39	0.12	41.0	90.0	66.5	0.22	
18	82.59	31	5.0	1.26	30	0.36	0.04	0.22	0.08	32.0	85.1	67.1	0.21	
19	84.87	15	3.3	1.06	14	0.16	0.07	0.33	0.16	44.5	87.6	70.1	0.19	Zone 4
20	84.65	16	3.6	1.45	15	0.18	0.08	0.48	0.17	33.5	90.0	68.4	0.25	
21	83.37	18	5.4	0.81	17	0.20	0.24	0.63	0.33	45.0	87.4	70.0	0.18	
22	81.97	7	4.5	0.99	7	0.09	0.18	1.07	0.23	30.9	90.0	66.5	0.30	
23	79.74	7	4.4	0.76	7	0.09	0.17	0.82	0.34	45.5	90.0	69.4	0.25	
24	80.99	2	0.5	0.23	1	0.01	0.16	0.16	0.16	51.9	51.9	51.9	-	
25	80.38	1	1.7	-	0	0.00	-	-	-	-	-	-	-	

Table 7.3: Fault offset and bed-section statistics by mapped horizons.

7.5.2. Whitley Bay exposure

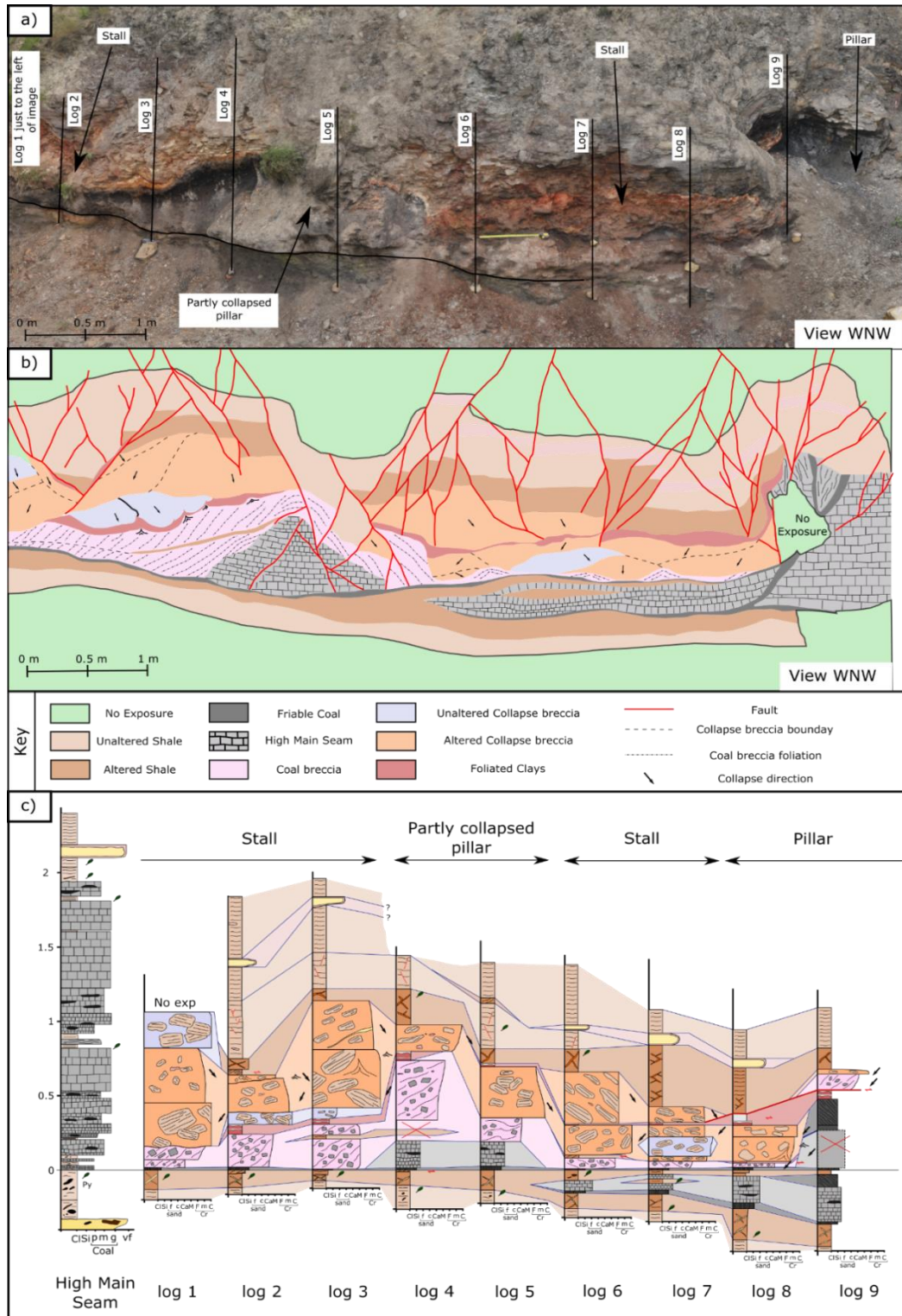


Figure 7.5: Workings of the High Main Seam (HMS) at Whitley Bay: a) photomontage of the workings with the location of logs marked; b) interpretation of collapse lithologies; and c) sedimentary logs through the undeformed HMS at the base of Hartley Steps and through the workings at the locations marked in (a).

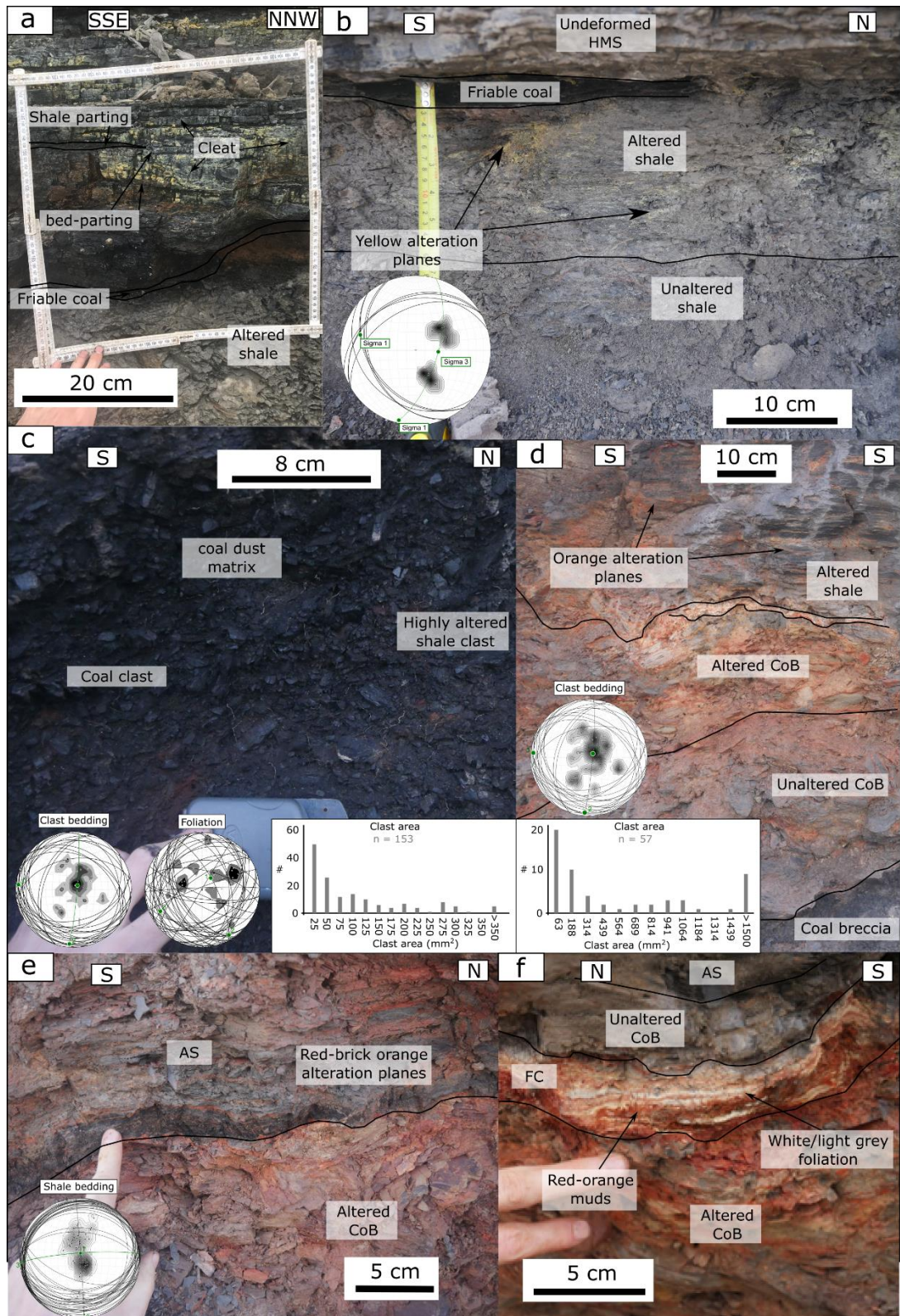


Figure 7.6: Facies photographs and associated clast and kinematic data. a) Undeformed High Main Seam, with yellow discolouration along the cleat network. B) Unaltered and altered shale underlying the unworked pillar. Stereonet displays the planes, poles to planes, and principle stress axis inferred for the yellow alteration planes. C) Coal breccia which onlaps (Figure 7.6

caption continued) onto the north of the pillar. Orientation data for clast bedding and foliation are presented, along with clast area distributions calculated using the equivalent circular area (ECA) method. D) CoB (altered and unaltered) which onlaps onto the coal breccia. The clast-area (ECA) distribution and orientation of clast bedding is presented. E) The overlying altered shale, with orange alteration along bedding planes. The dip of shale beds is presented, along with the inferred principle stress axis. F) Foliated red-orange foliated muds, which display onlapping relationships onto underlying clast

While the high wall at Spireslack SCM provides important information on the distribution of stalls and pillars, along with the deformation style above and below the NFC, it is not possible to see the internal structure of the worked layer. The exposure of the worked High Main Seam (HMS) at Whitey Bay (Figure 7.5a) enabled the internal structure of the abandoned underground workings to be investigated. Through detailed field observations and sedimentary logging 8 facies were identified (Table 7.4). In this section 'thickness' refers to the vertical thickness of a bed, pod, or lithology within the studied section.

The relationship between sedimentary facies within the workings can be split into two areas, pillars and stalls, depending on whether unworked HMS is present in the logged section (Figure 7.5). Two stalls are present, which make up 69% of the outcrop, with similar facies associations observed above the HMS in the central pillar, and edge of the northern pillar (Figure 7.5). The thickness of the collapsed stalls, defined as the distance between the laterally continuous Friable Coal (FC) layer, and the fractured Unaltered Shale (US) found at the top of the workings, ranges from 52 cm in log 7 to 114 cm in log 3 with the facies thicknesses and associations varying along the outcrop (Figure 7.5c). The relationships of US, Altered Shale (AS) and FC are the same as the undeformed section, however, the thickness of US is greater beneath stalls. Coal Breccia (CB) can be observed on-lapping onto the partially collapsed pillar (Figure 7.5b), with the maximum thickness (c 40 cm) and larger clast sizes (median = 144 mm²) found closest to the boundary of the pillar. CB does not show clear grading, however, a weak foliation is picked out by fines which dip down-dip and away from the pillar (Figure 7.6c). Towards the south of the outcrop CB occurs as a discontinuous layer, with the foliation suggesting that soft-sediment deformation caused by later collapses lead to the thinning and thickening of the unit.

Collapse Breccia (CoB) may be found across the full outcrop and displays areas which show alteration and those which do not (Figure 7.6d,e). Within CoB distinct 'pods' may be observed which are laterally discontinuous and pinch out over a 0.3 to 1.2 m scale. A total of 19 pods are identified, with the stacking patterns suggesting that the initial collapse

occurred at the centre of the stall, with later collapses acting to clog the old workings. The dip of clast bedding is generally shallow, agreeing with a NS trending fold axis which plunges shallowly to the SW (Figure 7.6d). Each pod stacks on previous pods, with the bedding of each pod rotated depending on the topography of the collapse (see arrows for collapse direction in Figure 7.7b). The top of CoB also develops a small scale topography due to presence of rotated, angular shale clasts.

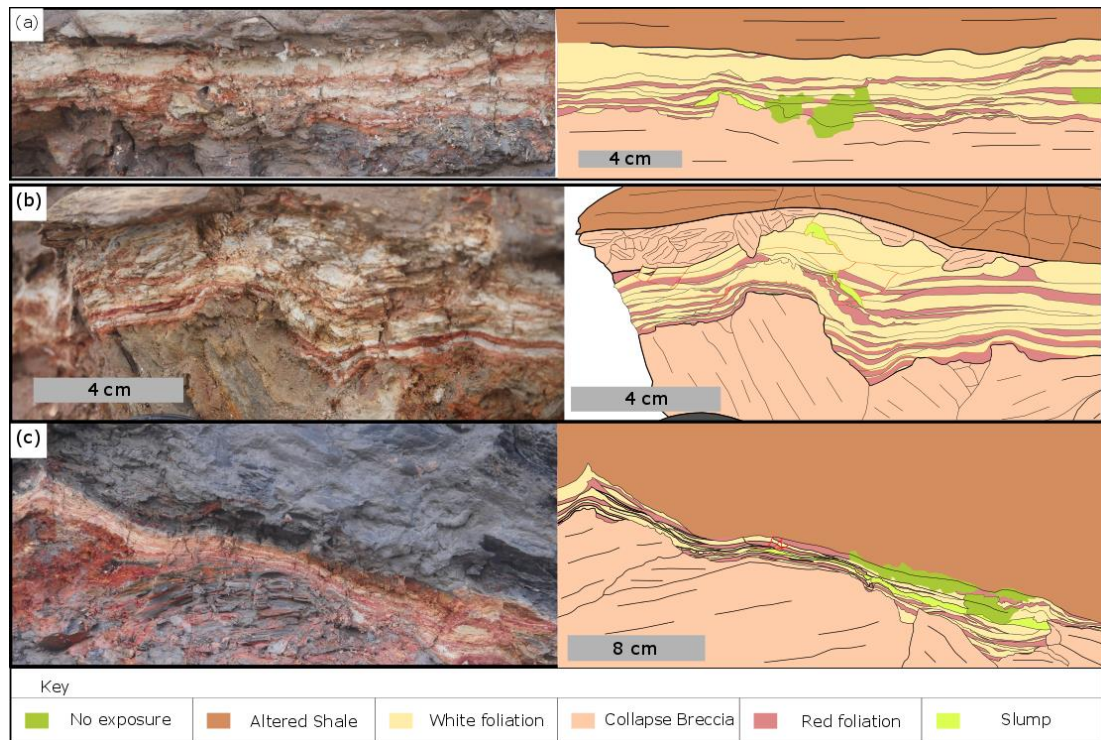


Figure 7.7: FC stacking patterns. View is towards the west onto the sub-vertical outcrop.

Foliated Muds (FM) typically dip towards the SW and are observed in both stalls, overlying coal breccia in the south and either coal breccia and CoB in the north. Complex stacking patterns and sedimentary structures are observed in the unit, controlled by the underlying topography (Figure 7.7). The alternating red- and white- layers are cyclical in nature, with the number of cycles varying from 7 to 13. At the base of FM the foliation can be seen on-lapping onto angular clasts of CoB, with the thickest deposits occurring in gaps between clasts (Figure 7.7). This shows that the collapse occurred and was followed by the deposition of FM, filling pods on the pre-existing topography on the top of CoB. Stacking patterns in Figure 7.7a suggest that rotation of this topography occurred throughout the deposition of the muds, leading to changes in depocenters probably caused by further collapse of workings disrupting CoB.

<i>Facies</i>	<i>Description</i>	<i>Depositional processes</i>
HMS Undeformed thickness =	Interbedded unit containing 16 coal beds (2 to 43 cm thick) and 7 organic rich shale partings (1 to 4 cm thick). Coal beds may be subdivided into three (HMS1-3) with euhedral pyrite crystals (<0.2 mm) occasionally visible along bedding in HMS2.	The deposition of peat in a swampy, anoxic environment which was sporadically interrupted by clastic deposition in a delta plain environment ¹ .
US Beds 0.2 to 1 cm thick	A mudstone to silty-mudstone, which can be either organic rich or organic poor. Coalified plant fossils and euhedral pyrite (<0.2 mm, <5%) are often found along bedding surfaces, particularly below the HMS.	Low energy deposition in a variably oxic environment, related to the flooding of peat swamps ^{1,2} .
AS Beds 0.2 to 0.8 cm	Found within 20 cm of the HMS in both undeformed and worked sections. Similar to US, however, weathers more readily and contains shallowly dipping alteration planes (yellow below & brick orange above).	The development of acid mine water following mining operation causes the degradation of clay minerals and movement of the sulphur from the pyrite within the seam ³ .
FC <15 cm thick. Figure 8b & d	FC may be observed along the base, and within the workings, as well as along the edge of the right-hand pillar (Figure 7.5). FC is black, dominated by organic material (> 95%) and characterised by a very tight fracture network which cause the lithology to erode as a black powder. Fractures either occur perpendicular to layering, or at an angle forming a well-developed foliation (Figure 7.8a, b).	FC1: Working related deformation of thin channel coals and stringers of the HMS. FC2: Development of tectonically deformed coals ⁴ along the edge of pillars during the collapse of workings.
CB Thickness 2 to 55 cm Figure 7.6c	CB occurs along the base of the workings, and varies in thickness considerably. CB is a chaotic to mesoic breccia ⁵ consisting of angular clast of coal (>90%) and highly altered shale. Coal clasts (median 60 mm ²) are bounded by bedding planes or cleats. Shale clasts are often altered to a red-orange, silt to clay grade dust (Figure 7.6c). The matrix is dominated (<95%) by silt grade organic fragments with the remaining 5% consisting of quartz and occasional <0.5 mm pyrite crystals.	May be formed either a) through the spalling of the pillars, whereby tallus like deposits occur as pillars corrode through time ⁶ or b) through the down-dip flow of coal during flooding events being deposited in the lee side of pillar in a similar manner to bridge abutments ⁷ .
CoB Thickness 20 to 90 cm Figure 7.6d & e	The dominant lithology in the collapsed stalls CoB is found as altered or unaltered pods of clast dominated (85 to 90%) crackle breccia ⁵ (Figure 7.5b, 7.6d). Clasts (median = XX mm ²), are dominated by shale clasts (90 %), with clasts of ironstone, coal and bleach-white sandstone or seat earth also present. Clasts typically show high aspect ratios (Median = X.X) elongated parallel to bedding. The matrix is clay-rich containing brick-orange, silt grade clasts of altered shale and sand grains.	Rotation of clasts away from pillars as material collapses into the stalls ⁸ . Where the permeability of the workings is low, and mine water develops, clays in CoB degrade and develops the orange alteration colour.
Foliated Muds (FM) Thickness 0.5 to 15 cm Figure 7.6f, 7.7	FM consists of mm to cm scale foliated muds which alternate between brick-red and off-white in coloration (Figure 7.6f). Foliations typically stack from brick-red to white, with the top of the white foliations marking distinct depositional phases. Between 7 and 13 cycles can be identified, filling from the deepest point and occasionally showing soft-sediment deformation indicative of mini-slumps (See text for further description).	Cyclical flooding and evaporation of salt-rich fluids, causing a stacked sequence above the pre-existing CoB. Slumps develop either due to rapid deposition on the CoB top topography, or due to the further collapse along the workings.

Table 7.4 (Previous page): Facies description and interpretation of depositional environment. References: 1) Fielding (1984b); 2) Fielding (1982); 3) Younger et al. (2002); 4) Godyń (2016); 5) c.f. Woodcock & Mort (2008); 6) Martin & Maybee (2000); 7) Koken & Constantinescu (2008); 8) Lokhande et al. (2005).

The bottom of FM is generally undisturbed, however, in the mid- to upper- sections of the deposit slumps, minor faulting and soft sediment deformation can be observed. Slumps occur where a paleoslope occurs either within the FM or from the top of the CoB, for example, in Figure 7.7c a laterally extensive slump deposit, with normal faults developed at its head, and compressional features at its foot. This can be observed along the shallowly dipping (c. 8° to 10°) paleo-slope of the CoB top. In Figure 7.7b, the top of FM has been deformed by a later collapse, which causes the soft-sediment deformation of a thick white layer, and small-scale faults and foliation rotation to occur.

FM may either be overlain by further collapses (CoB), which often cause soft-sediment deformation of the pre-existing units, or to the far north of the outcrop by altered shale. Altered shale makes up the top of the collapse lithologies and is brought down onto underlying lithologies by a series of fault strands which will lead to the closing of open space (Figure 7.5b) and the extrusion of FMs along the edge of the pillar (Figure 7.8a).

Two pillars, which make up 31% of the outcrop, are observed, one to the north and another near the centre of the studied section. In the northern outcrop, the top 0.45 m of the undeformed HMS succession may be observed and the base is visible in the foreshore up-dip of the studied section. This suggests that the full thickness of HMS (c. 2 m) is present at this location. The base of the HMS exposure in the centre of the outcrop (logs 4 and 5 of Figure 7.5c) closely matches that of the undeformed sequence. However, above the 16 to 18 cm thick bed of HMS2, 14 to >40 cms of CB are observed. This displays a subtle foliation, which dips away from the pillar and semi-randomly orientated clasts (Figure 7.6c). Above CB the central pillar shows facies associations more similar to that observed in the stalls (CoB, AS, US, see above). The US at both locations display low-amplitude folding (Figure 7.6e), with material subsiding from above the pillars into stalls (See Figure 7.5).

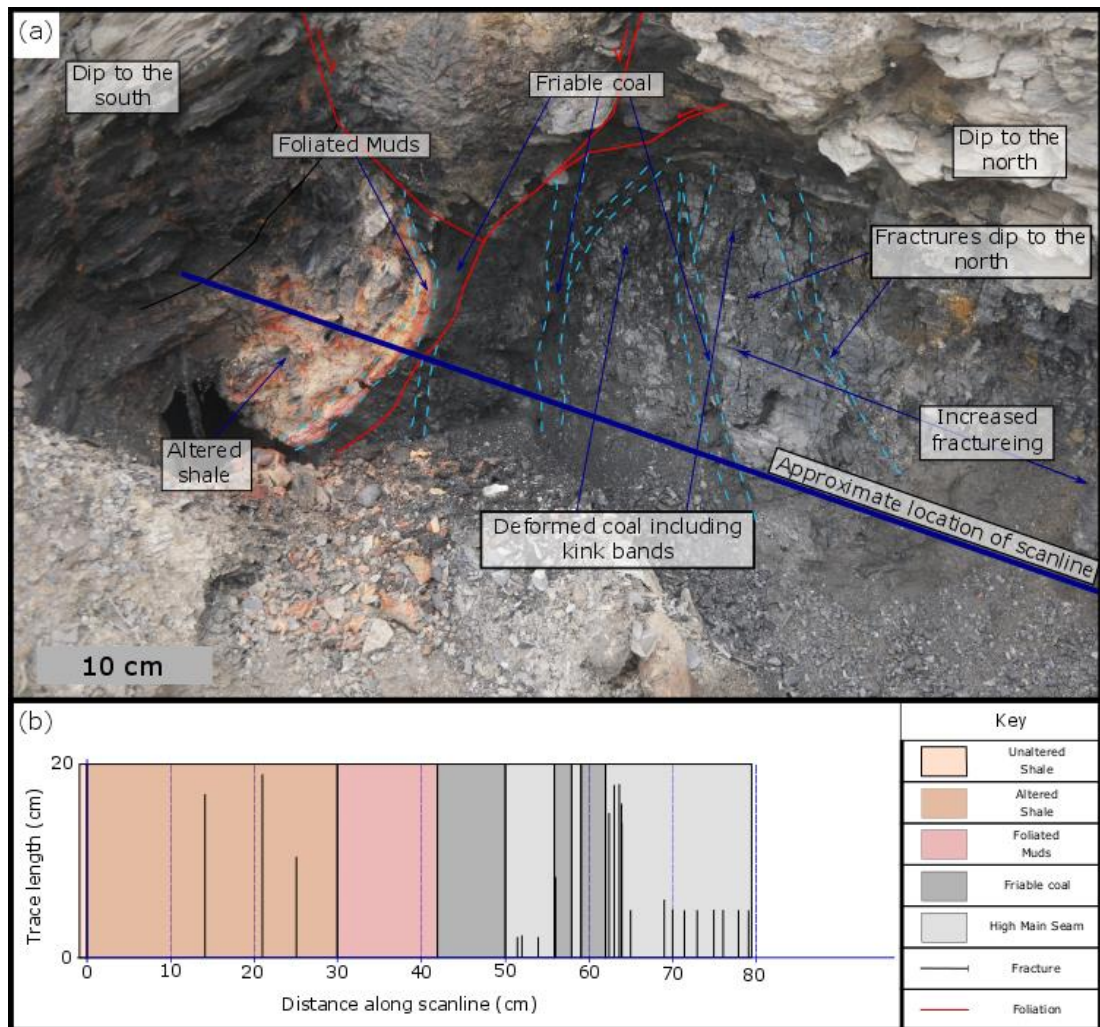


Figure 7.8: Northern Pillar: a) annotated field photograph displaying key structural elements of the pillar edge; b) scanline through the edge of the pillar, as marked in a.

The HMS in both pillars displays increased fracturing compared to the undeformed section, along with local development of FC (Figures 7a, 8b). The scanline taken through the northern outcrop (Figure 7.8b), highlights that in the vicinity to FC, the trace length and intensity of fracturing increases, with fracturing returning to more typical values for the undeformed cleat network. While the intensity and trace length changes, fractures often form parallel to, and utilising the pre-existing cleat network. Locally, particularly between strands of FC, the rotation of coal, including cleats, fractures, and coal bedding is observed (Figure 5.7a). This suggests that fracturing occurred prior to the block rotation of the coal, and that only later deformation (e.g. development of kink-bands) occurred during the rotation and development of FC.

Bedding below the HMS is similar to the seam itself (040°/10° W), however, bedding above the seam maintains thickness and dips to the north and south with a mean fold axis of 105°/80° N (Insert Figure 7.6a). Folding is subtle above stalls, however, above pillars it is clearly visible. At this location the folding and rotation of bedding along antithetic faults occurs such that two anticlines and three synclines with wavelengths of 0.5 m to 2 m are observed. We suggest folding is due to the rotation of the overburden following roof collapse.

7.6 Discussion

7.6.1. Processes involved in the formation of collapsed pillar and stall workings

We investigated the processes which occur during the collapse of abandoned pillar and stall mine workings. This has allowed for the first time a model for the temporal evolution of the internal structure be proposed. We find that the collapse at Whitley Bay occurred through five distinct phases, as evidenced by sedimentary facies and associations, deformation style and paleo-flow indicators. The stages are outlined below and summarised in Figure 7.9.

Stage 1 & 2: Extraction of coal and build-up of CB:

Estimated between 1550 and 1710 AD (see Table 7.1), the HMS was worked using pillar and stall mining methods. The shallow depth of the seam at this location suggests that access was most likely from an adit cut from the sea. Coastal erosion rates in the area range between 0.15 to 0.30 cm per year (Tingay and Ellis, 2016), suggesting that a minimum of between 46.5 m and 93 m of rock has been eroded. Assuming no disruption due to faulting in the eroded section the seam would have been 8 to 10 m above the mean high water mark. Lying above the water table, workings would not need to be pumped, and flooding would only occur following periods of heavy rain or winter storms. During the extraction of coal, small fragments of low-quality coal and coal dust would be left behind, flowing downstream (towards the SW) and building up against pillars during flood events. This process leads to the deposition of the coal breccia. The on-lapping of CB onto the degraded pillar (Figure 7.5b), orientation of the faint foliation (Figure 7.6c) and clast-bedding orientation (Figure 7.6c) matches the deposition pattern you would expect in a shallow channel flowing around an obstacle (e.g. scouring around

vertical dikes (Koken and Constantinescu, 2008)). Larger, high quality, clasts of coal will be added to the system following the end of mining operations (**Stage 2**), as upkeep was no longer required, and pillars gradually spalled and collapsed (Ebrahim F Salmi et al., 2019).

Stage 3: Incremental collapse and steady reduction in permeability:

As time passed, episodic flooding degraded pillars and pit-props and the roof of the workings began to sag and spall (e.g. Bruyn & Bell 1999). In agreement with the work of Helm *et al.* (2013), we find collapse initiates near the centre of stalls, which were only held up by pit-props, followed by several small collapses propagating towards the pillars. Initially collapses would do little to reduce the overall permeability of the workings, and episodic flood waters would flow around the collapsed sections. As the percentage of collapsed material increased, clays sourced from shales, would clog pore-space between clasts. The breccia, which is poorly sorted and already have a low permeability, would become saturated.

The pyrite within the saturated collapse breccia, oxidised to form weakly acidic mine waters (Younger, 1994; Younger, 1995; Turner and Richardson, 2004). Mine waters in the breccia altered clays in the matrix and clasts of CoB and caused the red-orange coloration. The presence of breccia pods which do not show alteration suggest that some earlier, and later collapses did not become saturated, potentially due to being above the water level or lacking hydro-geological connections with mine water. Onlapping relationships suggest the collapse at Whitley Bay occurred through a total of 19 events (Figure 7.5b).

Stage 4: Formation of the FC.

The fluid which formed FM was hyper-saline and occurred in a cyclical manner. As there was no flow, clays settled from suspension, and became deposited as a thin layer of mud (the red foliation) (Figures 7.6 and 7.7). The orange-red colour and silt-grade grains are similar to the altered shale clasts in CB, and likely represent clays sourced from shales altered by acid mine waters (c.f. Younger 1995). The top of each cycle were white to off white, clay-rich layers with a distinctly salty taste and appeared to contain evaporites, however, it is not possible to deduce the mineralogy from field observations. The deposits build up first in small pods in

topographic lows on top of CoB, suggesting that the hyper-saline fluid formed puddles on the breccia, and deposited through evaporation prior to the next pulse. This type of deposit is commonly seen where brines periodically flood areas with topography, essentially acting as a mini-basin which is infilled in a process called reflux (Warren, 2016).

While salt rich fluid could have been sourced from sea-water during winter storms, the more likely source is the hypersaline brines, that are well known to form springs in the Northumberland and Durham coal fields (Edmunds (1975) in Younger (1995)). Deep saline brines can mix with mine waters (Younger, 1998), as well as be diluted by groundwater recharge which also add pyrite oxidation products (Green et al., 1999). The acidity of mine-waters is a product of both 'vestigial acidity' caused by the past oxidation of pyrite, and 'juvenile acidity' caused by the products of seasonal pyrite oxidation above a fluctuating water table (Younger, 1998). Due to the presence of both altered and unaltered CoB, we suggest that the water table, and hence the composition of groundwater, varied through time. When pyrite oxidation is high, the acidity of the groundwater will increase and cause the proportion of acidic mine water relative to brines to increase. This will cause the breakdown of clays within the shales (Younger et al., 2002), which become entrained into the hypersaline fluid and carried in suspension. When the flow rate dropped, evaporation occurred leading to the deposition of the red-mud layer. In times when pyrite oxidation was lower, the brine component of groundwater dominated and less clays were held in suspension. This led to the deposition of salty muds (likely gypsum and anhydrite) in place of the red-muds. The annual cyclical variation suggests FM was deposited over a 7 to 13 year period.

The presence of slump-deposits and soft sediment deformation within FM occur either a) where the dip of the paleo-topography is high ($>8^\circ$), or b) in the vicinity of later CoB pods (Figure 7.7). Slump deposits may either be caused by the rapid build of sediment on a slope (Moore, 1961), or following the ground motions, for example earthquakes (Keefer, 1984). Both processes could be active in the workings, with large pulses of saline brines causing rapid deposition of muds and evaporites and ground motion caused by roof collapse. The slump deposits in both Figure 7.7a and b show no disruption of overlying layers, and have an open-toe

deposition style (c.f. Alsop *et al.* 2016) with units above on lapping onto the deposit. In contrast the deposit in Figure 7.7c has a longer run out, is thicker and overlying cycles are deformed through normal faulting at the head and compressional features at the toe. We suggest the slumps in Figure 7.7 a and b formed due to rapid sedimentation on the paleo-topography present on the top of CoB, possibly triggered by minor collapses. Figure 7.7c, however, was deposited following a large roof collapse which caused a slump to develop, utilising a shallowly dipping clay layer as a decollement, similar to large scale processes caused by earthquakes in the Dead Sea Basin (Alsop *et al.*, 2016). Collapse related slumps are found at different stratigraphic layers within FM, suggesting the workings collapsed over several years.

Stage 5: Final collapse of stall:

Eventually pillars degraded to the point where they could no longer support the overlying stratigraphy and the roof collapsed. The collapse and subsidence of overlying units is accommodated through normal faults which dip away from the zone of collapse. This caused triangular zones of deformation, with subsidiary faults coming off the main strands (e.g. Figure 7.3). The workings at Whitley Bay displays three triangle zones, one in the southern and two in the northern stall (Figure 7.5). The minor faulting pattern is controlled by the topography of the pre-existing collapse lithologies. For example, to the north of the partially collapsed pillar material is brought down by several small-offset fault strands which bound 'lenses' (c.f. Gabrielsen *et al.* (2016)) of undeformed shale and ironstone.

Similar patterns are observed at Spireslack SCM, where triangle zones of damage exist immediately above the workings of the NFC (Figure 7.3, Zone 2). Stalls at Spireslack have between 1 and 3 triangle zones. Depending on the spacing of the pillars, the height of the triangle zones can vary from <5 m up to 20 m, with the deformation interacting where triangle zones overlap (Zone 3). Deformation often diminishes, or becomes localised onto a small number of fault strands, at a competent lithology (e.g. sandstone or limestone). This is similar to natural faults in mechanically layered sequences, whose vertical growth is restricted by mechanical contrasts (Watterson, 1986; Childs *et al.*, 1996; Schöpfer *et al.*, 2006). Mine-related deformation above the workings occurs in 4 distinct zones controlled by a) the

mechanical strength of the succession, b) thickness and spacing of pillars and c) proximity to other collapsed stalls.

These findings are similar to those of Garrard & Taylor (1988), however, we find individual stalls in close proximity cause 'harmonic mining' style deformation effects (Lokhande et al., 2005). We also find pre-existing discontinuities (joints and cleats) play a small role in the deformation style above the workings. Sub-vertical joint patterns match what is to be expected in mechanically stratified lithologies (Laubach et al., 2009), apart from those in proximity to major faults which bound triangle zones. In these areas a zone of damage, similar to natural faults (Caine et al., 1996; Kim et al., 2004), is developed which consists of a network of highly connected, large trace length fractures which form sub-parallel to fault strands. Current models of mine collapse suggest deformation occurs in one shortlived event (Carter et al., 1981; Marino and Gamble, 1986), and that triangle zones develop from the centre of the stall, propagating towards the pillars (Bruyn and Bell, 1999; Lokhande et al., 2005). Our data from both sites show multiple triangle zones, and hence collapse events, can develop within a single stall. The interaction patterns and cross-cutting relationships of faults at Spireslack SCM support the findings of Bruyn and Bell (1999) that the collapse of a pillar can cause pillars close by to also fail.

The collapse lithologies at Whitley Bay appear to have been saturated at the time of collapse, with soft sediment deformation observed in CoB, FMs and CB (Figure 7.5b). While Stage 5 occurs following the deposition of FC, to the north of the outcrop, in the rest of the outcrop Stage 4 is followed by a return of Stage 3 and the deposition of CoB pods (Figure 7.5). Where CoB is not found, FC is thickest with the greatest number of cycles observed (13 as compared to 7 to 8 to the south). This suggests that the void near pillars was open to flow far longer than the rest of the workings. If our interpretation that the cycles represent annual pulses of saline-rich brines is correct this then suggests the stall closest to the pillar remained a conduit for flow six years longer than the centre of the void.

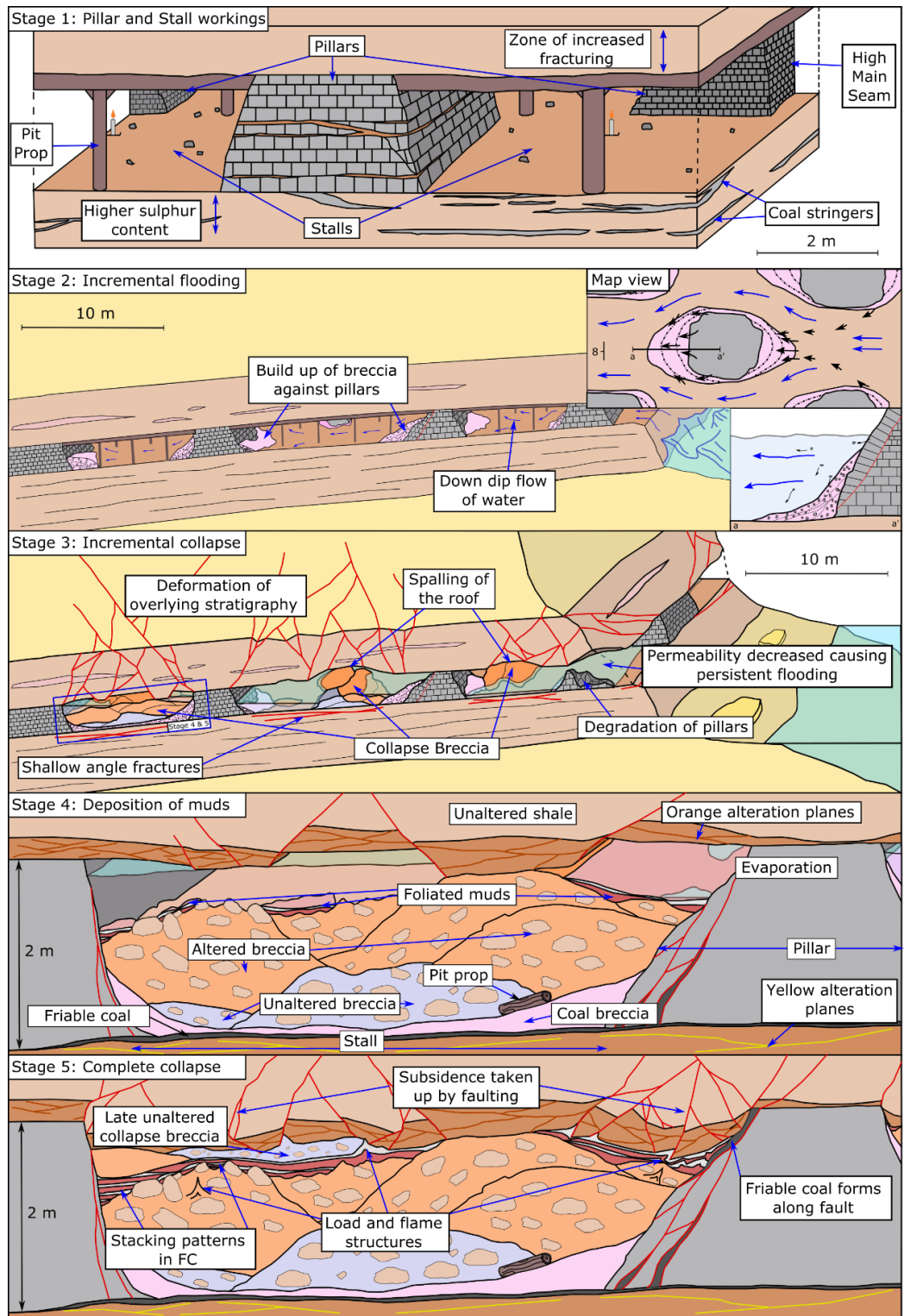


Figure 7.9: Evolution of mine collapse, see text for description of each stage.

While the exact stacking patterns at Whitley Bay are representative of a single location, the processes are comparable to other pillar and stall workings, and similar fault-patterns are observed at both study sites. Abandoned coal mines in the UK are known to have collapsed

following the post-mining groundwater recharge (e.g. Bathgate, (Carter et al., 1981)) and the degradation of the pit props (Donnelly, 2006) with collapses remaining a major geotechnical risk to this day (Donnelly et al., 2009; Helm et al., 2013; Gee et al., 2017). Stage 4 (the deposition of FM) will not be widely observed and is only present because the workings are above a variable water table and sourced by deep saline brines. Previous work has suggested that collapse occurs as a single event, over days to weeks (Carter et al., 1981; Marino and Gamble, 1986), however, our data suggests that at-least part of the workings remain open to flow for a significantly longer period of time. Wide spread regional subsidence in ex-mining areas is well known (e.g. Gee *et al.* (2017)), and it may be that these small sections which remain open to flow are not large enough to cause noticeable surface deformation when they fail.

A good analogue for the lithologies and processes described in this study is the collapse and sedimentation of modern and paleo-cave systems (e.g. (Loucks, 1999; Mcmechan et al., 2002; Loucks, 2007; Labourdette et al., 2007). Loucks *et al.* (2004) identified 5 paleo-cave facies from core and outcrop data which display distinct properties showing clear parallels to the facies observed at Whitley Bay (Table 7.5). The key differences in the depositional systems include: the scale of the facies; properties of the zone of damage; initial petrophysical properties; and finally that the collapse mine workings leave a low permeable, clay-rich layer and not a high permeable course chaotic collapse breccia (Loucks et al., 2004). The zone of damage above the workings is comprised of a well-connected fault and fracture network, similar to the disturbed host-rock observed around collapsed caves. However, due to the significant clay content of the succession the water capacity of this fracture network is likely to be low (Neuzil, 1994; Gautschi, 2001).

Cave collapse facies Louchs et al. (2004)	Equivalent collapse facies identified in this study
<i>Continuous Strata Facies:</i> Competent, coherent bedded carbonates, with only local evidence of deformation.	Same as the undeformed lithologies, or Stage 4 of the deformation above the NFC. Interbedded clastic lithologies with high clay content in the succession.
<i>Discontinuous Strata Facies:</i> Characterised by small scale folding and faulting, with some local brecciation. Bedding is generally continuous along strikes. The unit is highly fractured and has local development of mesoic breccia.	Similar to deformation observed in Zone 3 to 4 of the high wall at Spieslack SCM, where bedding can be easily traced across the high wall, but small scale faulting and the rotation of bedding is observed.
<i>Highly Disturbed Strata Facies:</i> Highly deformed, discontinuous bedded strata with considerable amounts of crackle and mosaic brecciation. Small scale fault and folding common and interbeds of clastic material mark where individual collapse events are recorded.	Immediately above the worked seams, both at Whitley Bay and Spieslack SCM, similar processes are observed. The difference being that deformation quickly interacts with nearby stalls (Stage 3), which will only occur in caves where two sections of caves are in close proximity.
<i>Course-Clast chaotic breccia facies:</i> Very poorly sorted, matrix to clast-supported granule- to boulder-sized chaotic breccia. Finer interbeds common, interpreted as sediment transport into the cave (Loucks, 1999). Overall volume of collapsed lithology increase by c. 40% (Labourdette et al., 2007). Where available rock is less than 2.5 times the volume a collapse sinkhole develops (e.g. Mylroie et al., 1991; Harris et al., 1995).	Similar to the collapse breccia (CoB), however, due to the shale top of the roof of the HMS, lower expansion of the breccia occurs during collapse, permeability will be low and only a small space is available to be filled with fines. The collapse of shallow workings can lead to sink hole development (Garrard and Taylor, 1988; B. A. Poulsen and Shen, 2013).
<i>Fine Chaotic Breccia:</i> Poorly to well sorted, matrix to clast-supported, granule- to cobble-sized chaotic breccia. Sediment fill commonly observed, but limited to small grain size. Sediment fill deposited by transport from within or outside the cave (Loucks, 1999).	CB develops from material left from mining operations and the spalling of pillars (Martin and Maybee, 2000). This then gets transported along the coal seam.
<i>Finer Grained Sediment Facies:</i> Consist of silt- to granule- size sediment, dominated by detrital carbonate. Siliclastic clay may reach 4%, but generally less than 1%. Sediment is interpreted as being transported in an open chamber by traction, mass-flow and suspension mechanisms.	FMs get deposited from the mixing of mine-waters and deep hyper-saline brines leading to the sedimentation of thin muds from evaporation, suspension and mass transport mechanisms.

Table 7.5: Comparison of mine and cave collapse facies.

7.6.2. Implications for shallow mine geothermal

7.6.2.1. Flow and groundwater capacity of a mine water geothermal site:

Ground water flow through abandoned mine workings can be considerable. For example, discharge flow rates from the Shilbottle Seam workings in Northumberland (UK) ranged from 0.8 ML/d to 2.6 ML/d (median = 1.7 ML/d) (Younger, 2004). Our work shows that while this is the case initially, where flow can occur along stalls (55 to 60% of the seams volume), any collapse, including early spalling of the roof, will act to clog up the system with low permeability, clay-rich, lithologies. Within the collapsed material (CoB), several distinct packages were observed, occasionally showing alteration. This shows that Stage 3 did not occur instantaneously, instead representing a gradual decrease in void space, the migration of the void upwards, and the development of a topography at the base of the seam associated with the sagging and spalling of the roof (Helm et al., 2013). During this time flow will still occur, however, where workings are only partly flooded, fluid pathways will become longer and localised around pillars.

The presence of FM suggest fluid flow occurred over a period of 7 to 13 years, however, this is a low estimate as it is not clear when pulses of hypersaline brines began, and it is likely linked to regional groundwater rebound following the end of mining operations (Burke and Younger, 2000). The thickest deposits of FM are in the vicinity to pillars, suggesting that this is the best location for flow, particularly as collapse in these areas occurs later than the rest of the workings. It is important, however, to not only consider the permeability of the lithologies which make up the mine workings, but also fracture networks which can combine to form flow pathways (e.g. McCay *et al.* 2019). Pillars display increased fracturing compared to the undeformed section (Figure 7.8), and the low angle faults which bring the final collapse propagate from the pillars into overlying units (Figure 7.3). Tectonically deformed coal, which may occur along the edge of pillars (Figure 7.5, and 7.8), have a significantly reduced permeability (Ju and Li, 2009) which will inhibit flow into stalls. The presence Fluid will always flow along the path of least resistance, and it is the relative permeability of the workings to surrounding lithologies that controls flow pathways (Hamm and Sabet, 2010). While large open voids remain, resource loss will likely be low, however, in the final stages of collapse (post stage 3/4) the risk will increase.

It is possible flow will occur along the fault and fracture network above the seam, connecting to shallower, cooler groundwater which acts to diminish the geothermal

potential of the site. However, in deeper workings, where fractures will not reach the surface or shallow aquifers, the zone of damage above the workings may act to increase the resource, particularly if complete collapse has not yet occurred. Fractures terminate at the base of competent layers, meaning that the zone of damage is confined to the four zones identified, with the majority of flow occurring in zones 2 and 3. Where a full collapse has not occurred, flow will be highest around pillars, which can easily become connected to the well-connected overlying fault-fracture network. This can also help form connective pathways between different levels of colliery where multiple seams have been worked. In the later stages of collapse, however, it is possible that further degradation of pillars and collapse can be stimulated by the movement of groundwater (Bruyn and Bell, 1999).

We show that the geothermal potential of pillar and stall workings decreases as the degradation of pillars cause the roof to sag, spall and eventually collapse. Workings in the final stages of collapse (post stage 3; Figure 7.9), have a greatly reduced volume where fluid can flow, and an increased number of potential flow pathways into overlying units. When assessing a site for geothermal potential it is therefore integral that the phase of collapse is considered, and where possible, the effect of different stages of collapse modelled. These findings combined with those outlined by Malolepszy (2003) will be key for assessing the water capacity of target workings (Hamm and Sabet, 2010).

7.6.2.2. Uncertainty in production and inflow locations:

For production to be successful, groundwater flow between the injection and extraction boreholes is required, which will only occur where void space is intersected by both boreholes, and the workings are open to flow (Lund, 2001; Loredó et al., 2016). The level of the seam is generally well constrained, particularly for post 1872 workings (Table 7.1), however, the location of pillar and stalls, and whether these were arranged in a regular pattern is often unknown (Bruyn and Bell, 1999). Using the proportion of pillars to stalls in the high wall at Spireslack SCM, and assuming no collapse had taken place (i.e. stalls were open to flow), only 55 % would be an appropriate drilling target, which is within the range of representative values reported by Bruyn and Bell (1999) (30 to 70%). The uncertainty at Spireslack SCM is further increased by the uneven spacing of the pillars, probably due to the complex geological conditions at the site (see Chapter 4). This drilling related uncertainty is of particular importance for commercial geothermal projects due to the high cost of drilling (Lukawski et al., 2016), with the geothermal potential of a target seam differing

considerably depending on if you hit a pillar, open stall, or collapsed stall (see section 7.5.3.1).

When a stall is encountered, the fill type depends on the stage of collapse as well as varying considerably along strike (Figure 7.5). For example, if perfect core recovery was attained, which is technically challenging in weak interbedded lithologies, a lateral change in borehole position of just 1 m can dramatically change the thickness of units encountered (Figure 7.5c). In general, the presence of a clay-rich collapse breccia will be a sign of at least partial collapse, and thicknesses of CoB above 60 cm indicate considerable reduction in permeability. As such we suggest if the thickness of this unit reaches above 0.7 m, then the target should not be considered for production as the risk of failure will be greatly elevated. When drilling the presence of shale and sandstone fragments/core with a brick-orange coloration could also be a sign that significant mine waters have developed, saturated the collapse lithologies and began to form low-permeable clay layers. Although these clay layers are low permeability, they are also highly plastic. This could mean that if your extraction borehole intersected part of a colliery which had collapsed, flow pathways may be able to be created by the pumping of high-pressure water to dislodge the plastic clays.

In many commercial projects, it will not be possible to core due to drilling costs, and it would be more appropriate to monitor the flow-rates and water chemistry during drilling (C. Loredó et al., 2017). If flow-rates drop, and high sulphur contents are observed, then it is likely this represents a partially- or fully- collapsed horizon, however, if more typical groundwater chemistry is observed (Younger et al., 2002), and flow rate increases the workings are likely to be conducive to flow. While the zone of damage for shallow workings will reach the surface (B. A. Poulsen and Shen, 2013), in many cases deformation will remain underground and only broad surface subsidence will occur. This makes predicting whether, and to what degree, collapse has occurred prior to drilling difficult. Remote sensing techniques, which measure regional subsidence patterns (Hu et al., 2012; Gee et al., 2017), could be used to apply a risk factor of collapse, enabling an appropriate zone of damage and permeability to be applied to flow models. Considering the flow rates and chemistry of mine waters discharging from ventilation shafts, or pre-existing boreholes used during mining operations, could also provide a low cost feasibility test for a target resource.

7.6.2.3. Extent of mine workings and effect of geological structure.

Since 1872, the UK Government has required underground coal mines to provide mine abandonment plans detailing the extent of underground workings, location of shafts and faults present within a coal mine (Bruyn and Bell, 1999). While older workings will not be recorded (e.g. the workings at Whitley Bay), and small errors exist in the geographical position of features due to surveying techniques, these plans provide a rich data-set covering much of the UK coal-fields. The connectivity of different levels of a mine, through roadways and ventilation shafts, is an important part of assessing the potential of any site (Malolepszy, 2003). Geological faults can also provide a significant conduit for flow (Bu, 2013), with groundwater inflow events acting as a major hazard to sub-surface mining operations (Sheng and Reddish, 2005; Islam and Shinjo, 2009; Ma and Bai, 2015). It is important to consider if major faults which cut the target resource may lead to a) loss of resource, b) unexpected connections to a long-strike or down-dip aquifers or c) a flow pathway to the surface which could lead to mine-water drainage (Younger et al., 2002).

The presence of faults complicates flow pathways of potential projects and also increases geotechnical risk. Faulting of coal often lead to the development of mechanically weak tectonically deformed coals (e.g. friable coal) (Ming et al., 2011; Ju et al., 2012; Godyń, 2016). During production, an open geothermal system needs to pump either hot or cold water in and extract warm/cool water from the workings (e.g. Malolepszy *et al.* 2005). This will cause the build-up of pressure in areas of low permeability and increase fluid pressure along faults. The increase of fluid pressure on faults can lead to the reactivation of faults (Handin et al., 1963; Byerlee, 1978) and has been widely recorded in ex-coal mining areas (Donnelly, 2006; Donnelly et al., 2009). For example, changes in groundwater levels through pumping led to the reactivation of the Houghton Cut Fault and widespread surface deformation in the Houghton-le-Spring area (near Sunderland, UK) (Young and Lawrence, 2001). It is important that water pressures and ground motions surrounding known structures are carried out during geothermal production to reduce the risk of unexpected mine water drainage (Younger, 1995; Younger et al., 2002; Younger, 2004) or significant damage to infrastructure (Bell and Donnelly, 2006; Donnelly, 2006; Donnelly et al., 2009).

In areas where workable seams reach shallow levels, such as the High Main Seam at Whitley Bay, the long mining legacy in the UK mean there is a high risk that unrecorded workings are present (Bruyn and Bell, 1999). Because of their depth, and that they are

often connected to the surface, the temperature of groundwater within the workings will be low. Many unrecorded workings could become connected to later deep workings, through boreholes, shafts or geological structures, which hydraulically link the two. For example, on the mine abandonment plans of the High Main Seam at Seaton Delevall colliery (roughly 2 miles inland from the coast), worked coal, which is assumed to be flooded, is recorded to the east of the plan, with boreholes recorded extending into the old workings. For similar reasons it is also important to consider whether the target seam could become connected to deeper workings, which may have been mined using different mining methods (e.g. longwall mining), or be linked to a different hydrogeological regime (Malolepszy, 2003; Malolepszy et al., 2005). Due to the risk posed by geological faults, unrecorded pillar-and-stall workings and ventilation shafts, it is vital that an extensive desk-study is undertaken for any potential geothermal site. We suggest targets in the proximity to shallow seams which are likely to contain unpredictable early workings are avoided unless high temperature and flow rates through available shafts are recognised.

7.7 Conclusions

We present for the first time a detailed study of the internal structure of a collapsed pillar and stall coal mine, along with assessing the deformation patterns above and below workings using surface outcrops. The internal structure of the workings at Whitley Bay comprises of 8 distinct facies, with lithology, kinematics, stacking patterns and structure informing the collapse processes. A 5 stage model of stall collapse is proposed, each acting to decrease the permeability of the mine. Stage 1 represents the methods used in initial coal extraction, and provides the starting framework for the rest of the collapse, during this time small fragments of coal become deposited on the seam floor, which become added to when the seam is abandoned (Stage 2). Following working (Stage 3) the roof begins to spall, gradually collapsing through multiple events (19 at Whitley Bay), and acid mine water begins to form. In Stage 4 due to the presence of hypersaline brines a cyclical deposition of salty muds suggests the stalls were open to flow for at least 7 to 13 years. Finally (Stage 5), the roof collapses along several normal faults, which form triangle zones and lead to the subsidence of the overlying stratigraphy. The last section to collapse is closest to the pillar, occurring 6 years after the rest of the workings.

The deformation surrounding the workings caused by the final collapse observed at Spireslack SCM, may be split into four distinct zones of damage. The majority of damage

occurring within 5 to 15 m above the worked seam. The dip, interaction, and termination of faults along with the intensity of deformation depends on the spacing and thickness of coal pillars, the mechanical strength of overlying units, and proximity to other stalls. Evidence of multiple collapse events (triangle zones) occurring in a single stall is also observed in the deformation of the overlying stratigraphy. This suggests that unlike previous models, collapse does not occur as a single event over days to weeks, but instead sections remain open to flow for years after the initial collapse.

Our findings have significant implications for the shallow mine geothermal sector, raising a number of factors which need to be considered when assessing a potential site.

Considerable drilling uncertainties exist and with up to 70% of coal left behind in some collieries there is a significant risk of a borehole intersecting a pillar. Even when a stall is intersected the stage of collapse will affect whether significant flow can be maintained. The water capacity of a potential mine geothermal site degrades through time as the roof spalls, and finally collapses. The well-connected fault and fracture network which overlies the workings can enhance or degrade the geothermal potential of a site. It is also important to consider the effect of pre-existing structures, particularly faults, and unrecorded workings, on the fluid-flow and geotechnical risk of a potential site. While this work is limited to a single site, we suggest the processes are widespread. We propose that pillar and stall workings be considered a heterogeneous, clay-rich anthropogenic layer whose properties vary through time as collapse progresses.

Chapter 8: Conclusions and further work

This thesis provides an extensive analysis of the effect of coal and mechanical stratigraphy on the properties of fault and fracture networks in the UK Carboniferous Coal Measures. A combination of detailed geological fieldwork, geological mapping at several scales of observation, and lineament mapping was used to answer four key research questions as introduced in Chapter 1. This chapter outlines the key findings of the thesis and provides recommendations for further work.

RQ1: How does subjective bias effect data collection methods used for the characterisation of fault and fracture networks? (Chapter 3, 5, 6)

To produce replicable studies it is important to understand the biases that exist in the data-collection and data analysis. This thesis investigates how biases effect the collection of fault (Chapter 6) and fracture data (Chapter 3, 4) highlighting areas where several subjective biases may strongly effect the data collected and interpretations drawn (Chapters 5 and 6).

Key Findings

1. Large, but consistent variability is observed between participants collecting fracture data from the same outcrop or field photograph using scanline techniques (i.e. participants consistently collected either a high or low volume of fractures across all experiments). This then impacts the derived network statistics (e.g. fracture trace length), which are often used to populate models for sub-surface fluid-flow or rock stability (Chapter 3).
2. Consistency and number of reported fractures did not correlate with the geological experience of the participant or the time taken to complete the scanlines, and instead it is likely due to an individual's personal characteristics (detailed vs pragmatic), and the purpose the data is collected for (Chapter 3).
3. Subjective biases may affect the way in which data is collected. Firstly, for the characteristics of a fracture network to be statistically valid, a circular scanline should aim to capture a minimum number of fractures in its area, and the radius adjusted to ensure that these conditions are met. However, to meet the necessary validity criteria, individuals who pay particular attention to small features could potentially use a circular scanline with much smaller radius (and consequently, can collect data

from smaller outcrops) than individuals who tend to dismiss small fractures. Secondly, by comparing fracture data collected in the field and from field photographs, it is suggested that if possible fracture data should be collected in the field, where the type of connections present can be examined in more detail (Chapter 3).

4. Best practice is suggested whereby the perceived fracture network is drawn out, either onto printed field photos or using a tablet computer, to minimise bias by prompting the operator to consider and report the observed trace length distribution and network topology (Chapter 3).
5. The properties vary depending on whether fractures are observed in the bed-parallel or bed-perpendicular plane. In the bed-parallel view networks are typically well connected, however, in section view joints terminate within beds (Chapter 4). The plane of observation also strongly effects the perceived fault-network (Chapters 4 and 6), with changes in lithology causing vertical restriction.
6. The connectivity and trace length characteristics of a fault or fracture network was found to be strongly affected by the plane of observation (Chapter 4, 6). In both planes there is an exposure bias towards competent lithologies (e.g. sandstone), with wave cut platforms typically comprised of bedding planes. This limits the collection of data from joints that display a wide range of orientations in surrounding incompetent layers (Chapter 4). It will also favour the collection of data from lens-forming lithologies, and not capture those whereby fault-gouge is more commonly observed (Chapter 6).
7. Flow properties of a fault-fracture network varies spatially and temporally (Chapter 5). The connectivity of a fault-fracture network at Spireslack SCM was found to drastically change through time following mineralisation and/or changes in stress orientation.
8. The faults captured at Whitley Bay were found to display predominantly dextral-strike slip geometries, with associated Riedel shears (Chapter 6). However, previous studies have interpreted many of these faults as normal faults and/or not considered how faults in the system relate to each other over multiple scales.
9. The biases towards studying normal faults likely imparts a strong bias on fault data collected in siliciclastic sediments.

10. To fully capture and correctly interpret a fault-fracture network it is important to consider: the scale of observation (Chapter 5); the plane of observation (Chapter 4, 5, 6); the age relationships and relative geometries of features that make up the network (Chapters 5 and 6); the presence and distribution of fracture/fault fill (Chapter 5 and 6); the effect of subjective biases on collected data particularly when collected as a team (Chapter 3); and the temporal evolution of the network, and how this can affect mechanical and fluid flow properties (Chapter 5).

Recommendations for further work

While this thesis has highlighted a number of subjective biases in the collection of fault and fracture data, there remains several questions as outlined below:

- Does the magnitude of variability increase or decrease when a whole fracture map is analysed, and what post-collection analysis (e.g. minimum trace length cut-offs) can be applied to improve the replicability of fracture studies?
- How do the identified differences effect up-scaled permeability estimates and which fracture attribute is most prone to propagate subjective biases?
- How do the identified biases effect the interpretation of age relationships based on the mapped features?
- How does the preference to record normal faults effect our understanding of basin evolution and stress inversions carried out in basins that have been subjected to transtension?
- How do subjective biases differ in studies which integrate fieldwork with fracture mapping from those which solely rely on remote sensing techniques?
- In addition to fault and fracture data collection, how does subjective biases effect other forms of data collection and how can its effect be quantified and limited?

RQ2: What role does lithology, sub-bed scale heterogeneity and pre-existing weaknesses play on joint network characteristics and the development of fault damage zones?

(Chapter 2, 4, 5 & 7)

It is well known that interbedded lithologies may develop a strong mechanical stratigraphy, and that this can affect faults and fractures in these lithologies. However, the majority of

work in coal measures had not considered the complex sedimentary architecture observed in coal measures (Chapter 2). This thesis investigates the effect of the following on fault and fracture networks: bed-and sub-bed scale heterogeneities (4, 5, 6), pre-existing weaknesses (Chapter 4, 5), and relative orientation of structures (Chapter 5, 6).

Key findings

1. Fluvio-deltaic successions typically contains complex stratigraphic relationships at both a bed and sub-bed scales (Chapter 2, 4). Coal constitutes less than 10% of the succession and is found in seams which do not reach more than a few meters. Coal cleats cause pre-existing weaknesses giving a weak anisotropic mechanical strength (Chapter 2). This and the typical thin bed thicknesses of other lithologies in the sequence means that a single point on a fault will be passed by multiple lithologies except small offset faults.
2. Lithology and sub-bed scale heterogeneities combine to develop a mechanical stratigraphy that strongly affects the style and properties of faults and fracture networks (Chapter 4, 5, 6). Faults with small throws can typically only be observed in single beds or sedimentary facies. Multiple small offset fault strands develop in competent lithologies that are not linked through incompetent lithologies (Chapter 5, 6, 7).
3. The stratigraphy occurs as predictable cycles, with beds containing typical lithologies and sedimentary structures. This enabled beds at Whitley Bay to be split into several lithofacies which were found to exhibit distinctive mechanical properties (Chapter 4). Characteristic properties were also observed in faults and fracture networks, which could be assessed using the lithofacies scheme (Chapter 4, 6).
4. Heterolithic sequences such as S3 and S4 displayed characteristic fracture heights that correlated to the percentage of bed-thickness in all but the thinnest beds. Within coal-bearing successions, there are an abundance of weak laminations and sedimentary structures (e.g. coal-drapes or mud-draped ripples) leading to the termination of joints within the bed. (Chapter 4). Heterolithic sequences also display wider fault-damage zones consisting of multiple anastomosing strands (Chapter 6). In both cases organic fragments, coal rip-up clasts, and channel coals were found to have a large effect on fault and fracture growth (Chapters 4, 6).

5. Because of the predictable manner of fluvio-deltaic sequences, and the strong control on the height of fractures it should be possible to use the vertical spacing of sedimentary features to inform on likely sub-surface fracture properties (Chapter 4).
6. Faults and joints in coal are strongly affected the presence and orientation of cleats. This causes the restriction of features, with individual strands abutting against favourably orientated structures (Chapter 4, 5, 6).
7. Faults at all sites rarely occurred as a single strand but instead as systematic zones of anastomosing fault strands which fit with a strike slip strain ellipse (Chapter 5, 6). Fault-zones are asymmetric, with the majority of strands occurring in the hanging wall block (Chapter 5, 6). This feature is observed over four orders of magnitude from field-site scale, down to single fault-core strands (Chapter 6).
8. The effect of small-scale strength inclusions caused by sub-bed scale sedimentary heterogeneity (e.g. mud-draped ripples) leads to the development of abundant strength concentrations within the host rock and the development of a heterogenous stress field. This increases the joint and fault intensity within these units and promotes the branching and termination of features (Chapter 4, 6, 7).
9. Favourably orientated pre-existing joints at Spirelack SCM were found to restrict the growth of faults cutting the limestone pavement (Chapter 5). The presence of only a single set of mineralised fractures highlights the temporal nature of fluid flow and provides evidence of an evolving stress state. The principle stress axis was found to rotate throughout the site, which coupled with the complex abutting relationships suggested a highly heterogeneous stress field existed during faulting.
10. Coal-measures cannot be considered a typical 'binary' mechanically layered sequence such as limestone-marls. Instead, the structure of faults in coal measures are strongly affected by: a) the lithology being faulted, b) the presence and distribution of sub-bed scale sedimentary features, c) whether multiple lithologies are cut by the fault or not, d) the presence and behaviour of shale interbeds, and/or e) the presence of pre-existing weaknesses (Chapters 2, 5, 6). Similar features are observed in anthropogenic faults related to the collapse of mine workings (Chapter 7).

Recommendations for further work

- Can the detailed topological and trace length approach used for joints in Chapter 4 be expanded to faults to gain insight into the effect of small scale structures?
- At both field sites, the proportion of coal (c. 5%) and rank were relatively low. How would the results at this study site compare to a study undertaken in a succession with thicker, higher rank coal seams?
- What is the effect of subtle changes in sedimentology in other geological settings (e.g. deep water systems) which display interbedded competent and incompetent layers and can the workflow presented in Chapter 4 be used to assess these successions?
- Can the sedimentary properties be used to inform fracture properties, in particular, height to improve predictions of sub-surface datasets?

RQ3: What are the types and spatial heterogeneity of fault rock developed in coal bearing succession, and how does this vary with displacement and different lithological juxtapositions? (Chapter 5, 6)

Key findings

1. Fault-rocks were found to develop across all three sites, with small offset faults strongly affected by the lithology cut by the fault (Chapter 5, 6). At Whitley Bay fault-rocks displayed a layered relationship, which was observed across all scales consisting of a planar PDZ, which often developed clay-rich fault gouges, followed by pods of cataclasite, fault breccia, and fault-core lenses (Chapter 6). At Spireslack SCM, this was only observed on large-offset faults and instead the behaviour of a fault was affected by the plane of observation, whether a fault cuts one or more lithologies, and/or the interaction with pre-existing features and lithology.
2. At small throws, coal was typically mineralised with a buff-orange colour mineral interpreted as ankerite (Chapter 5, 6). Small faults typically terminate within coal beds, interact with cleats, and develop conjugate zones that display evidence of multiple phases of slip. Mineralisation of the cleat network in the Muirkirk 6' Coal leads to an increase coal strength, with later reactivation effected by the presence of mineralised cleats (Chapter 5). For large faults, coal is brecciated, entrained into the fault zone as fault-core lenses, and preserved within asperities along the PDZ (Chapters 5, 6).

3. Fault-rock development was found to be lower at Spireslack SCM than Whitley Bay/Howick, with fault thickness at both sites not scaling with throw. This could be due to the large error bars on the apparent true displacement of strike-slip faults cutting shallowly dipping sediments, or that geometrical heterogeneities and development of asperities along fault strands are more important within these lithologies.
4. Across four orders of magnitude the orientation of fault-rock and subsidiary strands is not random, but instead fit a Riedel shear geometry whose orientation is controlled by the major feature for that scale of observation (Chapters 5, 6). Whitley Bay and Spireslack SCM are bounded by two larger offset regional faults, with faults between these consistent with sinistral Redial shear geometries for Spireslack SCM and dextral geometries for Whitley Bay and Howick. The development of T-shears and wide-damage zones within heterolithic units will likely promote the formation of fluid-assisted breccias.
5. Aspect ratio was found to increase towards the PDZ for a given scale of observation for clasts/lenses above 1 cm², however, below this the grinding of clasts causes aspect ratio to decrease.
6. Shale behaved in a ductile manner and was important in controlling the termination of faults, promoting the entrainment of fault-core lenses, and causing the folding of bedding towards the PDZ.
7. Organic fragments were found to be highly mobile within fault-zones and to become localised along PDZs, leading to the preservation within asperities along the PDZ (Chapter 5,6).

Recommendations for further work

- How widespread is the under-representation of strike-slip faults, and what effect will this have on basin-history models?
- Can the orientation of fault features over multiple scales be used to inform regional tectonics in areas where normal faults are misinterpreted?
- Can the normalised distance from a fault-zone be used to predict the change from lens-development and increased fracturing, to the grinding processes observed close to local PDZs at all scales?
- How do the findings compare to areas where shale behaves in a brittle manner?

RQ4: How do coal measures behave when abandoned pillar and stall mine workings collapse, and how will this affect the geothermal potential of a site? (Chapter 7)

Key findings

Flooded pillar and stall mine workings are found across much of the UK, many of which are close areas with high population density. The use of these sites for low-enthalpy mine geothermal provides great potential for a low-carbon heat source, however, the geotechnical risk associated with such targets remains largely unknown. Chapter 7 provides the first detailed characterisation of the internal structure and expands on work carried out on the collapse mechanisms of mine workings.

Key findings

1. The workings observed on the headland north of St. Mary's Island at Whitley Bay were found to consist of 8 lithofacies with distinctive lithology, orientations, stacking patterns, and structure. These lithologies display a high-clay content and lead to a succession of collapse lithologies which vary in thickness depending on the proximity to pillars.
2. Stacking patterns enabled a 5 stage model of stall collapse to be proposed, each acting to decrease the permeability of the mine. The flooding of the mine with hypersaline brines led to the cyclical (interpreted as annual) deposition of salty muds that suggests stalls were open to flow for at least 7 to 13 years prior to the final collapse of the roof closing off the system. The last section to collapse is closest to the pillar, occurring 6 cycles (years) after the rest of the workings.
3. Deformation above workings caused by the collapse occur in four distinct zones. The majority of damage occurring within 5 to 15 m above the worked seam. The dip, interaction, and termination of faults along with the intensity of deformation depends on the spacing and thickness of coal pillars, the mechanical strength of overlying units, and proximity to other stalls. Evidence of multiple collapse events occurring in a single stall is also observed in the deformation of the overlying stratigraphy.
4. Multiple collapse events recorded at both sites suggests that unlike previous models, collapse does not occur as a single event over days to weeks, but instead sections remain open to flow for years after the initial collapse.

5. Considerable drilling uncertainties exist and with up to 70% of coal left behind in some collieries there is a significant risk of a borehole intersecting a pillar. Even when a stall is intersected the stage of collapse will affect whether significant flow can be maintained. The water capacity of a potential mine geothermal site degrades through time as the roof spalls, and finally collapses.
6. This work suggests that pillar and stall workings be considered a heterogeneous, clay-rich anthropogenic layer whose properties vary through time as collapse progresses.

Recommendations for further work

- Does the well-connected fault and fracture network which overlies the workings enhance or degrade the geothermal potential of a site?
- How do the findings presented in Chapter 7 differ from observations from the UKGEOS research site, and how can field evidence be used to help de-risk potential targets?
- How does the collapse of a single seam effect the collapse of another, and does this effect the stacking patterns within the anthropogenic sedimentary layer?
- What is the permeability of the collapsed stalls, and will increased flow rates be able to displace collapsed material to create the flow path required for geothermal?
- Can the fracture map created at Spirelack SCM be restored, and used to model the temporal evolution of permeability within a collapsing pillar and stall working?

List of references

- Afşar, F., Westphal, H. and Philipp, S.L. 2014. How facies and diagenesis affect fracturing of limestone beds and reservoir permeability in limestone-marl alternations. *Marine and Petroleum Geology*. **57**, pp.418–432.
- Aggarwal, I. and Woolley, A.W. 2013. Do you see what I see? The effect of members' cognitive styles on team processes and errors in task execution. *Organizational Behavior and Human Decision Processes*. **122**(1), pp.92–99.
- Agosta, F., Alessandrini, M., Antonellini, M., Tondi, E. and Giorgioni, M. 2010. From fractures to flow: A field-based quantitative analysis of an outcropping carbonate reservoir. *Tectonophysics*. **490**(3–4), pp.197–213.
- Agosta, F. and Aydin, A. 2006. Architecture and deformation mechanism of a basin-bounding normal fault in Mesozoic platform carbonates, central Italy. *Journal of Structural Geology*. **28**(8), pp.1445–1467.
- Agosta, F., Wilson, C. and Aydin, A. 2015. The role of mechanical stratigraphy on normal fault growth across a Cretaceous carbonate multi-layer, central Texas (USA). *Italian Journal of Geosciences*. **134**(3), pp.423–441.
- Ajalloeian, R. and Lashkaripour, G.R. 2000. Strength anisotropies in mudrocks. *Bulletin of Engineering Geology and the Environment*. **59**(3), pp.195–199.
- Al-Awadi, A.M., Haines, T., Bertouche, M., Bonin, A., Fuchs, M., Deville De Periere, M., Challa, P. and Zaidi, S. 2017. Predictability of the Sedimentological Make-Up and Reservoir Quality in the Maaddud Formation Using FMI Logs - A Case Study from a North Kuwait Field *In: SPE Kuwait Oil & Gas Show and Conference*. Society of Petroleum Engineers.
- Allmendinger, R.W., Cardozo, N. and Fisher, D.M. 2013. *Structural Geology Algorithms: Vectors and Tensors*. Cambridge, UK: Cambridge University Press.
- Alsop, G.I., Marco, S., Weinberger, R. and Levi, T. 2016. Sedimentary and structural controls on seismogenic slumping within mass transport deposits from the Dead Sea Basin. *Sedimentary Geology*. **344**, pp.71–90.

- Andrews, B.J., Roberts, J.J., Shipton, Z.K., Bigi, S., Tartarello, M.C. and Johnson, G.O. 2019. How do we see fractures? Quantifying subjective bias in fracture data collection. *Solid Earth*. **10**(2), pp.487–516.
- Armstrong, S.J., Cools, E. and Sadler-Smith, E. 2012. Role of Cognitive Styles in Business and Management: Reviewing 40 Years of Research. *International Journal of Management Reviews*. **14**(3), pp.238–262.
- Aydin, A. 2000. Fractures, faults, and hydrocarbon entrapment, migration and flow. *Marine and Petroleum Geology*. **17**(7), pp.797–814.
- Aydin, A. and Basu, A. 2005. The Schmidt hammer in rock material characterization. *Engineering Geology*. **81**(1), pp.1–14.
- Aydin, A. and Eyal, Y. 2002. Anatomy of a normal fault with shale smear: Implications for fault seal. *AAPG Bulletin*. **86**(8), pp.1367–1381.
- Bahat, D. and Engelder, T. 1984. Surface morphology on cross-fold joints of the Appalachian Plateau, New York and Pennsylvania. *Tectonophysics*. **104**(3–4), pp.299–313.
- Bai, T. and Pollard, D.D. 2000. Fracture spacing in layered rocks: A new explanation based on the stress transition. *Journal of Structural Geology*. **22**(1), pp.43–57.
- Bailey, W.R., Walsh, J.J. and Manzocchi, T. 2005. Fault populations, strain distribution and basement fault reactivation in the East Pennines Coalfield, UK. *Journal of Structural Geology*. **27**(5), pp.913–928.
- Banks-Sills, L. and Schwartz, J. 2002. Fracture testing of Brazilian disk sandwich specimens. *International Journal of Fracture*. **118**(3), pp.191–209.
- Baptie, B. 2010. Seismogenesis and state of stress in the UK. *Tectonophysics*. **482**(1–4), pp.150–159.
- Bartlett, W.L., Friedman, M. and Logan, J.M. 1981. Experimental folding and faulting of rocks under confining pressure Part IX. Wrench faults in limestone layers. *Tectonophysics*. **79**(3–4), pp.255–277.
- Bastesen, E. and Braathen, A. 2010. Extensional faults in fine grained carbonates - analysis of fault core lithology and thickness-displacement relationships. *Journal of Structural Geology*. **32**(11), pp.1609–1628.

- Beamish, B.B. and Crosdale, P.J. 1998. Instantaneous outbursts in underground coal mines: an overview and association with coal type. *International Journal of Coal Geology*. **35**(1–4), pp.27–55.
- Becker, A. and Gross, M.R. 1996. Mechanism for joint saturation in mechanically layered rocks: an example from southern Israel. *Tectonophysics*. **257**(2–4), pp.223–237.
- Beidinger, A. and Decker, K. 2011. 3D geometry and kinematics of the Lasee flower structure: Implications for segmentation and seismotectonics of the Vienna Basin strike-slip fault, Austria. *Tectonophysics*. **499**(1–4), pp.22–40.
- Belayneh, M.W., Matthai, S.K., Blunt, M.J., Rogers, S.F., Matthäi, S.K., Blunt, M.J. and Rogers, S.F. 2009. Comparison of deterministic with stochastic fracture models in water-flooding numerical simulations. *AAPG Bulletin*. **93**(11), pp.1633–1648.
- Bell, F.G. 1986. Location of abandoned workings in coal seams. *Bulletin of the International Association of Engineering Geology*. **33**(1), pp.123–132.
- Bell, F.G. 1988. The history and techniques of coal mining and the associated effects and influence on construction. *Bulletin of the Association of Engineering Geologists*. **25**(4), pp.471–504.
- Bell, F.G. and Donnelly, L.J. 2006. *Mining and its Impact on the Environment*. Oxon: Taylor & Francis.
- Bense, V. and Van Balen, R. 2003. Hydrogeological aspects of fault zones on various scales in the Roer Valley Rift System *In: Journal of Geochemical Exploration*. Elsevier B.V., pp.317–320.
- Bense, V.F. and Balen, R.V. 2004. The effect of fault relay and clay smearing on groundwater flow patterns in the Lower Rhine Embayment. *Basin Research*. **16**, pp.397–411.
- Bense, V.F., Gleeson, T., Loveless, S.E., Bour, O. and Scibek, J. 2013. Fault zone hydrogeology. *Earth-Science Reviews*. **127**, pp.171–192.
- Bense, V.F., Shipton, Z.K., Kremer, Y. and Kampman, N. 2016. Fault zone hydrogeology: introduction to the special issue. *Geofluids*. **16**(4), pp.655–657.
- Berg, S.S. and Skar, T. 2005. Controls on damage zone asymmetry of a normal fault zone:

- Outcrop analyses of a segment of the Moab fault, SE Utah. *Journal of Structural Geology*. **27**(10), pp.1803–1822.
- Besly, B.M. and Fielding, C.R. 1989. Palaeosols in Westphalian coal-bearing and red-bed sequences, central and northern England. *Palaeogeography, Palaeoclimatology, Palaeoecology*. **70**(4), pp.303–330.
- Bhutto, A.W., Bazmi, A.A. and Zahedi, G. 2013. Underground coal gasification: From fundamentals to applications. *Progress in Energy and Combustion Science*. **39**(1), pp.189–214.
- Bigi, S., Battaglia, M., Alemanni, A., Lombardi, S., Campana, A., Borisova, E. and Loizzo, M. 2013. CO₂ flow through a fractured rock volume: Insights from field data, 3D fractures representation and fluid flow modeling. *International Journal of Greenhouse Gas Control*. **18**, pp.183–199.
- Bigi, S., Marchese, M., Meda, M., Nardon, S. and Franceschi, M. 2015. Discrete fracture network of the Latemar carbonate platform. *Italian Journal of Geosciences*. **134**(3), pp.474–494.
- Billi, A., Salvini, F. and Storti, F. 2003. The damage zone-fault core transition in carbonate rocks: Implications for fault growth, structure and permeability. *Journal of Structural Geology*. **25**(11), pp.1779–1794.
- Bisdom, K., Nick, H.M. and Bertotti, G. 2017. An integrated workflow for stress and flow modelling using outcrop-derived discrete fracture networks. *Computers and Geosciences*. **103**, pp.21–35.
- Bluck, B.J. 1984. Pre-Carboniferous history of the Midland Valley of Scotland. *Transactions of the Royal Society of Edinburgh: Earth Sciences*. **75**(2), pp.275–295.
- Bond, C.E., Gibbs, A.D., Shipton, Z.K. and Jones, S. 2007. What do you think this is? ‘Conceptual uncertainty’ In geoscience interpretation. *GSA Today*. **17**(11), pp.4–10.
- Bond, C.E., Johnson, G. and Ellis, J.F. 2015. Structural model creation: the impact of data type and creative space on geological reasoning and interpretation. *Geological Society, London, Special Publications*. **421**(1), pp.83–97.
- Bonnet, E., Bour, O., Odling, N.E., Davy, P., Main, I., Cowie, P. and Berkowitz, B. 2001.

- Scaling of fracture systems in geological media. *Reviews of geophysics*. **39**(3), pp.347–383.
- Broadhurst, F.M. and France, A.A. 1986. Time represented by coal seams in the coal measures of England. *International Journal of Coal Geology*. **6**(1), pp.43–54.
- Browne, M.A.E., Dean, M.T., Hall, I.H.S., McAdam, A.D., Monro, S.K. and Chisholm, J.I. 1999. *A lithostratigraphical framework for the Carboniferous rocks of the Midland Valley of Scotland*. Keyworth, Nottingham: British Geological Survey.
- Browne, M.A.E. and Monro, S.K. 1987. Evolution of the coal basins of Central Scotland *In: Congrès International de Stratigraphie et de Géologie du Carbonifère*. Beijing: Nanjing University Press, Nanjing, pp.1–19.
- Bruce, B. and Bowers, G. 2002. Pore pressure terminology. *Leading Edge (Tulsa, OK)*. **21**(2), pp.170–173.
- Bruyn, F.G. and Bell, D.I.A. 1999. Subsidence problems due to abandoned pillar workings in coal seams. *Bulletin of Engineering Geology and the Environment*. **57**(3), pp.225–237.
- BSi 2015. *BS 5930 - COP for ground investigations*. BSi Standards Ltd.
- Bu, W. 2013. Research on Effect of Fault Dip on Fault Activation and water inrush of coal floor. *Electronic Journal of Geotechnical Engineering*. **18**(L), pp.2323–2336.
- Bubeck, A., Walker, R.J., Healy, D., Dobbs, M. and Holwell, D.A. 2017. Pore geometry as a control on rock strength. *Earth and Planetary Science Letters*. **457**, pp.38–48.
- Bullock, R.J., De Paola, N., Holdsworth, R.E. and Trabucho-Alexandre, J. 2014. Lithological controls on the deformation mechanisms operating within carbonate-hosted faults during the seismic cycle. *Journal of Structural Geology*. **58**, pp.22–42.
- Burke, S.P. and Younger, P.L. 2000. Groundwater rebound in the South Yorkshire coalfield: a first approximation using the GRAM model. *Quarterly Journal of Engineering Geology and Hydrogeology*. **33**(2), pp.149–160.
- Burke, T. 2002. The use in Scotland of flooded mine workings as a source of geothermal energy. *Geothermal Energy in Underground Mines.*, pp.191–200.
- Burns, K.L. and Brown, G.H. 1978. The human perception of geological lineaments and

- other discrete features in remote sensing imagery: Signal strengths, noise levels and quality. *Remote Sensing of Environment*. **7**(2), pp.163–176.
- Burns, K.L., Shepherd, J. and Ryde, N. 1976. Reproducibility of Geological Lineaments and Other Discrete Features Interpreted from Imagery : Measurement by a Coefficient of Association. . **301**, pp.267–301.
- Busse, J., de Dreuzy, J.R., Galindo Torres, S., Bringemeier, D. and Scheuermann, A. 2017. Image processing based characterisation of coal cleat networks. *International Journal of Coal Geology*. **169**, pp.1–21.
- Bustin, R.M. 1983. Heating during thrust faulting in the rocky mountains: friction or fiction? *Tectonophysics*. **95**(3–4), pp.309–328.
- Bustin, R.M. 1986. Organic maturity of Late Cretaceous and Tertiary coal measures, Canadian Arctic Archipelago. *International Journal of Coal Geology*. **6**(1).
- Bustin, R.M. 1982. Striated conical structures and related fractures in bituminous coal of the southern Canadian Rocky Mountains. *International Journal of Coal Geology*. **2**(1), pp.1–16.
- Byerlee, J. 1978. Friction of Rocks *In: Rock friction and earthquake prediction*. Birkhäuser, Basel.: Birkhauser Verlag, B I, pp.615–626.
- Cai, Y., Liu, D., Pan, Z., Yao, Y. and Li, C. 2015. Mineral occurrence and its impact on fracture generation in selected Qinshui Basin coals: An experimental perspective. *International Journal of Coal Geology*. **150–151**, pp.35–50.
- Caine, J.S., Evans, J.P. and Forster, C.B. 1996. Fault zone architecture and permeability structure. *Geology*. **24**(11), pp.1025–1028.
- Cairncross, B., Stanistreet, I.G., McCarthy, T.S., Ellery, W.N., Ellery, K. and Grobicki, T.S.A. 1988. Palaeochannels (stone-rolls) in coal seams: Modern analogues from fluvial deposits of the Okavango Delta, Botswana, southern Africa. *Sedimentary Geology*. **57**(1–2), pp.107–118.
- Campbell, R.H. 1955. Developments in the Scottish Pig Iron Trade, 1844–1848. *The Journal of Economic History*. **15**(3), pp.209–226.
- Cao, Y., Davis, A., Li, R., Liu, X. and Zhang, Y. 2003. The influence of tectonic deformation on

- some geochemical properties of coals—a possible indicator of outburst potential. *International Journal of Coal Geology*. **53**(2), pp.69–79.
- Cao, Y., He, D. and Glick, D.C. 2001. Coal and gas outbursts in footwalls of reverse faults. *International Journal of Coal Geology*. **48**, pp.47–63.
- Cao, Y., Mitchell, G.D., Davis, A. and Wang, D. 2000. Deformation metamorphism of bituminous and anthracite coals from China. *International Journal of Coal Geology*. **43**(1–4), pp.227–242.
- Caputo, R. 1995. Evolution of orthogonal sets of coeval extension joints. *Terra Nova*. **7**(5), pp.479–490.
- Caputo, R. and Hancock, P.L. 1998. Crack-jump mechanism and its implications for stress cyclicity during extension fracturing. *Journal of Geodynamics*. **27**(1), pp.45–60.
- Cardozo, N. and Allmendinger, R.W. 2013. Spherical projections with OSXStereonet. *Computers and Geosciences*. **51**, pp.193–205.
- Carter, P., Jarman, D. and Sneddon, M. 1981. Mining Subsidence in Bathgate, a Town Study *In: J. D. Gredds, ed. Proceedings of the Second International Conference on Ground Movements and Structures*. Cardiff: Pentech Press, London, pp.101–124.
- Cartwright, J.A., Trudgill, B.D. and Mansfield, C.S. 1995. Fault growth by segment linkage: an explanation for scatter in maximum displacement and trace length data from the Canyonlands Grabens of SE Utah. *Journal of Structural Geology*. **17**(9), pp.1319–1326.
- Carvell, J., Blenkinsop, T., Clarke, G. and Tonelli, M. 2014. Scaling, kinematics and evolution of a polymodal fault system: Hail Creek Mine, NE Australia. *Tectonophysics*. **632**(C), pp.138–150.
- Chadwick, B.A., Holliday, D.W., Holloway, S., Hulbert, A.G. and Lawrence, D.J.D. 1995. The structure and evolution of the Northumberland-Solway Basin and adjacent areas. *London:HMSO*.
- Chadwick, R.A. and Holliday, D.W. 1991. Deep crustal structure and carboniferous basin development within the iapetus convergence zone, northern England. *Journal of the Geological Society*. **148**(1), pp.41–53.
- Chadwick, R.A., Holliday, D.W., Holloway, S. and Hulbert, A.G. 1993. The evolution and

- hydrocarbon potential of the Northumberland-Solway Basin *In: Geological Society, London, Petroleum Geology Conference series.*, pp.717–726.
- Chan, D. 1996. Cognitive misfit of problem-solving style at work: A facet of person-organization fit. *Organizational Behavior and Human Decision Processes*. **68**(3), pp.194–207.
- Chang, C. and Haimson, B. 2000. True triaxial strength and deformability of the German Continental Deep Drilling Program (KTB) deep hole amphibolite. *Journal of Geophysical Research: Solid Earth*. **105**(B8), pp.18999–19013.
- Chen, C.S., Pan, E. and Amadei, B. 1998. Determination of deformability and tensile strength of anisotropic rock using Brazilian tests. *International Journal of Rock Mechanics and Mining Sciences*. **35**(1), pp.43–61.
- Chen, K.P. 2011. A new mechanistic model for prediction of instantaneous coal outbursts - Dedicated to the memory of Prof. Daniel D. Joseph. *International Journal of Coal Geology*. **87**(2), pp.72–79.
- Chen, L., Feng, X., Xie, W. and Xu, D. 2016. Prediction of water-inrush risk areas in process of mining under the unconsolidated and confined aquifer: a case study from the Qidong coal mine in China. *Environmental Earth Sciences*. **75**(8), p.706.
- Cheng, M.M., Lockett, P.F. and Schulz, A.K. 2003. The Effects of Cognitive Style Diversity on Decision-Making Dyads: An Empirical Analysis in the Context of a Complex Task. *Behavioral Research in Accounting*. **15**(1), pp.39–62.
- Cherubini, Y., Cacace, M., Scheck-Wenderoth, M. and Noack, V. 2014. Influence of major fault zones on 3-D coupled fluid and heat transport for the Brandenburg region (NE German Basin). *Geothermal Energy Science*. **2**(1), pp.1–20.
- Chesnaux, R., Allen, D.M. and Jenni, S. 2009. Regional fracture network permeability using outcrop scale measurements. *Engineering Geology*. **108**(3–4), pp.259–271.
- Chester, F.M. and Chester, J.S. 1998. Ultracataclasite structure and friction processes of the Punchbowl fault, San Andreas system, California. *Tectonophysics*. **295**(1–2), pp.199–221.
- Chester, F.M., Evens, J.P. and Beigel, R.L. 1993. internal Structure and Weakening

- Mechanisms of the San Andreas Fault. *Journal of Geophysical Research*. **98**, pp.771–786.
- Chester, J.S. 2003. Mechanical stratigraphy and fault-fold interaction, Absaroka thrust sheet, Salt River Range, Wyoming. *Journal of Structural Geology*. **25**(7), pp.1171–1192.
- Childs, C., Manzocchi, T., Walsh, J.J., Bonson, C.G., Nicol, A. and Schöpfer, M.P.J. 2009. A geometric model of fault zone and fault rock thickness variations. *Journal of Structural Geology*. **31**(2), pp.117–127.
- Childs, C., Nicol, A., Walsh, J.J. and Watterson, J. 1996. Growth of vertically segmented normal faults. *Journal of Structural Geology*. **18**(12), pp.1389–1397.
- Chilton, M.A., Hardgrave, B.C. and Armstrong, D.J. 2005. Person-job cognitive style fit for software developers: The effect on strain and performance. *Journal of Management Information Systems*. **22**(2), pp.193–226.
- Cho, J.W., Kim, H., Jeon, S. and Min, K.B. 2012. Deformation and strength anisotropy of Asan gneiss, Boryeong shale, and Yeoncheon schist. *International Journal of Rock Mechanics and Mining Sciences*. **50**, pp.158–169.
- Choi, J.H., Edwards, P., Ko, K. and Kim, Y.S. 2016. Definition and classification of fault damage zones: A review and a new methodological approach. *Earth-Science Reviews*. **152**, pp.70–87.
- Cilona, A., Aydin, A., Likerman, J., Parker, B. and Cherry, J. 2016. Structural and statistical characterization of joints and multi-scale faults in an alternating sandstone and shale turbidite sequence at the Santa Susana Field Laboratory: Implications for their effects on groundwater flow and contaminant transport. *Journal of Structural Geology*. **85**, pp.95–114.
- Close, J.C. and Mavor, M.J. 1991. Influence of Coal Composition and Rank on Fracture Development in Fruitland Coal Gas Reservoirs of San Juan Basin *In*: S. Schwochow, D. K. Murray and M. F. Fahy, eds. *Coalbed Methane of Western North America*. Field Conf.: Rocky Mountain Association of Geologists, pp.109–121.
- Colback, P.S.B. and Wiid, B.L. 1965. The influence of moisture content on the compressive strength of rocks. *Geophysics*. **0**.

- Coleman, J.M. and Prior, D.B. 1982. Deltaic Environments of Deposition *In: Sandstone Depositional Environments.*, pp.139–178.
- Collettini, C., Niemeijer, A., Viti, C. and Marone, C. 2009. Fault zone fabric and fault weakness. *Nature*. **462**(7275), pp.907–910.
- Collier, R.E.L. 1989. Tectonic evolution of the Northumberland Basin; the effects of renewed extension upon an inverted extensional basin. *Journal - Geological Society (London)*. **146**(6), pp.981–989.
- Comerford, A., Fraser-Harris, A., Johnson, G. and McDermott, C.I. 2018. Controls on geothermal heat recovery from a hot sedimentary aquifer in Guardbridge, Scotland: Field measurements, modelling and long term sustainability. *Geothermics*. **76**, pp.125–140.
- Cooke, M.L. 1997. Predicting fracture localization in folded strata from mechanical stratigraphy and fold shape: case study of East Kaibab Monocline, Utah. *International journal of rock mechanics and mining sciences & geomechanics abstracts*. **34**(3–4), p.351.
- Coolen, J.M. 2003. Coal mining along the Warfield Fault, Mingo County, West Virginia: A tale of ups and downs. *International Journal of Coal Geology*. **54**(3–4), pp.193–207.
- Cope, J.C.W., Ingham, J.K. and Rawson, P.F. 1992. Atlas of palaeogeography and lithofacies. *Geological Society of London Memoir*. **No. 13**.
- Corbett, K., Friedman, M. and Spang, J. 1987. Fracture Development and Mechanical Stratigraphy of Austin Chalk, Texas. *AAPG Bulletin*. **71**(1), pp.17–28.
- Cowie, P.A. and Scholz, C.H. 1992. Displacement-length scaling relationship for faults: data synthesis and discussion. *Journal of Structural Geology*. **14**(10), pp.1149–1156.
- Crider, J.G. and Peacock, D.C.P. 2004. Initiation of brittle faults in the upper crust: A review of field observations. *Journal of Structural Geology*. **26**(4), pp.691–707.
- Culshaw, M.G., Mccann, D.M., Donnelly, L.J., Culshaw, M.G., Mccann, D.M. and Donnelly, L.J. 2013. Mining Technology Impacts of abandoned mine workings on aspects of urban development Impacts of abandoned mine workings on aspects of urban development. *Mining Technology*. **109**(3), pp.132-139

- Currie, J.B., Patnode, H.W. and Trump, R.P. 1962. Development of folds in sedimentary strata. *Bulletin of the Geological Society of America*. **73**(6), pp.655–673.
- Daunton, M.J. 1981. Down the pit: work in the Great Northern and South Wales coalfields, 1870-1914. *The Economic History Review*. **34**(4), pp.578–597.
- Davatzes, N.C. and Aydin, A. 2005. Distribution and nature of fault architecture in a layered sandstone and shale sequence: An example from the Moab fault, Utah. *AAPG Memoir*. **85**, pp.153–180.
- Davis, A. 1972. Carboniferous rocks of the Muirkirk, Gass Water and Glenmuir areas of Ayrshire. *Bull Geol Surv GB*. **40**, pp.1–49.
- Dawers, N.H. and Anders, M.H. 1995. Displacement-length scaling and fault linkage. *Journal of Structural Geology*. **17**(5).
- Dawers, N.H., Anders, M.H. and Scholz, C.H. 1993. Growth of normal faults: Displacement-length scaling. *Geology*. **21**, pp.1107–1110.
- Dawson, G.K.W. and Esterle, J.S. 2010. Controls on coal cleat spacing. *International Journal of Coal Geology*. **82**(3–4), pp.213–218.
- Dawson, G.K.W., Golding, S.D., Esterle, J.S. and Massarotto, P. 2012. Occurrence of minerals within fractures and matrix of selected Bowen and Ruhr Basin coals. *International Journal of Coal Geology*. **94**, pp.150–166.
- Dean, M.T., Browne, M.A.E., Waters, C.N. and Powell, J.H. 2011. A lithostratigraphical framework for the Carboniferous successions of northern Great Britain (onshore). *British Geological Survey Research Report*. **RR/10/07**, p.174.
- Dearman, W.R., Money, M.S., Strachan, A., Coffey, J.R. and Marsden, A. 2000. A regional engineering geological map of the Tyne and Wear County, NE England. *Bulletin of the International Association of Engineering Geology*. **19**(1), pp.5–17.
- Deb, D. and Choi, S.O. 2006. Analysis of sinkhole occurrences over abandoned mines using fuzzy reasoning: a case study. *Geotechnical & Geological Engineering*. **24**(5), pp.1243–1258.
- Dehler, W. and Labuz, J.F. 2007. Stress Path Testing of an Anisotropic Sandstone. *Journal of Geotechnical and Geoenvironmental Engineering*. **133**(1), pp.116–119.

- Delogkos, E., Childs, C., Manzocchi, T. and Walsh, J.J. 2018. The nature and origin of bed-parallel slip in Kardias Mine, Ptolemais Basin, Greece. *Journal of Structural Geology*. **113**, pp.115–133.
- Delogkos, E., Childs, C., Manzocchi, T., Walsh, J.J. and Pavlides, S. 2017. The role of bed-parallel slip in the development of complex normal fault zones. *Journal of Structural Geology*. **97**, pp.199–211.
- Delogkos, E., Manzocchi, T., Childs, C., Sachanidis, C., Barbas, T., Schoepfer, M.P.J., Schoepfer, S., Chatzipetros, A., Pavlides, S. and Walsh, J.J. 2017. Throw partitioning across normal fault zones in the Ptolemais Basin, Greece In: C Childs, R. E. Holdsworth, C. A. L. Jackson, T. Manzocchi, J.J. Walsh and G. Yeilding, eds. *The Geometry and Growth of Normal Faults*. Geology Society, London, Special Publications, pp.333–353.
- Dershowitz, W., Hermanson, J., Follin, S. and Mauldon, M. 2000. Fracture intensity measurements in 1-D, 2-D, and 3-D at Äspö, Sweden In: *4th North American Rock Mechanics Symposium*. Seattle: American Rock Mechanics Association.
- Dershowitz, W.S. and Einstein, H.. 1988. Characterizing Rock Joint Geometry with Joint System Models. *Rock Mechanics and Rock Engineering*. **21**(1), pp.21–51.
- Dickinson, J.L., Zuckerberg, B. and Bonter, D.N. 2010. Citizen Science as an Ecological Research Tool: Challenges and Benefits. *Annual Review of Ecology, Evolution, and Systematics*. **41**(1), pp.149–172.
- Van Dijk, J.P., Bello, M., Toscano, C., Bersani, A. and Nardon, S. 2000. Tectonic model and three-dimensional fracture network analysis of Monte Alpi (southern Apennines). *Tectonophysics*. **324**(4), pp.203-237.
- Dochartaigh, B.É.Ó. 2004. The Physical properties of the Upper Devonian/Lower Carboniferous aquifer in Fife. *British Geological Survey Research Report*. **IR/04/003**.
- Dochartaigh, B.É.Ó., Macdonald, A.M., Fitzsimons, V. and Ward, R. 2015. Scotland's aquifers and groundwater bodies. *British Geological Survey Research Report*. **OR/15/028**, p.63.
- Donnelly, L.J. 2006. A review of coal mining induced fault reactivation in Great Britain. *Quarterly Journal of Engineering Geology and Hydrogeology*. **39**, pp.5–50.
- Donnelly, L.J., Culshaw, M.G. and Bell, F.G. 2008. Longwall mining-induced fault reactivation

- and delayed subsidence ground movement in British coalfields. *Quarterly Journal of Engineering Geology and Hydrogeology*. **41**(3), pp.301–314.
- Donnelly, L.J., Culshaw, M.G., Bell, F.G. and Tragheim, D. 2009. Ground deformation caused by fault reactivation: some examples *In: The 10th IAEG International Congress*. Nottingham, UK, pp.1–13.
- Doyle, A.C. and Paget, S. 1892. *The Adventure of Silver Blaze* (M. McLaughlin & M. Einisman, eds.). Scotland Yard Bookstore.
- Dunham, J., Rieman, B. and Davis, K. 2004. Sources and Magnitude of Sampling Error in Redd Counts for Bull Trout. *North American Journal of Fisheries Management*. **21**(2), pp.343–352.
- Edmunds, R., Hunt, G.W. and Wadee, M.A. 2006. Parallel folding in multilayered structures. *Journal of the Mechanics and Physics of Solids*. **54**(2), pp.384–400.
- Edmunds, W.M. 1975. Geochemistry of brines in the Coal Measures of north east England *In: Transactions of the Institution of mining and Metallurgy (Section B: Applied Earth Sciences)*, **84**, pp.39–52.
- Eichhubl, P., Davatzes, N.C. and Becker, S.P. 2009. Structural and diagenetic control of fluid migration and cementation along the Moab fault, Utah. *AAPG Bulletin*. **93**(5), pp.653–681.
- Eidelman, A. and Reches, Z. 1992. Fractured pebbles - a new stress indicator. *Geology*. **20**(4), pp.307–310.
- Ellen, R., Browne, M.A., Mitten, A., Clarke, S.M., Leslie, A.G. and Callaghan, E. 2019. Sedimentology, architecture and depositional setting of the fluvial Spireslack Sandstone of the Midland Valley, Scotland: insights from the Spireslack surface coal mine. *Geological Society, London, Special Publications*. **488**, pp.SP488-2.
- Ellen, R., Callaghan, E., Leslie, A.G. and Browne, M.A.E. 2016. The rocks of Spireslack surface coal mine and its subsurface data: an introduction. *British Geological Survey Research Report*. **OR/16/053**, p.38.
- Elliott, T. 1989. Deltaic systems and their contribution to an understanding of basin-fill successions. *Geological Society Special Publication*. **41**, pp.3–10.

- Espinoza, D.N., Shovkun, I., Makni, O. and Lenoir, N. 2016. Natural and induced fractures in coal cores imaged through X-ray computed microtomography - Impact on desorption time. *International Journal of Coal Geology*. **154**, pp.165–175.
- Evans, J.P. 1990. Thickness-displacement relationships for fault zones. *Journal of Structural Geology*. **12**(8), pp.1061–1065.
- Færseth, R.B. 2006. Shale smear along large faults: Continuity of smear and the fault seal capacity. *Journal of the Geological Society*. **163**(5), pp.741–751.
- Færseth, R.B., Johnsen, E. and Sperrevik, S. 2007. Methodology for risking fault seal capacity: Implications of fault zone architecture. *AAPG Bulletin*. **91**(9), pp.1231–1246.
- Faulkner, D.R., Jackson, C.A.L., Lunn, R.J., Schlische, R.W., Shipton, Z.K., Wibberley, C.A.J. and Withjack, M.O. 2010. A review of recent developments concerning the structure, mechanics and fluid flow properties of fault zones. *Journal of Structural Geology*. **32**(11), pp.1557–1575.
- Faulkner, D.R., Lewis, A.C. and Rutter, E.H. 2003. On the internal structure and mechanics of large strike-slip fault zones: Field observations of the Carboneras fault in southeast Spain. *Tectonophysics*. **367**(3-4), pp.235–251.
- Faulkner, D.R., Mitchell, T.M., Healy, D. and Heap, M.J. 2006. Slip on ‘weak’ faults by the rotation of regional stress in the fracture damage zone. *Nature*. **444**(7121), pp.922–925.
- Faulkner, D.R., Mitchell, T.M., Jensen, E. and Cembrano, J. 2011. Scaling of fault damage zones with displacement and the implications for fault growth processes. *Journal of Geophysical Research*. **116**(B5), p.B05403.
- Ferrill, D. a. and Morris, A.P. 2003. Dilational normal faults. *Journal of Structural Geology*. **25**(2), pp.183–196.
- Ferrill, D.A., McGinnis, R.N., Morris, A.P. and Smart, K.J. 2012. Hybrid failure: Field evidence and influence on fault refraction. *Journal of Structural Geology*. **42**(9), pp.140–150.
- Ferrill, D.A., McGinnis, R.N., Morris, A.P., Smart, K.J., Sickmann, Z.T., Bentz, M., Lehrmann, D. and Evans, M.A. 2014. Control of mechanical stratigraphy on bed-restricted jointing and normal faulting: Eagle Ford Formation, south-central Texas. *AAPG Bulletin*. **98**(11),

pp.2477–2506.

Ferrill, D.A. and Morris, A.P. 2003. Dilational normal faults. *Journal of Structural Geology*. **25**(2), pp.183–196.

Ferrill, D.A. and Morris, A.P. 2008. Fault zone deformation controlled by carbonate mechanical stratigraphy, Balcones fault system, Texas. *AAPG Bulletin*. **92**(3), pp.359–380.

Ferrill, D.A., Morris, A.P., McGinnis, R.N., Smart, K.J., Wigginton, S.S. and Hill, N.J. 2017. Mechanical stratigraphy and normal faulting. *Journal of Structural Geology*. **94**(1), pp.275–302.

Fielding, Christopher R. 1984. A coal depositional model for the Durham Coal Measures of NE England. *Journal of the Geological Society*. **141**, pp.919–931.

Fielding, C.R. 1985. Coal depositional models and the distinction between alluvial and delta plain environments. *Sedimentary Geology*. **42**(1–2), pp.41–48.

Fielding, C.R. 1982. *Sedimentology and stratigraphy of the Durham coal measures, and comparisons with other British coalfields*. Durham University.

Fielding, C.R. 1986a. The anatomy of a coal seam split, Durham coalfield, Northeast England. *Geological Journal*. **21**(1), pp.45–57.

Fielding, C.R. 1986b. The anatomy of a coal seam split, Durham coalfield, Northeast England. *Geological Journal*. **21**(1), pp.45–57.

Fielding, C.R. 1984. Upper delta plain lacustrine and fluviolacustrine facies from the Westphalian of the Durham coalfield, NE England. *Sedimentology*. **31**(4), pp.547–567.

Finkbeiner, T. and Zoback, M. 2001. Stress, pore pressure, and dynamically constrained hydrocarbon columns in the South Eugene Island 330 field, northern Gulf of Mexico. *AAPG Bulletin*. **85**(6), pp.1007-1031.

Fischer, M.P. and Jackson, P.B. 1999. Stratigraphic controls on deformation patterns in fault-related folds: A detachment fold example from the Sierra Madre Oriental, northeast Mexico. *Journal of Structural Geology*. **21**(6), pp.613–633.

Forgeron, S., MacKenzie, B. and Macpherson, K. 1986. Effects of geological features on coal

- mining, Sydney Coalfield, Nova Scotia. *Bulletin Canadian Institute Mining*. **79**, pp.97–87.
- Fossen, H. and Rotevatn, A. 2016. Fault linkage and relay structures in extensional settings- A review. *Earth-Science Reviews*. **154**, pp.14–28.
- Fowler, P. and Gayer, R.A. 1999. The association between tectonic deformation , inorganic composition and coal rank in the bituminous coals from the South Wales coalfield , United Kingdom. *International Journal of Coal Geology*. **42**(1), pp.1–31.
- Francis, E.H. 1991. Carboniferous: in CRAIG In: *The Geology of Scotland*. Edinburgh: Scottish Academic Press, pp.253–296.
- Frodsham, K. and Gayer, R.A. 1999. The impact of tectonic deformation upon coal seams in the South Wales coalfield, UK. *International Journal of Coal Geology*. **38**(3–4), pp.297–332.
- Fuller, L.R. and Kaplan, S.E. 2004. A Note about the Effect of Auditor Cognitive Style on Task Performance. *Behavioral Research in Accounting*. **16**(1), pp.131–143.
- Gabrielsen, R.H. and Braathen, A. 2014. Models of fracture lineaments - Joint swarms, fracture corridors and faults in crystalline rocks, and their genetic relations. *Tectonophysics*. **628**, pp.26–44.
- Gabrielsen, R.H., Braathen, A., Kjemperud, M. and Valdresbraten, M.L.R. 2016. The geometry and dimensions of fault-core lenses. *Geological Society, London, Special Publications*. **439**, pp.1–21.
- Gale, J.J. 2004. Using Coal Seams for CO₂ Sequestration. *Geologica Belgica*. **7**(3–4), pp.99–103.
- Galloway, R.L. 1898. *Annals of Coal Mining and the Coal Trade Vol 1*. (C. Guardian, ed.). London.
- Gamson, P.D., Beamish, B.B. and Johnson, D.P. 1993. Coal microstructure and micropermeability and their effects on natural gas recovery. *Fuel*. **72**(1), pp.87–99.
- Gao, F., Kang, H. and Wu, Y. 2016. Experimental and numerical study on the effect of calcite on the mechanical behaviour of coal. *International Journal of Coal Geology*. **158**, pp.119–128.

- Gao, R., Yan, H., Ju, F., Mei, X. and Wang, X. 2018. Influential factors and control of water inrush in a coal seam as the main aquifer. *International Journal of Mining Science and Technology*. **28**(2), pp.187–193.
- Garland, C.R., Haughton, P., King, R.F. and Moulds, T.P. 1999. Capturing reservoir heterogeneity in a sand-rich submarine fan, Miller Field *In: Petroleum Geology Conference Proceedings.*, pp.1199–1208.
- Garrard, G.F.. and Taylor, R.K. 1988. Collapse mechanisms of shallow coal-mine workings from field measurements. *Geological Society, London, Engineering Geology Special Publications*. **5**(1), pp.181–192.
- Gautschi, A. 2001. Hydrogeology of a fractured shale (Opalinus Clay): Implications for deep geological disposal of radioactive wastes. *Hydrogeology Journal*. **9**(1), pp.97–107.
- Gee, D., Bateson, L., Sowter, A., Grebby, S., Novellino, A., Cigna, F., Marsh, S., Banton, C. and Wyatt, L. 2017. Ground Motion in Areas of Abandoned Mining : Application of the Intermittent SBAS (ISBAS) to the. *Geosciences*. **7**(3), pp.1–26.
- van Gent, H.W., Holland, M., Urai, J.L. and Loosveld, R. 2010. Evolution of fault zones in carbonates with mechanical stratigraphy - Insights from scale models using layered cohesive powder. *Journal of Structural Geology*. **32**(9), pp.1375–1391.
- Gibson, H., Stewart, I.S., Pahl, S. and Stokes, A. 2016. A ‘mental models’ approach to the communication of subsurface hydrology and hazards. *Hydrology and Earth System Sciences*. **20**(5), pp.1737–1749.
- Godyń, K. 2016. Structurally Altered Hard Coal in the Areas of Tectonic Disturbances – An Initial Attempt at Classification. *Archives of Mining Sciences*. **61**(3), pp.677–694.
- Golab, A., Ward, C.R., Permana, A., Lennox, P. and Botha, P. 2013. High-resolution three-dimensional imaging of coal using microfocus X-ray computed tomography, with special reference to modes of mineral occurrence. *International Journal of Coal Geology*. **113**, pp.97–108.
- Greb, S.F., Eble, C.F., Williams, D.A. and Nelson, W.J. 2001. Dips, ramps, and rolls- Evidence for paleotopographic and syn-depositional fault control on the Western Kentucky No. 4 coal bed, tradewater formation (Bolsovian) Illinois Basin. *International Journal of*

- Coal Geology*. **45**(4), pp.227–246.
- Greb, S.F., Williams, D.A. and Williamson, A.D. 1992. Geology and Stratigraphy of the Western Kentucky Coal Field. *Kentucky Geological Survey Bulletin*. **3**.
- Green, R., Lord, R.A. and Giusti, L. 1999. Hydrogeochemistry of Durham Coalfield Minewater Pumped To the River Wear, NE England. *Environmental Geochemistry and Health*. **21**(4), pp.339–345.
- Gross, M.R., Bahat, D. and Becker, A. 1997. Relations between jointing and faulting based on fracture-spacing ratios and fault-slip profiles: A new method to estimate strain in layered rocks. *Geology*. **25**(10), pp.887–890.
- Gudmundsson, A., Simmenes, T.H., Larsen, B. and Philipp, S.L. 2010. Effects of internal structure and local stresses on fracture propagation, deflection, and arrest in fault zones. *Journal of Structural Geology*. **32**, pp.1643–1655.
- Guerriero, V., Vitale, S., Ciarcia, S. and Mazzoli, S. 2011. Improved statistical multi-scale analysis of fractured reservoir analogues. *Tectonophysics*. **504**(1–4), pp.14–24.
- Guo, D. and Han, D. 1999. Electron paramagnetic resonance studies of the structurally disturbed coals. *J. China Univ. Min. Technol.* **28**(In Chinese with English abstract), pp.94–97.
- Guo, H., Adhikary, D.P. and Craig, M.S. 2009. Simulation of mine water inflow and gas emission during longwall mining. *Rock Mechanics and Rock Engineering*. **42**(1), pp.25–51.
- Guo, P., Cheng, Y., Jin, K. and Liu, Y. 2014. The impact of faults on the occurrence of coal bed methane in Renlou coal mine, Huaibei coalfield, China. *Journal of Natural Gas Science and Engineering*. **17**, pp.151–158.
- Gupta, A. and Scholz, C.H. 2000. A model of normal fault interaction based on observations and theory. *Journal of Structural Geology*. **22**(7), pp.865–879.
- Gutierrez, M. and Youn, D.J. 2015. Effects of fracture distribution and length scale on the equivalent continuum elastic compliance of fractured rock masses. *Journal of Rock Mechanics and Geotechnical Engineering*. **7**(6), pp.626–637.
- Haimson, B. and Chang, C. 2000. A new true triaxial cell for testing mechanical properties of

- rock, and its use to determine rock strength and deformability of Westerly granite *In: International Journal of Rock Mechanics and Mining Sciences*. Elsevier Science Ltd, pp.285–296.
- Hamilton, S.K., Esterle, J.S. and Sliwa, R. 2014. Stratigraphic and depositional framework of the Walloon Subgroup, eastern Surat Basin, Queensland. *Australian Journal of Earth Sciences*. **61**(8), pp.1061–1080.
- Hamm, V. and Sabet, B.B. 2010. Geothermics Modelling of fluid flow and heat transfer to assess the geothermal potential of a flooded coal mine in Lorraine , France. *Geothermics*. **39**(2), pp.177–186.
- Hammer, E., Mørk, M.B.E. and Næss, A. 2010. Facies controls on the distribution of diagenesis and compaction in fluvial-deltaic deposits. *Marine and Petroleum Geology*. **27**(8), pp.1737–1751.
- Hancock, P.L. and Barka, A.A. 1987. Kinematic indicators on active normal faults in Western Turkey. *Journal of Structural Geology*. **9**(5–6), pp.573–584.
- Handin, J., Hager Jr, R.V., Friedman, M. and Feather, J.. 1963. Experimental Deformation of Sedimentary Rocks Under Confining Pressure: Pore Pressure Tests. *AAPG Bulletin*. **47**(5), pp.717–755.
- Harthong, B., Scholtès, L. and Donzé, F. 2012. Strength characterization of rock masses, using a coupled DEM-DFN model. *Geophysical Journal International*. **191**(2), pp.467–480.
- Hathaway, T.M. and Gayer, R.A. 1996. Thrust-related permeability in the South Wales Coalfield. *Geological Society, London, Special Publications*. **109**, pp.121–132.
- Hawkins, A.B. and McConnell, B.J. 1992. Sensitivity of sandstone strength and deformability to changes in moisture content. *Quarterly Journal of Engineering Geology*. **25**(2), pp.115–130.
- Healy, D., Jones, R.R. and Holdsworth, R.E. 2006. Three-dimensional brittle shear fracturing by tensile crack interaction. *Nature*. **439**(7072), pp.64–67.
- Healy, D., Rizzo, R.E., Cornwell, D.G., Farrell, N.J.C., Watkins, H., Timms, N.E., Gomez-Rivas, E. and Smith, M. 2017. FracPaQ: A MATLAB™ toolbox for the quantification of fracture

- patterns. *Journal of Structural Geology*. **95**, pp.1–16.
- Healy, P.R. and Head, J.M. 1984. *Construction over abandoned mine workings*. No 34.
- Heidbach, O., Tingay, M., Barth, A., Reinecker, J., Kurfeß, D. and Müller, B. 2008. The world stress map database release. *WSM*. **Rel2008(9)**.
- Helgeson, D.E. and Aydin, A. 1991. Characteristics of joint propagation across layer interfaces in sedimentary rocks. *Journal of Structural Geology*. **13(8)**, pp.897–911.
- Helm, P.R., Davie, C.T. and Glendinning, S. 2013. Numerical modelling of shallow abandoned mine working subsidence affecting transport infrastructure. *Engineering Geology*. **154**, pp.6–19.
- Hillier, J.K., Smith, M.J., Armugam, R., Barr, I., Boston, C.M., Clark, C.D., Ely, J., Frankl, A., Greenwood, S.L., Gosselin, L., Hättestrand, C., Hogan, K., Hughes, A.L.C., Livingstone, S.J., Lovell, H., McHenry, M., Munoz, Y., Pellicer, X.M., Pellitero, R., Robb, C., Roberson, S., Ruther, D., Spagnolo, M., Strandell, M., Stokes, C.R., Storrar, R., Tate, N.J. and Wooldridge, K. 2015. Manual mapping of drumlins in synthetic landscapes to assess operator effectiveness. *Journal of Maps*. **11(5)**, pp.719–729.
- Hilt, C. 1873. Die Beziehungen zwischen der Zusammensetzung und den technischen Eigenschaften der Steinkohle. *Ver. Dtsch. Ing. Z.* **17(2)**, pp.194–202.
- Hobbs, D.W. 1964. The tensile strength of rocks. *International Journal of Rock Mechanics and Mining Sciences & Geomechanics Abstracts*. **1(3)**, pp.385–396.
- Holz, M., Kalkreuth, W. and Banerjee, I. 2002. Sequence stratigraphy of paralic coal-bearing strata: An overview. *International Journal of Coal Geology*. **48(3–4)**, pp.147–179.
- Hooker, J.N., Laubach, S.E., Gomez, L., Marrett, R., Eichhubl, P., Diaz-Tushman, K. and Pinzon, E. 2011. Fracture size, frequency, and strain in the Cambrian Eriboll Formation sandstones, NW Scotland. *Scottish Journal of Geology*. **47(1)**, pp.45–56.
- Hooker, J.N., Laubach, S.E. and Marrett, R. 2014. A universal power-law scaling exponent for fracture apertures in sandstones. *Bulletin of the Geological Society of America*. **126(9–10)**, pp.1340–1362.
- Hooker, J.N., Laubach, S.E. and Marrett, R. 2013. Fracture-aperture sizedfrequency, spatial

distribution, and growth processes in strata-bounded and non-strata-bounded fractures, cambrian mesón group, NW argentina. *Journal of Structural Geology*. **54**, pp.54–71.

Horne, J.C., Ferm, J.C., Caruccio, F.T. and Baganz, B.P. 1978. Depositional models in coal exploration and mine planning in Appalachian region. *AAPG Bulletin*. **62**(12), pp.2379–2411.

Houtgast, R.F., Van Balen, R.T., Bouwer, L.M., Brand, G.B.M. and Brijker, J.M. 2002. Late Quaternary activity of the Feldbiss Fault Zone, Roer Valley Rift System, the Netherlands, based on displaced fluvial terrace fragments. *Tectonophysics*. **352**(3–4), pp.295–315.

Hu, Z., Xu, X. and Zhao, Y. 2012. Dynamic monitoring of land subsidence in mining area from multi-source remote-sensing data - a case study at Yanzhou, China. *International Journal of Remote Sensing*. **33**(17), pp.5528–5545.

Hua, W. 2016. Development of Theories and Methods on Water-Inrush Risk Evaluation and Grouting Reinforcement Technique for Lower Group Coal Seam Floor in Northern China Typed Coalfields. . **3**(5), pp.108–124.

Huang, H., Mao, X., Yao, B. and Pu, H. 2012. Numerical simulation on fault water-inrush based on fluid-solid coupling theory. *Journal of Coal Science and Engineering (China)*. **18**(3), pp.291–296.

Huang, Q. and Angelier, J. 1989. Fracture spacing and its relation to bed thickness. *Geological Magazine*. **126**(4), pp.355–362.

Huang, Z. 2014. Analytical and experimental study of water seepage propagation behavior in the fault. *Acta Geodynamica et Geomaterialia*. **11**(4), pp.1–10.

Huang, Z., Jiang, Z., Zhu, S., Qian, Z. and Cao, D. 2014. Characterizing the hydraulic conductivity of rock formations between deep coal and aquifers using injection tests. *International Journal of Rock Mechanics and Mining Sciences*. **71**(16), pp.12–18.

Huggins, P., Watterson, J., Walsh, J.J. and Childs, C. 1995. Relay zone geometry and displacement transfer between normal faults recorded in coal-mine plans. *Journal of Structural Geology*. **17**(12), pp.1741–1755.

- Hull, E. 1873. *The Coal Fields of Great Britain: Their History, Structure, and Resources; with Notices of the Coal-fields of Other Parts of the World* 3rd ed. London, UK: Edward Stanford.
- Huntington, J.F. and Raiche, A.P. 1978. A multi-attribute method for comparing geological lineament interpretations. *Remote Sensing of Environment*. **7**(2), pp.145–161.
- Islam, M.R. and Shinjo, R. 2009. Mining-induced fault reactivation associated with the main conveyor belt roadway and safety of the Barapukuria Coal Mine in Bangladesh: Constraints from BEM simulations. *International Journal of Coal Geology*. **79**(4), pp.115–130.
- Jackson, C.A.L., Gawthorpe, R.L. and Sharp, I.R. 2002. Growth and linkage of the East Tanka fault zone, Suez rift: Structural style and syn-rift stratigraphic response. *Journal of the Geological Society*. **159**(2), pp.175–187.
- Jackson, C.A.L. and Rotevatn, A. 2013. 3D seismic analysis of the structure and evolution of a salt-influenced normal fault zone: A test of competing fault growth models. *Journal of Structural Geology*. **54**, pp.215–234.
- Jackson, I., Lawence, D.J.. and Frost, D.V. 1985. Geological notes and local details for Sheet NZ 27 Cramlington, Killingworth and Wide Open (SE Northumberland). *Memoir of the British Geological Survey*. **Sheets 14**.
- Jardine, P.M., Sanford, W.E., Gwo, J.P., Reedy, O.C., Hicks, D.S., Riggs, J.S. and Bailey, W.B. 1999. Quantifying diffusive mass transfer in fractured shale bedrock. *Water Resources Research*. **35**(7), pp.2015–2030.
- Jébrak, M. 1997. Hydrothermal breccias in vein-type ore deposits: A review of mechanisms, morphology and size distribution. *Ore Geology Reviews*. **12**(3), pp.111–134.
- Jefferies, S.P., Holdsworth, R.E., Shimamoto, T., Takagi, H., Lloyd, G.E. and Spiers, C.J. 2006. Origin and mechanical significance of foliated cataclastic rocks in the cores of crustal-scale faults: Examples from the Median Tectonic Line, Japan. *Journal of Geophysical Research: Solid Earth*. **111**(B12).
- Jessop, A. 1995. Geothermal energy from old mines at Springhill, Nova Scotia, Canada. *Proceedings*. **17**, pp.463–468.

- Jiang, B., Yiwen, J. and Quin, Y. 2004. Textures of tectonic coals and their porosity *In: Mining and Science technology*. London: Taylor & Group, pp.317–320.
- Jing, L. and Hudson, J.A. 2002. Numerical methods in rock mechanics. *International Journal of Rock Mechanics & Mining Sciences*. **39**(4), pp.409–427.
- Johnson, G.A.L. 1984. Subsidence and sedimentation in the Northumberland Trough. *Proceedings of the Yorkshire Geological Society*. **45**(1–2), pp.71–83.
- Johnson, S.A. and Huntoon, P.W. 1994. *Permeability Architecture and Groundwater Circulation Along a Fault-Severed Margin, Northern Hanna Basin, Carbon County, Wyoming*. University of Wyoming.
- Jolley, S.J., Fisher, Q.J. and Ainsworth, R.B. 2010. Reservoir compartmentalization: An introduction. *Geological Society Special Publication*. **347**, pp.1–8.
- Jolley, S.J., Freeman, S.R., Barnicoat, A.C., Phillips, G.M., Knipe, R.J., Pather, A., Fox, N.P.C., Strydom, D., Birch, M.T.G., Henderson, I.H.C. and Rowland, T.W. 2004. Structural controls on Witwatersrand gold mineralisation. *Journal of Structural Geology*. **26**(6–7), pp.1067–1086.
- Jolly, R. and Cosgrove, J. 2003. Geological evidence of patterns of fluid flow through fracture networks: examination using random realizations and connectivity analysis. *Geological Society, London, Special Publications*. **209**(1), pp.177–186.
- Jones, J.. and Dearman, W.R. 1967. Geology of the coast section from Tynemouth to Seaton Sluice *In: Natural History Society of Northumberland, Durham and Newcastle upon Tyne*. Natural History Society of Northumberland, Durham and Newcastle up on Tyne.
- Jones, R.R., Pringle, J.K., Mccaffrey, K.J., Imber, J., Wightman, R.H., Guo, J. and Long, J.J. 2010. Extending digital outcrop geology into the subsurface. *SEPM Concepts in Sedimentology and Paleontology*. **10**, pp.31–50.
- Ju, Y. and Li, X. 2009. New research progress on the ultrastructure of tectonically deformed coals. *Progress in Natural Science*. **19**(11), pp.1455–1466.
- Ju, Y., Yan, Z., Li, X., Hou, Q., Zhang, W., Fang, L., Yu, L. and Wei, M. 2012. Structural Characteristics and Physical Properties of Tectonically Deformed Coals. *Journal of Geological Research*. **2012**, pp.1–14.

- Jung, C. 2016. *Psychological types*. Routledge.
- Kaiser, P.K. and Cai, M. 2012. Design of rock support system under rockburst condition. *Journal of Rock Mechanics and Geotechnical Engineering*. **4**(3), pp.215–227.
- Karacan, C.Ö., Ulery, J.P. and Goodman, G.V.R. 2008. A numerical evaluation on the effects of impermeable faults on degasification efficiency and methane emissions during underground coal mining. *International Journal of Coal Geology*. **75**(4), pp.195–203.
- Katz, O., Reches, Z. and Roegiers, J.C. 2000. Evaluation of mechanical rock properties using a Schmidt Hammer. *International Journal of Rock Mechanics and Mining Sciences*. **37**(4), pp.723–728.
- Kearsey, T., Gillespie, M., Entwisle, D., Damaschke, M., Wylde, S., Fellgett, M., Kingdon, A., Burkin, J., Starcher, V., Shorter, K., Barron, H., Elsome, J., Barnett, M. and Monaghan, A. 2019. UK Geoenergy Observatories Glasgow: GGC01 Cored, seismic monitoring borehole-intermediate data release. *British Geological Survey Open Report*. **OR/19/049**, p.36pp.
- Keefer, D.K. 1984. Landslides caused by earthquakes. *GSA Bulletin*. **95**(4), pp.406–421.
- Kim, Y.-S. and Sanderson, D.J. 2005. The relationship between displacement and length of faults: a review. *Earth-Science Reviews*. **68**, pp.317–334.
- Kim, Y.S., Peacock, D.C.P. and Sanderson, D.J. 2004. Fault damage zones. *Journal of Structural Geology*. **26**(3), pp.503–517.
- Kimbell, G.S., Chadwick, R.A., Holliday, D.W. and Werngren, O.C. 1989. The structure and evolution of the Northumberland Trough from new seismic reflection data and its bearing on modes of continental extension. *Journal - Geological Society (London)*. **146**(5), pp.775–787.
- Knipe, R.J. 1993. The Influence of Fault Zone Processes and Diagenesis on Fluid Flow: Chapter 10: DIAGENESIS AND FAULTS. . **67**, pp.135–151.
- Knott, S.D. 1994. Fault zone thickness versus displacement in the Permo-Triassic sandstones of NW England. *Journal of the Geological Society*. **151**(1), pp.17–25.
- Koike, K., Nagano, S. and Kawaba, K. 1998. Construction and analysis of interpreted fracture planes through combination of satellite-image derived lineaments and digital

- elevation model data. *Computers and Geosciences*. **24**(6), pp.573–583.
- Koken, M. and Constantinescu, G. 2008. An investigation of the flow and scour mechanisms around isolated spur dikes in a shallow open channel: 1. Conditions corresponding to the initiation of the erosion and deposition process. *Water Resources Research*. **44**(8).
- Kolyukhin, D. and Torabi, A. 2012. Statistical analysis of the relationships between faults attributes. *Journal of Geophysical Research: Solid Earth*. **117**(B5).
- Kuchler, M. and Bridge, G. 2018. Down the black hole: Sustaining national socio-technical imaginaries of coal in Poland. *Energy Research and Social Science*. **41**, pp.136–147.
- Kulander, B.R. and Dean, S.. 1993. Coal-Cleat Domains and Domain Boundaries in the Allegheny Plateau of West Virginia. *AAPG Bulletin*. **77**(8), pp.1374–1388.
- Labourdette, R., Lascu, I., Mylroie, J. and Roth, M. 2007. Process-like modeling of flank-margin caves: from genesis to burial evolution. *Journal of Sedimentary Research*. **77**(11), pp.965–979.
- Ladeira, F.L. and Price, N.J. 1981. Relationship between fracture spacing and bed thickness. *Journal of Structural Geology*. **3**(2), pp.179–183.
- Lăpădat, A., Imber, J., Yielding, G., Iacopini, D., McCaffrey, K.J.W., Long, J.J. and Jones, R.R. 2017. Occurrence and development of folding related to normal faulting within a mechanically heterogeneous sedimentary sequence: A case study from Inner Moray Firth, UK *In: Geological Society Special Publication*. Geological Society of London, pp.373–394.
- Laubach, S.E., Eichhubl, P., Hargrove, P., Ellis, M.A. and Hooker, J.N. 2014. Fault core and damage zone fracture attributes vary along strike owing to interaction of fracture growth, quartz accumulation, and differing sandstone composition. *Journal of Structural Geology*. **68**(PA), pp.207–226.
- Laubach, S.E., Lamarche, J., Gauthier, B.D.M., Dunne, W.M. and Sanderson, D.J. 2018. Spatial arrangement of faults and opening-mode fractures. *Journal of Structural Geology*. **108**, pp.2–15.
- Laubach, S.E., Marrett, R.A., Olson, I.E. and Scott, A.R. 1998. Characteristics and origins of coal cleat: a review. *International Journal of Coal Geology*. **35**(1–4), pp.175–207.

- Laubach, S.E., Olson, J.E. and Cross, M.R. 2009. Mechanical and fracture stratigraphy. *AAPG Bulletin*. **93**(11), pp.1413–1426.
- Laubach, S.E. and Tremain, C.M. 1991. Regional coal fracture patterns and coalbed methane development *In: The 32nd US Symposium on Rock Mechanics (USRMS)*. Norman, Oklahoma: American Rock Mechanics Association.
- Lavenu, A.P.C. and Lamarche, J. 2018. What controls diffuse fractures in platform carbonates? Insights from Provence (France) and Apulia (Italy). *Journal of Structural Geology*. **108**, pp.94–107.
- Law, B.E. 1993. The relationships between coal rank and cleat spacing: implications for the prediction of permeability in coal. *In: Proceedings of the 1993 International Coalbed Methane Symposium*. Twscalooosa, Alabama: University of Alabama.
- Lawrence, D.J.. and Jackson, I. 1986. Geology of the Ponteland-Morpeth District. *Memoir of the British Geological Survey*. **Sheets 9 a**.
- Le, Q., Chen, P. and Yang, W. 2010. The relation between modes of lithologic association and interlayer-gliding structures in coal mine. *Journal of Coal Science and Engineering (China)*. **16**(1), pp.47–52.
- Leeder, M.R. 1974. Lower border group (Tournaisian) fluvio-deltaic sedimentation and palaeogeography of the Northumberland basin *In: Proceedings of the Yorkshire Geological Society.*, pp.129–180.
- Leeder, M.R. 1988. Recent developments in Carboniferous geology: a critical review with implications for the British Isles and N.W. Europe. *Proceedings of the Geologists' Association*. **99**(2), pp.79–100.
- Leeder, M.R. 1982. Upper Palaeozoic basins of the British Isles-Caledonide inheritance versus Hercynian plate margin processes. *Journal of the Geological Society, London*. **139**(1980), pp.479–491.
- Leeder, M.R., Portman, C., Andrews, J.E., Collier, R.E.L., Finch, E., Gawthorpe, R.L., McNeill, L.C., Pérez-Arlucea, M. and Rowe, P. 2005. Normal faulting and crustal deformation, Alkyonides Gulf and Perachora peninsula, eastern Gulf of Corinth rift, Greece. *Journal of the Geological Society*. **162**(3), pp.549–561.

- Lehner, F.K. and Pilaar, W.F. 1997. The emplacement of clay smears in synsedimentary normal faults: inferences from field observations near Frechen, Germany. *Norwegian Petroleum Society Special Publications*. **7(C)**, pp.39–50.
- Lei, Q., Latham, J.P. and Tsang, C.F. 2017. The use of discrete fracture networks for modelling coupled geomechanical and hydrological behaviour of fractured rocks. *Computers and Geotechnics*. **85**, pp.151–176.
- Leslie, A.G., Browne, M.A.E., Cain, T. and Ellen, R. 2016. From threat to future asset—The legacy of opencast surface-mined coal in Scotland. *International Journal of Coal Geology*. **164**, pp.123–133.
- Leslie, A.G., Millward, D., Pharaoh, T., Monaghan, A.A., Arsenikos, S. and Quinn, M. 2016. Tectonic synthesis and contextual setting for the Central North Sea and adjacent onshore areas , 21CXR Palaeozoic Project. *British Geological Survey Commissioned Report*. **CR/15/125**, p.18.
- Li, H. 2001. Major and minor structural features of a bedding shear zone along a coal seam and related gas outburst , Pingdingshan coalfield , northern China. *International Journal of Coal Geology*. **47**, pp.101–113.
- Li, H., Bai, H., Yao, B., Yang, C. and Wei, X. 2012. The Influence of Fault Dip Angle on the Floor Fault Activation. *Advanced Materials Research*. **524–527**, pp.375–381.
- Li, H., Ogawa, Y. and Shimada, S. 2003. Mechanism of methane flow through sheared coals and its role on methane recovery. *Fuel*. **82(10)**, pp.1271–1279.
- Li, T., Mu, Z., Liu, G., Du, J. and Lu, H. 2016. Stress spatial evolution law and rockburst danger induced by coal mining in fault zone. *International Journal of Mining Science and Technology*. **26(3)**, pp.409–415.
- Li, W., Ren, T., Busch, A., den Hartog, S.A.M., Cheng, Y., Qiao, W. and Li, B. 2018. Architecture, stress state and permeability of a fault zone in Jiulishan coal mine, China: Implication for coal and gas outbursts. *International Journal of Coal Geology*. **198**, pp.1–13.
- Li, Y.W., Zhang, J. and Liu, Y. 2016. Effects of loading direction on failure load test results for Brazilian tests on coal rock. *Rock Mechanics and Rock Engineering*. **49(6)**, pp.2173–

2180.

- Lianchong, L., Tianhong, Y., Zhengzhao, L., Wancheng, Z. and Chunan, T. 2011. Numerical investigation of groundwater outbursts near faults in underground coal mines. *International Journal of Coal Geology*. **85**(3–4), pp.276–288.
- Lindsay, N.G., Murphy, F.C., Walsh, J.J., Watterson, J., Flint, S. and Bryant, I. 1993. Outcrop studies of shale smears on fault surfaces *In: The geological modelling of hydrocarbon reservoirs and outcrop analogues.*, pp.113–123.
- Liu, S., Sang, S., Pan, Z., Tian, Z., Yang, H., Hu, Q., Sang, G., Qiao, M., Liu, H. and Jia, J. 2016. Study of characteristics and formation stages of macroscopic natural fractures in coal seam #3 for CBM development in the east Qinnan block, Southern Quishui Basin, China. *Journal of Natural Gas Science and Engineering*. **34**, pp.1321–1332.
- Liu, Y., Lu, C.-P., Liu, B., Xiao, Z.-Y. and Zhang, H. 2019. Slip and instability mechanisms of coal-rock parting-coal structure (CRCS) under coupled dynamic and static loading. *Energy Science & Engineering*.
- Liu, Y., Lu, C.P., Zhang, H. and Wang, H.Y. 2019. Numerical investigation of slip and fracture instability mechanism of coal- rock parting-coal structure (CRCS). *Journal of Structural Geology*. **118**, pp.265–278.
- Lohr, T., Krawczyk, C.M., Oncken, O. and Tanner, D.C. 2008. Evolution of a fault surface from 3D attribute analysis and displacement measurements. *Journal of Structural Geology*. **30**(6), pp.690–700.
- Lokhande, R.D., Prakash, A., Singh, K.B. and Singh, K.K.K. 2005. Subsidence control measures in coalmines : A review. . **64**(May), pp.323–332.
- Long, J.J. and Imber, J. 2011. Geological controls on fault relay zone scaling. *Journal of Structural Geology*. **33**(12), pp.1790–1800.
- Loredo, C, Ordóñez, A., Garcia-ordiales, E., Álvarez, R., Roqueñi, N. and Cienfuegos, P. 2017. Science of the Total Environment Hydrochemical characterization of a mine water geothermal energy resource in NW Spain. *Science of the Total Environment*. **576**, pp.59–69.
- Loredo, C., Ordóñez, A., Garcia-Ordiales, E., Álvarez, R., Roqueñi, N., Cienfuegos, P., Peña, A.

- and Burnside, N.M. 2017. Hydrochemical characterization of a mine water geothermal energy resource in NW Spain. *Science of the Total Environment*. **576**, pp.59–69.
- Loredo, C., Roqueñí, N. and Ordóñez, A. 2016. Modelling flow and heat transfer in flooded mines for geothermal energy use: A review. *International Journal of Coal Geology*. **164**, pp.115–122.
- Loredo, J., Ordóñez, A., Jardón, S. and Álvarez, R. 2011. Mine water as geothermal resource in Asturian coal mining basins (NW Spain) In: T. R. Rude, A. Freund and C. Wolkersdorfer, eds. *Proc. IMWA Congress*. Aacehn, Germany: IMWA, pp.177–182.
- Loucks, R.G. 2007. A Review of Coalesced , Collapsed-Paleocave Systems and Associated Suprastratal Deformation. *Acta Carsologica*. **36**(1), pp.121–132.
- Loucks, R.G. 1999. Paleocave carbonate reservoirs: origins, burial-depth modifications, spatial complexity and reservoir implications. *AAPG Bulletin*. **83**, pp.1795–1834.
- Loucks, R.G., Mescher, P.K., Mcmechan, G.A., John, A., Jackson, K.G., Veritas, P.K.M. and Drive, P. 2004. Three-dimensional architecture of a coalesced , collapsed- paleocave system in the Lower Ordovician Ellenburger Group , central Texas. . **5**(5), pp.545–564.
- Lu, C.P., Liu, G.J., Liu, Y. and Zhang, H. 2019. Mechanisms of Rockburst Triggered by Slip and Fracture of Coal–Parting–Coal Structure Discontinuities. *Rock Mechanics and Rock Engineering*.
- Lukawski, M.Z., Silverman, R.L. and Tester, J.W. 2016. Uncertainty analysis of geothermal well drilling and completion costs. *Geothermics*. **64**, pp.382–391.
- Lund, J.. 2001. Geothermal Heat Pumps - An overview. *GHC Bulletin*. **22**(1), pp.1–8.
- Lunn, R.J., Shipton, Z. and Bright, A. 2008. How can we improve estimates of bulk fault zone hydraulic properties? *Geological Society London Special Publications*. **299**, pp.231–237.
- Lunn, Rebecca J., Willson, J.P., Shipton, Z.K. and Moir, H. 2008. Simulating brittle fault growth from linkage of preexisting structures. *Journal of Geophysical Research: Solid Earth*. **113**(7).
- Lyman, G.J. 2003. Stereological and Other Methods Applied to Rock Joint Size Estimation - Does Crofton’s Theorem Apply? *Mathematical Geology*. **35**(1), pp.9–23.

- Ma, D. and Bai, H. 2015. Groundwater inflow prediction model of karst collapse pillar: a case study for mining-induced groundwater inrush risk. *Natural Hazards*. **76**(2), pp.1319–1334.
- MacDonald, A.M., Robins, N.S., Ball, D.F. and Ó Dochartaigh, B.É. 2005. An overview of groundwater in Scotland. *Scottish Journal of Geology*. **41**(1), pp.3–11.
- Macrae, E.J., Bond, C.E., Shipton, Z.K. and Lunn, R.J. 2016. Increasing the quality of seismic interpretation. *Interpretation*. **4**(3), pp.T395–T402.
- Madden, B.J. and Hardmam, D.R. 1992. Long-term stability of bord-and-pillar workings *In: Proceedings of the Symposium on Construction Over Mined Areas*. Petoria, Republic of South Africa.
- Majewska, Z., Ceglarska-Stefańska, G., Majewski, S. and Zietek, J. 2009. Binary gas sorption/desorption experiments on a bituminous coal: Simultaneous measurements on sorption kinetics, volumetric strain and acoustic emission. *International Journal of Coal Geology*. **77**(1–2), pp.90–102.
- Malolepszy, Z. 2003. Man-made, low-temperature reservoirs in abandoned workings of underground mines on example of Nowa Ruda coal mine, Poland *In: International Geothermal Conference*. Reykjavík, pp.23–29.
- Malolepszy, Z., Demollin-Schneiders, E. and Bowers, D. 2005. Potential Use of Geothermal Mine Waters in Europe *In: Proceedings World Geothermal Congress*. Antalya, Turkey, pp.24–29.
- Manzocchi, T. 2002. The connectivity of two-dimensional networks of spatially correlated fractures. *Water Resources Research*. **38**(9), pp.1-1-1–20.
- Marino, G.G. and Gamble, W. 1986. Mine subsidence damage from room and pillar mining in Illinois. *International Journal of Mining and Geological Engineering*. **4**(2), pp.129–150.
- Marrett, R., Gale, J.F.W., Gómez, L.A. and Laubach, S.E. 2018. Correlation analysis of fracture arrangement in space. *Journal of Structural Geology*. **108**, pp.16–33.
- Martin, C.D. and Maybee, W.G. 2000. The strength of hard-rock pillars. *International Journal of Rock Mechanics and Mining Sciences*. **37**(8), pp.1239–1246.

- Mas Ivars, D., Pierce, M.E., Darcel, C., Reyes-Montes, J., Potyondy, D.O., Paul Young, R. and Cundall, P.A. 2011. The synthetic rock mass approach for jointed rock mass modelling. *International Journal of Rock Mechanics and Mining Sciences*. **48**(2), pp.219–244.
- Mauldon, M., Dunne, W.M. and Rohrbaugh, M.B. 2001. Circular scanlines and circular windows: New tools for characterizing the geometry of fracture traces. *Journal of Structural Geology*. **23**(2–3), pp.247–258.
- Mauldon, M. and Mauldon, J.G. 1997. Fracture sampling on a cylinder: From scanlines to boreholes and tunnels. *Rock Mechanics and Rock Engineering*. **30**(3), pp.129–144.
- McCay, A.T., Shipton, Z.K., Lunn, R.J. and Gale, J.F. 2019. Mini thief zones: Subcentimeter sedimentary features enhance fracture connectivity in shales. *AAPG Bulletin*. **103**(4), pp.951–971.
- McConaughy, D.T. and Engelder, T. 2001. Joint initiation in bedded clastic rocks. *Journal of Structural Geology*. **23**(2–3), pp.203–221.
- McGinnis, R.N., Ferrill, D.A., Morris, A.P., Smart, K.J. and Lehrmann, D. 2017. Mechanical stratigraphic controls on natural fracture spacing and penetration. *Journal of Structural Geology*. **95**, pp.160–170.
- McKay, L., Shipton, Z.K., Lunn, R.J., Andrews, B.J., Raub, T. and Boyce, A.J. 2019. Detailed Internal Structure and Along-Strike Variability of the Core of a Plate Boundary Fault: The Highland Boundary Fault, Scotland. *Journal of the Geological Society*.
- McLoughlin, N. 2006. Geothermal heat in Scotland. *SB06-54*. [Online]. [Accessed 13 September 2019]. Available from: www.scottish.parliament.uk/business/research/briefings-06.
- Mcmechan, G.A., Loucks, R.G., Mescher, P. and Zeng, X. 2002. Characterization of a coalesced , collapsed paleocave reservoir analog using GPR and well-core data. . **67**(4), pp.1148–1158.
- Mcquillan, H. 1973. Small-Scale Fracture Density in Asmari Formation of Southwest Iran and its Relation to Bed Thickness and Structural Setting'. *AAPG Bulletin*. **57**(12), pp.2367–2385.
- Menéndez, J., Ordóñez, A., Álvarez, R. and Loredó, J. 2019. Energy from closed mines:

- Underground energy storage and geothermal applications. *Renewable and Sustainable Energy Reviews*. **108**, pp.498–512.
- Micarelli, L., Moretti, I. and Daniel, J.M. 2003. Structural properties of rift-related normal faults: The case study of the Gulf of Corinth, Greece. *Journal of Geodynamics*. **36**(1–2), pp.275–303.
- Min, K.B., Jing, L. and Stephansson, O. 2004. Determining the equivalent permeability tensor for fractured rock masses using a stochastic REV approach: Method and application to the field data from Sellafield, UK. *Hydrogeology Journal*. **12**(5), pp.497–510.
- Ming, L., Jiang, B., Lin, S., Wang, J., Ji, M. and Qu, Z. 2011. Tectonically deformed coal types and pore structures in Puhe and Shanchahe coal mines in western Guizhou. *Mining Science and Technology*. **21**(3), pp.353–357.
- Moir, H. 2010. *Modelling fault zone evolution : the effect of heterogeneity*. University of Strathclyde.
- Moir, H., Lunn, R.J., Shipton, Z.K. and Kirkpatrick, J.D. 2010. Simulating brittle fault evolution from networks of pre-existing joints within crystalline rock. *Journal of Structural Geology*. **32**(11), pp.1742–1753.
- Molnár, L., Tóth, T.M. and Schubert, F. 2014. Statistical characterization of brittle and semi-brittle fault rocks: a clast geometry approach. *Acta Geodaetica et Geophysica*. **49**(4), pp.527–550.
- Monaghan, A.. 2014. *The Carboniferous shales of the Midland Valley of Scotland : geology and resource estimation*. London, UK: British Geological Survey for Department of Energy and Climate Change.
- Monaghan, A.A., Dochartaigh, B.O., Fordyce, F., Loveless, S., Entwisle, D., Quinn, M., Smith, K., Ellen, R., Arkley, S., Kearsley, T., Campbell, S.D., Fellgett, M. and Mosca, I. 2017. UKGEOS - Glasgow Geothermal Energy Research Field Site (GGERFS): Initial summary of the geological platform. *British Geological Survey Open Report*. **OR/17/006**, p.205.
- Moon, V.G. 1993. Microstructural controls on the geomechanical behaviour of ignimbrite. *Engineering Geology*. **35**(1–2), pp.19–31.

- Moore, D.G. 1961. Submarine Slumps. *Journal of Sedimentary Research*. **31**(3), pp.343–357.
- Moore, T.A. 1991. The effects of clastic sedimentation on organic facies development within a Tertiary subbituminous coal bed, Powder River Basin, Montana, U.S.A. *International Journal of Coal Geology*. **18**(3–4), pp.187–209.
- Morettini, E., Thompson, A., Eberli, G., Rawnsley, K., Roeterdink, R., Asyee, W., Christman, P., Cortis, A., Foster, K., Hitchings, V. and Kolkman, W. 2005. Combining high-resolution sequence stratigraphy and mechanical stratigraphy for improved reservoir characterisation in the Fahud field of Oman. *GeoArabia*. **10**(3), pp.17–44.
- Morris, A.P., Ferrill, D.A. and McGinnis, R.N. 2009. Mechanical stratigraphy and faulting in Cretaceous carbonates. *AAPG Bulletin*. **93**(11), pp.1459–1470.
- Mort, K. and Woodcock, N.H. 2008. Quantifying fault breccia geometry: Dent Fault, NW England. *Journal of Structural Geology*. **30**(6), pp.701–709.
- Murchison, D. and Pearson, J. 2000. The anomalous behaviour of properties of seams at the Plessey (M) horizon of the Northumberland and Durham coalfields. . **79**, pp.865–871.
- Myers, I.B. 1962. *The myers-Briggs Type Indicator manual*. Princeton, N.J.: Educational Testing Service.
- Myers, I.B., McCaulley, M.H., Quenk, N.L. and Hammer, A.L. 1998. *MBTI Manual: A guide to the development and use of the Myers-Briggs Type Indicator* 3rd ed. (C. P. Press, ed.). Palo Alto, California.
- Napolitano, R. and Glisic, B. 2019. Methodology for diagnosing crack patterns in masonry structures using photogrammetry and distinct element modeling. *Engineering Structures*. **181**, pp.519–528.
- Narr, W. 1991. Fracture Density in the Deep Subsurface: Techniques with Application to Point Arguello Oil Field (1). *AAPG Bulletin*. **75**(8), pp.1300–1323.
- Narr, W. and Suppe, J. 1991. Joint spacing in sedimentary rocks. *Journal of Structural Geology*. **13**(9), pp.1037–1048.
- Nef, J.. 1965. *The Rise of the British Coal Industry* 2nd ed. Abingdon: Frank Cass & Co. Ltd.
- Nemser, E.S. and Cowan, D.S. 2009. Downdip segmentation of strike-slip fault zones in the

- brittle crust. *Geology*. **37**(5), pp.419–422.
- Neuman, S.P. 1993. Generalized scaling of permeabilities: Validation and effect of support scale. *Geophysical Research Letters*. **21**(5), pp.349–352.
- Neuzil, C.E. 1994. How permeable are clays and shales? *Water Resources Research*. **30**(2), pp.145–150.
- Newman, M.E.J. 2005. Power laws, Pareto distributions and Zipf's law. *Contemporary Physics*. **46**(5), pp.323–351.
- Nicol, A., Watterson, J., Walsh, J.J. and Childs, C. 1996. The shapes, major axis orientations and displacement patterns of fault surfaces. *Journal of Structural Geology*. **18**(2–3), pp.235–248.
- Nixon, C.W., Sanderson, D.J. and Bull, J.M. 2012. Analysis of a strike-slip fault network using high resolution multibeam bathymetry, offshore NW Devon U.K. *Tectonophysics*. **541–543**, pp.69–80.
- Nixon, C.W., Sanderson, D.J. and Bull, J.M. 2011. Deformation within a strike-slip fault network at Westward Ho!, Devon U.K.: Domino vs conjugate faulting. *Journal of Structural Geology*. **33**(5), pp.833–843.
- Nordahl, K., Martinius, A.W. and Kritski, A. 2006. Time-series analysis of a heterolithic, ripple-laminated deposit (Early Jurassic, Tilje Formation) and implications for reservoir modelling. *Marine Geology*. **235**(1-4 SPEC. ISS.), pp.255–271.
- Nriagu, J.O. and Dell, C.I. 1974. Diagenetic Formation of Iron Phosphates in Recent Lake Sediments. *American Mineralogist*. **59**, pp.934–946.
- Nyberg, B., Nixon, C.W. and Sanderson, D.J. 2018. NetworkGT: A GIS tool for geometric and topological analysis of two-dimensional fracture networks. *Geosphere*. **14**(4), pp.1618–1634.
- Nygård, R., Gutierrez, M., Bratli, R.K. and Høeg, K. 2006. Brittle-ductile transition, shear failure and leakage in shales and mudrocks. *Marine and Petroleum Geology*. **23**(2), pp.201–212.
- O'Keefe, J.M.K., Bechtel, A., Christanis, K., Dai, S., DiMichele, W.A., Eble, C.F., Esterle, J.S., Mastalerz, M., Raymond, A.L., Valentim, B. V., Wagner, N.J., Ward, C.R. and Hower,

- J.C. 2013. On the fundamental difference between coal rank and coal type. *International Journal of Coal Geology*. **118**, pp.58–87.
- O Dochartaigh, B.E. 2009. A scoping study into shallow thermogeological resources beneath Glasgow and the surrounding area. *British Geological Survey Research Report*. **IR/09/024**, p.17pp.
- Olson, J.E. 1993. Joint pattern development: effects of subcritical crack growth and mechanical crack interaction. *Journal of Geophysical Research*. **98**(B7).
- Olson, J.E. 2004. Predicting fracture swarms - The influence of subcritical crack growth and the crack-tip process on joint spacing in rock. *Geological Society Special Publication*. **231**, pp.73–87.
- Olson, J.E., Laubach, S.E. and Lander, R.H. 2009. Natural fracture characterization in tight gas sandstones: Integrating mechanics and diagenesis. *AAPG Bulletin*. **93**(11), pp.1535–1549.
- Ortega, O. and Marrett, R. 2000. Prediction of macrofracture properties using microfracture information, Mesaverde Group sandstones, San Juan basin, New Mexico. *Journal of Structural Geology*. **22**(5), pp.571–588.
- Ortega, O.J., Marrett, R.A. and Laubach, S.E. 2006. A scale-independent approach to fracture intensity and average spacing measurement. *AAPG Bulletin*. **90**(2), pp.193–208.
- Page, W. 1907. *The Victoria History of the Counties of England: A History of Durham (Volume 2)* Vol 2. London, UK: Archibald Constable and company limited.
- Pahl, P.J. 1981. Estimating the mean length of discontinuity traces. *International Journal of Rock Mechanics and Mining Sciences and*. **18**(3), pp.221–228.
- De Paola, N., Collettini, C., Faulkner, D.R. and Trippetta, F. 2008. Fault zone architecture and deformation processes within evaporitic rocks in the upper crust. *Tectonics*. **27**(4), pp.1–21.
- De Paola, N., Holdsworth, R.E., McCaffrey, K.J.W. and Barchi, M.R. 2005. Partitioned transtension: An alternative to basin inversion models. *Journal of Structural Geology*. **27**(4), pp.607–625.

- Paterson, M.S. and Wong, T. 2005. *Experimental rock deformation-the brittle field*. Springer Science & Business Media.
- Patsa, L., Zarrouk, S.J., Patsa, E., Van Zyl, D. and Arianpoo, N. 2015. *Geothermal Energy in Mining Developments: Synergies and Opportunities Throughout a Mine's Operational Life Cycle* [Online]. [Accessed 13 September 2019]. Available from: <https://www.researchgate.net/publication/269395965>.
- Paul, S. and Chatterjee, R. 2011. Mapping of cleats and fractures as an indicator of in-situ stress orientation, Jharia coalfield, India. *International Journal of Coal Geology*. **88**(2–3), pp.113–122.
- Peacock, D.C.P. 2001. The temporal relationship between joints and faults. *Journal of Structural Geology*. **23**(2–3), pp.329–341.
- Peacock, D.C.P., Dimmen, V., Rotevatn, A. and Sanderson, D.J. 2017. A broader classification of damage zones. *Journal of Structural Geology*. **102**, pp.179–192.
- Peacock, David C. P., Rotevatn, A. and Sanderson, D.J. 2019. Brecciation driven by changes in fluid column heights. *Terra Nova*. **31**(1), pp.76–81.
- Peacock, D.C.P. and Sanderson, D.J. 2018. Structural analyses and fracture network characterisation: Seven pillars of wisdom. *Earth-Science Reviews*. **184**(June), pp.13–28.
- Peacock, D C P, Sanderson, D.J., Bastesen, E., Rotevatn, A. and Storstein, T.H. 2019. Causes of bias and uncertainty in fracture network analysis. *Journal of Norwegian Geology*. **99**(1), pp.1–16.
- Peacock, D.C.P., Sanderson, D.J. and Rotevatn, A. 2018. Relationships between fractures. *Journal of Structural Geology*. **106**, pp.41–53.
- Peacock, D.C.P. and Zhang, X. 1994. Field examples and numerical modelling of oversteps and bends along normal faults in cross-section. *Tectonophysics*. **234**(1–2), pp.147–167.
- Pei, Y., Paton, D.A., Knipe, R.J. and Wu, K. 2015. A review of fault sealing behaviour and its evaluation in siliciclastic rocks. *Earth-Science Reviews*. **150**, pp.121–138.
- Peterson, E.R., Rayner, S.G. and Armstrong, S.J. 2009. Researching the psychology of cognitive style and learning style: Is there really a future? *Learning and Individual Differences*. **19**(4), pp.518–523.

- Petukhov, I.M. and Linkov, A.M. 1979. The theory of post-failure deformations and the problem of stability in rock mechanics. *International Journal of Rock Mechanics and Mining Sciences and*. **16**(2), pp.57–76.
- Pollard, D. and Segall, P. 1987. Theoretical displacements and stresses near fractures in rock: with applications to faults, joints, veins, dikes, and pressure solution surfaces *In*: B. K. Atkinson, ed. *Fracture mechanics of rock*. London: Academic Press, pp.277–349.
- Pollard, D.D. and Aydin, A. 1988. Geological Society of America Bulletin Progress in understanding jointing over the past century Progress in understanding jointing over the past century. *Geological Society of America Bulletin*. **100**(8), pp.1181–1204.
- Porter, M.L., Sprague, A.R.G., Sullivan, M.D., Jennette, D.C., Beaubouef, R.T., Garfield, T.R., Rossen, C., Sickafoose, D.K., Jensen, G.N., Friedmann, S.J. and Mohrig, D.C. 2006. Stratigraphic Organization and Predictability of Mixed Coarse- and Fine-grained Lithofacies Successions in a Lower Miocene Deep-water Slope-channel System, Angola Block 15 *In*: *AAPG Memoir*. American Association of Petroleum Geologists, pp.281–305.
- Poulsen, B A and Shen, B. 2013. International Journal of Rock Mechanics & Mining Sciences Subsidence risk assessment of decommissioned bord-and-pillar collieries. *International Journal of Rock Mechanics and Mining Sciences*. **60**, pp.312–320.
- Poulsen, B. A. and Shen, B. 2013. Subsidence risk assessment of decommissioned bord-and-pillar collieries. *International Journal of Rock Mechanics and Mining Sciences*. **60**, pp.312–320.
- Pounds, J. and Bailey, L.L. 2001. Cognitive Style and Learning: Performance of Adaptors and Innovators in a Novel Dynamic Task. *Applied Cognitive Psychology*. **15**(5), pp.547–563.
- Power, W.L., Tullis, T.E., Brown, S.R., Boitnott, G.N. and Scholz, C.H. 1987. Roughness of natural fault surfaces. *Geophysical Research Letters*. **14**(1), pp.29–32.
- Powley, A. and Gillian, R. 2015. *Shankly's Village: The Extraordinary Life and Times of Glenbuck and its famous sons*. Durrington, UK: Pitch Publishing.
- Priest, S.D. 1993. *Discontinuity analysis for rock engineering*. Springer Science & Business Media.

- Priest, S.D. and Hudson, J.A. 1981. Estimation of discontinuity spacing and trace length using scanline surveys. *International Journal of Rock Mechanics and Mining Sciences and*. **18**(3), pp.183–197.
- Procter, A. and Sanderson, D.J. 2017. Spatial and layer-controlled variability in fracture networks. *Journal of Structural Geology.*, pp.1–14.
- Qi, Y., Li, M. and Wang, G. 2014. Characteristics of Mine Water Inrush and Its Mechanisms — a Case Study in the Ganhe Coal Mine , Shanxi , China *In: Sui, Sun and Wang, eds. An Interdisciplinary Response to Mine Water Challenges*. Xuzhou: China University of Mining and Technology Press, pp.46–51.
- Qi, Y., Stern, N., Wu, T., Lu, J. and Green, F. 2016. China’s post-coal growth. *Nature Geoscience*. **9**(8), pp.564–566.
- Qiao, W., Hu, G. and Li, W. 2013. Experimental study on the conversion from seepage to flow of water inrush aroused by fault activation in fully mechanized top-coal caving. *Journal of Mining & Safety Engineering*. **1**, p.007.
- Rippon, J., Read, W.A. and Park, R.G. 1996. The Ochil Fault and the Kincardine basin: Key structures in the tectonic evolution of the Midland Valley of Scotland. *Journal of the Geological Society*. **153**(4), pp.573–587.
- Rippon, J.H. 1985. New methods of forecasting the throw and hade of faults in some North Derbyshire collieries. *Mining Engineering*. **145**, pp.198–204.
- Rippon, J.H., Ellison, R.A. and Gayer, R.A. 2006. A review of joints (cleats) in British Carboniferous coals : indicators of palaeostress orientation. *Proceedings of the Yorkshire Geological Society*. **56**(Part 1), pp.15–30.
- Ritchie, J.D., Johnson, H., Browne, M.A.E. and Monaghan, A.A. 2003. Late Devonian-Carboniferous tectonic evolution within the Firth of Forth, Midland Valley: As revealed from 2D seismic reflection data. *Scottish Journal of Geology*. **39**(2), pp.121–134.
- Robeck, E. 2005. *The effects of fault-induced stress anisotropy on fracturing, folding, and sill emplacement: Insights from the Bowie coal mines, southern Piceance basin, western Colorado*. Brigham Young University.
- Roberts, J.J., Wilkinson, M., Naylor, M., Shipton, Z.K., Wood, R.A. and Haszeldine, R.S. 2017.

- Natural CO₂ sites in Italy show the importance of overburden geopressure, fractures and faults for CO₂ storage performance and risk management *In: Geological Society Special Publication*. Geological Society of London, pp.181–211.
- Roche, V., Homberg, C. and Rocher, M. 2013. Fault nucleation, restriction, and aspect ratio in layered sections: Quantification of the strength and stiffness roles using numerical modeling. *Journal of Geophysical Research: Solid Earth*. **118**, pp.4446–4460.
- Rodrigues, C.F., Laiginhas, C., Fernandes, M., Lemos de Sousa, M.J. and Dinis, M.A.P. 2014. The coal cleat system: A new approach to its study. *Journal of Rock Mechanics and Geotechnical Engineering*. **6**(3), pp.208–218.
- Rohrbaugh, J.B., Dunne, W.M. and Mauldon, M. 2002. Estimating fracture trace intensity, density, and mean length using circular scan lines and windows. *AAPG Bulletin*. **86**(12), pp.2089–2104.
- Romano, C., Minto, J.M., Shipton, Z.K. and Lunn, R.J. 2019. Automated high accuracy, rapid beam hardening correction in X-Ray Computed Tomography of multi-mineral, heterogeneous core samples. *Computers & Geosciences*. **131**, pp.144–157.
- Romano, V., De'Haven Hyman, J., Karra, S., Valocchi, A.J., Battaglia, M. and Bigi, S. 2017. Numerical modeling of fluid flow in a fault zone: A case of study from Majella Mountain (Italy). *Energy Procedia*. **125**, pp.556–560.
- De Rosa, S., Shipton, Z., Lunn, R., Kremer, Y. and Murry, T. 2018. Along-strike fault core thickness variations of a fault in poorly lithified sediments, Miri (Malaysia). *Journal of Structural Geology*. **116**, pp.189–206.
- Ryan, B. 2003. *Cleat Development in Some British Columbia Coals* 1st ed. British Columbia Geological Survey, Geological Fieldwork 2002.
- Sagy, A. and Brodsky, E.E. 2009. Geometric and rheological asperities in an exposed fault zone. *Journal of Geophysical Research*. **114**(B2), p.B02301.
- Sagy, A., Brodsky, E.E. and Axen, G.J. 2007. Evolution of fault surface roughness with slip. *Geology*. **35**(3), pp.283–286.
- Salmi, E F, Karakus, M. and Nazem, M. 2019. Assessing the effects of rock mass gradual deterioration on the long-term stability of abandoned mine workings and the

- mechanisms of post-mining subsidence – A case study of Castle Fields mine. *Tunnelling and Underground Space Technology*. **88**(March), pp.169–185.
- Salmi, Ebrahim F, Malinowska, A. and Hejmanowski, R. 2019. Investigating the post-mining subsidence and the long-term stability of old mining excavations : case of Cow Pasture Limestone Mine , West Midlands, UK. *Bulletin of Engineering Geology and the Environment.*, pp.1–18.
- Salvini, R., Mastrorocco, G., Seddaiu, M., Rossi, D. and Vanneschi, C. 2017. The use of an unmanned aerial vehicle for fracture mapping within a marble quarry (Carrara, Italy): photogrammetry and discrete fracture network modelling. *Geomatics, Natural Hazards and Risk*. **8**(1), pp.34–52.
- Sammis, C., King, G. and Biegel, R. 1987. The kinematics of gouge deformation. *Pure and Applied Geophysics PAGEOPH*. **125**(5), pp.777–812.
- Sanderson, D.J. 2015. Field-based structural studies as analogues to sub-surface reservoirs *In: Geological Society Special Publication*. Geological Society of London, pp.207–217.
- Sanderson, D.J. and Nixon, C.W. 2015. The use of topology in fracture network characterization. *Journal of Structural Geology*. **72**, pp.55–66.
- Sanderson, D.J. and Nixon, C.W. 2018. Topology, connectivity and percolation in fracture networks. *Journal of Structural Geology*. **115**(August 2016), pp.167–177.
- Sanderson, D.J., Peacock, D.C.P., Nixon, C.W. and Rotevatn, A. 2018. Graph theory and the analysis of fracture networks. *Journal of Structural Geology*. (April), pp.0–1.
- Sanner, B. 2001. Shallow Geothermal Energy. *GHC Bulletin*. **June**(19).
- Scheiber, T., Fredin, O., Viola, G., Jarna, A., Gasser, D. and Łapińska-viola, R. 2015. Manual extraction of bedrock lineaments from high-resolution LiDAR data : methodological bias and human perception. *GFF*. **137**(4).
- Schmatz, J., Vrolijk, P.J. and Urai, J.L. 2010. Clay smear in normal fault zones - The effect of multilayers and clay cementation in water-saturated model experiments. *Journal of Structural Geology*. **32**(11), pp.1834–1849.
- Scholz, C.H. 1998. Earthquakes and friction laws. *Nature*. **391**, pp.37–42.

- Scholz, C.H. 2019. *The mechanics of earthquakes and faulting* 3rd ed. Cambridge, UK: Cambridge University Press.
- Scholz, C.H., Dawers, N.H., Yu, J.-Z., Anders, M.H. and Cowie, P.A. 1993. Fault growth and fault scaling laws: Preliminary results. *Journal of Geophysical Research: Solid Earth* **98**(B12), pp.21951–21961.
- Schöpfer, M.P.J., Childs, C. and Walsh, J.J. 2006. Localisation of normal faults in multilayer sequences. *Journal of Structural Geology*. **28**(5), pp.816–833.
- Schöpfer, M.P.J., Childs, C. and Walsh, J.J. 2007. Two-dimensional distinct element modeling of the structure and growth of normal faults in multilayer sequences: 2. Impact of confining pressure and strength contrast on fault zone geometry and growth. *Journal of Geophysical Research: Solid Earth*. **112**(10).
- Schöpfer, M.P.J., Childs, C., Walsh, J.J. and Manzocchi, T. 2016. Evolution of the internal structure of fault zones in three-dimensional numerical models of normal faults. *Tectonophysics*. **666**, pp.158–163.
- Schulz, S.E. and Evans, J.P. 2000. Mesoscopic structure of the Punchbowl Fault, Southern California and the geologic and geophysical structure of active strike-slip faults. *Journal of Structural Geology*. **22**(7), pp.913–930.
- Scibek, J., Gleeson, T. and McKenzie, J.M. 2016. The biases and trends in fault zone hydrogeology conceptual models : global compilation and categorical data analysis. *Geofluids*. **16**(4), pp.782–798.
- Scotese, C.R. and McKerrow, W.S. 1990. Revised world maps and introduction. *Geological Society, London, Memoirs*. **12**(1), pp.1–21.
- Shackleton, J.R., Cooke, M.L. and Sussman, A.J. 2005. Evidence for temporally changing mechanical stratigraphy and effects on joint-network architecture. *Geology*. **33**(2), pp.101–104.
- Shanmugam, G., Bloch, R., Mitchell, S., Damuth, J.E., Beamish, G.W.J., Hodgkinson, R.J., Straume, T., Syvertsen, S. and Sheilds, K.. 1996. Slump and debris-flow dominated basin-floor fans in the North Sea: an evaluation of conceptual sequence-stratigraphical models based on conventional core data. *Geological Society, London, Special*

Publications. **103**, pp.145–176.

Sheldon, H.A. and Ord, A. 2005. Evolution of porosity, permeability and fluid pressure in dilatant faults post-failure: Implications for fluid flow and mineralization. *Geofluids*. **5**(4), pp.272–288.

Sheng, Y. and Reddish, D. 2005. Assessment of the water inflow to the mine workings by numerical modelling *In: Post-Mining*. Nancy, France.

Shepherd, J., Rixon, L.K. and Griffiths, L. 1981. Outbursts and geological structures in coal mines: A review. *International Journal of Rock Mechanics and Mining Sciences and*. **18**(4), pp.267–283.

Shi, L. and Singh, R.N. 2001. Study of mine water inrush from floor strata through faults. *Mine Water and the Environment*. **20**(3), pp.140–147.

Shiotani, T., Ohtsu, M. and Ikeda, K. 2001. Detection and evaluation of AE waves due to rock deformation. *Construction and Building Materials*. **15**(5–6), pp.235–246.

Shiple, T.F. and Tikoff, B. 2016. Linking Cognitive Science and Disciplinary Geoscience Practice: The Importance of the Conceptual Model. , pp.219–237.

Shipton, Z.K., Evans, J.P., Kirschner, D., Kolesar, P.T., Williams, A.P. and Heath, J. 2004. Analysis of CO₂ leakage through ‘low-permeability’ faults from natural reservoirs in the Colorado Plateau, east-central Utah. *Geological Society Special Publication*. **233**, pp.43–58.

Shipton, Z.K., Evans, J.P. and Thompson, L.B. 2005. The Geometry and thickness of deformation-band fault core and its influence on sealing characteristics of deformation-band fault zones. *AAPG Memoir*. **85**, pp.181–195.

Shipton, Z.K., Roberts, J.J., Comrie, E.L., Kremer, Y., Lunn, R.J. and Caine, J.S. n.d. Fault Fictions: Cognitive biases in the conceptualization of fault zones *In: S. Ogilvie, J. L. Urai, S. Dee, R. W. Wilson and W. Bailey, eds. Geological Society London Special Publication*.

Shipton, Z.K., Roberts, J.J., Comrie, E.L., Kremer, Y., Lunn, R.J. and Caine, J.S. 2019. Fault Fictions: Systematic biases in the conceptualization of fault zone architecture. *Geological Society, London, Special Publications*., pp.SP496-2018–161.

- Shipton, Z.K., Soden, A., Kirkpatrick, J.D., Bright, A.M. and Lunn, R.J. 2006. How thick is a fault? Fault displacement thickness scaling revisited *In: R. Abercrombie, ed. Earthquakes: Radiated energy and the physics of faulting*. AGU, pp.193–198.
- Shuichang, Z., Jingkui, M., Lihong, L. and Shizhen, T. 2009. Geological features and formation of coal-formed tight sandstone gas pools in China: Cases from Upper Paleozoic gas pools, Ordos Basin and Xujiahe Formation gas pools, Sichuan Basin. *Petroleum Exploration and Development*. **36**(3), pp.320–330.
- Sibson, R.H. 1990. Conditions for fault-valve behaviour R. J. Knipe & E. . Rutter, eds. *Geological Society, London, Special Publications*. **54**(1), pp.15–28.
- Sibson, R.H. 1977. Fault rocks and fault mechanisms. *Journal of the Geological Society*. **133**(3), pp.191–213.
- Sibson, R.H. 1992. Implications of fault-valve behaviour for rupture nucleation and recurrence. *Tectonophysics*. **211**(1–4), pp.283–293.
- Sibson, R.H. 1996. Structural permeability of fluid-driven fault-fracture meshes. *Journal of Structural Geology*. **18**(8), pp.1031–1042.
- Sibson, R.H. 2003. Thickness of the seismic slip zone. *Bulletin of the Seismological Society of America*. **93**(3), pp.1169–1178.
- Sillitoe, R.H. 2000. Styles of High-Sulphidation Gold, Silver and Copper Mineralisation in Porphyry and Epithermal Environments *In: Proceedings of the Australasian Institute of Mining and Metallurgy*. Parkville, Vic, pp.19–34.
- Singhal, B.B.S. and Gupta, R.P. 2010. Fractures and Discontinuities *In: Applied Hydrogeology of Fractured Rocks*. Dordrecht: Springer Netherlands, pp.13–33.
- Sizer, K.E. and Gill, M. 2000. Pillar failure in shallow coal mines—a recent case history. *Mining Technology*. **109**(3), pp.146–152.
- Smailes, A.E. 1938. Population Changes in the Colliery Districts of Northumberland and Durham. *The Geographical Journal*. **91**(3), p.220.
- Smailes, A.E. 1935. The development of the Northumberland and Durham coalfield. *Scottish Geographical Magazine*. **51**(4), pp.201–214.

- Smeraglia, L., Bettucci, A., Billi, A., Carminati, E., Cavallo, A., Di Toro, G., Natali, M., Passeri, D., Rossi, M. and Spagnuolo, E. 2017. Microstructural evidence for seismic and aseismic slips along clay-bearing, carbonate faults. *Journal of Geophysical Research: Solid Earth*. **122**(5), pp.3895–3915.
- Soden, A.M. and Shipton, Z.K. 2013. Dilational fault zone architecture in a welded ignimbrite: The importance of mechanical stratigraphy. *Journal of Structural Geology*. **51**, pp.156–166.
- Soden, A.M., Shipton, Z.K., Lunn, R.J., Pytharouli, S.I., Kirkpatrick, J.D., Do Nascimento, A.F. and Bezerra, F.H.R. 2014. Brittle structures focused on subtle crustal heterogeneities: implications for flow in fractured rocks. *Journal of the Geological Society*. **171**(4), pp.509–524.
- Soliva, R. and Benedicto, A. 2005. Geometry, scaling relations and spacing of vertically restricted normal faults. *Journal of Structural Geology*. **27**(2), pp.317–325.
- Soliva, R., Benedicto, A. and Maerten, L. 2006. Spacing and linkage of confined normal faults: Importance of mechanical thickness. *Journal of Geophysical Research: Solid Earth*. **111**(1).
- Solomon, S. 2007. Carbon Dioxide Storage: Geological Security and Environmental Issues- Case Study on the Sleipner Gas field in Norway. *Bellona report.*, p.128.
- Soper, N.J., Webb, B.C. and Woodcock, N.H. 1987. Late Caledonian (Acadian) transpression in north-west England: timing, geometry and geotectonic significance. *Proceedings of the Yorkshire Geological Society*. **46**(3), pp.175–192.
- Stach, E., Murchison, D., Taylor, G.H. and Zierke, F. 1982. *Stach's textbook of coal petrology* Third. Berlin: Borntraeger.
- Stimpson, B. and Walton, G. 1970. Clay Mylonites in English Coal Measures-their significance in opencast slope stability *In: Conf. Rock Mechanics*. Lisbon, p.355.
- Su, X., Feng, Y., Chen, J. and Pan, J. 2001. The characteristics and origins of cleat in coal from Western North China. *International Journal of Coal Geology*. **47**(1), pp.51–62.
- Sun, Y. and Xu, Z. 2016. Monitoring and numerical simulation of water inrush pathway caused by coal mining above karstic confined aquifer with high water pressure *In:*

- Drebenstedt, Carsten, Paul and Michael, eds. *Proceedings IMWA - Mining Meets Water - Conflicts and Solutions*. Freiburg/Germany, pp.1099–1103.
- Swift, G. 2014. Relationship between joint movement and mining subsidence. *Bulletin of Engineering Geology and the Environment*. **73**(1), pp.163–176.
- Sylvester, A.G. 1988. Strike-slip faults. *Bulletin of the Geological Society of America*. **100**(11), pp.1666–1703.
- Takahashi, M. 2003. Permeability change during experimental fault smearing. *Journal of Geophysical Research: Solid Earth*. **108**(B5).
- Tan, Y.L., Guo, W.Y., Gu, Q.H., Zhao, T. Bin, Yu, F.H., Hu, S.C. and Yin, Y.C. 2016. Research on the Rockburst Tendency and AE Characteristics of Inhomogeneous Coal-Rock Combination Bodies. *Shock and Vibration*. **2016**(Article ID 9271434).
- Tannert, C., Elvers, H.-D. and Jandrig, B. 2007. The Ethics of Uncertainty. *EMBO reports*. **8**(10), pp.892–896.
- Tarasewicz, J.P.T., Woodcock, N.H. and Dickson, J.A.D. 2005. Carbonate dilation breccias: Examples from the damage zone to the Dent Fault, northwest England. *Bulletin of the Geological Society of America*. **117**(5–6), pp.736–745.
- Taylor, G.H., Teichmüller, M., Davis, A.C.F.K., Diessel, C.F.K., Littke, R. and Robert, P. 1998. *Organic Petrology*. Stuttgart: Gebrüder Borntraeger.
- Taylor, W.L., Pollard, D.D. and Aydin, A. 1999. Fluid flow in discrete joint sets: Field observations and numerical simulations. *Journal of Geophysical Research: Solid Earth*. **104**(B12), pp.28983–29006.
- Tchalenko, J.S. 1970. Similarities between shear zones of different magnitudes. *Bulletin of the Geological Society of America*. **81**(6), pp.1625–1640.
- Terzaghi, R.D. 1965. Sources of Error in Joint Surveys. *Géotechnique*. **15**(3), pp.287–304.
- Thomas, L. 2013. *Coal Geology* Second. Chichester: Wiley-Blackwell.
- Ting, F.T.C. 1977. Origin and spacing of cleats in coal beds. *Journal of Pressure Vessel Technology*. **99**(4), pp.626–626.
- Tingay, J. and Ellis, M. 2016. *Hartley Cove to the River Tyne Coastal Strategy Coastal*

- Van Tongeren, P. and Laenen, B. 2005. *Reservoir compartmentalization and anticipated flow-behaviour of the minewater in the former Oranje Nassau coal mining concession area*. Heerlen, The Netherlands.
- Torabi, A., Alaei, B. and Libak, A. 2019. Normal fault 3D geometry and displacement revisited: Insights from faults in the Norwegian Barents Sea. *Marine and Petroleum Geology*. **99**, pp.135–155.
- Torabi, A. and Berg, S.S. 2011. Scaling of fault attributes: A review. *Marine and Petroleum Geology*. **28**(8), pp.1444–1460.
- Torabi, A., Johannessen, M.U. and Ellingsen, T.S.S. 2019. Fault Core Thickness: Insights from Siliciclastic and Carbonate Rocks. *Geofluids*. (Article ID 2918673), pp.1–24.
- Tóth, T.M. 2010. Determination of geometric parameters of fracture networks using 1D data. *Journal of Structural Geology*. **32**(7), pp.878–885.
- Tremain, C.M. and Laubach, S.E. 1991. Coal Fracture (Cleat) Patterns in Upper Cretaceous Fruitland Formation, San Juan Basin, Colorado and New Mexico - Implications for Coalbed Methane Exploration and Development. *Rocky Mountain Association of Geologists*.
- Tripp, G.I. and Vearncombe, J.R. 2004. Fault/fracture density and mineralization: A contouring method for targeting in gold exploration. *Journal of Structural Geology*. **26**(6–7), pp.1087–1108.
- Turner, B.R. and Richardson, D. 2004. Geological controls on the sulphur content of coal seams in the Northumberland Coalfield, Northeast England. *International Journal of Coal Geology*. **60**(2–4), pp.169–196.
- Ulusay, R. and Yoleri, M.F. 1993. Shear strength characteristics of discontinuities in weak, stratified, clay-bearing coal measures encountered in Turkish surface coal mining. *Bulletin of the International Association of Engineering Geology*. **48**(1), pp.109–117.
- Underhill, J.R., Monaghan, A.A. and Browne, M.A.E. 2008. Controls on structural styles, basin development and petroleum prospectivity in the Midland Valley of Scotland. *Marine and Petroleum Geology*. **25**(10), pp.1000–1022.

- Underwood, C.A., Cooke, M.L., Simo, J.A., Muldoon, M.A., Underwood Geological, C.A. and Cooke Geosciences, M.L. 2003. Stratigraphic controls on vertical fracture patterns in Silurian dolomite, northeastern Wisconsin. *AAPG Bulletin*. **87**(1), pp.121–142.
- Vishal, V., Ranjith, P.G. and Singh, T.N. 2015. An experimental investigation on behaviour of coal under fluid saturation, using acoustic emission. *Journal of Natural Gas Science and Engineering*. **22**, pp.428–436.
- Waldron, J.W.F. 2004. Anatomy and evolution of a pull-apart basin, Stellarton, Nova Scotia. *Bulletin of the Geological Society of America*. **116**(1–2), pp.109–127.
- Waldron, J.W.F. 2005. Extensional fault arrays in strike-slip and transtension. *Journal of Structural Geology*. **27**(1), pp.23–34.
- Walker, R.J., Holdsworth, R.E., Imber, J., Faulkner, D.R. and Armitage, P.J. 2013. Fault zone architecture and fluid flow in interlayered basaltic volcanoclastic-crystalline sequences. *Journal of Structural Geology*. **51**, pp.92–104.
- Walsh, J. and Watterson, J. 1988. Dips of normal faults in British Coal Measures and other sedimentary sequences. *Journal of the Geological Society*. **145**, pp.859–873.
- Walsh, J.J., Bailey, W.R., Childs, C., Nicol, A. and Bonson, C.G. 2003. Formation of segmented normal faults: A 3-D perspective. *Journal of Structural Geology*. **25**(8), pp.1251–1262.
- Walsh, J.J., Nicol, A. and Childs, C. 2002. An alternative model for the growth of faults. *Journal of Structural Geology*. **24**(11), pp.1669–1675.
- Walsh, J.J. and Watterson, J. 1989. Displacement gradients on fault surfaces. *Journal of Structural Geology*. **11**(3), pp.307–316.
- Wang, F.P. and Gale, G.F.. 2009. Screening Criteria for Shale-Gas Systems. *Gulf Coast Assoc Geol Soc Trans*. **59**, pp.779–93.
- Wang, J.A. and Park, H.D. 2003. Coal mining above a confined aquifer. *International Journal of Rock Mechanics and Mining Sciences*. **40**(4), pp.537–551.
- Wang, S., Elsworth, D. and Liu, J. 2013. Permeability evolution during progressive deformation of intact coal and implications for instability in underground coal seams. *International Journal of Rock Mechanics and Mining Sciences*. **58**, pp.34–45.

- Ward, C.R. 1984. *Coal geology and coal technology*. United States: Blackwell, Scientific Publications, Inc., Palo Alto, CA.
- Wardell, K. and Wood, J.C. 1965. Ground instability problems arising from the presence of shallow old mine workings. *Proceedings of the Midland Society of Soil Mechanics and Foundation Engineering*. **7**, pp.7–30.
- Warren, J.K. 2016. Hypersaline Fluid Evolution During Burial and Uplift *In: Evaporites*. Springer International Publishing, pp.763–832.
- Watkins, H., Bond, C.E., Healy, D. and Butler, R.W.H. 2015. Appraisal of fracture sampling methods and a new workflow to characterise heterogeneous fracture networks at outcrop. *Journal of Structural Geology*. **72**(February), pp.67–82.
- Watterson, J. 1986. Fault Dimensions, Displacements and Growth. *Pure and Applied Geophysics*. **124**(1–2), pp.365–373.
- Watterson, J., Nicol, A., Walsh, J.J. and Meier, D. 1998. Strains at the intersections of synchronous conjugate normal faults. *Journal of Structural Geology*. **20**(4), pp.363–370.
- Watzlaf, G.R. and Ackman, T.E. 2006. Underground mine water for heating and cooling using geothermal heat pump systems. *Mine Water and the Environment*. **25**(1), pp.1–14.
- Weber, K.J., Mandl, G., Pilaar, W.F., Lehner, F. and Precious, R.G. 1978. The role of faults in hydrocarbon migration and trapping in Nigerian growth fault structures *In: Proceedings of the Annual Offshore Technology Conference*. Offshore Technology Conference, pp.2643–2647.
- Whitaker, F.F. and Smart, P.L. 1997. Groundwater circulation and geochemistry of a karstified bankmarginal fracture system, South Andros Island, Bahamas. *Journal of Hydrology*. **197**(1–4), pp.293–315.
- Whittles, D.N., Yasar, E., Reddish, D.J. and Lloyd, P.W. 2002. Anisotropic strength and stiffness properties of some UK coal measure siltstones. *Quarterly Journal of Engineering Geology and Hydrogeology*. **35**(2), pp.155–166.
- Wibberley, C.A.J., Yielding, G., Giulio, &, Toro, D. and Di Toro, G. 2008. Recent advances in

- the understanding of fault zone internal structure: a review. In: *Wibberley, C. A. J., Kurz, W., Imber, J., Holdsworth, R. E. & Collettini, C. (eds). The internal structure of fault zones: Implications for mechanical and fluid-flow properties. Geological Society, London, Special Publications. 299(1), pp.5–33.*
- Widera, M. 2013. Changes of the lignite seam architecture - A case study from Polish lignite deposits. *International Journal of Coal Geology. 114*, pp.60–73.
- Wilcox, R., Harding, T.P. and Seely, D.R. 1981. Basic Wrench Tectonics. *AAPG Bulletin. 57(1)*, pp.74–96.
- Wilkins, S.J. and Gross, M.R. 2002. Normal fault growth in layered rocks at Split Mountain, Utah: Influence of mechanical stratigraphy on dip linkage, fault restriction and fault scaling. *Journal of Structural Geology. 24(9)*, pp.1413–1429.
- Wilkins, S.J., Gross, M.R., Wacker, M., Eyal, Y. and Engelder, T. 2001. Faulted joints: Kinematics, displacement-length scaling relations and criteria for their identification. *Journal of Structural Geology. 23(2–3)*, pp.315–327.
- Wilson, C.G., Bond, C.E. and Shipley, T.F. 2019. How can geologic decision-making under uncertainty be improved? *Solid Earth. 10*, pp.1469–1488.
- Witkin, H.A. and Goodenough, D.R. 1977. Field dependence and interpersonal behavior. *Psychological bulletin. 84(4)*, p.661.
- Wolf, K.H. and Bruining, H. 2007. Modelling the interaction between underground coal fires and their roof rocks. *Fuel. 86(17–18)*, pp.2761–2777.
- Wood, R. and Curtis, A. 2004. Geological prior information and its applications to geoscientific problems. *Geological Society, London, Special Publications. 239(1)*, 1.2-14.
- Woodcock, N.H. and Mort, K. 2008. Classification of fault breccias and related fault rocks. *Geological Magazine. 145(3)*, pp.435–440.
- Wright, T.D. and Turner, J.P. 2006. *Characterization of 3D fault curvature.*
- Wright, V., Woodcock, N.H. and Dickson, J.A.D. 2009. Fissure fills along faults: Variscan examples from Gower, South Wales. *Geological Magazine. 146(6)*, pp.890–902.

- Wu, H. and D. Pollard, D. 1995. An experimental study of the relationship between joint spacing and layer thickness. *Journal of Structural Geology*. **17**(6), pp.887–905.
- Wu, Q. and Wang, M. 2006. Characterization of water bursting and discharge into underground mines with multilayered groundwater flow systems in the North China coal basin. *Hydrogeology Journal*. **14**(6), pp.882–893.
- Wu, Q., Wang, M. and Wu, X. 2004. Investigations of groundwater bursting into coal mine seam floors from fault zones. *International Journal of Rock Mechanics and Mining Sciences*. **41**(4), pp.557–571.
- Xu, D. 2011. Advances in the research on mechanisms of the groundwater inrush caused by the fault reactivation in coalmines. *Procedia Engineering*. **26**, pp.824–831.
- Yang, S., Wang, J., Ning, J. and Qiu, P. 2019. Experimental Study on Mechanical Properties, Failure Behavior and Energy Evolution of Different Coal-Rock Combined Specimens. *Applied Sciences*. **9**(20), p.4427.
- Yielding, G., Needham, T. and Jones, H. 1996. Sampling of fault populations using sub-surface data: A review. *Journal of Structural Geology*. **18**(2–3), pp.135–146.
- Yin, G., Jiang, C., Wang, J.G. and Xu, J. 2015. Geomechanical and flow properties of coal from loading axial stress and unloading confining pressure tests. *International Journal of Rock Mechanics and Mining Sciences*. **76**, pp.155–161.
- Yin, S., Zhang, J. and Liu, D. 2015. A study of mine water inrushes by measurements of in situ stress and rock failures. *Natural Hazards*. **79**(3), pp.1961–1979.
- Young, B. and Lawrence, D.J.D. 2001. Recent fissuring in the Magnesian Limestone at Houghton-le-Spring, City of Sunderland Urban Geoscience and Geological Hazards Programme. *British Geological Survey Research Report*. **RR/02/03**, p.22.
- Younger, P.L. 1998. Coalfield abandonment: geochemical processes and hydrochemical products. In: K. Nicholson, ed. *Energy and the environment-geochemistry of fossil, and renewable resources*. Aberdeen (UK): Environmental Geochemistry Series No. 1, p.200.
- Younger, P.L. 2004. Environmental impacts of coal mining and associated wastes: A geochemical perspective. *Geological Society Special Publication*. **236**, pp.169–209.

- Younger, P.L. 1995. Hydrogeochemistry of minewaters flowing from abandoned coal workings in County Durham The Durham minewater study Scope of the study. *Quarterly Journal of Engineering Geology and Hydrogeology*. **28**(Supplement 2), pp.S101–S113.
- Younger, P.L. 1994. Minewater pollution; the revenge of Old King Coal. *geoscientist*. **4**(5), pp.6–8.
- Younger, P.L., Banwart, S.A. and Hedin, R.S. 2002. *Mine water: hydrology, pollution, remediation* Vol. 5. Springer Science & Business Media.
- Yu, M., Jefferson, I.A.N. and Culshaw, M. 2006. Geohazards caused by rising groundwater in the Durham Coalfield , U . K . *Society*. (367), pp.1–12.
- Yuan, Y.S., Jin, Z.J., Zhou, Y., Liu, J.X., Li, S.J. and Liu, Q.Y. 2017. Burial depth interval of the shale brittle–ductile transition zone and its implications in shale gas exploration and production. *Petroleum Science*. **14**(4), pp.637–647.
- van der Zee, W. and Urai, J.L. 2005. Processes of normal fault evolution in a siliciclastic sequence: A case study from Miri, Sarawak, Malaysia. *Journal of Structural Geology*. **27**(12), pp.2281–2300.
- Van Der Zee, W., Urai, J.L. and Richard, P.D. 2003. Lateral clay injection into normal faults. *GeoArabia*. **8**(3), pp.501–522.
- Van der Zee, W., Wibberley, C.A.J. and Urai, J.L. 2008. The influence of layering and pre-existing joints on the development of internal structure in normal fault zones: The Lodève basin, France. *Geological Society Special Publication*. **299**, pp.57–74.
- Zeeb, C., Gomez-Rivas, E., Bons, P.D. and Blum, P. 2013. Evaluation of Sampling methods for fracture network characterization using Outcrops. *AAPG Bulletin*. **97**(9), pp.1545–1566.
- Zhang, X.P., Wong, L.N.Y., Wang, S.J. and Han, G.Y. 2011. Engineering properties of quartz mica schist. *Engineering Geology*. **121**(3–4), pp.135–149.
- Zhang, Y., Oldenburg, C.M., Finsterle, S., Jordan, P. and Zhang, K. 2008. Energy Procedia Probability Estimation of CO₂ Leakage Through Faults at Geologic Carbon Sequestration Sites. *Energy Procedia*. **1**, pp.41–46.

- Zhang, Y.X., Hu, S.R., Peng, J.C. and Zhang, X.Q. 2014. The Analysis of the Coal Floor Water Inrush Effected by the Fault. *Applied Mechanics and Materials*. **535**(2), pp.626–630.
- Zhao, C.H. 2012. Fluid-Solid Coupling Analysis the Safety and Critical Distance of the Water-Filled Faults. *Applied Mechanics and Materials*. **204–208**, pp.88–92.
- Zhao, Y., Liu, S., Jiang, Y., Wang, K. and Huang, Y. 2016a. Dynamic Tensile Strength of Coal under Dry and Saturated Conditions. *Rock Mechanics and Rock Engineering*. **49**(5), pp.1709–1720.
- Zhao, Y., Liu, S., Jiang, Y., Wang, K. and Huang, Y. 2016b. Dynamic Tensile Strength of Coal under Dry and Saturated Conditions. *Rock Mechanics and Rock Engineering*. **49**(5), pp.1709–1720.
- Zwingmann, H., Offler, R., Wilson, T. and Cox, S.F. 2004. K-Ar dating of fault gouge in the northern Sydney Basin, NSW, Australia - Implications for the breakup of Gondwana. *Journal of Structural Geology*. **26**(12), pp.2285–2295.